

MOHSIN HABIB

Light Manipulation in Multilayer Metamaterials

MOHSIN HABIB

Light Manipulation in Multilayer Metamaterials

ACADEMIC DISSERTATION

To be presented, with the permission of
the Faculty of Engineering and Natural Sciences
of Tampere University,
for public discussion in the auditorium TB109
of the Tietotalo building, Korkeakoulunkatu 3, 33720, Tampere,
on 20th June 2022, at 12 o'clock.

ACADEMIC DISSERTATION
Tampere University, Faculty of Engineering and Natural Sciences
Finland

<i>Responsible supervisor and Custos</i>	Associate Professor Humeyra Caglayan Tampere University Finland	
<i>Pre-examiners</i>	Assistant Professor Nicolò Maccaferri Umeå University Sweden	Associate Professor Jussi Toppari University of Jyväskylä Finland
<i>Opponent</i>	PD Dr. Tobias Kipp Universität Hamburg Germany	

The originality of this thesis has been checked using the Turnitin OriginalityCheck service.

Copyright ©2022 Mohsin Habib

Cover design: Roihu Inc.

ISBN 978-952-03-2450-6 (print)
ISBN 978-952-03-2451-3 (pdf)
ISSN 2489-9860 (print)
ISSN 2490-0028 (pdf)
<http://urn.fi/URN:ISBN:978-952-03-2451-3>

PunaMusta Oy – Yliopistopaino
Joensuu 2022

Dedicated to my son "**Syed Arham Mohsin**"

ACKNOWLEDGMENTS

In 2018, I decided to move to Finland and pursue my Ph.D. at the Metaplasmonics research group, and since then life has been exciting with ups and downs. Today, I am happy to choose such a peaceful country and especially the student-friendly city of Tampere. The completion of my dissertation was possible because of the support and guidance that I received from my family and my supervisor.

First and foremost, I would like to thank my supervisor, Associate Professor Humeyra Caglayan for providing me the opportunity to work on the aQUARiUM project. I am thankful, for her trust and encouragement during the optimization of different fabrication methods. I would like to thank PD Dr. Tobias Kipp for being my opponent. I am really grateful for the time and effort of my examiners (Assistant professor Nicolò Maccaferri and Associate Professor Jussi Toppari), in order to improve the quality of my dissertation. I am thankful to Dr. Esteban Bermúdez-Ureña for his valuable input in the optimization of the fabrication process.

I appreciate the effort of our group members in the characterization of the samples. I enjoyed working with my office mates both Bilge and Ibrahim and feel very grateful for the help and effort they used to put to finalize my projects. I wish to thank all of the students especially Daria who put a lot of effort into sample fabrication.

I am also thankful to the laboratory staff for keeping the cleanroom operational and providing valuable input based on their experience in different fabrication processes. I wish to thank Anne Viherkoski and Marketta Myllymäki for their help in all my administrative issues.

I am grateful for the support of my friends Nouman and Waleed. The coffee breaks and the discussions we had on research, sports, current affairs, and life in general.

I would like to use this opportunity to once again thank my parents and siblings for their support and encouragement.

Last but not the least, I am blessed to have a kind and supporting wife (Rabia), who has always been there during thick and thin in my life. I dedicate this dissertation to my son "Arham" as he was the best stress buster during the whole writing process and I used to forget my tiredness when he smiled.

Thank you!

Tampere, May 2022

Mohsin Habib

ABSTRACT

Light manipulation has become much more sophisticated with the development of artificial metamaterials. Here, I have studied multilayer thin film-based hyperbolic metamaterials (HMM) in both planar and cylindrical formations. First, the planar HMMs are used as epsilon-near-zero (ENZ) substrates to control the spectral position of plasmonic resonance. The resonance shift is reduced three times on top of HMM compared to a glass substrate. Next, the thin films are rolled to form three-dimensional (3D) rolled-up tubes (RUT) using a strained induced self-rolling mechanism. The RUTs offer flexibility to use a broad range of materials for rolling by using photoresist and germanium as a sacrificial layer. The RUTs are fabricated with different diameters ranging from $\sim 1 \mu\text{m}$ to $10 \mu\text{m}$ by simply changing the thicknesses of dielectric and metal layers. The walls of the RUTs offer tunable material dispersion and can be used as 3D ENZ metamaterials. While, the core of these RUTs can be used as waveguides, which can support the ENZ mode. The modeling manifests that the material dispersion is a function of the thicknesses of the layers and the number of turns and ENZ mode is very sensitive to the diameter of the RUT. Finally, the upper side of the RUT is patterned to form 3D fishnet metamaterials, which exhibit a negative index of refraction in the near-infrared region with low loss and a better figure of merit. The patterning is further upgraded to form nanohole-based metasurfaces that can control the wavefront of light. The curved metasurfaces outperform the conventional planar metasurfaces. The large diameter of RUTs provides enough area to pattern a good number of unit cells, that can be optically characterized. The results of this thesis show that the planar HMMs can be used to effectively reduce the fabrication error for advanced metasurfaces and plasmonic applications. The cylindrical HMMs can serve as a unique platform for 3D metamaterials suitable for sensing applications, trapping biological cells, neurons, and optical trapping of particles.

CONTENTS

1	Introduction	1
1.1	Metamaterials	1
1.2	Outline of thesis	4
2	Hyperbolic metamaterials as ENZ substrates	7
2.1	Hyperbolic metamaterials	7
2.1.1	Multilayer thin films	9
2.2	Plasmonic antennas on conventional substrates	11
2.3	Epsilon-near-zero materials	13
2.4	Plasmonic antennas on ENZ materials	16
2.5	Multilayer ENZ metamaterials as substrate	17
2.6	Controlling Plasmon Resonance	20
3	Self-rolling multilayer metamaterials	27
3.1	Rolled up tubes	28
3.1.1	Photoresist based rolled-up tubes	29
3.1.2	Germanium based rolled-up tubes	32
3.2	Diameter of rolled-up tubes	34
3.3	Rolled up hyperbolic metamaterials	37
3.4	Epsilon near zero properties	39
3.5	Structural dispersion	43
4	Low loss 3D fishnet metamaterial	47
4.1	Fishnet metamaterials	47
4.2	Design and fabrication	48

4.3	Results and discussion	54
4.3.1	S-parameter calculation	56
5	Out-of-plane metasurfaces	59
5.1	Metasurfaces	59
5.2	Results and Discussion	63
6	Thesis Summary	69
6.1	Possible extension of thesis	73
	References	75
	Appendix A	93
	A.1 List of other publications	93
	Publication I	97
	Publication II	111
	Publication III	119
	Publication IV	129
	Publication V	145
	Publication VI	151

List of Figures

1.1	Optical materials definition in ϵ and μ space.	3
1.2	Orientation of field quantities (E , H , S , and k) in (a) RHM and (b) LHM.	4
2.1	Dispersion relation of different materials. (a) Comparison of air and glass, that have isotropic dispersion which can be extended to a spherical shape in 3D. (b) Elliptical dispersion relation for anisotropic medium, that happens by changing the magnitude of one component in ϵ tensor. This change in magnitude allows longer k in one direction and forms an ellipse. (c) Hyperbolic isofrequency of type I and (d) type II HMM.	8
2.2	The schematic of thin film-based multilayer HMM, composed of alternating layers of metal and dielectric with the thicknesses of t_m and t_d , respectively.	9
2.3	Illustration of LSPR, resulting from collective oscillation of electrons in the response of an E -field.	12
2.4	Schematic illustration of plasmonic antennas on top of (a) dielectric (b) metal/dielectric hybrid structure, and (c) metal substrate used to study photoluminescence, hybridization, and sensing application, respectively.	13
2.5	The wave propagation inside a conventional medium with $\epsilon > 1$ and an ENZ material.	14
2.6	The 40 nm of thin film of ITO and (b) measured ϵ via ellipsometer with $\lambda_{\text{ENZ}} = 1340$ nm.	15
2.7	The schematics of (a) HMM, and (b) permittivity values for two different HMM with $ff = 26\%$, and 31%	15

2.8	The schematic representation of HMM-1 and HMM-2 substrates with three bi-layers. (b) The $\text{Re}(\epsilon_{\parallel})$ (black lines) and $\text{Im}(\epsilon_{\parallel})$ (red lines) of HMM-1 (solid lines) and HMM-2 (dashed lines). The crossover of $\text{Re}(\epsilon_{\parallel})$ for HMM-1 (violet dotted line) and HMM-2 (magenta dotted line) are highlighted.	18
2.9	The SEM image of (a) HMM-1 and HMM-2 using FIB (scale bar is 50 nm). The simulated (dashed lines) and measured (solid lines) spectra of transmission (black lines) and reflection (red lines) results for (c) HMM-1 and (d) HMM-2.	19
2.10	The schematic illustration of ND on top of (a) glass and (b) HMM sample. (c) The SEM image of NDs on HMM-1 (scale bare of inset is 200 nm).	20
2.11	Evolution of the plasmon resonance with varying diameters of NDs on (a) glass (b) HMM-1, (c) HMM-2 and (d) spectral shift of the resonance, calculated by FDTD simulations.	22
2.12	Normalized transmission spectra of the fabricated ND arrays, with disk diameters of 120, 140, 160, and 180 nm on three different substrates; (a) glass (green), (b) HMM-1 (red), and (c) HMM-2 (blue). The ENZ points of HMM-1 and HMM-2 are highlighted by violet and magenta vertical dashed lines in the associated graphs, respectively. (d) The spectral shifts in the resonance wavelengths of the NDs on glass, HMM-1, and HMM-2.	23
2.13	Normalized E -field profiles of NDs ($D = 180\text{nm}$) at 684 nm on (a) glass, (b) HMM-1 (PEMA) and (c) HMM-1 (ML stack), and similarly, at 751 nm on (d) glass, (e) HMM-2 (PEMA) and (f) HMM-2 (multi-layer stack).	24

2.14	Phase profiles (in the unit of radian) of x component of the scattered E-field up to 2λ from the NDs of diameters (A) 120 nm, and (B) 180 nm on glass at $\lambda = 684$ nm, (C) 120 nm, and (D) 180 nm on HMM-1 at 684 nm. Similarly, (E) 120 nm, and (F) 180 nm on glass $\lambda = 751$ nm, (G) 120 nm, and (H) 180 nm on HMM-2 at $\lambda = 751$ nm. White dotted lines are added for better visual comparison.	25
3.1	Schematic illustration of self-rolling tubes, the rolling process starts when the sacrificial layer is etched and the stressed layers on top are released by rolling the layers in an upward direction.	28
3.2	Sketch of the sample geometry showing the thin films deposited on top of photoresist. The thin film starts to roll when resist is removed using acetone.	30
3.3	Optical microscope image of SiO_2/Au based RUTs fabricated using resist as a sacrificial layer in single step lithography.	31
3.4	Schematic representation of the fabrication steps for obtaining RUTs. The first step consists of defining the Ge layer pattern. The second step opens a window to define the SiO_2 and Au bilayer, with reduced dimensions on the front and lateral sides in order to facilitate the next step, which is the etching process of the Ge, leading to the self-rolling of the SiO_2/Au layers into a RUT.	33
3.5	Optical microscope image of SiO_2/Au based RUTs fabricated using Ge as a sacrificial layer.	34
3.6	Analytically calculated diameter of a self-rolled structure as a function of Au and SiO_2 thicknesses.	35

3.7	The SEM images of RUTs with (a) $t_d/t_m=5/20$ nm, (b) $t_d/t_m=10/10$ nm, (c) $t_d/t_m=20/10$ nm, (d) $t_d/t_m=20/20$ nm, (e) $t_d/t_m=40/10$ nm, and (f) $t_d/t_m=40/20$ nm. The green scale bar is $2 \mu\text{m}$ and red one is $10 \mu\text{m}$	36
3.8	Schematic representation of a multilayer structure and corresponding ε values defined CEMA method.	38
3.9	$\text{Re}(\varepsilon_\theta)$ for RUTs with two different diameters (600 and 900 nm), three different thicknesses of SiO_2 (10, 20 and 30 nm) and increasing number of bilayers.	40
3.10	(a) Calculated $\text{Re}(\varepsilon_\theta)$ of the fabricated RUTs using CEMA method. (b) Simulated and measured reflectance spectra from RUTs of diameters $2 \mu\text{m}$ (cyan), $3 \mu\text{m}$ (magenta), $5 \mu\text{m}$ (dark yellow) and $7.5 \mu\text{m}$ (navy blue).	41
3.11	(a) $\text{Re}(\varepsilon_{ })$ obtained from PEMA calculations for eight different fabricated RUTs.	42
3.12	(a) The dependence of the waveguide mode effective indices n_{eff} on the wavelengths for the selected diameters. (b) Fundamental TE_{11} electric field $ E $ distribution for the selected diameters of the RUT at their corresponding cutoff wavelength.	44
4.1	Schematic representation of a metal/insulator/metal as a functional layer with magnetic and electric response if used individually. When these two elements are combined, they form a fishnet structure with negative μ and ε at the resonance wavelength.	48
4.2	Schematic representation of a fishnet structure unit cell, where P_x and P_x are set to be 400 nm, $w=230$ nm and l is changed from 190 to 270 nm.	49

4.3	a) The geometry of a metal/dielectric interface, with a dielectric sandwiched between two metal layers. (b) Dispersion relation of SPPs excited by the metal-insulator-metal structure that depicts the internal and external SPP modes which propagate along the internal and external metal-insulator interfaces. The light line ϵ_{air} and ϵ_d show the dispersion relation in free space and the dielectric medium, respectively. The SPPs even and odd show the symmetric and anti-symmetric modes excited by a dielectric sandwiched between two metal layers.	50
4.4	(a) Dispersion curves of the external and gap modes excited by metamaterials milled with holes. The light-line ϵ_d shows the dispersion relation of the dielectric medium and the G parameter corresponds to the reciprocal lattice vector of the stacked holes. The two orange circular insets illustrate the relation of SPPs and the conservation of momentum as a function of the lattice periodicity.	52
4.5	The y component of electric (E) fields from the top at 640 and 780 nm are presented in top panels. Similarly, the x component of H -fields from the cross-section are presented in bottom panels at 640 and 780 nm.	53
4.6	Numerically calculated reflectance response of fishnet structures with length fixed along x -axis and changed in y -axis, 190 nm (black), 210 nm (red), 230 nm (green), 250 nm (blue), and 270 nm (cyan).	54
4.7	a) A microscope image of RUT with 8 alternating metal and dielectric layers with a fishnet pattern on the upper curvature (top view). b) SEM image of the same RUT. A zoom-in of a fishnet with a hole size c) 270, d) 250, e)230, f) 210, and g) 190 nm. h) An SEM cross-section image of the RUT wall.	55

4.8	Experimentally measured reflectance from the RUT-based fishnet structure with five different hole sizes.	56
4.9	The refractive index calculated with S-parameter retrieval method for fishnet structure with hole size a) 190 b) 210 and c) 230 nm. d) FOM of all fishnet structures versus the holes' size.	57
5.1	(a) The top view of varied hole size structures are used to obtain wavefront control. A unit cell is composed of five different hole sizes. (b) The schematics of inclined wavefront transmitted inside the RUT with nanoholes on the top curvature.	61
5.2	Phase profile (units in radians) of y component of the E-field up to 2λ from the nano-holes changing along y axis from 190 to 270 nm at $\lambda=750$ nm. A white arrow is added for better visual comparison. . . .	62
5.3	Released thin films resulting in the formation of RUT with a diameter of $10 \mu\text{m}$. a) Optical microscope image of RUT with nanoholes. The SEM images from (b-c) top, (d) cross-section, and (e-f) bottom corner.	64
5.4	The comparison of different hole size transmission intensity and phase at $\lambda=750$ nm.	65
5.5	Phase response of the y -component of the E-field at $\lambda= 780$ nm for planar and curved metasurfaces with same hole size, respectively. . . .	66
5.6	Phase response of the y -component E-field at $\lambda= 750$ nm for planar and curved metasurfaces with different hole sizes, respectively. . . .	66
5.7	The simulated and measured reflectance spectra of the fabricated sample with nano-holes of different sizes from the planar (black) and curved metasurface (red (simulation) and blue (experiment)). The light is illuminated from the top of the RUT with y -polarization. . . .	67

List of Tables

3.1	Measured approximate inner diameters of the RUTs formed using corresponding t_d and t_m	37
3.2	Comparison of ENZ wavelengths calculated using CEMA and PEMA for the fabricated RUTs.	42

ABBREVIATIONS

$\Delta\epsilon$	Strain difference
β	Propagation wave number
\perp	Perpendicular
δ	Resonant mode
λ	Wavelength
\mathbb{E}	Young's modulus
\mathbb{S}	Scattering parameter
μ	Permiability
ν	Poisson's ratio
ω	Angular frequency
ρ	Radial distance
θ	Theta
ϵ	Permittivity
\vec{G}	Reciprocal lattice vectors
Al_2O_3	Aluminum oxide
EMT	Effective medium theory
E	Electric field
H	Magnetic field
N	Number of turns
S	Poynting vector
ZnO	Zinc oxide

Z	Impedence
c_0	Speed of light in vacuum
c	Speed of light
d	Dielectric
ff	Filling fraction
f	Frequency
k	Wave vector
l	Length
m	Metal
r	Radius
t_d	Dielectric thickness
t_m	Metal thickness
v_p	Phase velocity
w	Width
	Parallel
3D	Three dimensional
4H-SiC	4H-silicon carbide
Ag	Silver
Al: ZnO	Aluminum-doped zinc oxide
AlAs	Aluminum arsenide
Au	Gold
BC	Boundary condition
CEMA	Circular effective medium approximation
D	Diameter
DI	Di-ionized
EBL	Electron beam lithography
ENZ	Epsilon near zero

EOT	Extra ordinary transmission
FDE	Finite Difference Eigenmode
FDTD	Finite-difference time-domain
Fe	Iron
FIB	Focused ion beam
FOM	Figure of merit
Ga: ZnO	Gallium-doped zinc oxide
GaAs	Gallium arsenide
Ge	Germanium
GeOx	Germanium oxide
GPa	Giga pascal
H ₂ O ₂	Hydrogen peroxide
HMDS	Hexamethyldisilazane
HMM	Hyperbolic metamaterial
Im	Imaginary
InGaAs	Indium gallium arsenide
IPA	Isopropanol
ITO	Indium tin oxide
LHM	Left handed material
LSPR	Localized surface plasmon resonance
MBE	Molecular beam epitaxy
MIBK	Metylisobutylketon
min	Minutes
MIR	Mid-infrared
n	index of refraction
N ₂	Nitrogen
n _{eff}	Effective index

NA	Numerical aperture
ND	Nano-disk
NIM	Negative index material
NIR	Near-infrared
O ₂	Oxygen
PECVD	Plasma enhanced chimerical vapor deposition
PEMA	Planar effective medium approximation
PML	Perfect matched layers
PMMA	Poly(methyl methacrylate)
Pt	Platinum
Q-factor	Quality factor
Re	Real
RHM	Right handed material
RIE	Reactive ion etching
RPM	rotations per minute
RUT	Rolled-up tube
sec	Seconds
SEM	Scanning electron microscopy
SiN	Silicon nitride
SiO ₂	Silicon dioxide
SPP	Surface plasmon polariton
SRR	Split ring resonator
TCO	Transparent conductive oxides
TE	Transverse electric
TFSF	Total-Field Scattered-Field
Ti	Titanium
TiO ₂	Titanium dioxide

TM	Transverse magnetic
UV	Ultraviolet
VO ₂	Vanadium dioxide

ORIGINAL PUBLICATIONS

- Publication I A. R. Rashed, M. Habib, N. Das, E. Ozbay and H. Caglayan. Plasmon-modulated photoluminescence enhancement in hybrid plasmonic nano-antennas. *New Journal of Physics* **22**, 9 (2020), 093033.
- Publication II B. Yildiz, M. Habib, A. Rashed and H. Caglayan. Hybridized plasmon modes in a system of metal thin film-nanodisk array. *Journal of Applied Physics* **126**, 11 (2019), 113104.
- Publication III M. Habib, D. Briukhanova, N. Das, B. C. Yildiz and H. Caglayan. Controlling the plasmon resonance via epsilon-near-zero multilayer metamaterials. *Nanophotonics* **9**, 11 (2020), 3637–3644.
- Publication IV M. Habib, I. Issah, D. Briukhanova, E. Bermúdez-Ureña and H. Caglayan. Self-rolling epsilon-near-zero metamaterials. *Accepted for publication in Advanced Optical Materials* **X**, X (2022), X.
- Publication V D. Briukhanova, M. Habib, I. Issah and H. Caglayan. Low loss fishnet metamaterial via self-rolled nanotechnology. *Applied Physics Letters* **119**, 14 (2021), 141101.
- Publication VI M. Habib, I. Issah, D. Briukhanova, A. R. Rashed and H. Caglayan. Wavefront control with nanohole array-based out-of-plane metasurfaces. *ACS Applied nano materials* **4**, 9 (2021), 8699–8705.

Author's contribution

- Publication I The author's contribution was as a co-author. The author optimized the fabrication method for the samples on different substrates and helped to analyze the reflection and transmission response of the samples. Alireza R. Rashed and Nekhel Das characterized the samples. The author helped writing the paper with Alireza R. Rashed under the supervision of Humeyra Caglayan.
- Publication II The author fabricated the samples and helped in analyzing the reflection response of the samples. Bilge Can Yildiz did numerical modeling. The fabricated samples were characterized by Alireza R. Rashed. Humeyra Caglayan supervised and contributed to the manuscript writing process.
- Publication III The author worked with Daria Briukhanova in analytical calculations and numerical modelling of the structures. The author fabricated the samples with Daria Briukhanova. The author characterized the samples with Nekhel Das. Bilge Can Yildiz helped to model the simulation setup and analyze the data. The manuscript was written by the author with the help of Humeyra Caglayan. All the work was guided by Humeyra Caglayan.
- Publication IV The author contributed to the work as a lead author. The author performed the literature survey with Humeyra Caglayan and optimized the fabrication method with the help of Esteban Bermúdez-Ureña. Daria Briukhanova helped with the fabrication method, and Ibrahim Issah performed numerical simulations and characterization. All the authors contributed to writing the manuscript.
- Publication V The author contributed to this work equally with Daria Briukhanova. The author brought the idea and fabricated the samples with the help of Daria Briukhanova. Ibrahim Issah and Daria Briukhanova analytically model the structures. The author measured samples with Ibrahim Issah. Daria Briukhanova

and the author analyzed the results and wrote the manuscript with the help of Humeyra Caglayan.

Publication VI

The author worked on the design, fabrication, and numerical simulations of the structures. Ibrahim Issah helped to model the structures, Daria Briukhanova helped in the deposition process and Alireza R. Rashed characterized the sample. The author analyzed the data with Humeyra Caglayan. The author wrote the manuscript and Humeyra Caglayan supervised the work.

1 INTRODUCTION

Humans have always been fascinated with the development of new materials. From the ability to carve stone, bronze, and iron the early humans have achieved great advances in their lives. The current sophistication of our lives is in a large part bestowed by our ability to make things with different materials. There are two extremes in building things, the huge machines, and the tiny circuits. For example, the best contrast is the large Hadron collider, built to study subatomic particles, the tiniest of things. My interest is somewhere close to the tiniest things and my inspiration comes from the quote by Professor Richard Feynman, "*There is plenty of room at the bottom*" [1]. This is very true, because now we can use nanotechnology to design, control, and shape materials down to the nanometer scale.

1.1 Metamaterials

One of the categories of materials is metamaterials, used to control light in ways that have not been possible before. Light is a form of electromagnetic waves, that can be controlled by materials affecting their electrical and magnetic response. However, the full control of electromagnetic waves/light is still not fully possible because not all the electromagnetic properties are available through the naturally occurring materials. Therefore, a wide range of engineered materials known as metamaterials are studied quite extensively over the last two decades. The prefix "meta" is taken from the Greek language meaning "beyond", as these materials furnish unconventional properties. The metamaterials are man-made materials using subwavelength structural units (meta-atoms) and the electromagnetic properties depend upon the size, shape, and arrangement of these meta-atoms. The concept of metamaterials seems revolutionary; however, it is quite interesting that the history of metamaterials dates back to centuries ago when people used metamaterials in art pieces without understanding the physics. One such example is *Lycurgus Cup* from 1st century BC when

Romans mastered the skill of making gold (Au) nanoparticles and embedding them in the ruby glass [2].

Maxwell's equations govern the optical/electromagnetic response of materials, which describe the inter-relationship between the electric and magnetic fields. An electromagnetic field impinging into a material can induce polarization and magnetization depending on the permittivity (ϵ) and permeability (μ) of the material and define its index of refraction (n). This means the electromagnetic response of materials is the function of their ϵ and μ , ($n=\sqrt{\epsilon\mu}$). Figure 1.1 presents how materials can be divided into four different quadrants based on the value of the ϵ and μ . The transparent dielectric media (e.g. glass) are found in the first quadrant with positive ϵ and μ , and they allow the light to propagate in the medium. The second and fourth quadrants consist of metals and ferrites with negative ϵ or μ , respectively. In these cases, ϵ and μ have opposite signs and the index is imaginary with no propagation of light inside the medium. These three categories of materials have been well known for centuries and are considered as naturally occurring materials [3].

The concept of engineered metamaterials was first introduced by Russian physicist Veselago in the 1960s. He proposed that materials with both negative ϵ and μ can be used to achieve optical response, which had never existed before in nature [4]. For conventional materials, the vectors electric field (E), magnetic field (H) and wavevector (k) form a right-handed triplet. However, the material proposed by Veselago forms a left-handed set, therefore they are labeled as left-handed media (LHM). Figure 1.2 describes the orientation of field quantities E , H , Poynting vector (S) and k for right-handed media (RHM) and LHM. The wavevector in RHM has the same direction as the S . On the other hand, the wavevector is heading in the reverse direction in LHM and results in backward propagation.

This idea of backward propagation of waves was compelling, however, the metamaterial research hadn't started for decades due to the lack of practical designs of metamaterials and as well the applications. Pendry *et al.* attempted to fill the gap between the concept of metamaterials and the exciting applications by introducing the concept of split-ring resonators (SRR) in 1999 [5] and perfect lensing in 2000 with negative refraction of light [6]. These two works encouraged the scientist to look deeper into the topic of metamaterials. Smith *et al.* in 2000, used the concept of SRR and combined it with continuous wires, to exhibit metamaterials with simultaneously negative values of ϵ and μ [7]. These seminal papers by Pendry and

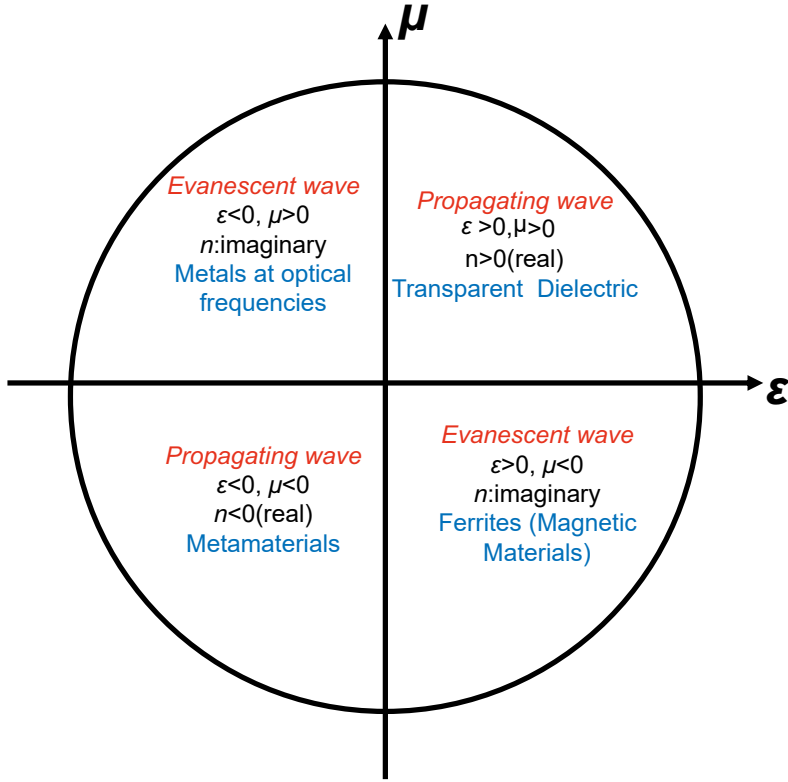


Figure 1.1 Optical materials definition in ϵ and μ space.

Smith instigated the idea of bringing the concept of metamaterials into the optics community for the manipulation of light. However, this was challenging for optical wavelengths because the basic idea of metamaterials requires an array of meta-atoms (artificial atoms) much smaller than the operational wavelength. Over the last two decades, a lot of effort has been put into miniaturizing the design of metamaterials for optical wavelengths. Recent advancement in the field of nanofabrication has allowed the realization of structures much smaller than the wavelength of light.

Among these metamaterials, the multilayer thin film-based hyperbolic metamaterials (HMM) have been studied quite extensively due to their astonishing applications in the field of sensing [8–10] and quantum information processing [11, 12]. One of the reasons for the interest in the topic of HMM is the simple thin film-based design. The thin films used in these metamaterials are easy to fabricate and readily available [13]. However, most of these works on the topic of HMM are limited to planar systems and it is very hard to integrate materials inside these films once the

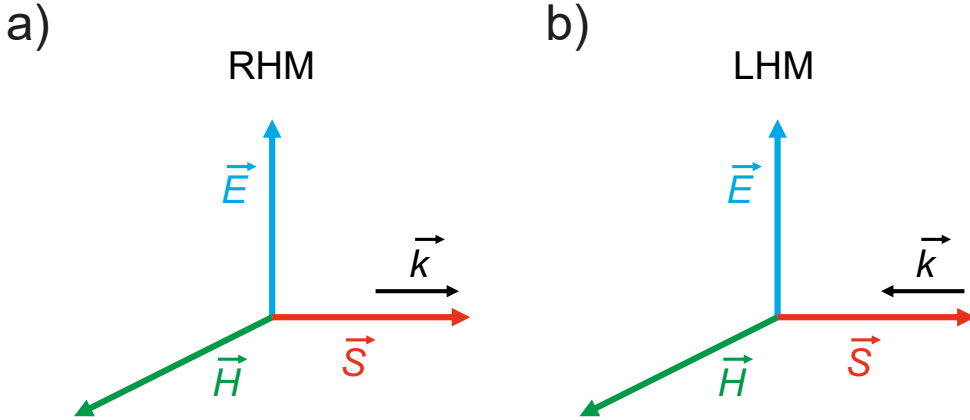


Figure 1.2 Orientation of field quantities (E , H , S , and k) in (a) RHM and (b) LHM.

fabrication is done. This limits their applications and therefore, in this dissertation, I have uncovered new possibilities to use this thin film based HMM by using them as a substrate and by rolling the thin films of metal and the dielectric layers to form a rolled-up tube (RUT), that serves as three dimensional (3D) HMM. These RUTs were then further patterned to obtain 3D fishnet metamaterials and curved meta-surfaces. From another perspective, I have used the multilayer thin films in three different applications, i.e. planar substrate, cylindrical ENZ metamaterials for enhanced light-matter interaction, and modification of light propagation. The focus of the dissertation is to use thin film-based metamaterials to their true potential by optimizing the fabrication methods, structure, and optical properties.

1.2 Outline of thesis

This thesis is for a better understanding of fundamental physics, design, and fabrication of multilayer thin film-based metamaterials. The thesis provides a solution to the problems associated with the fabrication of multilayer thin film-based structures and opens a new avenue for 3D metamaterials. The thesis is a compilation of several works done during my Ph.D. The thesis is a compilation of six publications and divided into four chapters, starting from the second chapter, the results work from PUBLICATION I, II, and III are presented, which are focused on studying the

plasmonic nanoantenna on top of planar substrates. In the third chapter, the idea of self-rolling multilayer metamaterials will be discussed from PUBLICATION number IV. Similarly, the fishnet and out-of-plane metasurfaces are presented in chapter 4 (PUBLICATION V) and chapter 5 (PUBLICATION VI), respectively. The detailed topics that each chapter covers are discussed in detail as:

Chapter 1: The first chapter starts with the motivation of my work in the field of nanotechnology and the topic of metamaterials. The field of metamaterial is briefly introduced in the context of history by discussing some of the pioneering works.

Chapter 2: The second chapter presents the basic concepts of HMM, and discusses in detail the thin film-based fabrication method, and their epsilon-near-zero (ENZ) feature. The second section discusses the topic of ENZ materials and their applications. In the third section, the localized surface plasmon resonance (LSPR) is explained in detail, especially how it can be controlled by using three different types of substrates. Then, the use of ENZ materials as a substrate to control the plasmon resonance is explained and some of the recent works on the topic are discussed briefly. In the fifth section, the design of the HMMs as an ENZ substrate is presented, first, the numerically calculated ϵ values are presented, and then their fabrication is explained. Next, the detail about the design, fabrication, and characterization of the plasmonic antenna on top of HMM as an ENZ substrate and on top of the glass as a reference sample is presented in detail.

Chapter 3: It starts with the motivation behind the use of the self-rolling fabrication method and its possible applications in the field of metamaterials. The unique self-rolling fabrication method is explained in detail with a literature survey about different works done over the last two decades. Then, the top-down and bottom-up approaches used to obtain self-rolling tubes are presented. The explanation continues with two methods used in this thesis to fabricate the silicon dioxide (SiO_2) and Au-based RUTs. Next, the tube diameter is modeled analytically to predict the diameter of the tubes. The results on different fabricated samples are presented and the dispersion as an effective medium is discussed in detail for each RUT. The ENZ feature of the RUTs is identified with materials dispersion and structural dispersion.

Chapter 4: The fourth chapter is an extension of the third chapter, the chapter is one step forward in using thin films as curved metamaterials. This time the RUTs are patterned as a fishnet structure. The chapter first explains the concept of fishnet metamaterials, the design, and fabrication adopted in this thesis. The results

section presents the images of fabricated samples, their reflection spectrum, and the numerically calculated refractive index.

Chapter 5: This chapter is another extension of the previous work; the chapter starts with the motivation to use the RUTs to form more complex metamaterials. It first introduces the concept of metasurfaces and how it is different from conventional metamaterial. Then, the design of nanohole-based metasurfaces on top RUTs is presented and how it controls the phase response by changing hole sizes. The fabricated samples are presented, and the phase response is investigated in more detail for curved and planar cases. In the end, the reflection response of metasurfaces is measured and compared with the simulations.

Chapter 6: The works done in this thesis are summarized in chapter 6 and the possible extension of the thesis is presented to the readers.

2 HYPERBOLIC METAMATERIALS AS ENZ SUBSTRATES

2.1 Hyperbolic metamaterials

In air the propagating light has a linear dispersion and isotropic behavior which forms a spherical isofrequency contour given by:

$$k_x^2 + k_y^2 + k_z^2 = \frac{\omega^2}{c^2} \quad (2.1)$$

Here, ω is frequency of radiation c is speed of light in vacuum. The transverse magnetic (TM) wave in a uniaxial medium will change the infrequency relation to

$$\frac{k_x^2 + k_y^2}{\varepsilon_z} + \frac{k_z^2}{\varepsilon_x} = \frac{\omega^2}{c^2} \quad (2.2)$$

The ε of uniaxial medium is given by a tensor, where in-plane isotropic component $\varepsilon_x = \varepsilon_y = \varepsilon_{\parallel}$ and out of plane component is $\varepsilon_z = \varepsilon_{\perp}$.

$$\varepsilon = \begin{pmatrix} \varepsilon_x & 0 & 0 \\ 0 & \varepsilon_y & 0 \\ 0 & 0 & \varepsilon_z \end{pmatrix} = \begin{pmatrix} \varepsilon_{\parallel} & 0 & 0 \\ 0 & \varepsilon_{\parallel} & 0 \\ 0 & 0 & \varepsilon_{\perp} \end{pmatrix} \quad (2.3)$$

The normal spherical isofrequency contour in air changes to ellipsoid for an anisotropic medium. However, if one of the principal components of the ε tensor is opposite in sign to the other two principal components, this results in extreme anisotropy and the isofrequency contour will be an open hyperboloid. The hyperbolic word used for HMM originated from the topology of this isofrequency

contour. These materials behave like metal in one direction and as an insulator in the other [14]. Although, these kinds of materials are not easily accessible in nature; they can be artificially created using nanostructures and thin films. The isofrequency contours in the air are presented in Figure 2.1 (a) and compared with a glass medium. Similarly, Figure 2.1 (b) presents the contours for ellipsoid/anisotropic medium. Next, the isofrequency contours of HMM type I and type II are presented in Figure 2.1 (c) and (d), respectively.

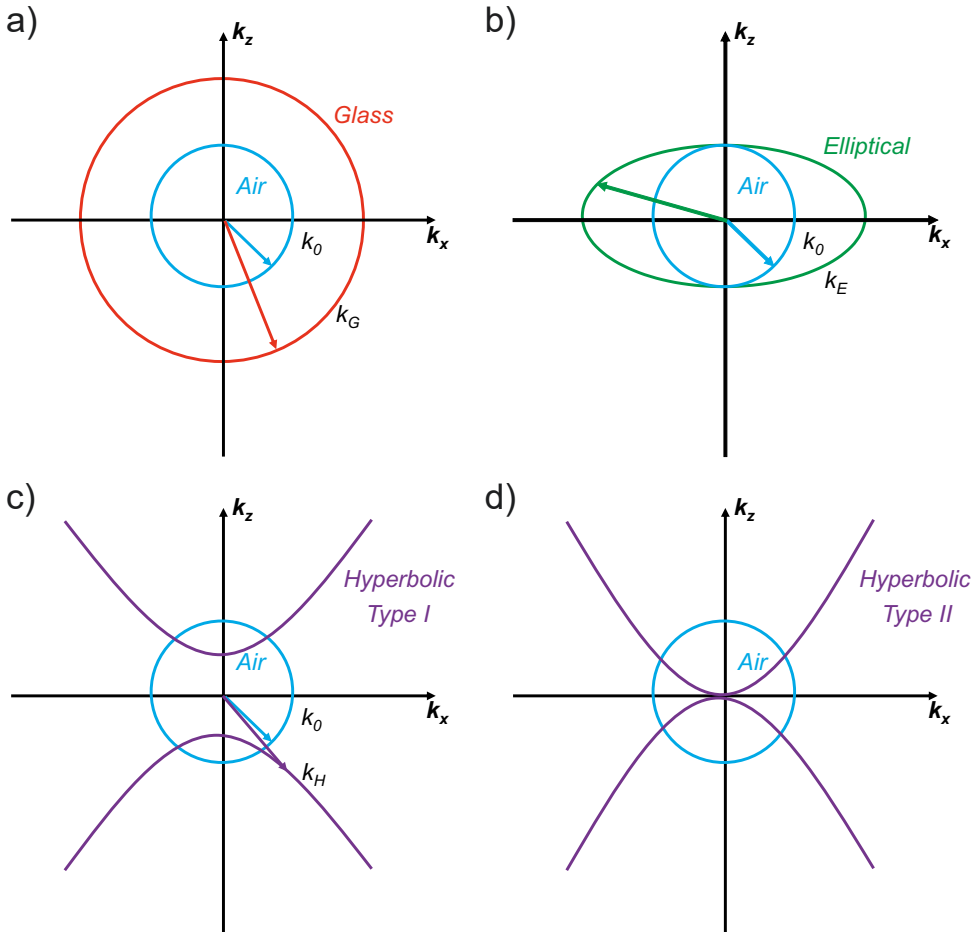


Figure 2.1 Dispersion relation of different materials. (a) Comparison of air and glass, that have isotropic dispersion which can be extended to a spherical shape in 3D. (b) Elliptical dispersion relation for anisotropic medium, that happens by changing the magnitude of one component in ϵ tensor. This change in magnitude allows longer k in one direction and forms an ellipse. (c) Hyperbolic isofrequency of type I and (d) type II HMM.

The classification of HMM is based on how many components of ϵ tensor are negative, the type I HMMs have only one ($\epsilon_z < 0$ and $\epsilon_x; \epsilon_y > 0$) while type II HMMs have two negative components ($\epsilon_z > 0$ and $\epsilon_x; \epsilon_y < 0$). In addition to that, the type I isofrequency contours are separated into two sheets. On the other hand, type II has only a single sheet, this is because type II is more metallic than type I. There are two common methods to realize HMMs: multilayer thin films and nanowires [15]. In this dissertation (PUBLICATION III, IV, V, and VI), I have used multilayer thin film based HMM, therefore, the working principle will be discussed in more detail.

2.1.1 Multilayer thin films

This method uses alternating layers of metal and dielectric to achieve extreme anisotropy. The thicknesses of these layers are very low compared to the operating wavelength. An example of multilayer HMM is presented in Figure 2.2. The optical properties of thin film based HMMs are modelled by effective medium approximation (EMT) [14–20]. The EMT is an approximation of the effective permittivity of planar thin films and here it is defined as the planar effective medium approximation (PEMA), where in-plane isotropic/parallel components are defined as $\epsilon_{xx} = \epsilon_{yy} = \epsilon_{\parallel}$. The third component which is out of the plane (perpendicular component) is defined as $\epsilon_{zz} = \epsilon_{\perp}$.

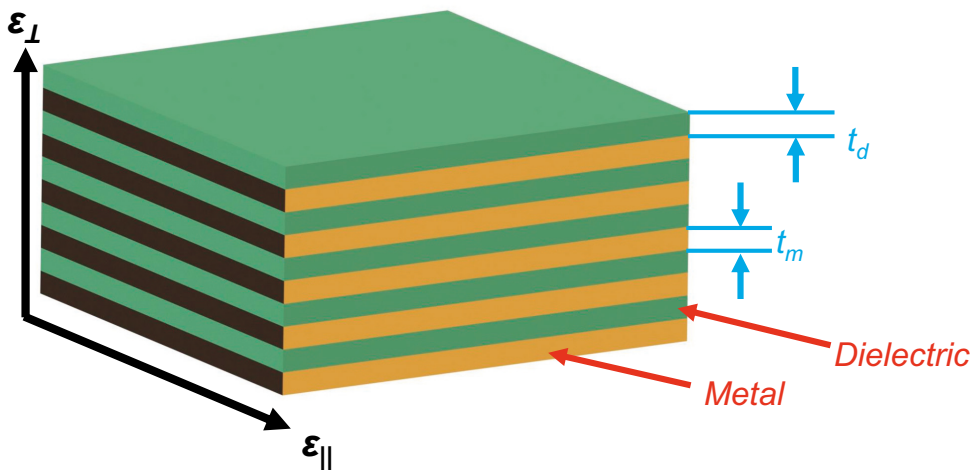


Figure 2.2 The schematic of thin film-based multilayer HMM, composed of alternating layers of metal and dielectric with the thicknesses of t_m and t_d , respectively.

The parallel and perpendicular components of ε of a medium composed of alternating thin layers of metal and dielectric are defined using a generalized Maxwell-Garnett approach [14]. First the filling fraction ($ff = t_m/(t_m + t_d)$) is defined, with $t_{m(d)}$ being the thickness of the metal (dielectric) layer. The displacement (D) field in an effective material is defined as:

$$D = \varepsilon_{eff} E \quad (2.4)$$

where ε_{eff} is the effective permittivity of the material. It is well-known that the tangential component of the E -field should be continuous across a boundary of two different media. Therefore, the E -fields along the parallel axis is defined as:

$$E_{\parallel(m)} = E_{\parallel(d)} = E_{\parallel} \quad (2.5)$$

and the over all displacement can be defined as:

$$D_{\parallel} = ff D_{\parallel(m)} + (1 - ff) D_{\parallel(d)} \quad (2.6)$$

by rearranging the equations

$$\varepsilon_{\parallel} E_{\parallel} = ff \varepsilon_m E_{\parallel} + (1 - ff) \varepsilon_d E_{\parallel} \quad (2.7)$$

by solving the equation:

$$\varepsilon_{\parallel} = ff \varepsilon_m + (1 - ff) \varepsilon_d \quad (2.8)$$

Similarly, the ε_{\perp} is calculated by using boundary condition of normal components:

$$D_{\perp(m)} = D_{\perp(d)} = D_{\perp} \quad (2.9)$$

$$E_{\perp} = ff E_{\perp(m)} + (1 - ff) E_{\perp(d)} \quad (2.10)$$

by using Maxwell's equation:

$$\varepsilon_{\perp} = \frac{\varepsilon_m \varepsilon_d}{ff \varepsilon_d + (1 - ff) \varepsilon_m} \quad (2.11)$$

Therefore, the effective material dispersion of such metamaterials can be controlled by changing the amount of metal and dielectric materials forming the structure [16]. Some of the promising applications of HMM are near-perfect absorption [21], abnormal scattering [22], high-sensitivity sensors [23], and long-range energy transfer [24].

2.2 Plasmonic antennas on conventional substrates

In parallel to metamaterials, the topic of plasmonics has also been studied quite extensively with the development of nanofabrication for two decades. The excitation of the surface plasmons on the interface of thin metal/dielectric films initiated the plasmonic research [25–29].

The surface waves propagate near the surface interacting with the electronic cloud of the metal. This interaction generates electron oscillations near the surface when excited with an electromagnetic field. The surface plasmons are bounded to the interface of metal/dielectric layers and they decay exponentially. In 1971 Kretschmann and Raether introduced the Kretschmann configuration in order to excite these surface plasmon and this is the most widely used excitation method [30]. As the SPP dispersion curve lies outside the light cone, the momentum of light and SPP can be matched using different coupler configurations such as prism couplers. The working principle of configuration is to first pass light through a dense glass (a prism with ϵ), in order to change the phase velocity of light. The wave vector (k_{sp}) that is propagating along the interface is given as:

$$k_{sp} = \frac{\omega_{sp}}{c} \sqrt{\frac{\epsilon_m \epsilon_d}{\epsilon_m + \epsilon_d}} \quad (2.12)$$

where ω_{sp} is the angular frequency of surface plasmon and ϵ_m and ϵ_d are permittivity values for metal and dielectric. When the wave vector of the excitation light (k_{in}) matches with the k_{sp} , the surfaces plasmon are generated along the interface [31].

Similar to a thin metal film, when the light interacts with a metallic nanoparticle much smaller than the wavelength of light the surface plasmons confine around the nanoparticle. Figure 2.3 presents the light incident on an Au nanosphere, which generates the oscillation of an electron cloud. This oscillation will trap the light around

subwavelength metal nanoparticle and generate the LSPR [32, 33], with enhanced E -field [34]. This enhanced local E -field is used for miniaturizing optical devices, cellular imaging devices [35], surface-enhanced Raman spectroscopy [36] and nano-plasmonic rulers [37, 38]. Additionally, the resonance frequency of this nanoparticle is dependent upon the density of electrons, the effective electron mass, size, and as well as shape of the nanoparticle. Moreover, the environment surrounding the nano-antenna can also change the LSPR mode, which has been used for sensing applications [39, 40].

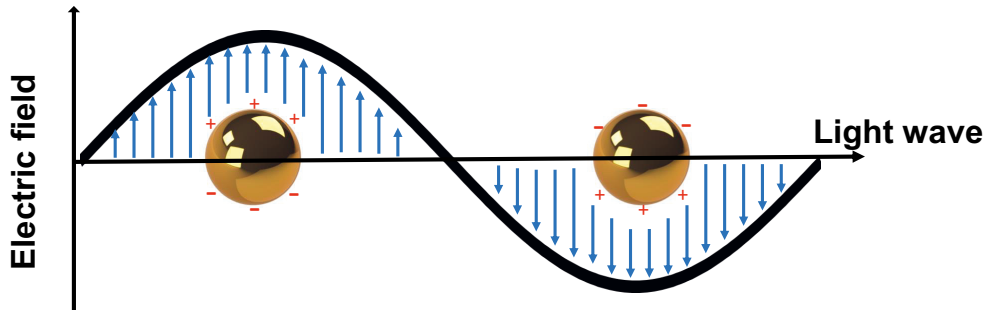


Figure 2.3 Illustration of LSPR, resulting from collective oscillation of electrons in the response of an E -field.

Although the integration and accurate placement of these nanoparticles on a sample are rather limited, with the advancement in nanofabrication, it is possible to fabricate such particles in the form of nano-antenna on top of a substrate. There are several different shapes and organization of plasmonic antenna such as nano-disk (ND) [41, 42], nano-rods [43], dimers [44], bow-tie antenna [45, 46], V-shaped antenna [47] and several others [34, 48]. All these works concentrate on designing the plasmonics antenna based on shape, size, and arrangement. Yet, the effect of the substrate that holds these nanoantennas has been overlooked, since mostly dielectric substrates e.g. glass or silicon were used. The study by Michelle *et al.* show the shift of the LSPR from 611 to 635 nm [49] using Ag nanoparticles on top of different dielectric substrates by changing the index of the substrate from 1.46 to 1.73.

In this dissertation, NDs on top Si/SiO₂ are fabricated with a fixed period and changing diameter to study the photoluminescence enhancement (PUBLICATION I) [42]. In PUBLICATION II, NDs are fabricated on thin metal and dielectric hybrid substrate to study hybridization between localized and propagating surface plas-

mons [41]. Later, Prof. Halas's group studied dimer nano-antenna on top of metal as a substrate for refractive index sensing [34]. Figure 2.4 presents schematics of three different substrates used to modify the LSPR.

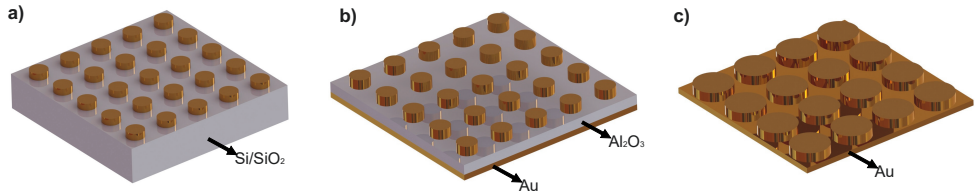


Figure 2.4 Schematic illustration of plasmonic antennas on top of (a) dielectric (b) metal/dielectric hybrid structure, and (c) metal substrate used to study photoluminescence, hybridization, and sensing application, respectively.

It is important to note that, both dielectric and metallic nature of the substrate can affect the plasmon resonance. The ϵ of the dielectric can shift the response of the antenna, on the other hand, by using metal as a substrate the LSPR is broader compared to the dielectric substrate [34]. Modification of the substrate can be a tool to tune, shift or modify the resonance band. In addition, recently, the unusual ENZ materials were used as substrates to control the LSPR of plasmonic antennas, revealing their great potential for plasmon-ENZ systems.

2.3 Epsilon-near-zero materials

The permittivity window where there is shift from dielectric to metallic nature is very exciting because it exhibits the ENZ feature of a material, where ϵ is close to zero [13, 50, 51]. The ENZ materials have become a topic of interest in recent years, because of their ability to form novel platform for unique nanophotonics devices [52]. In recent years, the ENZ materials have helped the photonic community to study novel phenomena such as electromagnetic field energy squeezing [53, 54], slow light trapping [55], sub-wavelength field confinement [56], large non-linearity [57, 58], second [59], third [60] and even higher order harmonic generation [61], and super coupling [62]. In addition to these the ENZ materials have also proved to be significantly better performing in tunable system such as; electric-optical [63], all optical [64] and heat [65] based tunable devices. The peculiar optical property of ENZ materials is used quite extensively in electro-optical switches [66], modulators

[67], absorbers [68] and isolators [69] as well as on-chip quantum networks [70], and better imaging and lithography systems [71].

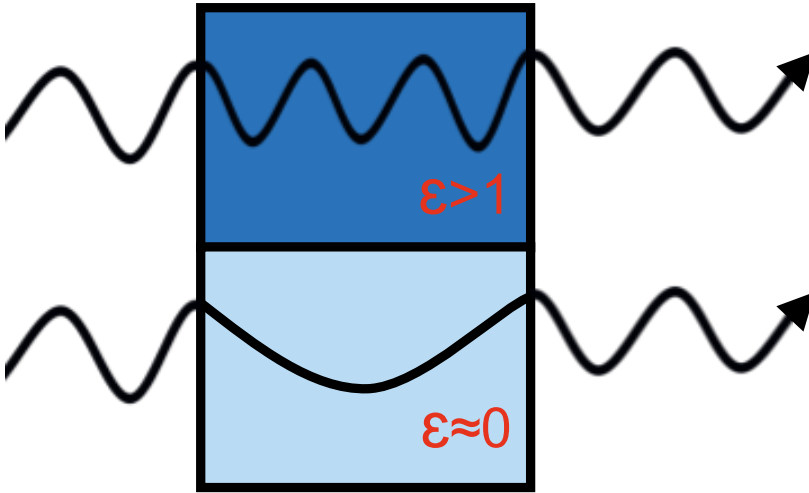


Figure 2.5 The wave propagation inside a conventional medium with $\epsilon > 1$ and an ENZ material.

The unique optical properties of ENZ materials can be explained by investigating their electromagnetic response. In any medium, the speed at which the wave/light propagates is defined as phase velocity (v_p). Both the frequency (f) and wavelength (λ) inside a medium are related to v_p and change by traveling in a medium. Analytically they can be defined:

$$v_p = f \lambda = \frac{c_0}{\sqrt{\epsilon}} \quad (2.13)$$

while propagating inside the medium due to the divergence, the frequency of the light changes, which is defined in terms of wavelength as:

$$\lambda_{ENZ} = \lambda_0 / \sqrt{\epsilon \mu} \quad (2.14)$$

for an ENZ material with $\epsilon = 0$, this means that the effective wavelength is significantly large compared to free space. Figure 2.5 presents the wave propagation inside a conventional and an ENZ medium [72].

There are several ENZ materials accessible through bulk materials. The most popular category is a set of transparent conductive oxides (TCOs) such as: indium tin oxide (ITO) [73], aluminum-doped zinc oxide (Al:ZnO) [74] and gallium-doped ZnO (Ga: ZnO) [75]. Their ENZ properties fall in the near-infrared (NIR) region

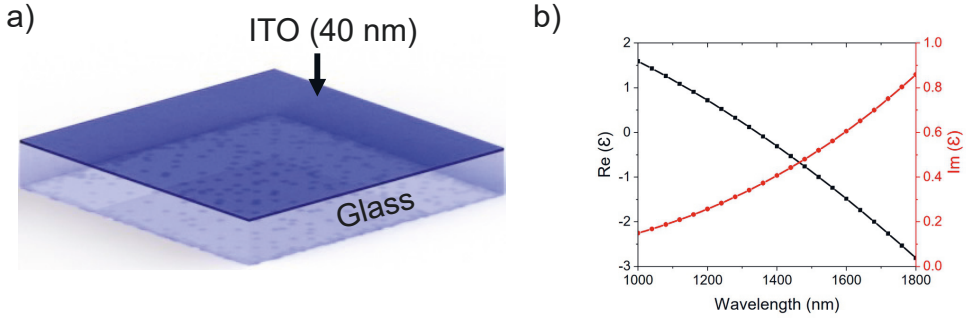


Figure 2.6 The 40 nm of thin film of ITO and (b) measured ϵ via ellipsometer with $\lambda_{\text{ENZ}}=1340$ nm [43].

and can be slightly changed by doping. This limits their application to the NIR region. Figure 2.6 presents the ϵ of 40 nm thick ITO film measured using spectroscopic ellipsometry used for gating study [43].

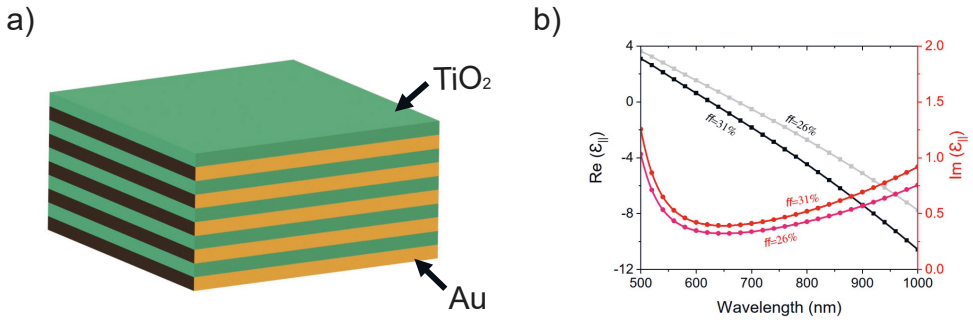


Figure 2.7 The schematics of (a) HMM, and (b) permittivity values for two different HMM with $ff=26\%$, and 31% [76].

In 2013, Mass *et al.* presented an HMM design composed of alternating layers of silver (Ag) and silicon nitride (SiN) with subwavelength layer thicknesses with vanishing effective ϵ [13]. The ϵ_{\parallel} of HMM changes from ellipsoid (dielectric) to hyperbolic (metallic) region at different wavelengths, depending upon the ratio of metal and dielectric layers [77]. Similarly, Rashed *et al.* used Au and titanium dioxide (TiO_2) to form two different HMMs in the visible region, Figure 2.7 shows the reproduced ϵ of two HMMs with different ff used in the paper [76]. Therefore, the ENZ region of these HMM can be tuned from visible to NIR region by simply changing the material composition.

2.4 Plasmonic antennas on ENZ materials

As discussed earlier, the resonance wavelength of the plasmonic antenna is influenced by the substrate. Both dielectric and metallic substrates were used to shape the resonance of plasmonic antennas earlier. However, in 2016 Kim *et al.* used ENZ materials to control the plasmon resonance much more significantly [78]. In their study, they initially study the radiation pattern of a dipole antenna on top of arbitrary substrates with $\epsilon=2$, 0.5, and 0. The simulation results show that E -field is forward scattered from the antenna into the substrate for $\epsilon=2$. When an antenna is placed on top of the substrate with $\epsilon<\text{air}$ (0.5), the E -field is scattered back into the air at an angle of 45 degrees. However, when the antenna is placed on top of an ENZ substrate resultant beam is directed back towards the normal. A nanoantenna scatters the incident field in all directions towards two different media: substrate and air. The relative efficiency of the scattering is determined by the dielectric constants of the two media. Therefore, effective ϵ of the local environment can be defined as:

$$\epsilon_{eff} = (\epsilon_{sub} + \epsilon_{air})/2 \quad (2.15)$$

When the substrate is a low-loss ENZ medium, the value of the effective index:

$$n_{eff} = \sqrt{[\sqrt{\text{Re}(\epsilon_{eff})^2 + \text{Im}(\epsilon_{eff})^2} + \text{Re}(\epsilon_{eff})]/2} \quad (2.16)$$

The resonance frequency of an antenna can be approximated as $\lambda_{res} \simeq 2n_{eff}(D + 2\delta)$, where $D+2\delta$ is the effective length of the antenna with a diameter (D) and evanescent extension of the resonant mode (δ) [78]. The effective index of refraction (reduced real ϵ) of the substrate limits the spectral shifting of the antenna resonance beyond the ENZ condition compared to a dielectric substrate. They experimentally realize the concept of slowing down the resonance shift (pinning effect) on top of three different materials Al: ZnO, Ga: ZnO, and 4H-silicon carbide (4H-SiC). The fabricated Au nanorod antenna with different lengths (400, 600, and 800 nm) on top of Al: ZnO and Ga: ZnO and compared the resonance shift with the ZnO substrate. The numerical simulations and optical characterization show that the resonance of the plasmonic antenna is fixed near the ENZ point of these two substrates in the NIR region. Similarly, the 4H-SiC substrate was used to exhibit the pinning effect in the MIR region with a longer antenna.

Later the same year, Prof. Boyd's group show a similar type of response of nanorod antenna on top of ITO with $\lambda_{ENZ}=1417$ nm [79]. In 2018 DeVault *et al.* showed that the Al: ZnO can be used as an ENZ substrate to suppress the near field coupling in plasmonic antennas [80]. However, only transparent TCOs, such as ITO, Al: ZnO, and Ga: ZnO are used in these studies. These are naturally occurring ENZ materials with ENZ wavelengths in NIR and MIR regions; hence, applications involving these materials are limited to those wavelength ranges. On the other hand, noble metals, such as Au and Ag, have real permittivity $Re(\epsilon)$ close to zero in the ultraviolet region with very high imaginary permittivity ($Im(\epsilon)$), preventing them from being effective ENZ materials. Therefore, Duan *et al.* in 2019 showed that an arbitrary ENZ material with $\lambda_{ENZ}=657$ nm can be used to study a similar type of effect in the visible region. However, they overlooked the idea of using metamaterials as an ENZ substrate. In my work (PUBLICATION III), by employing HMMs as ENZ substrates, I experimentally demonstrate how to control the LSPR of a plasmonic nanoantenna array without changing its dimensions in the visible region.

2.5 Multilayer ENZ metamaterials as substrate

The HMM substrates used in PUBLICATION III, are composed of three bilayers of Au and TiO_2 . The optical properties of these metamaterials are modelled using PEMA, discussed in section 2.1.1. The multilayer HMM shows the ENZ properties when the real part of $\epsilon_{||}$ ($Re(\epsilon_{||})$) component crosses zero and imaginary component ($Im(\epsilon_{||})$) is very small [14]. Figure 2.8 (a) presents two substrates referred as HMM-1 and HMM-2 are designed to study their effect on the plasmon resonance at their corresponding ENZ region, shown in Figure 2.8 (a). The Au thickness is set at 10 nm for both, but TiO_2 thickness is 25 nm for HMM-1, whereas 45 nm for HMM-2, providing the ENZ conditions at 684 nm and 751 nm, respectively. The experimental dielectric functions used here are taken from the literature to model Au [81], and TiO_2 [82]. Figure 2.8 (b) shows numerically calculated $Re(\epsilon_{||})$ and $Im(\epsilon_{||})$ using Equation 2.4 and 2.5, respectively.

3D electromagnetic simulations of transmission, reflection, and field profiles of the samples were performed using Ansys Lumerical Finite-difference time-domain (FDTD) Solutions. HMM-1 and HMM-2 media are modeled with the help of dielec-

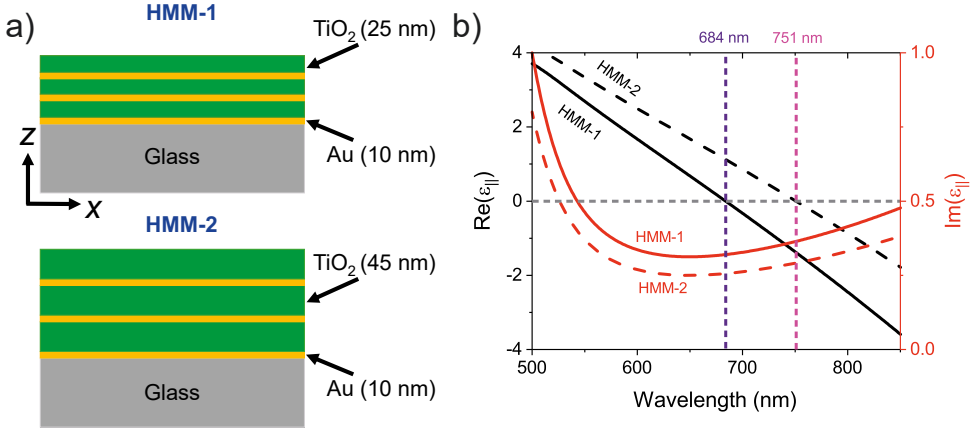


Figure 2.8 The schematic representation of HMM-1 and HMM-2 substrates with three bi-layers. (b) The $\text{Re}(\epsilon_{||})$ (black lines) and $\text{Im}(\epsilon_{||})$ (red lines) of HMM-1 (solid lines) and HMM-2 (dashed lines). The crossover of $\text{Re}(\epsilon_{||})$ for HMM-1 (violet dotted line) and HMM-2 (magenta dotted line) are highlighted.

tric functions obtained by the effective medium approach, as shown in Figure 2.8 (b). The overall thicknesses of the HMM-1 and HMM-2 media are 105 and 165 nm, respectively. For the transmission and reflection simulations, the unit cell of size 360 nm is illuminated by a linearly (x) polarized plane wave source of wavelengths 500-900 nm. The boundary conditions (BCs) are set to periodic in the x, y directions and perfect matched layers (PMLs) in the direction z direction. For the fabrication of HMM substrates, the 500 μm thick fused glass substrate is cleaned in acetone, isopropanol (IPA) with 10 minutes (min) sonication, and blow-drying under nitrogen (N_2) flow. The oxygen (O_2) plasma cleaning is used for thorough cleaning of organic contaminants from the surface. Once the samples are cleaned, 10 nm of Au and 25/45 nm of TiO_2 are deposited using electron beam evaporation. 1 nm of titanium (Ti) is deposited at the rate of 0.5 $\text{\AA}/\text{s}$ before each Au layer to improve the adhesion. The scanning electron microscope (SEM) images of HMM-1 and HMM-2 are obtained after focused ion beam (FIB) milling, shown in Figure 2.9 (a) and (b), respectively. The scale bar used for the SEM images is 50 nm. The contrast between the metal and dielectric layers is very clear in this image which verifies the thickness of thin films.

Transmission spectra of the fabricated structures are measured using a microscope from WiTec (alpha300 R- Confocal Raman Imaging). The samples are excited with

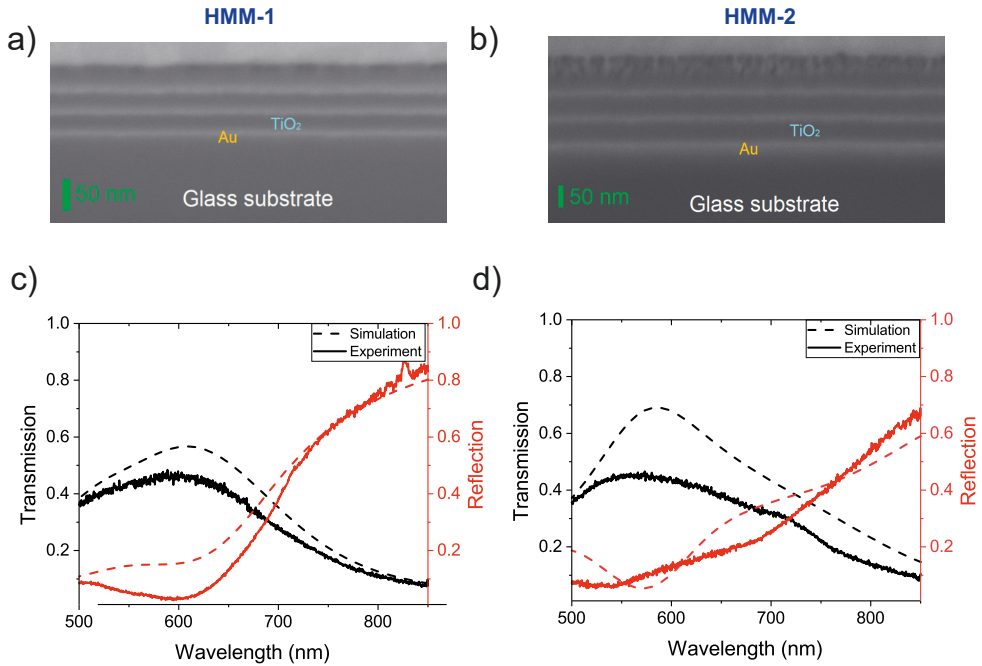


Figure 2.9 The SEM image of (a) HMM-1 and HMM-2 using FIB (scale bar is 50 nm). The simulated (dashed lines) and measured (solid lines) spectra of transmission (black lines) and reflection (red lines) results for (c) HMM-1 and (d) HMM-2.

a broadband light source (Energetiq EQ-99XFC LDLS, spectrum 190 nm to 2100 nm). The optical pump beam is focused on the sample surface by using a 20x objective (Zeiss numerical aperture (NA)=0.4) at normal incidence. To detect the transmission spectra, a 50x objective (Zeiss, NA=0.75) is placed at the back focal plane to collect transmitted light in the normal direction. The collected light is coupled to an optical fiber connected to a spectrometer (Ocean Optics Flame, detection range 40 nm-900 nm). The transmission of glass is first measured and then the normalized transmission spectrum of HMM is measured with respect to glass.

Similarly, reflectance spectra are measured using the same microscope and light source. To detect the reflected signal, the same objective is used to excite the sample and collect the light in the normal direction. The collected light is coupled to an optical fiber connected to a spectrometer. The reflection spectrum of HMM is measured with respect to the Ag mirror. The simulated and measured transmission and reflection spectra of HMM-1 and HMM-2, are presented in Figure 2.9 (c) and (d), respectively. The simulated (dotted) and measured (solid) transmission spectra

of HMMs are indicated in black and the reflection spectra in red color. The results show that HMM behaves as a dielectric below their respective ENZ wavelengths 684 nm for HMM-1 in Figure 2.9 (c) and 751 nm for HMM-2 in Figure 2.9 (d) with low reflection and high transmission. However, beyond the ENZ wavelength, the HMM has high reflectivity. The results of simulation and measurement are in good agreement and clearly show a transition from dielectric to metallic region. Moreover, these results, support the argument that by changing the dielectric thickness (TiO_2 in this case) the ENZ wavelength can be significantly shifted and easily observed.

2.6 Controlling Plasmon Resonance

Once the HMM with ENZ properties is realized, these samples can be used as substrates to control the plasmon resonance. Therefore, I have fabricated several ND samples on top of two HMMs and on a glass substrate for comparison. The schematics of ND on top of glass and HMM are presented in Figure 2.10 (a) and (b), respectively. The periodic arrays of NDs are fabricated by standard electron beam lithogra-

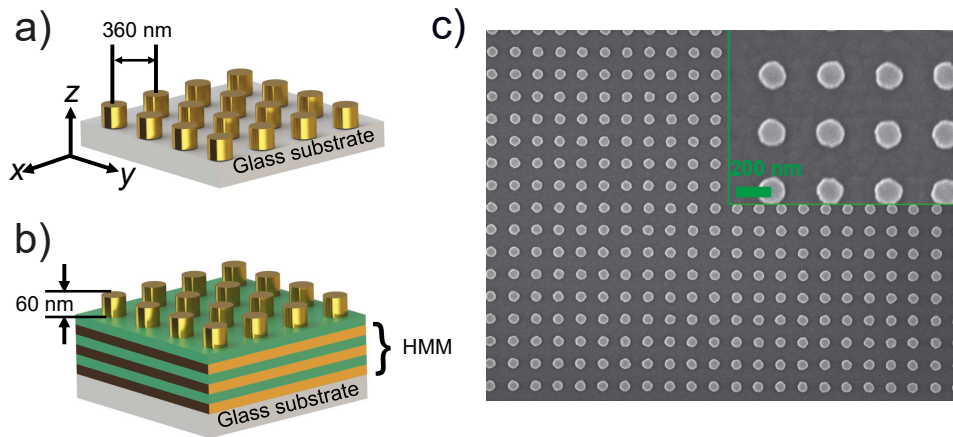


Figure 2.10 The schematic illustration of ND on top of (a) glass and (b) HMM sample. (c) The SEM image of NDs on HMM-1 (scale bare of inset is 200 nm) [83].

phy (EBL) using 20 KeV and $10 \mu\text{m}$ aperture. The cleaned glass and fabricated HMM samples (ENZ substrates) are spin-coated with Poly(methyl methacrylate) (PMMA)-A4 at 3000 rotation per minute (RPM) for 40 seconds (sec). The spin-coated samples are baked at 180°C for 90 sec in order to evaporate the anisole solution in PMMA-

A4. The $100 \times 100 \mu\text{m}^2$ write field is used to create the NDs with the area dose of $300 \mu\text{C}/\text{cm}^2$. The exposed samples are developed for 60 sec in 1:3 Metylisobutylketon (MIBK): IPA solution and 30 sec in IPA to stop the development process. The developed samples are loaded in the electron beam evaporation deposition chamber. Similar to HMM fabrication, 1 nm of Ti is used as an adhesion layer, followed by 60 nm of Au deposition at the rate of $0.5 \text{ \AA}/\text{s}$. The S-1165 remover is used to lift off the metals, the samples are left in the solution to heat up to 80°C . When the desired temperature is reached, the hot plate is turned off and the samples are kept in the solution for 5 min. Once the cracks start to appear in the thin metal films, the gentle stirring removes all the unwanted metal from the sample. The sample is rinsed in water, acetone, and IPA, and blow-dried under N_2 flow to get rid of residual metal films. Four different matrices are fabricated for 120, 140, 160, and 180 nm disk size, by changing the dose factor. The SEM image of one of the samples on top of HMM is presented in Figure 2.10 (c).

For the transmission and reflection simulations, the unit cell of size 360 nm is illuminated by a linearly (x) polarized plane wave source of wavelengths 500-900 nm. The BCs are set to periodic in the (x, y) directions, and PMLs in the direction z direction. The diameter of the NDs on glass and HMM are changed from 120 nm to 180 nm, while the thickness is kept at 60 nm, as in the fabricated samples.

The evolution of the calculated nanoantenna resonances (transmission dip) with increasing diameter, on different substrates (glass, HMM-1, and HMM-2) are presented in Figure 2.11. Figure 2.11 (a) shows that the LSPR of the ND antenna on the top glass shifts quite significantly by increasing the diameter. On the other hand, the shift in the resonance of NDs is much smaller on top of HMM-1 and HMM-2, presented in Figure 2.11 (b) and (c), respectively. The comparison of the spectral shifts of the plasmon resonances reveals that the change is much smaller when the NDs are on the ENZ substrates, compared to the case of the glass substrate. That is to say, the resonance of the NDs on the ENZ substrates is pinned near the ENZ wavelengths. Moreover, the ENZ substrates having different ENZ wavelengths control the pinning effect at those wavelengths.

Then, the transmission spectra of NDs on the glass substrate with different diameters are measured, which are presented in Figure 2.12. A resonance shift from 628 nm to 678 nm is observed, by changing the disk diameter from 120 nm to 180 nm on top of the glass. The same amount of modification in the diameter for the NDs on

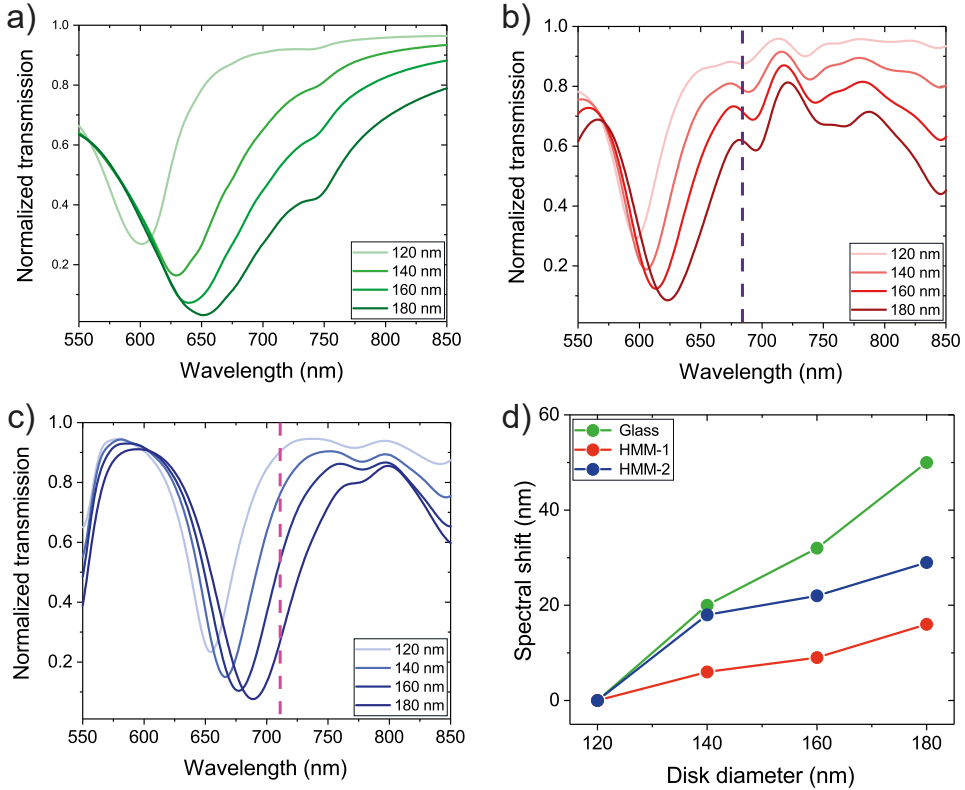


Figure 2.11 Evolution of the plasmon resonance with varying diameters of NDs on (a) glass (b) HMM-1, (c) HMM-2 and (d) spectral shift of the resonance, calculated by FDTD simulations [83].

HMM-1 changes the plasmon resonance only in a narrow wavelength region of $659 \text{ nm} \leq \lambda \leq 675 \text{ nm}$, as shown in Figure 2.12 (b). The LSPR of the antenna is not only determined by its size when it is located on the ENZ substrate. This phenomenon is a consequence of the interaction between the resonating antennas and the ENZ substrate. It is also possible to obtain this effect for an antenna array of the same size, at a different wavelength region, by adjusting the composition of the substrate. When the ND array is on HMM-2 having an ENZ wavelength at 751 nm, the pinning effect is observed in the region $703 \text{ nm} \leq \lambda \leq 732 \text{ nm}$, as shown in 2.12 (c). The pinning effect is observed around the ENZ region of the corresponding HMM substrate.

When an antenna is on an ENZ substrate, an increase in the diameter of the ND antenna is compensated by small n_{eff} , reducing the amount of the shift in the LSPR near the ENZ wavelength, as observed in the experiments. The spectral shift in the plasmon resonance, with respect to the resonance wavelength of the ND arrays with

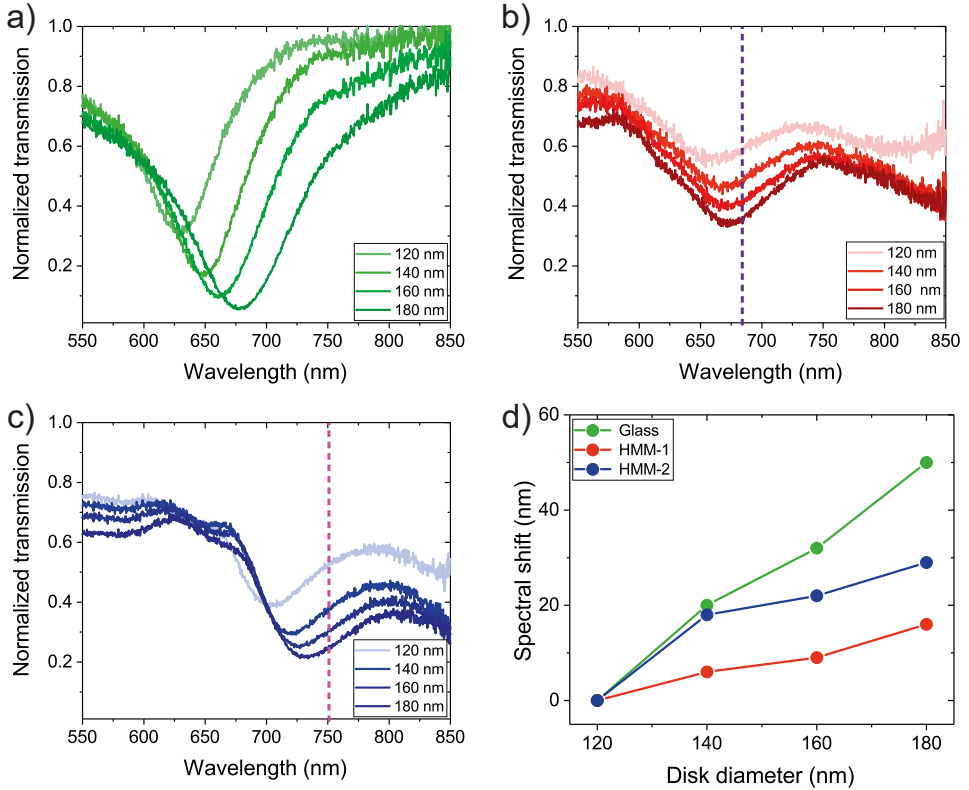


Figure 2.12 Normalized transmission spectra of the fabricated ND arrays, with disk diameters of 120, 140, 160, and 180 nm on three different substrates; (a) glass (green), (b) HMM-1 (red), and (c) HMM-2 (blue). The ENZ points of HMM-1 and HMM-2 are highlighted by violet and magenta vertical dashed lines in the associated graphs, respectively. (d) The spectral shifts in the resonance wavelengths of the NDs on glass, HMM-1 and HMM-2 [83].

120 nm diameter, for each sample, is shown in Figure 2.12 (d). The experimental results display a good agreement with the simulation results. The ND arrays on glass exhibit a total shift of 50 nm, whereas the shifts observed in the ND arrays on HMM-1 and HMM-2 are 16 and 29 nm, respectively. The shift in the resonance for HMM-1 is 3 times less than the one for glass. However, for HMM-2, it is half of the resonance shift obtained for the glass case. The shift in the resonance for HMM-1 is more suppressed compared to HMM-2 because the ENZ region of HMM-1 ($660 \text{ nm} \leq \lambda \leq 690 \text{ nm}$) is intentionally designed at the resonance wavelength of the antenna (on glass). On the other hand, the ENZ region ($730 \text{ nm} \leq \lambda \leq 780 \text{ nm}$) of HMM-2 is far away from the resonance of the antenna (on glass). The possibility to tune the ENZ region by simply changing the thickness of TiO_2 allows us to probe the pinning effectively

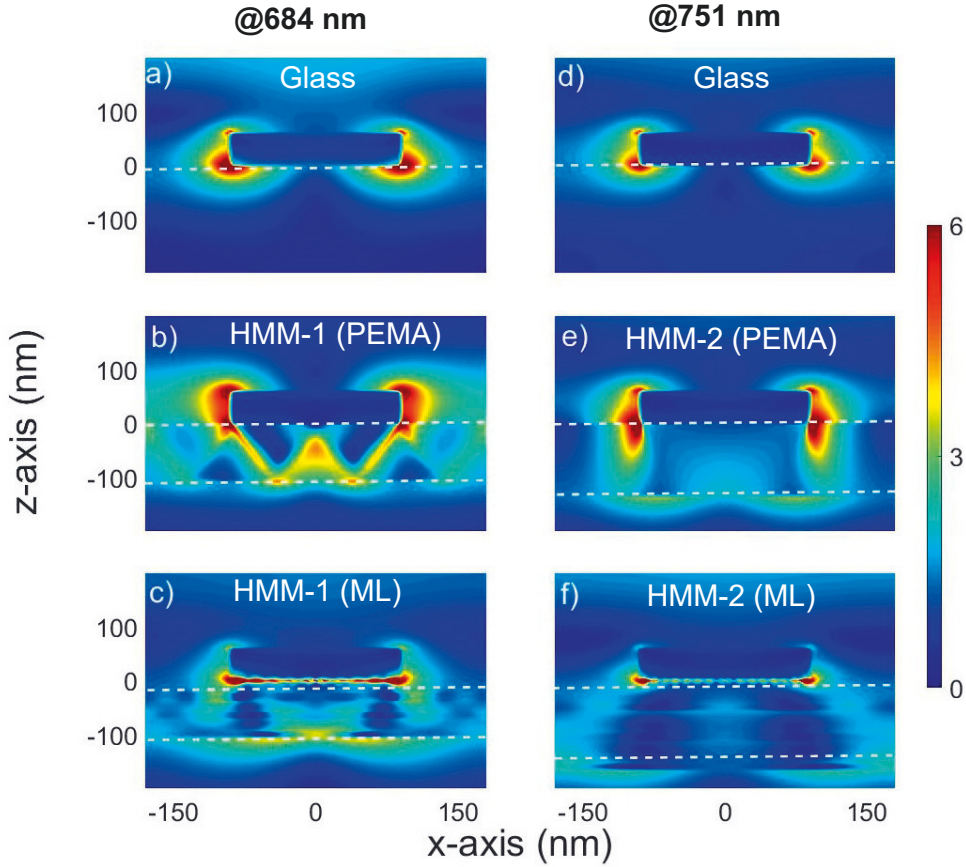


Figure 2.13 Normalized E -field profiles of NDs ($D = 180\text{nm}$) at 684 nm on (a) glass, (b) HMM-1 (PEMA) and (c) HMM-1 (ML stack), and similarly, at 751 nm on (d) glass, (e) HMM-2 (PEMA) and (f) HMM-2 (multilayer stack) [83].

for HMM-1 and HMM-2 at two different wavelengths. ENZ materials exhibit high impedance ($Z = \sqrt{\mu/\epsilon}$) mismatch with respect to their surrounding environment, which limits the penetration of the incident field. Normalized E -field profiles of the ND arrays ($D = 180\text{ nm}$) on glass and HMM substrates, calculated at the associated ENZ wavelengths of HMM-1 (684 nm) and HMM-2 (751 nm), are shown in Figure 2.13. The ENZ substrates restrict the penetration of fields throughout the HMM media at the ENZ wavelengths, leading to back-scattering. The simulations for ENZ substrates were performed using the material properties calculated with PEMA and multilayer stack of Au and TiO_2 .

To further examine the scattering of NDs on different substrates, the phase of

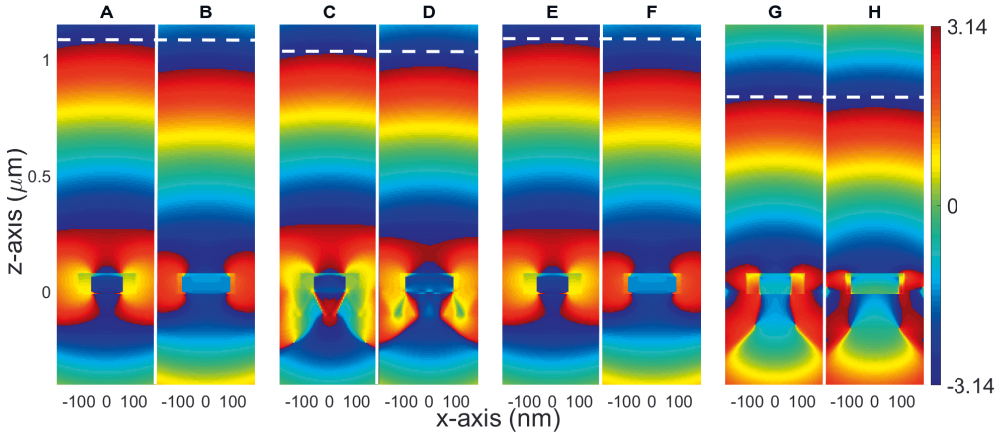


Figure 2.14 Phase profiles (in the unit of radian) of x component of the scattered E -field up to 2λ from the NDs of diameters (A) 120 nm, and (B) 180 nm on glass at $\lambda = 684$ nm, (C) 120 nm, and (D) 180 nm on HMM-1 at 684 nm. Similarly, (E) 120 nm, and (F) 180 nm on glass $\lambda = 751$ nm, (G) 120 nm, and (H) 180 nm on HMM-2 at $\lambda = 751$ nm. White dotted lines are added for better visual comparison [83].

the x -component of the scattered E -field is calculated for the NDs of 120 nm and 180 nm diameter, on glass and HMM-1 at 684 nm (Figure 2.14(A-D)), and on glass and HMM-2 at 751 nm (Figure 2.14 (E-H)). The difference in the phase of the E -fields at a distance of $\sim 2\lambda$ from the surface of the NDs (120 nm and 180 nm diameters), is 56 degrees when the substrate is glass. However, this difference reduces to 21 degrees when the substrate is changed to ENZ metamaterial. This provides possibilities for the effective control of the phase contribution of each nanostructure.

3 SELF-ROLLING MULTILAYER METAMATERIALS

The notable application of HMM as an ENZ substrate is significant and important progress in the field of metamaterials and plasmonics [83, 84]. However, the planar nature of these thin film-based HMMs fundamentally limits their applications for 3D metamaterials. Furthermore, the fabrication of these thin films is challenging because it is done by subsequential layer evaporation to form a stack. During each deposition, there is a possibility to have some error, that can multiply to a significantly large value if the number of layers is very high, like in reference [13]. The fabrication process can be time-consuming and laborious. In another study, Vesseur *et al.* fabricated a rectangular plasmonic ENZ waveguide structure to study the resonant guided plasmon modes [85]. Similarly, the fabrication steps involved are very complex because it requires a sequence of metal and dielectric deposition and multiple FIB milling steps. In addition to the complication of the process, the throughput of the FIB-based method is very limited. Therefore, the solution to these limitations is to adopt a fabrication method that can limit the number of deposition steps, and allow the use of these thin films as 3D metamaterials or waveguides. Moreover, the fabrication method should be easily reproducible with high throughput. In this thesis (PUBLICATIONS IV, V, and VI), I have used a unique self-rolling fabrication method on thin films of SiO_2 and Au to form RUTs to obtain 3D ENZ metamaterials, 3D fishnet metamaterials, and curved metasurfaces. The fabrication method allows to obtain multiple devices with simple photolithography steps and has proven to be used at wafer-scale fabrication [86]. Besides this the method allows the integration of different materials such as liquids [87] and cells for sensing applications [88], and a platform for guiding the neurons to simulate brain activities [89].

3.1 Rolled up tubes

The strained-induced RUTs [90], have been investigated as a rapid and cost-efficient fabrication method for multilayer structures [91]. This self-rolling method, also known as the thin film self-rolling technique for 3D RUTs, has been used in different fields after it was introduced in semiconductor bilayers grown by molecular beam epitaxy (MBE). The RUTs were first investigated by Prinz *et al.* in 2000 using strained semiconductor layers which start to roll once the strain is released by etching the sacrificial layer [92], presented in Figure 3.1.

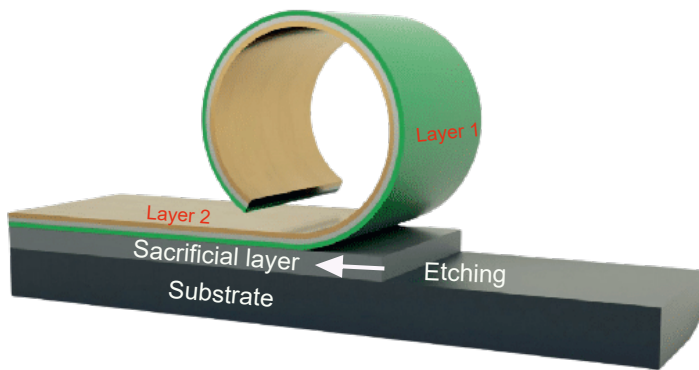


Figure 3.1 Schematic illustration of self-rolling tubes, the rolling process starts when the sacrificial layer is etched and the stressed layers on top are released by rolling the layers in an upward direction.

Since the introduction of obtaining 3D structures using strained semiconductor layers [92], several fabrication methods have emerged [93, 94], enabling a wide variety of applications in different fields, from microelectronics and flexible devices [95, 96], to optics [91, 97] and biology [98, 99]. All these methods are based on the exploitation of the residual strain developed in different composition layers. When these layers with appropriate strain gradient across the film thickness are selectively released from the substrate, for example by selective etching an underlying layer; thin films undergo a stress release-driven self-rolling mechanism.

There are two main methods to obtain RUTs. The first one is a top-down approach, in which two semiconductor layers with different compositions are grown

on top of a sacrificial layer. The difference in the compositions develops the strain between the two layers. The sacrificial layer is exposed to the etchant using photolithography and the strain is released by etching the sacrificial layer, which instigates the rolling process [92]. The second method uses basic fabrication materials (e.g. a resist [100], germanium (Ge) [101] or germanium oxide (GeO_x) [102]) as a sacrificial layer. The size and shape of the patterns of these sacrificial layers define the length and the number of turns of the RUTs. Almost, all materials can be deposited on top of these sacrificial layers using standard deposition systems such as electron-beam evaporation, sputtering, and plasma-enhanced chemical vapor deposition (PECVD) to obtain RUTs [103]. However, the combination of materials is important to inherit the strain gradient necessary to help the rolling process once the sacrificial layer is removed. The well-known material combinations are silica (SiO/SiO_2) [104], SiO_2/Au [100, 101], Ag/SiO_2 [91], and SiN_x [105]. In this thesis, the bottom-up approach of self-rolling tubes is adopted with two different types of sacrificial layers: photoresist and Ge.

3.1.1 Photoresist based rolled-up tubes

The use of resist as a sacrificial layer was derived from the idea to make the rolling process simple and more flexible with all possible materials. The problem with the initial works on semiconductor-based RUTs was that it required a selective under-etching procedure to release the strained layers from their substrate. This becomes significantly challenging when the thicknesses of these layers are in the nanometer range. The selective under-etching limits the type of materials used for RUTs, which means only selected materials can be used for these tubes. The semiconductor-based RUTs were unsuited for both metamaterials and biomedical applications, because of the high refractive index and bio-compatibility issue, respectively. Therefore, to circumvent the problem for a wide range of materials, the idea of using a photoresist/polymer as a sacrificial layer coated with stressed layers of any materials. The resist can be removed very easily using acetone which has almost 100% selectivity with any inorganic material. This makes the etching process much simple, fast, and safe without the use of any harmful hydrofluoric acid.

In 2008, Prof. Schmidt's group from Dresden fabricated RUTs for different materials using resist as a sacrificial layer. They did an extensive study by first optimizing

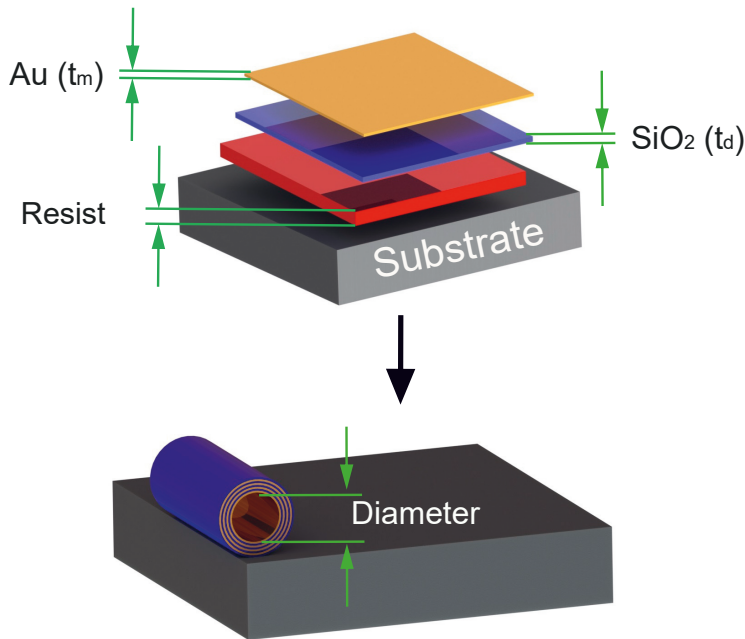


Figure 3.2 Sketch of the sample geometry showing the thin films deposited on top of photoresist. The thin film starts to roll when resist is removed using acetone.

the major parameters influencing the strain and fabricated tubes of materials such as platinum (Pt), palladium/iron (Fe), TiO₂, aluminum oxide (Al₂O₃), zinc oxide (ZnO), SiN, SiN/Ag, and diamond-like carbon. They controlled the temperature of the substrate during a deposition for each material, and change the deposition rate and stress appearing during each deposition. This gave them a very good control of the rolling mechanism, and they were able to even control the diameter of tubes. They patterned the resist as square, rectangle, or circular shapes and deposited the materials with an angle to create a shadow and leaving an opening for etching of resist [93]. In their other work, they fabricated Pt/Au/Fe/Ti microtubes using resist as a sacrificial layer and later used them as microtubular jet engines by a catalytic reaction [106, 107]. They also fabricated the silica (SiO/SiO₂) based RUTs using the same resist as a substrate [104]. These tubes are then quite extensively studied in applications like a lab on chip [108], photon-plasmon coupling in microtubes [109], and solvent sensing [110]. One of the advantages of silica-based tubes is their high transparency which helps to study human cancer cells [111] or detection system based on photoluminescence [112]. Similar to that SiN based tubes were also quite

extensively studied and used for cell study [113].

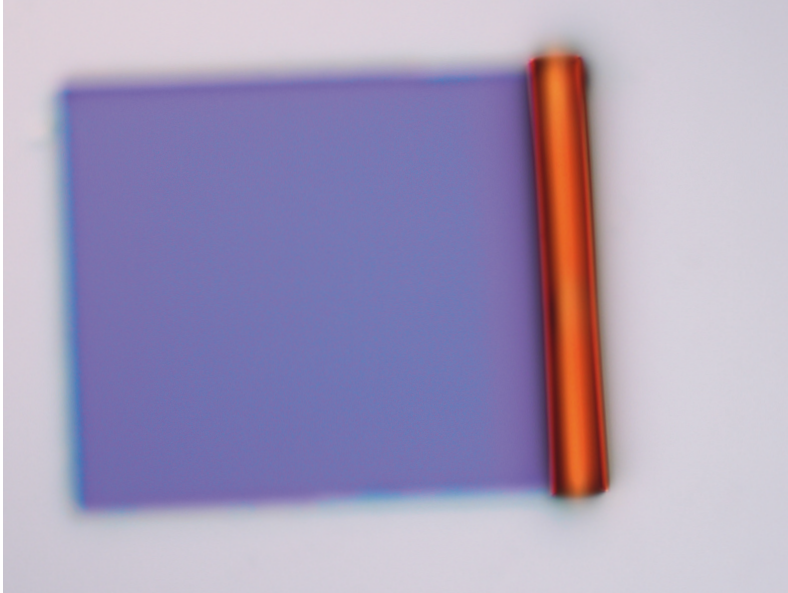


Figure 3.3 Optical microscope image of SiO₂/Au based RUTs fabricated using resist as a sacrificial layer in single step lithography.

Figure 3.2, presents the fabrication steps involved to obtain RUTs using resist in PUBLICATION V and VI. For the fabrication of resist-based RUTs the substrates are thoroughly cleaned, they are coated with a thin layer of Hexamethyldisilazane (HMDS) at 125° C to improve the adhesion of the photo-lithography resist. The AZECI3012 positive resist is spin-coated at 3000 RPM for 40 sec. The resist is soft-baked at 90 °C for 90 sec. The spin-coated samples are exposed using the Suss MA6 mask aligner for 4 sec under an ultraviolet (UV) lamp using the rectangular pattern in the mask. The post-baking process is done at 110 °C for 60 sec. The samples are developed for 60 sec using MIF 726 developer and then rinsed three times in di-ionized (DI) water.

The developed samples are coated with 60 nm of SiO₂ using electron beam evaporation at the rate of 0.1 nm/sec. The thickness of SiO₂ is confirmed using an ellipsometer. In the second step of deposition, the samples are coated with 2 nm of Ti and 20 nm of Au at 0.3 nm/sec at an angle of 60 degrees to create a shadow effect. Ti layer is used for better adhesion of Au and angle deposition guides the rolling process. Acetone is used to lift off the thin films deposited on top of the resist. The

samples are placed gently inside the beaker containing acetone. The samples are kept in acetone for 5 minutes, then moved to IPA for 30 s, and blow-dried under N₂ flow. While removing the resist SiO₂ and Au layer starts to roll due to the stress introduced during the deposition process. The optical microscope is used to ensure the quality of the tubes. Figure 3.3, presents microscope images of RUTs fabricated using resist as a sacrificial layer.

3.1.2 Germanium based rolled-up tubes

The second approach adopted in this thesis (PUBLICATION IV) is using Ge as a sacrificial layer. The resist-based technique has proven to be very dominant in applications where bigger diameters are required. However, in order to obtain more control over the rolling mechanism and the freedom to have RUTs with different combinations of materials, Ge was used as a sacrificial layer to fabricate ultra-compact rolled-up capacitors [114]. In 2014 TiO₂/Chrome/Au based ultra-compact RUTs were obtained using Ge as a sacrificial layer. The RUT was integrated into a setup for in-flow sensing [115]. The use of Ge allowed the etching process to be as slow as in the semiconductor-based tubes with high selectivity by using hydrogen peroxide (H₂O₂). The use of Ge also allows the second step of lithography that can be used to pattern the strain layer inside the RUTs. For this, the second step lithography is used to create a window for the etching process. Bermúdez-Ureña and Steiner recently showed how Ge can be used efficiently for EBL and FIB processes [101]. Most recently, the Ge-based RUTs are used for magnetic induction by patterning the metal in a way they form coils [116].

For the fabrication of Ge-based RUTs, two-step lithography is required. Figure 3.4 presents the schematic of the two-step photolithography fabrication process combined with electron-beam-based layer deposition and lift-off to define the rolling areas. The image reversal lithography is done to form Ge patterns. The samples are coated with a thin layer of HMDS at 125°C to improve the adhesion of the photolithography resist. AZ5214E image reversal resist is spin-coated at 3000 RPM for 40 sec. The resist is soft-baked at 100 °C for 60 sec. The spin-coated samples are exposed using the Suss MA6 mask aligner for 4 sec under a UV lamp using the rectangular pattern in the mask. The post-baking process is done at 115 °C for 120 sec. For image reversal, the samples are exposed a second time without a mask using the

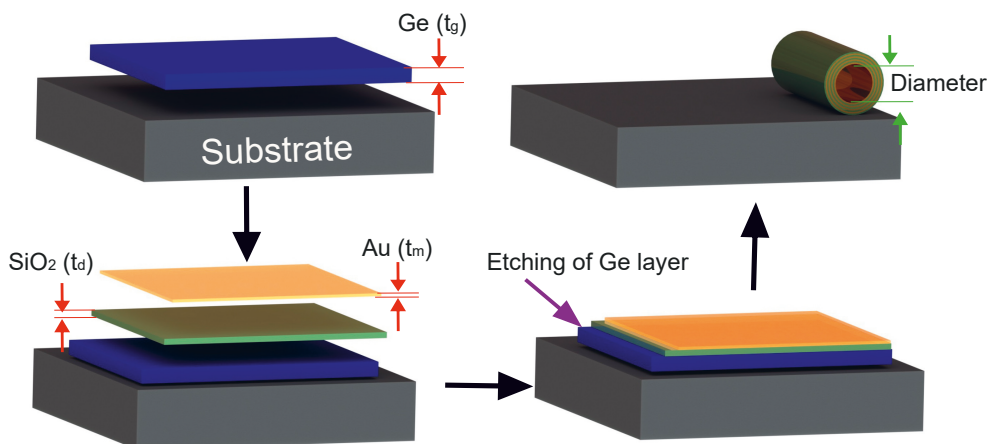


Figure 3.4 Schematic representation of the fabrication steps for obtaining RUTs. The first step consists of defining the Ge layer pattern. The second step opens a window to define the SiO_2 and Au bilayer, with reduced dimensions on the front and lateral sides in order to facilitate the next step, which is the etching process of the Ge, leading to the self-rolling of the SiO_2 /Au layers into a RUT.

same Suss MA6 mask aligner for 30 sec (also known as flood exposure). The samples are developed for 45 sec using MIF 726 developer and then rinsed three times in DI water. The developed samples are coated with 40 nm of Ge using electron beam evaporation. The S-1165 remover is used to lift off the Ge, with the same parameters discussed in section 2.6. To further clean the resist residue, the reactive ion etching (RIE) with O_2 plasma for 2 min is applied. The quality of Ge patterns is verified using a microscope. Once Ge patterns are obtained, the second step of lithography is done by using a positive resist to create an opening for Ge etching. The same parameters for the HMDS adhesion layer are used. Then, AZ3421E positive is spin-coated, soft-baked, exposed, post-baked, and developed with exactly the same parameters discussed in section 3.1.1. The developed samples are then coated with SiO_2 at 0.1 nm/sec and Ti/Au at 0.3 nm with different thickness combinations. Au is deposited at an angle of 60° , to further guide the rolling direction. Once the samples are coated, the lift-off is done by using the S1165 remover, which opened the window for the wet etching of Ge. The etching is done by leaving the samples in 35% of H_2O_2 for 90 min, which allowed the rolling of the strained SiO_2 /Au layers. The microscope image is presented in Figure 3.5.



Figure 3.5 Optical microscope image of SiO₂/Au based RUTs fabricated using Ge as a sacrificial layer.

3.2 Diameter of rolled-up tubes

The better control of the diameters using Ge as a sacrificial layer provides a platform to study the strain mechanism between SiO₂/Au much more carefully. Therefore, this section focuses on the Ge-based tubes, and the diameters of such tubes are numerically modelled. The strain introduced between the layers arises from the fact that a slow deposition rate of SiO₂ induces compressive stress within the first layer while a relatively high deposition rate of Au creates tensile stress within the second layer. In addition to the deposition rate, the adhesive Ti layer under the Au layer contributes to the strain [100].

Once such a combination of films under stress is released by selectively etching the sacrificial layers, it results in the self-rolling of the films into RUTs. Although it is possible to deposit different thickness layers, the strain between these layers is one of the important parameters that define the final RUT's diameter. Therefore, initially, the diameter of RUTs is modelled as a function of the thickness of the strained layers as [104]:

$$D = \frac{\mathbb{E}_m^2 t_m^4 + \mathbb{E}_d^2 t_d^4 + 4\mathbb{E}_m \mathbb{E}_d (t_m^3 t_d + t_m t_d^3) + 6\mathbb{E}_m \mathbb{E}_d (t_m^2 t_d^2)}{3|\Delta\epsilon|(1+\nu)\mathbb{E}_m \mathbb{E}_d (t_m + t_d)(t_m t_d)}, \quad (3.1)$$

where, subscript m and d represent metal (Au) and dielectric (SiO₂), respectively,

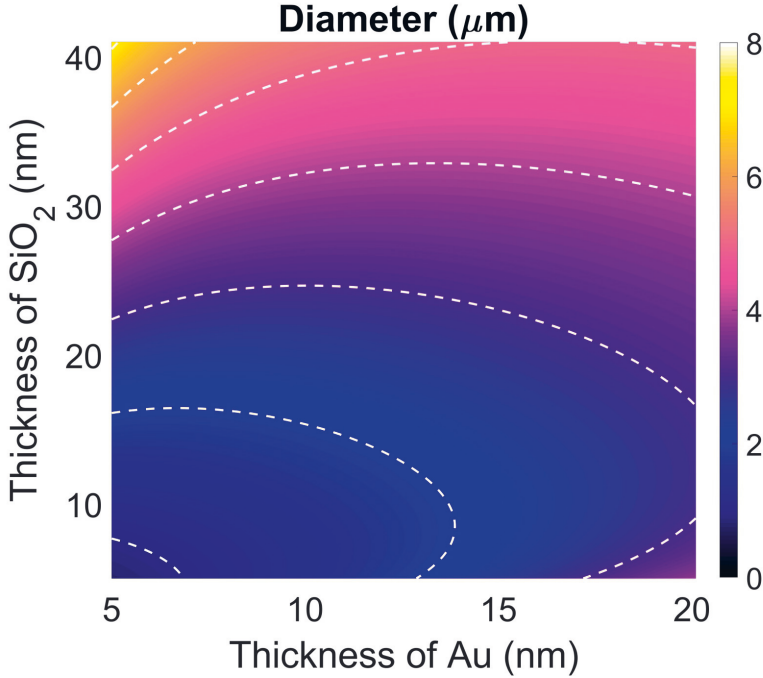


Figure 3.6 Analytically calculated diameter of a self-rolled structure as a function of Au and SiO₂ thicknesses.

$\Delta\epsilon$ is the strain difference between the two layers, \mathbb{E} is the Young's modulus, t is the thickness of films in nanometers (nm) and ν is the Poisson's ratio (set at 0.422). The \mathbb{E} of Au is set at 79 gigapascal (GPa) [117] and SiO₂ at 50 GPa [118]. The calculated diameter D of the RUTs as a function of the dielectric (t_d) and metal (t_m) thickness is presented in Figure 3.6. The analytically calculated diameter of the RUT, based on this model, shows that the thicker layers create larger diameters. However, I focus on broader range of dielectric thickness (5-40 nm) compared to metallic layer (5-20 nm) as the thick metal layers won't provide the optical properties and effective medium of the HMM required for this study. To fit the model with experimentally measured diameters, an average value of $\Delta\epsilon=1.2\%$ is used.

In the systematic experimental study to identify the effect of different parameters on Ge-based RUTs, eight different samples are fabricated. Four different dielectric thickness t_d (5, 10, 20 and 40 nm) and two different metal layer thickness t_m (10 and 20 nm) are used. The SEM images of the self-rolled structures at an angle of 40° are presented in Figure 3.7. The RUTs ranging from sub-micron diameters ($\sim 0.63 \mu\text{m}$)

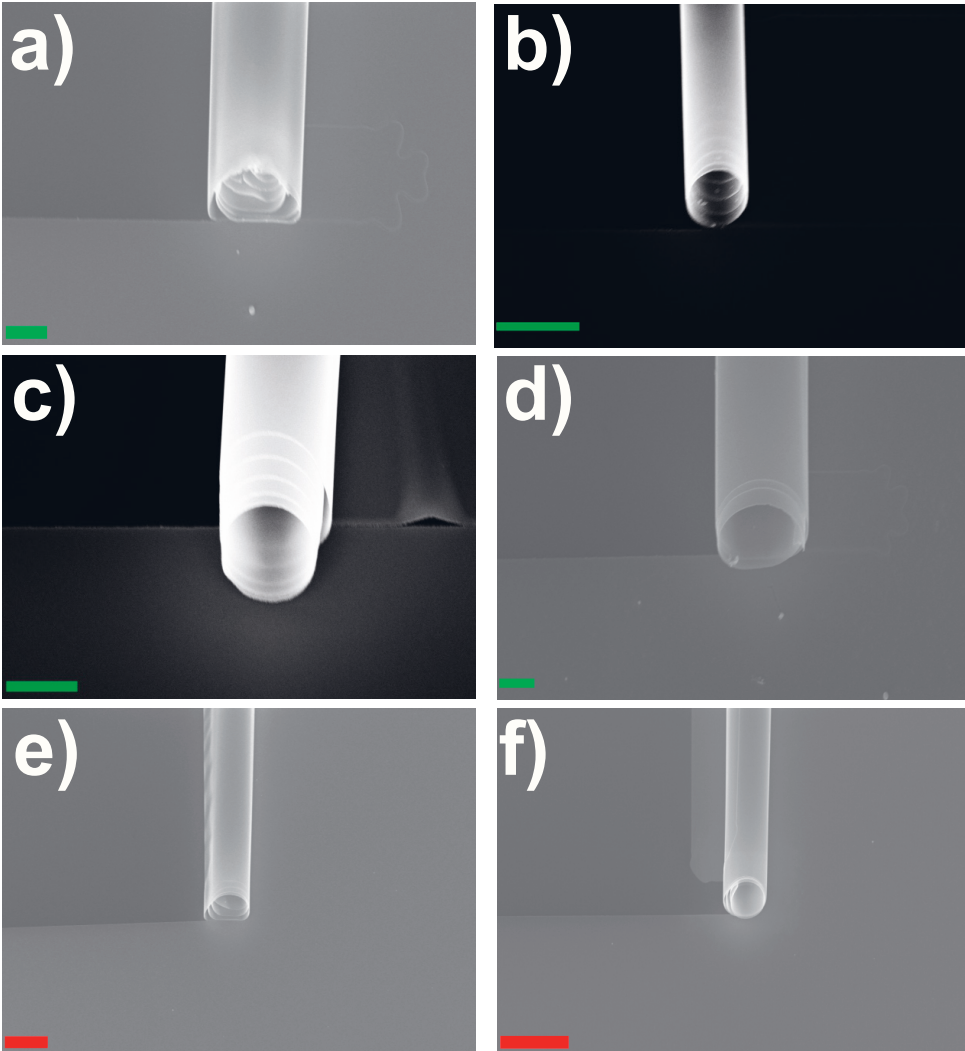


Figure 3.7 The SEM images of RUTs with (a) $t_d/t_m=5/20$ nm, (b) $t_d/t_m=10/10$ nm, (c) $t_d/t_m=20/10$ nm, (d) $t_d/t_m=20/20$ nm, (e) $t_d/t_m=40/10$ nm, and (f) $t_d/t_m=40/20$ nm. The green scale bar is $2 \mu\text{m}$ and red one is $10 \mu\text{m}$.

up to $\sim 7.5 \mu\text{m}$ are obtained. Note that the diameter of the RUTs depends on the strain, hence the thickness of SiO_2 and Au layers are used to form the multilayer metamaterial. Table 3.1 presents the inner diameters from eight different samples, and the number of turns is given in parenthesis.

In this fabrication process, the width (w_g) of rectangular pattern of Ge defines the length of the RUT, while the length (l_g) of the pattern controls the number of

Table 3.1 Measured approximate inner diameters of the RUTs formed using corresponding t_d and t_m .

$(t_m \downarrow)(t_d \rightarrow)$	40 nm	20 nm	10 nm	5 nm
10 nm	7.5 μm (3)	2 μm (5)	712 nm (13)	632 nm (15)
20 nm	5 μm (5)	3 μm (3)	1250 nm (8)	1.5 μm (6)

the turns (N). As N depends upon the diameter of the RUT through the fix area of the rectangular pattern, the number of turns can be approximated as a function of D and l_g as $N = l_g / \pi D$. In each sample, several pattern designs with varying length and width dimensions are included. The analysis of the results revealed that the thin layers yield smaller diameters while the rolling success is better in smaller patterned areas. For example, the areas of 30×25 ($w_g \times l_g$) μm^2 provided compact RUTs with diameters below 3 μm , while areas of 90×75 μm^2 allowed proper rolling of the tubes with the diameters above 3 μm .

3.3 Rolled up hyperbolic metamaterials

Although applying a self-rolling method to fold more complex structures opens new ways to produce 3D photonic micro-objects with novel designs and optical properties, it has not been adopted yet into metamaterials. So far, most of the works have focused on the possibility to stack optically active semiconductor heterostructures [119, 120] and metallic nanostructures [101, 121]. Moreover, Smith *et al.* pointed out that these RUTs can be promising candidates for waveguides [122] and hyperlenses [123]. Later these tubes are used for the realization of 3D metamaterials [124], fishnet HMMs [125], and active metamaterials [126]. However, the predominant use of semiconductor layers in RUT-based metamaterials limits the design flexibility and extension of these applications towards engineered ENZ-metamaterials. Therefore, the unique ENZ features of HMMs via self-rolling systems have not been explored. In this study (PUBLICATION IV), I utilized cylindrical multilayer structures/RUTs based on Ge as a sacrificial layer to explore the engineered ENZ metamaterials. The use of Ge allowed better control on the diameter and as well as the number of layers for each metamaterial.

Previously, the material dispersion of planar multilayer metamaterials/HMM has been qualitatively defined using the PEMA. The effective permittivity of HMM is

divided into in-plane ε_{\parallel} and out of plane ε_{\perp} components. Both components only depend upon the ratio of metal and dielectric in the metamaterial. This approximation method works based on the assumption that the number of layers is infinite and effective ε is independent of the number of layers. Moreover, the metamaterial is considered as an infinite planar sheet, and the dispersion is independent of the shape. However, due to these considerations in the PEMA method, the calculations may not be precisely suitable to describe the optical response of cylindrical HMMs with a finite number of Au/SiO₂ layers. Therefore, in this work, a cylindrical effective medium approximation (CEMA) is implemented to define the effective dispersion properties of a curved multilayer medium [127]. Figure 3.8 (a) shows a transversal view schematic of a cylindrical multilayer structure and the parameters defined in the model, with ε_{ρ} , ε_{θ} and ε_z as the principal permittivities in the ρ , θ and z directions, respectively in the cylindrical coordinate system.

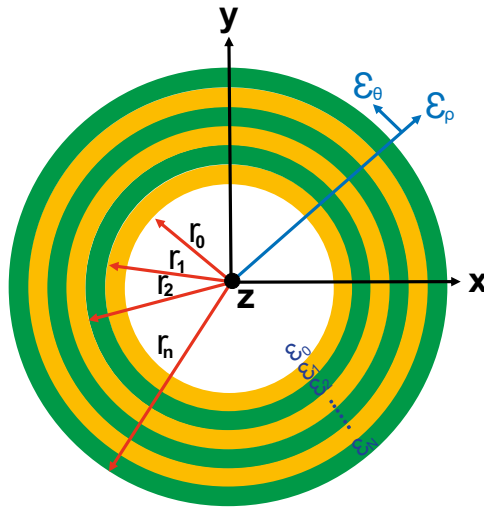


Figure 3.8 Schematic representation of a multilayer structure and corresponding ε values defined CEMA method.

In CEMA method, the effective ε values for the multilayer structures are expressed as [127]:

$$\varepsilon_{\rho} = \log(r_N/r_0) \left(\sum_{n=1}^N (\log(r_n/r_{n-1})/\varepsilon_n) \right)^{-1} \quad (3.2)$$

$$\varepsilon_{\theta} = \varepsilon_z = (\log(r_N/r_0))^{-1} \left(\sum_{n=1}^N (\log(r_n/r_{n-1})) \varepsilon_n \right) \quad (3.3)$$

where ε_m and ε_d are ε of Au and SiO₂, respectively. The innermost and outermost radii are denoted by (r_0) and (r_N), respectively. Each layer is defined by the radius (r_n) and permittivity (ε_n) and the total number of layers are denoted by N . The thickness of each layer is $t_n = r_n - r_{n-1}$. This model considers the thicknesses of SiO₂/Au, the inner radius of the tube, and the number of turns e.g. number of bilayers. As discussed in section 3.2, the thickness of the layers defines the diameter of a RUT. However, one advantage of the RUT fabrication approach is that one can obtain varying numbers of layers for fixed inner diameter and layer thickness values, which depend mainly on the length of the patterned area.

In order to envision the effect of the diameter, number of turns and the ratio (t_d/t_m), the $\text{Re}(\varepsilon_{\theta})$ is calculated for the RUTs with diameters 600 and 900 nm. Three different ratios and change the number of bilayers from 1 to 10 are used. Figure 3.9, presents the heat map of $\text{Re}(\varepsilon_{\theta})$, for the same ratio (10/10) with three different diameters in first row. Similarly, 10/20 and 10/30 in the second and third row, respectively.

The heat maps show that by changing the ratio of the thicknesses of SiO₂ and Au (t_d/t_m), the $\text{Re}(\varepsilon_{\theta})$ values are changed significantly. Similarly, the $\text{Re}(\varepsilon_{\theta})$ is changed by changing the number of bilayers up to 4 and saturates afterward. This means the RUT with 7.5 μm diameter with 3 number of turns it is significant to use the CEMA method for accurate calculation of the ENZ wavelength. However, the diameter of the RUT does not play a very significant role, because the sizes are not subwavelength range.

3.4 Epsilon near zero properties

Next, based on the knowledge obtained in the previous section, I focus on the analysis of the dispersion of the fabricated samples. Figure 3.10 (a) presents ε values for the fabricated RUTs based on the CEMA calculation by comparing the effect of ratio of the thicknesses of SiO₂ and Au (t_d/t_m), and the diameter ($2r_0$). The first part of Figure 3.10 (a) shows the dispersion of the RUTs with different thickness ratios [5/20, 20/20, and 40/10], presented by blue, magenta, and dark blue lines. The thickness

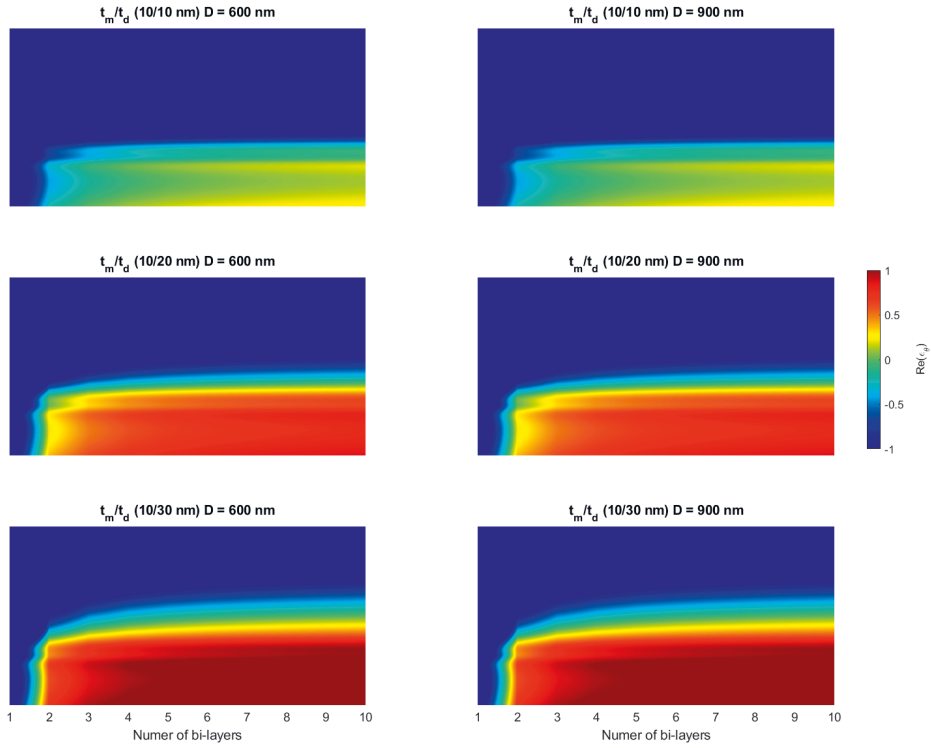


Figure 3.9 $\text{Re}(\varepsilon_\theta)$ for RUTs with two different diameters (600 and 900 nm), three different thicknesses of SiO_2 (10, 20 and 30 nm) and increasing number of bilayers.

of the layers defined the dispersion of the circular multilayer metamaterial. In addition, the large difference in the thickness ratios results in different diameters (1.5, 3, and 7.5 μm) as they provide different strain values but also modify the ε value and change the ENZ wavelength range quite significantly. Overall, the ENZ wavelength of the RUT is tuned from 400 nm to 600 nm, and it is possible to obtain the same or similar ENZ ranges using different diameters of RUTs by arranging the metal and dielectric layers. The second part of Figure 3.10 (a) shows $\text{Re}(\varepsilon_\theta)$ of some of the fabricated samples with identical thickness ratios (t_d/t_m) but different diameters (D). The dispersion results for 5/10 (632 nm) and 10/20 (1250 nm) as shown in black and green dotted lines are identical although having different diameters. Similarly, $\text{Re}(\varepsilon_\theta)$ for 10/10 and 20/20 with diameters of 712 nm and 3 μm shown in red and dotted magenta lines, are almost identical. Whereas the RUTs (2 and 5 μm) with a ratio of 20/10 and 40/20 have slightly different dispersion and ENZ wavelength

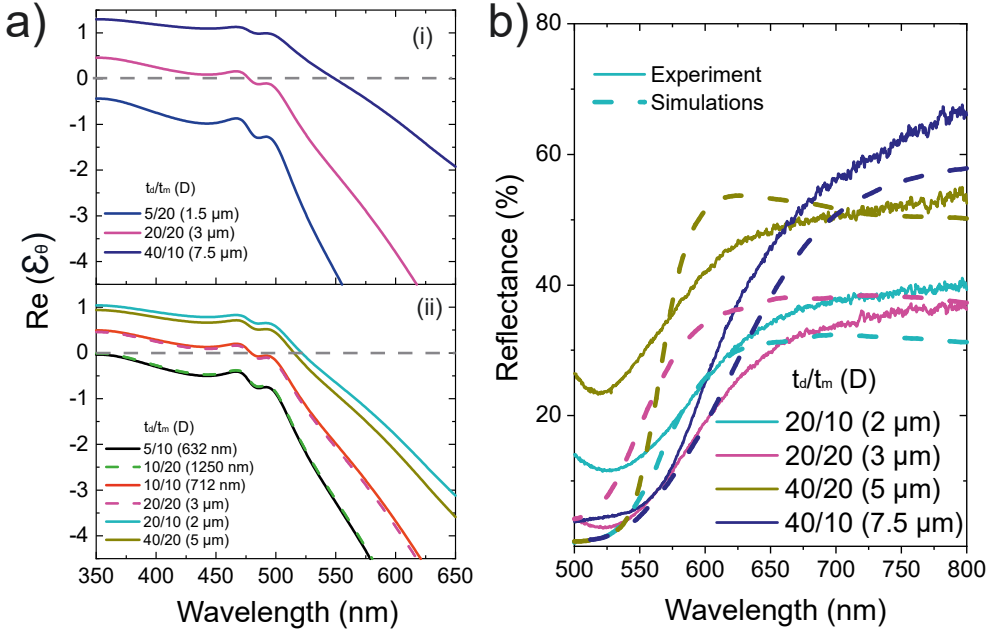


Figure 3.10 (a) Calculated $\text{Re}(\epsilon_\theta)$ of the fabricated RUTs using CEMA method. (b) Simulated and measured reflectance spectra from RUTs of diameters 2 μm (cyan), 3 μm (magenta), 5 μm (dark yellow) and 7.5 μm (navy blue).

regions. Note that, in all these tubes, the number of turns is higher than 4, and the ϵ values are almost identical even though the thicknesses and diameter are different.

The calculation of the material dispersion reveals that one can obtain quite similar results although the diameter of the RUT can be different. Therefore, one can design the ENZ wavelength range as well as the diameter based on the application needs such that it is possible to use a RUT with a diameter of 3 μm instead of 712 nm while exploiting the same material dispersion. Furthermore, the reflectance response of the same RUTs is investigated, which allows measurable areas using 100X air objective, Figure 3.10 (b) presents the simulation (dashed lines) and experimental (solid lines) for RUT with diameters of 2 μm (cyan), 3 μm (magenta), 5 μm (dark yellow) and 7.5 μm (navy blue). The results show the general trend for the reflection of the metamaterial with increasing reflectance above the ENZ wavelengths. The reflection spectra of the RUTs with diameters of 2 μm and 5 μm confirm that they exhibit a very similar ENZ transition (onset of the reflection band); however, the 5 μm RUT represents a more convenient platform for certain applications as it provides a larger collection area.

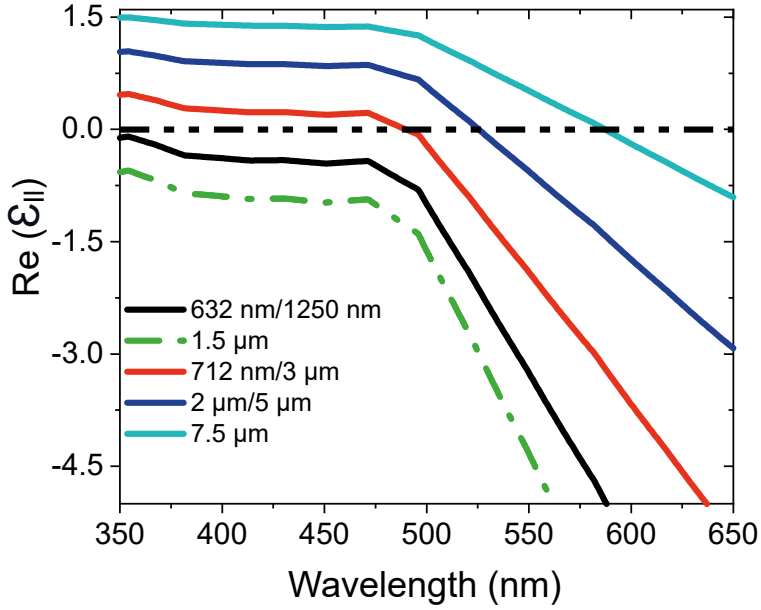


Figure 3.11 (a) $\text{Re}(\epsilon_{||})$ obtained from PEMA calculations for eight different fabricated RUTs.

Table 3.2 Comparison of ENZ wavelengths calculated using CEMA and PEMA for the fabricated RUTs.

t_d/t_m (D)	CEMA	PEMA
5/10 (632 nm)	362 nm	342 nm
10/10 (712 nm)	478 nm	488 nm
10/20 (1250 nm)	362 nm	362 nm
5/10 (1.5 μm)	340 nm	340 nm
20/10 (2 μm)	523 nm	524 nm
20/20 (3 μm)	478 nm	488 nm
40/20 (5 μm)	515 nm	524 nm
40/10 (7.5 μm)	548 nm	587 nm

For comparison purpose, $\epsilon_{||}$ and ϵ_{\perp} using PEMA are calculated. Figure 3.11, shows that the ϵ values are only the function of $(ff=t_m/(t_m+t_d))$ and there is no effect of the diameter of the tube [14]. As PEMA ignores the effect of the number of layers and the diameter of RUT, the ENZ wavelength is calculated using CEMA and PEMA as a function of the diameter of the RUTs, shown in Table 3.2. The results show

that when the tubes have a low number of turns, the ENZ wavelength values are significantly different. The RUT with $7.5 \mu\text{m}$ has ENZ wavelength $\sim 39 \text{ nm}$ longer when it is calculated with PEMA rather than CEMA. Therefore, it is more accurate to use CEMA for the material dispersion calculation of cylindrical HMM.

3.5 Structural dispersion

Beside the material dispersion of ENZ materials, there is also a technique based on structural dispersion to exploit the dispersion characteristics of composite metal-dielectric waveguides. Nanoscale plasmonic waveguides support a fundamental guided mode with a cutoff wavelength where the mode effective index vanishes, Light propagation in the ENZ media has the property of a stretched wavelength as a consequence of the near-zero refractive index, leading to a relatively small phase variation over the physically large region of such media. One of the advantages to use Ge as a sacrificial layer is to obtain tubes with a diameter $< 1 \mu\text{m}$. This allows to use of the tubes as waveguides and produces wafer-scale ENZ waveguides compared to rectangular waveguides fabricated [85] and numerically proposed [128]. Here, the smaller diameter tubes are investigated as waveguides with ENZ mode by taking advantage of structural dispersion. To study this dispersion phenomenon, first, the RUTs are considered as cylindrical waveguides. The Eigenmode simulation is used to study the fundamental modes excited at the cutoff wavelength of the RUTs.

The fundamental mode profiles and structural dispersion of the RUT were characterized using a Finite Difference Eigenmode (FDE) solver in Ansys Lumerical MODE. The numerical simulation is set up by building up different thickness dependent alternating layers of SiO_2 and Au with a hollow air core using Ansys Lumerical script commands. The solver type is set to 2D normal to calculate the mode profiles that exist in the RUT in the x-y plane. A minimum mesh step of 0.001 nm is used, grading factor of $\sqrt{2}$ and conformer variant 1 mesh refinement to attain mode profiles with good resolution. The mode profiles and the cutoff wavelength of the rolled-up waveguide are determined for different selected core diameters (D) (i.e. 632 nm , 712 nm , 1250 nm , and 1500 nm). In addition, parametric sweeps of the fundamental transverse electric (TE_{11}) mode at different spectral wavelengths are implemented for the different diameters of the waveguide to obtain their corresponding effective index (n_{eff}). The structural dispersion relation of the selected RUT diam-

eters is presented as the relation between the n_{eff} and the cutoff wavelengths of the RUT structure.

The dispersion relation of the selected RUTs exhibits the dependence of the waveguide effective mode indices n_{eff} as a function of wavelength. Figure 3.12 (a) illustrates the structural dispersion relation of the RUT with different core D. This helped in identifying the cutoff wavelengths where the effective refractive index of the medium is approximately zero ($n_{eff} \approx 0$) for the different RUTs. Since the index of refraction is directly related to the permittivity, these structures exhibit effective ENZ features.

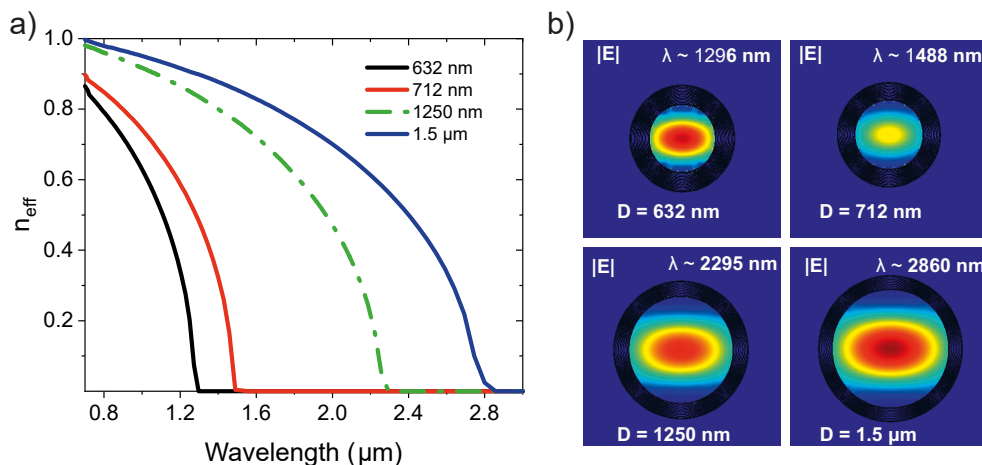


Figure 3.12 (a) The dependence of the waveguide mode effective indices n_{eff} on the wavelengths for the selected diameters. (b) Fundamental TE_{11} electric field $|E|$ distribution for the selected diameters of the RUT at their corresponding cutoff wavelength.

As the diameter of the RUT is the main defining parameter of the structural dispersion, for different diameters (i.e. 632, 712, 1250, and 1500 nm), the cutoff wavelengths obtained are $\sim 1296 \text{ nm}$, $\sim 1488 \text{ nm}$, $\sim 2295 \text{ nm}$, and $\sim 2860 \text{ nm}$, respectively. This illustrates the dependence of the cutoff wavelength as a function of varying diameters of the selected RUTs where the cutoff wavelength redshifts with an increase in the diameter of the RUT. This illustrates the structural dispersion phenomena where a structural parameter such as the diameter of the RUT determines the zero-index mode that can be excited in the RUT (Fig 3.12 (b)). Note that a circular waveguide structure, similar to our RUTs, illustrates a fundamental (TE_{11}) mode at their corresponding cutoff wavelengths. At the cutoff wavelength, the TE_{11} mode of the RUT has a dispersion curve that begins at the light line and cuts off the wave-

length axis at $k = 0$. A wave vector that is vanishingly small at the cutoff wavelength implies a waveguide mode with a near-zero index ($n_{eff} = k/k_0$) where the wave displays little or no spatial variations. Overall, these waveguide structures around the cutoff frequency of its fundamental mode behave as a metamaterial with effective ENZ features.

4 LOW LOSS 3D FISHNET METAMATERIAL

Besides the use of RUTs as multilayer metamaterials, these thin films can be further patterned to obtain much more complex metamaterials such as fishnet metamaterials [129], nanoholes based structures with Fano resonances [130], and nanohole based plasmonic sensor [131]. Using RUTs will bring an advantage by allowing us to study them in 3D. For example, using the nanoholes on the walls of RUTs as sensors can be a microfluidic channel and sensing platform at the same time. In order to pattern the walls and later characterize their optical properties, the resist-based technique is more efficient and flexible to the integration of a broad range of materials. Therefore, in PUBLICATION V, the resist-based tube is used to form 3D fishnet metamaterials as a prototype for nanohole-based 3D metamaterial platforms.

4.1 Fishnet metamaterials

The concept introduced by Veselago in the 1960s of negative refraction of light and later the application as perfect lensing [6] motivated scientists to work extensively on the topic of optical negative-index metamaterials (NIM). Typically, a pair of short wires aligned with E supports resonance with $\epsilon < 0$, and the wires along H , direction act as magnetic resonators, providing negative μ [132, 133]. Even though such an arrangement supports NIM, overlapping electric and magnetic resonances is a very difficult task. As a solution to this, a fishnet structure was introduced to realize both $\mu < 0$ and $\epsilon < 0$ at NIR frequencies [134, 135]. Figure 4.1 presents the schematic illustration of basic fishnet metamaterial [136]. Most of the experimentally implemented optical fishnet metamaterials consist of a multilayer structure and require multiple evaporation steps to obtain a bulk fishnet metamaterial [137–139]. The fabrication process can be laborious, especially when many functional layers are needed with precise thicknesses. The RUT fabrication can be used to overcome the problem of multiple depositions steps. Rottler *et al.* have shown curved fishnet metamaterial

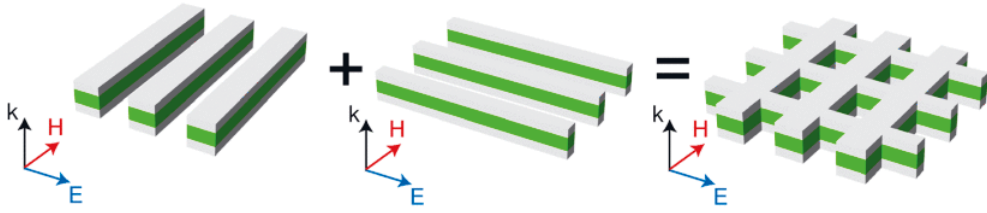


Figure 4.1 Schematic representation of a metal/insulator/metal as a functional layer with magnetic and electric response if used individually. When these two elements are combined, they form a fishnet structure with negative μ and ε at the resonance wavelength [136].

consisting of six alternating layers, using semiconductor strained gallium arsenide (GaAs)/ indium GaAs (InGaAs) layers on top of aluminum arsenide (AlAs) sacrificial layer [140]. Upon etching the sacrificial layer, the strained layers start to roll, and, in this way, it simplifies the process of multiple depositions and obtaining fishnet metamaterials.

However, the circular nature of the rolled-up structure brings a challenge to the spectral characterization of the fishnet metamaterials especially when the diameter is small. Therefore, although a prototype of a fishnet metamaterial was fabricated, the NIM behavior of such curved fishnet structures has not been realized. In this study, I experimentally demonstrate a curved fishnet metamaterial that consists of eight alternating layers of Au and SiO_2 . RUTs are fabricated by utilizing resist as a sacrificial layer as discussed in Chapter 3. The resist-based RUTs provide the possibility to include different kinds of materials into the layers of a tube with bigger diameters.

4.2 Design and fabrication

The studied fishnet structure consists of rectangular nanoholes on eight alternating layers of Au and SiO_2 with the periodicity of 400 nm along the x - and y - axes. The schematic of the structure is shown in Figure 4.2. To investigate the type of the modes supported by the fishnet structure the dispersion relation is calculated.

The dispersion relation of multilayered metamaterial helps to determine the existence of surface plasmon polaritons (SPPs) excited through a metal layer sandwiched between two dielectric media. To comprehend the excitation of internal and external SPPs in stacked hole, the dispersion relation is formulated using the Helmholtz

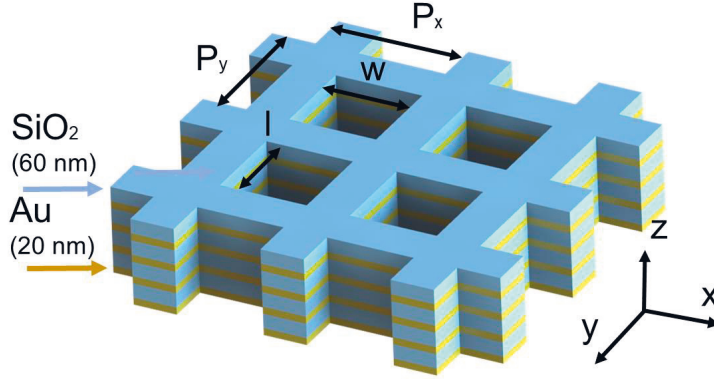


Figure 4.2 Schematic representation of a fishnet structure unit cell, where P_x and P_y are set to be 400 nm, $w=230$ nm and l is changed from 190 to 270 nm [125].

equations. The field solutions along the propagation direction as well as the evanescent fields confined in the transverse direction of the multilayered structure are determined. As shown in Figure 4.3 (a), the layers are assumed to be parallel in the x -axis with a relative ϵ dependent on one spatial coordinate ($\epsilon = \epsilon(z)$). The y -direction of the multilayered structure is considered to be infinite and homogeneous ($\partial/\partial y = 0$). The transverse confined field in the z -direction is related to the attenuation coefficients in two metallic media with a field dependence of $z > t_d/2 + t_m$, $t_d/2 < z < (t_d/2 + t_m)$, $-t_d/2 < z < t_d/2$, and $(-t_d/2 + t_m) < z < -t_d/2$ as shown in Figure 4.3 (a). Here, the TM plasmonic modes is considered in each region by applying the required boundary conditions. The vector potentials of the E -field and H -field are defined as \vec{F} and \vec{A} , respectively. For simplicity, the formulation is limited to the symmetric case whereby both the semi-infinite layers relative to the dielectric constants are equal to $\epsilon_1 = \epsilon_2 = \epsilon_{air}$ while $\epsilon_{m1} = \epsilon_{m2} = \epsilon_{Au}$ depicts the Au region. ϵ_d represents the ϵ of the sandwiched dielectric region (SiO_2 in this case). Based on the aforementioned conditions, the \vec{A} can be expressed as $A_z \hat{z} = A e^{k_z z} e^{i\beta x \hat{x}}$, where $e^{k_z z}$ describes the electromagnetic field depth dependence with $k_z = \pm \sqrt{\beta^2 - k_0^2 \epsilon}$ and $k_0 = 2\pi/\lambda$. k_0 depicts the vacuum wavenumber and propagation wavenumber along x direction shown in Figure 4.3 (b) is represented as β . Since metals are intrinsically lossy, the field penetration depth is minimal and essentially the dominant field will be surface waves concentrated at the metal-dielectric interfaces.

The dispersion relation helps to predict analytically the extraordinary optical

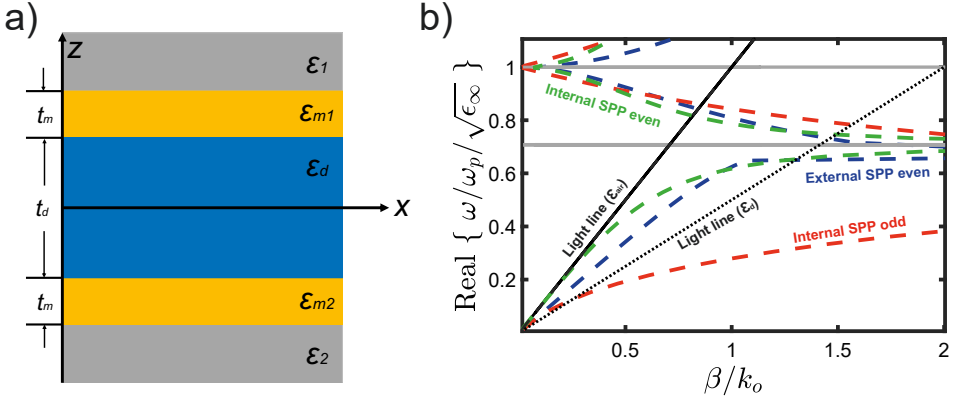


Figure 4.3 (a) The geometry of a metal/dielectric interface, with a dielectric sandwiched between two metal layers. (b) Dispersion relation of SPPs excited by the metal-insulator-metal structure that depicts the internal and external SPP modes which propagate along the internal and external metal-insulator interfaces. The light line ϵ_{air} and ϵ_d show the dispersion relation in free space and the dielectric medium, respectively. The SPPs even and odd show the symmetric and anti-symmetric modes excited by a dielectric sandwiched between two metal layers [125].

transmission (EOT) peaks from the excitation of both internal and external SPP modes. This model formulated to depict the EOT peaks at different spectral wavelengths does not consider the holes stacked in the multilayered structure. Stacked holes can be accounted for by implementing the conservation of momentum and energy between the incident optical field and the periodicity of the rectangular array. The relation of SPPs and conservation of momentum can be expressed as

$$\left| \vec{k}_{spp} \right| = \left| \vec{k}_x + \vec{G}_{i,j} \right| = \left| \vec{k}_0 \sin \phi + i \vec{G}_x + j \vec{G}_y \right| \quad (4.1)$$

where $\left| \vec{k}_{spp} \right| \equiv \beta(\omega)$ is the wave vector of the SPP, $\left| \vec{G}_x \right| = 2\pi/a_x$, and $\left| \vec{G}_y \right| = 2\pi/a_y$ are the reciprocal lattice vectors for the stacked holes, and $\vec{k}_0 \sin \phi$ is the in-plane component of the incident wave vector. a_x and a_y are the lattice periodicity in the x and y -directions. Notably, the normalized frequency at large Bloch wave vectors tend to approach the SPP frequency, which is expressed as

$$\omega_{spp} = \frac{\omega_p}{\sqrt{\epsilon_\infty + \epsilon_i}} \quad (4.2)$$

with $\epsilon_i = \epsilon_{air}$ or ϵ_d for external or internal SPPs, respectively. However, for a short-

wave vectors $\beta \ll k_p$, the SPP propagation constant is related to the internal SPPs, and is expressed as

$$\beta^{\text{int}} \equiv \left| \vec{k}_{sp}^{\text{int}} \right| = \left| \vec{k}_o \right| \sqrt{\varepsilon_{t_d}} \left[\frac{t_d}{t_d + \lambda_p \coth(k_p t_m) / \pi} \right]^{-1/2}, \quad (4.3)$$

where $k_p = 2\pi/\lambda_p$, and the external frequency of the low frequency range can be formulated as

$$\beta^{\text{ext}} \equiv \left| \vec{k}_{sp}^{\text{ext}} \right| = \left| \vec{k}_o \right| \sqrt{\frac{\varepsilon_{\text{air}} \varepsilon_m}{\varepsilon_{\text{air}} + \varepsilon_m}}. \quad (4.4)$$

Although the proposed formulation is an approximation of the metasurface design, it can be extended to the general case of multiple layers with random permittivities. This formulation is used to elucidate the properties of SPPs, the propagating modes on the surface and inside of the stacked hole metal-dielectric layers. Predominately, surface plasmons excitation in metamaterials is relevant due to its distinguishing feature of confining optical field in the sub-wavelength regime and guiding it to relatively long distances. These external and gap plasmon modes, excited by the metamaterials with holes, have been of interest and used to understand the acquired resonances in the reflectance spectra [141].

To account for the periodic nanoholes embedded in the multilayered structure (20 nm of Au layer and 60 nm of SiO₂), the dispersion relation is implemented between the wavevector $|\vec{k}_{spp}|$ and the reciprocal lattice vectors where the interaction between an incident optical field and SPP obeys the conservation of energy and momentum. Figure 4.4 illustrates the reciprocal lattice vectors $\vec{G}_{i,j}$ for the stacked hole arrays, the external SPP, gap SPP and the light-line of the dielectric media.

Next, the mode profile at 640 nm and 780 nm for the 230 nm nanohole case is calculated which corresponds to external SPP and gap SPP, respectively. In Figure 4.5, the top two panels show the y component of the E field in the y - x plane. The bottom panels show the x component of the H field, the cutting plane was in the middle of the unit cell with normalized color codes. The first mode at 640 nm indicates the fields are propagating on the top layer of the metal and air interface, an indication of external SPP. On the other hand, in the other mode, the fields are localized inside the hole and dielectric between the metal layers at 780 nm. Thus, the mode profile at 780 nm is evidence of the gap SPPs, which can be controlled by changing the hole

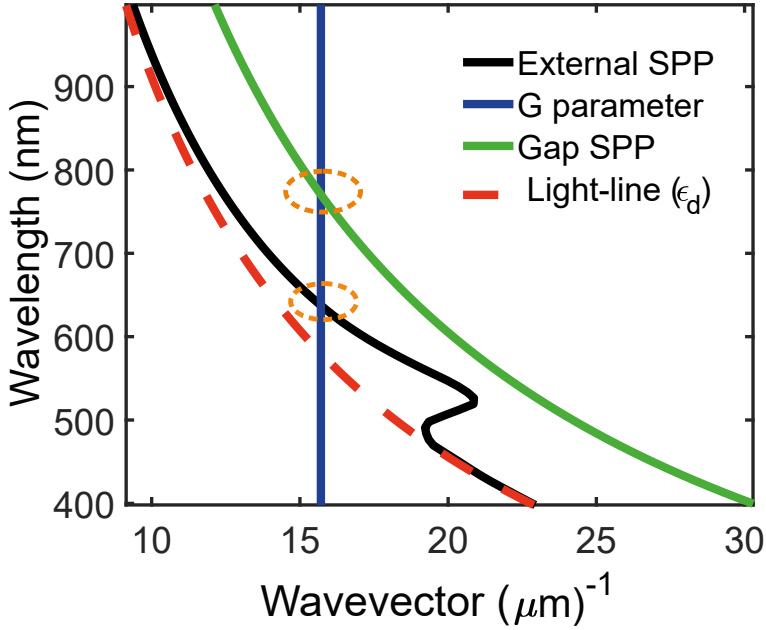


Figure 4.4 (a) Dispersion curves of the external and gap modes excited by metamaterials milled with holes. The light-line ϵ_d shows the dispersion relation of the dielectric medium and the G parameter corresponds to the reciprocal lattice vector of the stacked holes. The two orange circular insets illustrate the relation of SPPs and the conservation of momentum as a function of the lattice periodicity [125].

size.

Once the dispersion of the stacked layers is identified, the effect of the rectangular hole size on the resonance is investigated numerically. The reflectance spectra of fishnet structure with different hole sizes excited with γ -polarized plane wave source are presented in Figure 4.6. By increasing the size of the hole along y -axis a blueshift is observed in the resonance from 828 to 727 nm. The holes embedded in SiO_2/Au layers will have two resonances relative to the direction of the incident E and H field components. The cross-section along the H field exhibits magnetic resonance while the opposite cross-section along the E -field exhibits electric resonance. These two resonance effects result in the negativity of μ and ϵ of the proposed fishnet structure.

To experimentally realize the fishnet structure, the resist-based rolled-up technique is adopted to reduce the deposition steps for metal and dielectric layers. Instead of costly and tedious MBE deposition, The photoresist is spin-coated as a sacrificial layer. Such a sacrificial layer can be easily etched without compromising the qual-

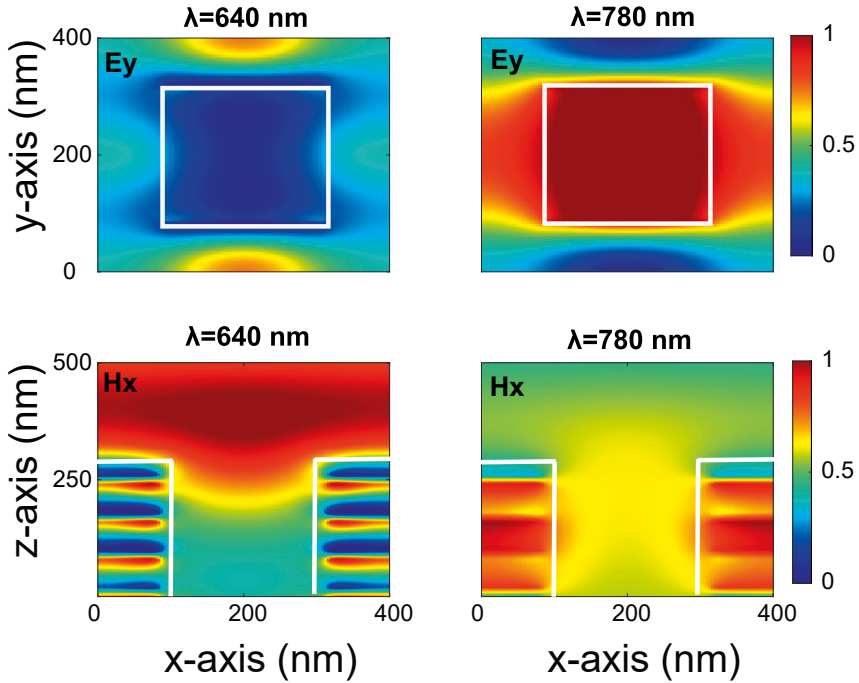


Figure 4.5 The y component of electric (E) fields from the top at 640 and 780 nm are presented in top panels. Similarly, the x component of H -fields from the cross-section are presented in bottom panels at 640 and 780 nm [125].

ity of obtained tubes. In addition, the fishnet structure integrated into the wall of RUT eliminates an undesirable effect caused by the substrate of decreasing negative refractive response, especially prominent in the structures with a small number of functional layers [142]. Si/SiO₂ is used as a substrate, and 60 nm of SiO₂ and 20 nm of Au are deposited on top of the photoresist using the same fabrication method discussed in detail earlier (section 3.1.1). By quickly removing the photoresist with acetone the tubes are formed with large diameters ($\sim 10 \mu\text{m}$).

Finally, the fishnet structures are created on this fabricated RUT using the FIB milling method. A Zeiss Crossbeam 540 FIB machine is used to ion mill the holes through the upper wall of the RUT. The acceleration energy of gallium ions is 30 KeV. The ion current used in the experiments is not determined because it is not calibrated, but a 1 pA probe is used.

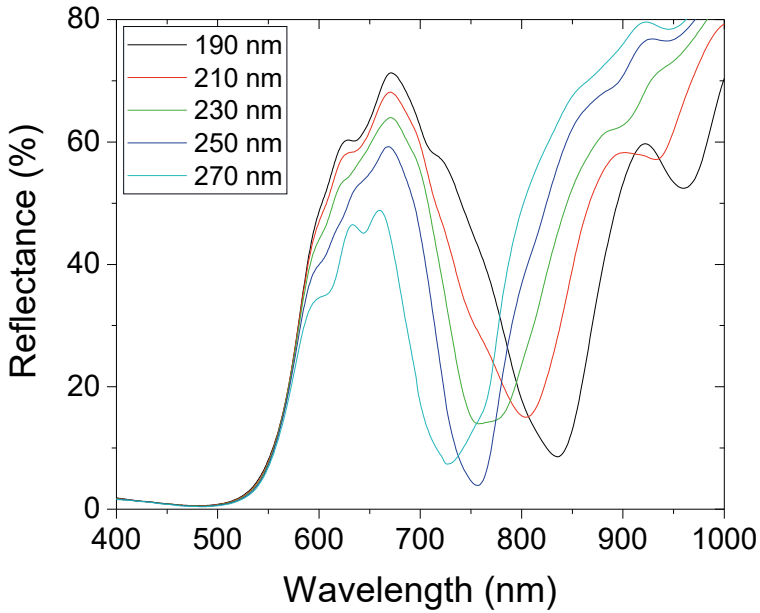


Figure 4.6 Numerically calculated reflectance response of fishnet structures with length fixed along x -axis and changed in y -axis, 190 nm (black), 210 nm (red), 230 nm (green), 250 nm (blue), and 270 nm (cyan) [125].

4.3 Results and discussion

The large diameter of RUT supported an array with 20 unit cells along x -axis and 30 unit cells along y -axis on the upper curvature of the tube. The number of unit cells is limited by the size of the curvature of the tube. As the length of the tube is sufficient, all of the five designs are fabricated on the same tube to maintain the same material environment and focusing surface for the measurements. Overall, five different fishnet structures are fabricated on 75 μm long RUT. Figure 4.7 shows the microscope and the SEM images of the fabricated structure on top of RUT. The RUTs formation is confirmed by taking microscopy images. The SEM images are taken from the top of the tube to verify the quality of the structure, see Figure 4.7 (c-g). For structural analysis such as the RUT quality and the number of layers, a cross-sectional SEM image is taken, as shown in Figure 4.7 (h).

The large diameter of $\sim 10 \mu\text{m}$ allowed the optical measurement of the patterns

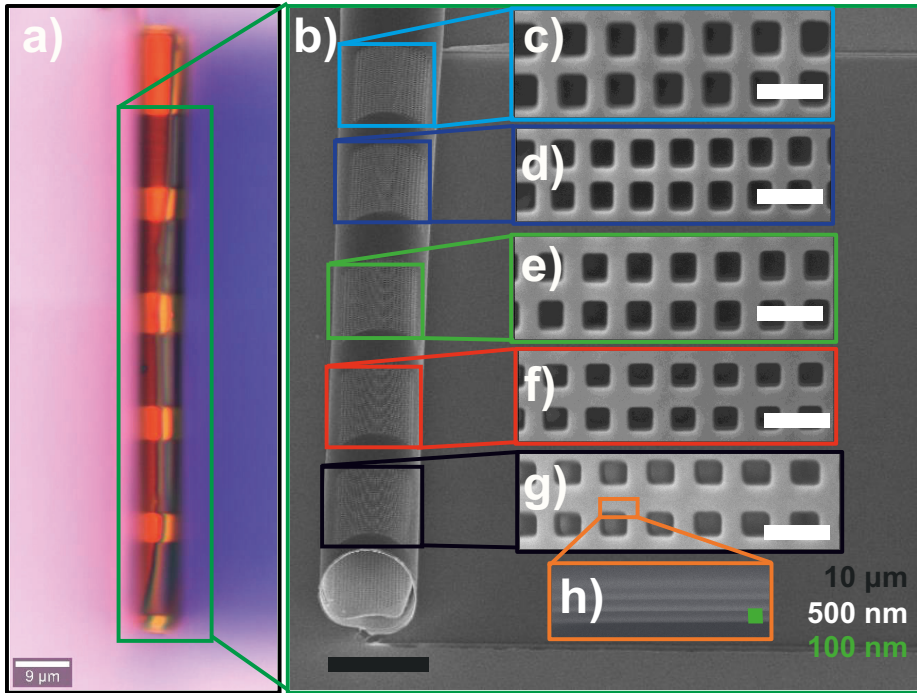


Figure 4.7 a) A microscope image of RUT with 8 alternating metal and dielectric layers with a fishnet pattern on the upper curvature (top view). b) SEM image of the same RUT. A zoom-in of a fishnet with a hole size c) 270, d) 250, e) 230, f) 210, and g) 190 nm. h) An SEM cross-section image of the RUT wall [125].

with standard techniques. The fabricated fishnet structures are characterized using 100X objective and y -polarized broadband white light source. The reflection spectrum of the fishnet from the upper curvature of RUT is obtained with respect to the acquired reflection from the unpatterned area of the Si/SiO₂ substrate. Figure 4.8 presents the reflectance measurements for different hole diameters. The resonance for the smallest hole size appears at 870 nm, and blueshifts towards the lower wavelength as the size of the holes are increased. These results are in good agreement with the simulated results presented in Figure 4.6, however, the air gaps in the layers may create some interference effect and result in the ripples.

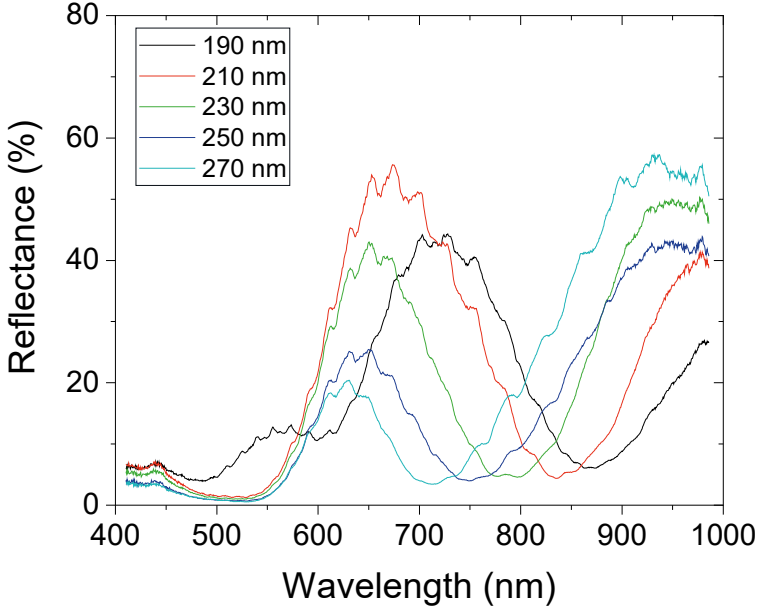


Figure 4.8 Experimentally measured reflectance from the RUT-based fishnet structure with five different hole sizes [125].

4.3.1 S-parameter calculation

The refractive index of the simulated and fabricated fishnet structures is analytically calculated with the scattering matrix (\mathbb{S}) parameters:

$$\mathbb{S}_{21} = \mathbb{S}_{12} = \frac{1}{\cos(nkd) - \frac{i}{2} \left(Z + \frac{1}{Z} \right) \sin(nkd)}, \quad (4.5)$$

$$\mathbb{S}_{11} = \mathbb{S}_{22} = \frac{i}{2} \left(\frac{1}{Z} - Z \right) \sin(nkd), \quad (4.6)$$

where \mathbb{S}_{21} , \mathbb{S}_{12} , \mathbb{S}_{11} , \mathbb{S}_{22} , Z , n , k , and d represent the \mathbb{S} parameters, the impedance, the effective refractive index, the propagation constant (wave vector) and the thickness of the fishnet structure, respectively. \mathbb{S}_{21} represents the forward transmission, \mathbb{S}_{12} is the backward transmission, \mathbb{S}_{11} is the forward reflection, and \mathbb{S}_{22} is the backward reflection. From the effective retrieval formulation, the (n_{eff}), which represents the material properties of the fishnet structure can be obtained using the scattering pa-

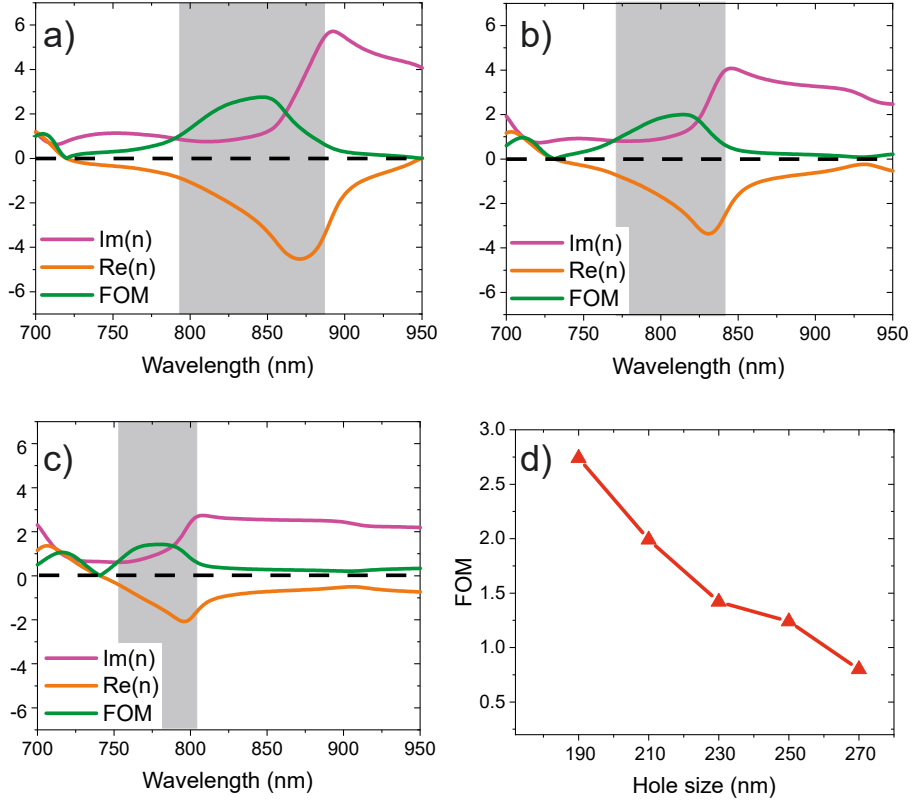


Figure 4.9 The refractive index calculated with \mathbb{S} -parameter retrieval method for fishnet structure with hole size a) 190 b) 210 and c) 230 nm. d) FOM of all fishnet structures versus the holes' size [125].

rameters and the inverse of the optical path length (kL) as a function of wavelength,

$$n_{eff}(\omega) = \pm \left(\frac{1}{kL} \right) \arccos \left(\frac{1 - S_{11}^2 + S_{21}^2}{2S_{21}} \right), \quad (4.7)$$

where k and L denote the propagation wavenumber and the size of the unit cell, respectively [143]. The negative index is observed around the resonance region of the reflectance spectrum of the structures. Therefore, the calculation range of the \mathbb{S} -parameters is set from 700 to 950 nm. In addition to resonance wavelength, the quality factor (Q-factor) of the resonance is important. The Q-factor of the last two structures (Fig. 4.6 (f) and (g)) is low. Therefore, the index of the first three structures (190, 210, and 230 nm) is calculated. Figure 4.9 (a-c) shows real and imaginary parts

of refractive index for 190, 210 and 230 nm case, respectively.

The fishnet design with a high Q-factor (190 nm case) has the largest negative index value compared to two other cases. The negative index region is highlighted by gray colour in each graph. However, the large value of the real index ($Re(n)$) is not the only criteria to design NIM. In order to define a high-quality NIM, one needs to define the imaginary part ($Im(n)$) as well as the $Re(n)$. The figure of merit (FOM) is used to calculate the ratio between $Re(n)$ and $Im(n)$ as:

$$FOM = Re(n)/Im(n) \quad (4.8)$$

The maximum value of the calculated FOM for the fabricated structures is 2.76. This FOM is three times higher than in the work based on the rolled-up structures reported earlier [140], which indicates the low-loss feature of the fishnet metamaterial studied in this work.

5 OUT-OF-PLANE METASURFACES

Although metasurfaces have currently been under heavy investigation for numerous numbers of applications, there are only a few works that investigated the curved metasurfaces, Burch and Falco attached the metasurfaces on a nonflat platform to obtain curved metasurfaces [144]. Wu *et al.* numerically modeled the curved metasurfaces to investigate the effect of nonflat design [145]. However, the designs are limited in terms of fabrication and integration. The patterning of RUTs as 3D fishnet metamaterials allows a platform to study advanced devices such as curved metasurfaces on RUTs. One of the examples of this advancement is to use these nanoholes as metasurfaces to shape the wavefront of light inside the RUTs. The purpose of using RUTs is to take the advantage of curved nature of RUTs and provide a much simpler way to obtain the curved metasurfaces. Therefore, in PUBLICATION VI, the nanoholes are designed to control the wavefront of light and investigate the effect of the curved design of the metasurfaces compared to the planar case.

5.1 Metasurfaces

In recent years, the two-dimensional counterparts of metamaterials (metasurfaces) have been extensively studied to achieve applications such as metalenses [146–148], beam steering devices [149], color filters [150], visual gas sensing [151], holography [152], and optical trapping devices [153]. The basic principle of metasurfaces is to modify the wavefront of light by changing the phase, amplitude, and polarization in the desired fashion. Earlier this was done using bulky optics which work on the principle of refraction and reflection of light. This required propagation of light through the media with different indexes of refraction to control the light. This limits their ability to steer light in an unusual way. Therefore, metasurfaces which use the metallic [154] and dielectric [155] nanostructures or nanoholes [156, 157] to control the light much more significantly compared to the conventional optics. The

essence of these metasurfaces is to use them as an array of nanostructures with unit cells much smaller than the wavelength of light with varying the spatially the geometry to achieve a spatially varying optical collective response [158, 159]. This response can then mold the wavefront into different shapes that can be easily designated. Different level of manipulation and efficiency was obtained in these applications which are provided by the arrangement of different antennas.

The V-shaped antennas are one of the earlier metasurfaces designed to control light. Yu *et al.* presented the use V-shaped antenna which can abruptly change the phase of light [160]. Later these were used quite extensively for spatially varying phase and polarization responses [161, 162]. The other shapes include elliptical [163], square nanoposts [164], and perforated nano-voids or nanoholes [165, 166]. Among all these metasurfaces, the nanohole arrays contribute to the flexible metasurface platforms with different applications due to their top-down approach to incorporating various materials [167].

When these nanohole arrays are obtained on the structures comprising stacked metal-dielectric layers, the spectral response will be much richer as the additionally supported SPP modes arise, discussed earlier in detail in section 4.2. Not only single-interface (external) SPP [168] but also a gap (internal) SPP [169, 170] are supported in these nanohole arrangements introduced on a thin metal layer or metal/dielectric stacks. Over the last several years, these nanohole arrays delivered interesting features and applications from EOT [171] to enhanced biosensing [172] and realization of the negative refractive index [173–175]. Lately, Matusui *et al.* brought metal-dielectric hole arrays to the metasurface applications using different shapes to control the phase of the transmitted light [176]. Additionally, an inclined wavefront for beam steering in the near-infrared range has been achieved using a gradual change in the hole size [177]. These inverted metasurfaces in contrast to the regular ones lead to a significantly higher signal-to-noise ratio, and efficient focusing of the incident light [166]. However, the fabrication of such structures is typically based on sub-sequential layer deposition of metal and dielectric, which require precise control of the deposition of each layer. As highlighted earlier, such an approach is not only time-consuming but also limited by the uniformity and reproducibility of each layer, given the involvement of multiple steps of deposition. Therefore, in this work, nanohole-based metasurfaces are fabricated on top of RUTs similar to fishnet structures in the previous chapter. In addition to the reduction in deposition steps, the

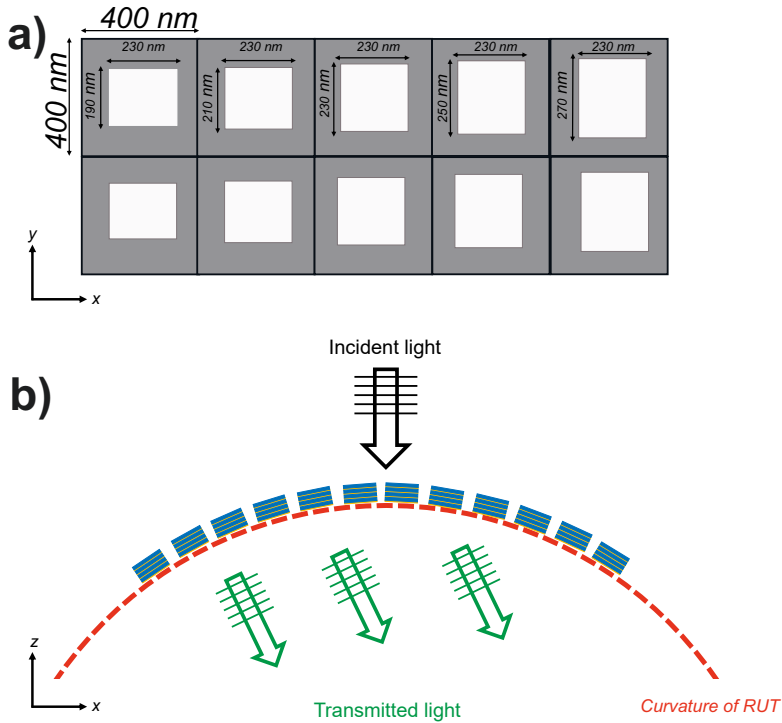


Figure 5.1 (a) The top view of varied hole size structures are used to obtain wavefront control. A unit cell is composed of five different hole sizes. (b) The schematics of inclined wavefront transmitted inside the RUT with nanoholes on the top curvature [100].

curved nature of RUTs allowed designing out-of-plane metasurfaces.

The metasurface design is based on fishnet structures/nanoholes. As the modes provided by the different size nanoholes are identified in the previous chapter, it is possible to bring them together in the design of the metasurface. Figure 5.1 (a) presents the top view of the proposed design of the nanoholes with different side lengths changing from 190 to 270 nm along the y -axis which is placed in a supercell of $2 \mu\text{m}$. Although this simple planar design based on the metal-dielectric stacks works efficiently to control the wavefront, it is limited by the variation of the planar nanohole dimensions. Therefore, the additional phase control requires the extension of the metasurfaces design to out-of-plane. Motivated by the recent advances in the 3D self-rolling RUTs and the fabrication of inverse metasurfaces, and by combining these features in the out-of-plane metasurface on these 3D photonic microstructures. Figure 5.1 (b) shows the cross-sectional view of the proposed metasurface design

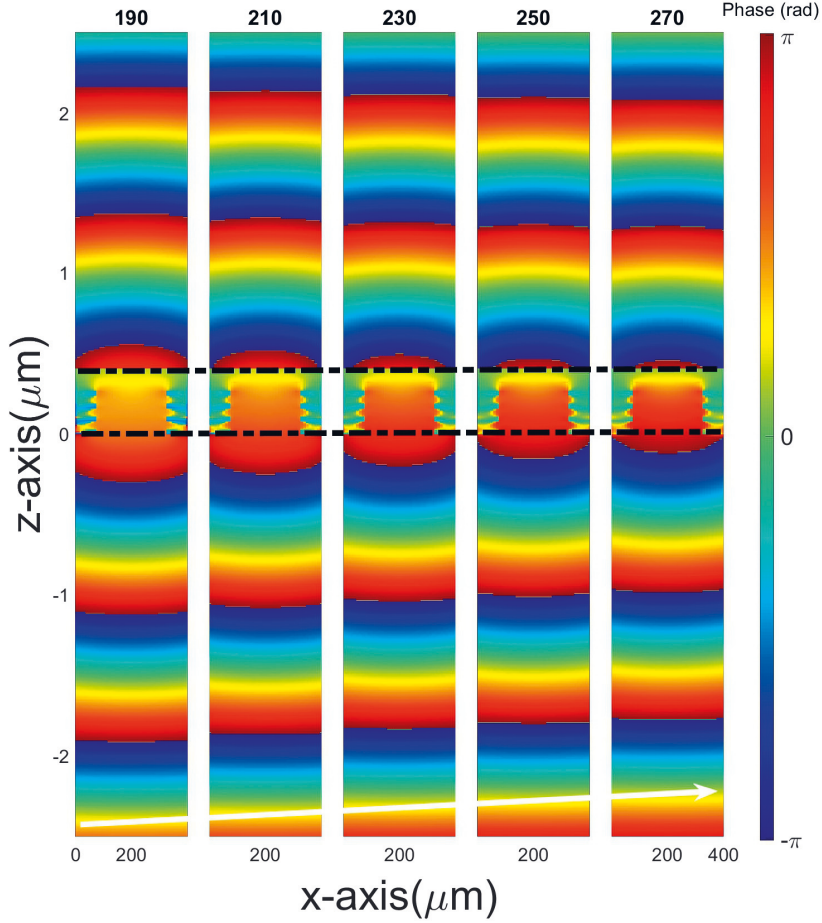


Figure 5.2 Phase profile (units in radians) of y component of the E -field up to 2λ from the nano-holes changing along y axis from 190 to 270 nm at $\lambda=750$ nm. A white arrow is added for better visual comparison [100].

with the additional control which is achieved by introducing a curve to the planar nanohole array.

To investigate the metasurfaces, the change in the phase of the E -field by increasing the hole size is simulated at $\lambda=750$ nm. The E -field is calculated by exciting the samples with the same linearly polarized Total-Field Scattered-Field (TFSF) source in the y direction with PML BCs along with all directions. The complete supercell with the same and different holes is designed to see the effect of planar and curved RUTs on the wavefront control and electromagnetic field manipulations. A uniform

mesh of 4 nm is used to obtain a better resolution in the distribution of the E -field.

Figure 5.2, shows the numerically calculated phase profile of five different hole sizes up to 2λ along the direction of the propagation (z -axis). As the hole size changes from 190 nm to 270 nm, the transmitted light experiences an additional phase. Thus, increasing the hole size from 190 to 270 nm gradually with a step size of 20 nm along the normal to the polarization direction (while keeping other parameters fixed) will introduce a gradual change of 0.95 radians in the phase. Although this can be optimized further for specific applications, this is sufficient to explore the proof-of-concept in this work. The numerical results confirm that using a transition in the hole sizes leads to an inclined phase that can be used to control the wavefront for changing the propagation direction or focusing.

5.2 Results and Discussion

To experimentally realize out-of-plane metasurfaces for wavefront control, RUTs are fabricated using a resist-based self-rolling mechanism, used for fishnet metamaterials. A tube with a diameter of $10\ \mu\text{m}$ supplies a surface area that is big enough to accommodate 20 unit cells of 400 nm (or 4 supercells). Besides, the curvature of such diameter provides the out-of-plane effect with respect to the operating wavelength. Once the desired diameter of $10\ \mu\text{m}$ is achieved, the number of turns and the size of the tube by designing the rectangular pattern. The short side of the rectangle defines the length of the tube, and the number of turns is defined by the longer side of the rectangle, as the rolling happens along the shorter edge of the rectangle. $75 \times 125\ \mu\text{m}^2$ rectangular pattern was used to achieve the $75\ \mu\text{m}$ long tube with 4 turns meaning 8 alternative layers of SiO_2 and Au. The nanohole arrays were obtained using FIB milling on the upper curvature of RUT. The optical microscope image and the SEM images of the milled area ($8 \times 12\ \mu\text{m}^2$) are presented in Figure 5.3 (c-f). The quality of the tube is first confirmed using an optical microscope, as shown in Figure 5.3 (a), the FIB milling is performed on the center of curvature, to achieve better quality metasurfaces, presented in Figure 5.3 (b) as a complete device and a supercell in Figure 5.3 (c). The cross-section SEM image is taken to confirm the number of bilayers, shown in Figure 5.3 (d). The tilted images are used to measure the diameter and rolling quality of the tubes, shown in Figure 5.3 (e) and (f), respectively. To control the wavefront of light, it is important to achieve maximum phase difference. However,

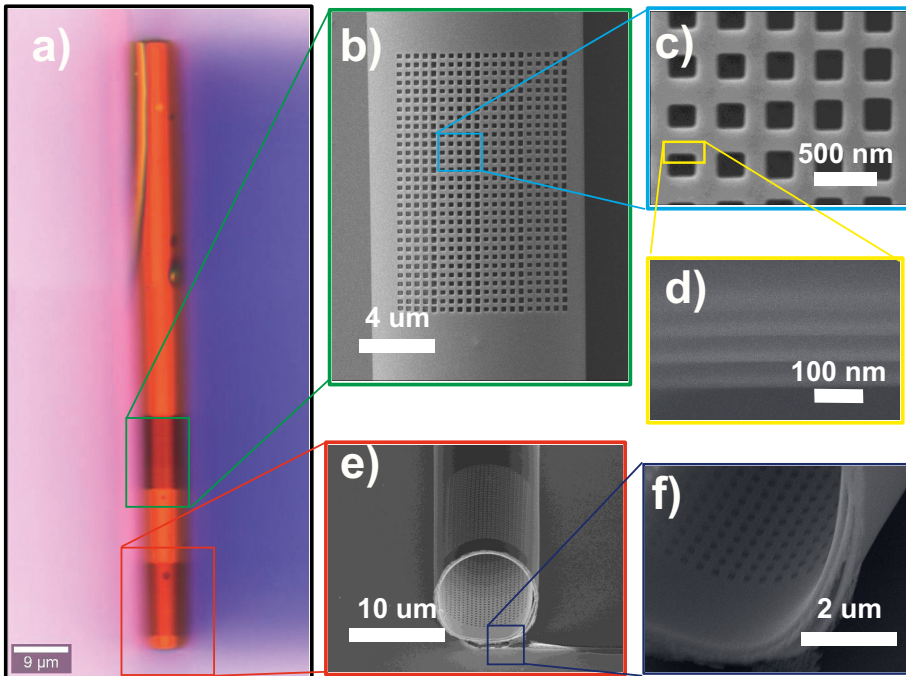


Figure 5.3 Released thin films resulting in the formation of RUT with a diameter of $10\ \mu\text{m}$. a) Optical microscope image of RUT with nanoholes. The SEM images from (b-c) top, (d) cross-section, and (e-f) bottom corner [100].

this phase difference should be achieved with less modulation in the intensity of the transmitted light. Figure 5.4, presents the comparison between the transmission intensity (red line with circles) and phase (black line with rectangles) of the transmitted light at $\lambda=750\ \text{nm}$, showing that the proposed metasurface has minimum intensity modulation. Changing the hole size from 190 to 270 nm results in ~ 1 radian phase difference, which is suitable for the proof-of-concept phase control in out-of-plane metasurfaces.

Figure 5.5 comparatively presents the phase profile for two different cases (planar metasurfaces and curved metasurfaces) with a single hole size (190 nm). The planar metasurfaces with equal hole size confirm no phase gradient and the electromagnetic field propagates in the straight direction without any change in the propagation direction. Contrary to that, the curved metasurfaces with the same hole size will slightly bend the light towards the center of the tube. This unique nature of the curved metasurface introduces an additional control to the light propagating inside

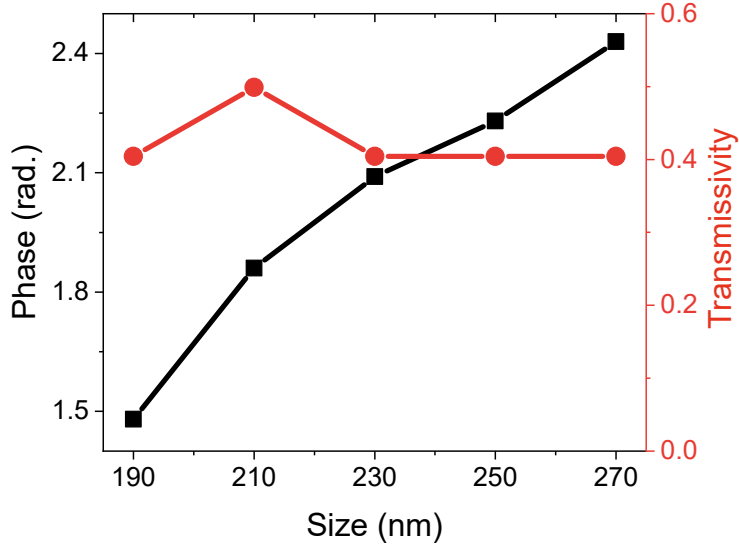


Figure 5.4 The comparison of different hole size transmission intensity and phase at $\lambda=750$ nm [100].

the tube compared to that of the planar case. The curvature of RUT brings a new degree of freedom to control light more effectively compared to planar metasurfaces. Finally, the role of the curvature on the wavefront propagation inside the RUT with nano-hole arrays is investigated. To identify this, first, the phase response from the metasurfaces with a uniform hole size at $\lambda=750$ nm was calculated. Then, to mimic the effect of the curvature, the phase response is calculated for the metasurfaces with different hole sizes in a supercell ($2 \mu\text{m}$) with five different hole sizes. The change in the hole size along the y axis introduces a gradual change in phase, leading to steady wavefront control in one direction (Figure 5.6).

The change in the phase for the planar case is due to the change in the hole size. However, the phase response for the out-of-plane metasurfaces has additional bending which is the outcome of the curvature of the tube. The curvature of the RUT defines the additional phase component for the out-of-plane nanohole-based metasurfaces. For this RUT, each hole has a tilt of 6° compared to the adjacent nanohole. The results show that the curvature of the RUT brings an additional phase control compared to the planar case, that only depends on the size of the hole. For a single unit cell, the phase is changed up to 0.77 radians, while changing the tilt angle from 12° to -12° .

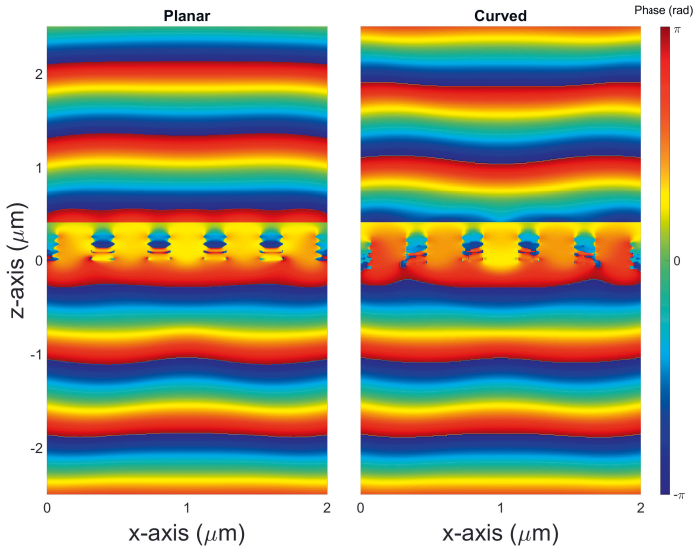


Figure 5.5 Phase response of the y -component of the E-field at $\lambda = 780$ nm for planar and curved metasurfaces with same hole size, respectively [100].

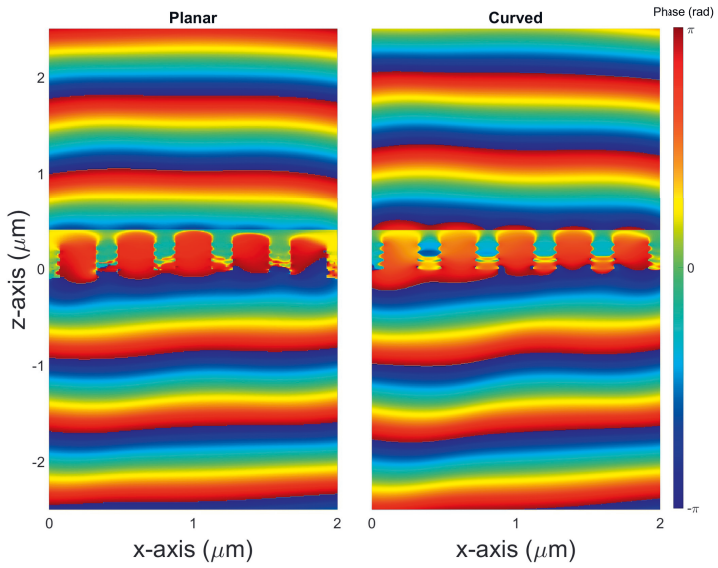


Figure 5.6 Phase response of the y -component E-field at $\lambda = 750$ nm for planar and curved metasurfaces with different hole sizes, respectively [100].

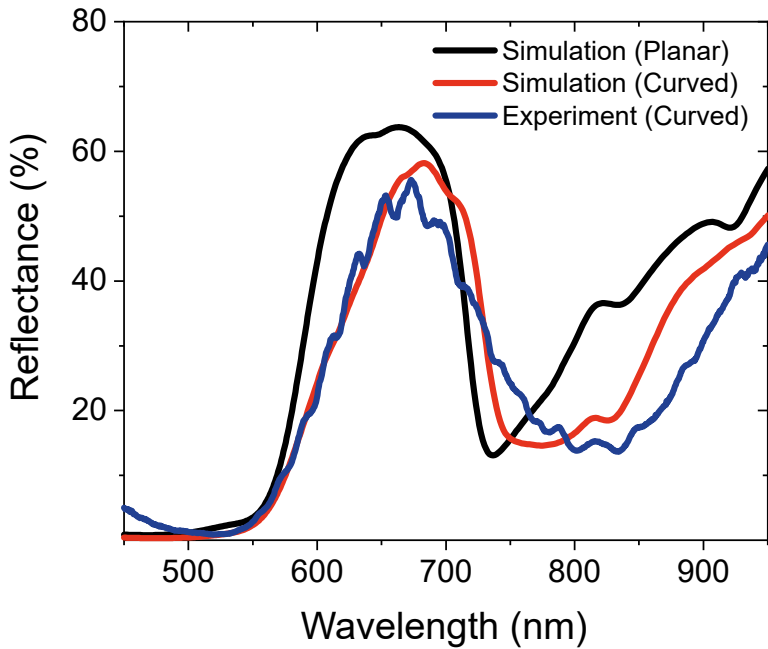


Figure 5.7 The simulated and measured reflectance spectra of the fabricated sample with nano-holes of different sizes from the planar (black) and curved metasurface (red (simulation) and blue (experiment)). The light is illuminated from the top of the RUT with y -polarization [100].

The fabricated samples were characterized using a confocal microscope with results presented in Figure 5.7. The simulation results are presented in the same figure, for two different metasurfaces with planar (in black) and curved (in red) metasurfaces, that are illuminated by y -polarized light source. The measurement (in blue) has a better agreement with the numerically calculated results for the curved metasurface design.

The spectral response of the supercell is an average of all the individual holes. The experimental results show that the out-of-plane metasurfaces will be different from the planar metasurfaces. This new degree of freedom will allow better control of light and will open an entirely new avenue to utilize the light inside the tube. This controlled propagation of light can be then used to selectively manipulate the particles as well as sense them inside the RUTs.

6 THESIS SUMMARY

The work in this thesis is aimed to study thin film-based metamaterials from a different perspective. The thesis introduces the basic concept of metamaterials and their significance in present-day technology.

The thesis begins with the introduction of important topics, such as HMM and how multilayer thin films can be used to design metamaterials. Next, the topic of the plasmonic antenna is elucidated and the importance of substrate on the plasmon resonance is highlighted. The ENZ metamaterials used in this thesis are based on HMMs. This allows using these ENZ metamaterials with a significant amount of flexibility to tune the ENZ spectral region. The ENZ feature is used to control the plasmon resonance of the plasmonic antenna by slowing down their spectral shift. This is possible because of the high impedance of ENZ materials and restricting the field propagation inside them leading to less shift in the resonance. Two different ENZ substrates are designed by changing the thicknesses of TiO_2 and therefore, the pinning effect is observed at two different wavelengths. Due to the unique feature of ENZ media, one can diminish the effects of the size of the nanostructure on the spectral position of plasmon resonance. Transmission spectra of the NDs, fabricated on glass, HMM-1 (ENZ at 684 nm) and HMM-2 (ENZ at 751 nm) display 50, 16, and 29 nm of spectral shifts in the resonance, respectively, as the disk diameter increases. The spectral shift of the NDs on HMMs is suppressed at least three times due to almost zero index of the substrate. The phase of the scattered field from an ND is affected by the ENZ properties of the substrate providing flexibility on the phase modification. In addition to that, the phase shift on top of ENZ substrates is significantly low compared to a glass substrate. The total shift in the resonance is reduced almost 3 times for HMM-1 (ENZ at 684 nm) and 2 times for HMM-2 (ENZ at 751 nm). Thus, better control of the LSPR can be achieved using HMM-based ENZ substrates.

Controlling the plasmonic resonance via substrate properties will open an en-

tirely new avenue. For example, this will provide an efficient method to control the emission properties of quantum emitters and the scattering properties of nanoparticles. I foresee that the improved low-loss ENZ substrates and dynamic tunability of the ENZ wavelength will bring more implementations to this platform. Recently, it has been shown that the large non-linear optical response of ENZ materials [58, 76] provides optical tuning of ENZ wavelength. Similarly, the graphene-based tunable HMM [178] can be used in the MIR range to electrically tune the pinning wavelength. Another perspective would be using the function of Vanadium dioxide (VO_2) as a phase-changing material in the HMM layers [179] to thermally turn on and off the pinning effect. The control over the plasmon resonance by designing an ENZ substrate and tuning its properties dynamically enables compensation of the fabrication error from the visible to infrared region. Metal-insulator-metal-based tunable ENZ cavities [180] can be used to obtain a pinning effect in waveguides. Overall, these results may facilitate efficient sensing, better beam-steering applications, and less crosstalk for on-chip nanophotonic devices in flat optics designs.

Although the multilayer metamaterials hold great potential, the fabrication of multilayer thin film requires subsequent deposition steps. In order to overcome the limitations introduced due to the consequent deposition process of a planar HMM, a new fabrication approach is required. To address this, the self-rolling technique that has been used for MBE growth materials is adapted to the multilayer materials using commonly used dielectric and metal layers for HMMs.

The strain-induced self-rolling mechanism is used to fabricate RUTs multilayer metamaterials. The diameters of the Ge-based RUTs are modelled and controlled as a function of thicknesses of SiO_2 and Au. The RUTs with diameter ranges from ~ 632 nm to $7.5 \mu\text{m}$ are obtained. The RUTs with small diameters are suitable for waveguide application, while the bigger diameter RUTs can be used in 3D metamaterials. The material dispersion is modelled using CEMA for 3D HMM which is controlled by the thicknesses, the number of layers, and the diameter of the RUT. The optical dispersion of circular multilayer structures is qualitatively defined using an effective medium approximation method. This analytical model reveals that the ENZ wavelength range of RUTs can be tuned by the ratio of the metal and dielectric content. However, the diameter of the RUT which is also a parameter in these calculations is interrelated to the thicknesses of the layers and their ratio via the strain-induced fabrication method. Hence, it is possible to obtain similar disper-

sion properties for RUTs with different diameters but similar thickness ratios. The fabricated RUTs in this study, exhibit ENZ wavelengths in the visible range for various diameters. The RUTs are also characterized and compared with the numerically obtained reflection response of the RUTs with a diameter bigger than $1.5 \mu\text{m}$.

The RUTs are also an excellent structure as a hollow cylindrical waveguide that supports the guided mode. Here, the RUTs are used as ENZ waveguides with the index zero effective modes that vanish and stretch the wavelength. The ENZ waveguide mode is very sensitive to the diameter and is studied through the ENZ waveguide mode. In addition to the material dispersion, the structural dispersion of RUTs is studied by considering the fabricated RUTs as cylindrical waveguides. The waveguide modes are supported inside the core of the RUTs and identify the cutoff wavelength of the fundamental mode which supports the ENZ medium. A strong shift is observed in the cut-off wavelength from 1296 nm to $2.86 \mu\text{m}$ for RUTs with diameters ranging from $\sim 632 \text{ nm}$ to $1.5 \mu\text{m}$, respectively. This makes the ENZ mode very sensitive to the diameter of the RUT. The use of a self-rolling mechanism for the ENZ waveguide overcomes the limitation of the fabrication process and the throughput is faster and higher.

Overall, a self-rolling ENZ medium-based platform is presented whose optical properties can be engineered through material dispersion. Therefore, this work opens new applications for ENZ metamaterials, such as studying the integration of phase-changing materials on a planar layer and rolling them to form multilayer tunable ENZ (e.g. graphene and vanadium dioxide). Moreover, the integration of quantum emitters in an ENZ medium can be used for quantum information processing and communication applications.

These self-rolling tubes with bigger diameters supply a unique platform to design and fabricate 3D metamaterials and metasurfaces. The use of RUTs as HMM can be further extended to exotic metamaterials by patterning from the top to form curved metamaterials. The curved metamaterials, in general, open the possibility to prepare 3D devices. The RUTs are further patterned with FIB milling to form fishnet structures on the upper wall of the RUTs. The nanoholes are analytically modelled to identify different modes. The fabricated samples are numerically modelled and characterized by measuring their reflection response. The bigger diameter allows the characterization of 3D fishnet metamaterials. Moreover, the fishnet structures are further analyzed by calculating their index of refraction. The numerical calcu-

lations demonstrate that the structures exhibit a negative index. The negative index region can be tuned by precise control of the size of the holes, from $\lambda = 887$ nm to $\lambda = 717$ nm. The maximum value of the calculated FOM for the fabricated structures is 2.76 which is three times higher than earlier reported structures. Hence, low loss 3D fishnet metamaterials are introduced with a simple resist-based fabrication method and characterized for the first time.

The results obtained are especially beneficial from the point of view of the easily available fabrication materials. Indeed, the results show a simple and flexible platform for the fabrication of RUT-based metamaterials. It is possible to shift the NIM response towards the visible spectrum by using Ag-based RUTs. Moreover, the RUT with an embedded fishnet structure can serve as a microfluidic channel where biological imaging and sensing can be done.

The patterning of RUTs to form a 3D fishnet metamaterial opened a new avenue for studying curved metasurfaces. By extending the idea of nanohole for fishnet metamaterials, a supercell with different hole sizes was formed to gradually change the phase of light. First, each unit cell was simulated to study its phase response, and a change in the transitivity was calculated. For a single unit cell phase is changed up to 0.77 radians. Next, the effect of RUTs is studied by modelling the collective phase response of five different holes in curved geometry and as well as planar geometry. The out-of-plane metasurfaces have a large phase difference compared to the planar case. To investigate that, I studied the phase response of the same hole in a curved and planar geometry and realized that the curvature itself adds a phase difference. This means the RUT-based metasurfaces have an additional parameter for phase control. This opens a unique platform for out-of-plane metasurface design which provides possibilities for the new kind of metalenses, and beam steering devices.

It is possible to further improve the properties by using the optimized RUT curvature for the operating wavelength. Additionally, the out-of-plane metasurfaces can be improved further by using the neural network techniques for the metasurface design, a better modeling approach [145] and increasing the number of meta-atoms (nanoholes) in a supercell. This will allow higher phase difference and even better wavefront control. Moreover, the signal-to-noise ratio/efficiency of meta-atoms can be improved by using thin metal layers. Apart from that, this approach can be used to fabricate more complex structures on RUTs, for example, Babinet-inverted nanoantennas [166], to achieve metalenses for focusing and imaging purposes inside

the tube. Overall, the results of this study open a unique platform for out-of-plane metasurface design which provides possibilities for the new kind of metalenses, beam steering, and optical trapping of particles inside the RUTs. These applications may also lead to different platforms when integrated with already demonstrated properties of the RUTs such as wireless energy transfer, tunable shape, and neural guidance.

6.1 Possible extension of thesis

As further work, the multilayer thin films can be used for dynamically tunable ENZ substrates with graphene and VO_2 as a dielectric with electrical and thermal actuation. Tunable ENZ substrate and controlled LSPR through this, can be an ideal platform for efficient sensing, better beam-steering applications, and flat optics designs. Furthermore, using the self-rolling mechanism for the integration of tunable materials provides multifunctional smart metamaterials while taking the advantage of wafer-scale fabrication [86]. The integration of quantum emitters in RUT-based ENZ waveguides creates an extraordinary platform for quantum information processing and communication applications.

Combining the RUTs with advanced lithography either before or after the rolling process opens the door for many other applications. The 3D fishnet metamaterials can be further improved to serve as a microfluidic channel for different sensing applications. The out-of-plane metasurfaces design can be advanced with more complex metalens designs that couple the light inside RUT where optical trapping can be utilized.

Overall, the thesis work can be extended from tunable RUTs-based HMMs to metalenses that can be formed on the walls to take the advantage of the curve effect. On one hand, the results can be utilized by integrating different emitters to study their response in cylindrical HMM and waveguides for quantum applications, on the other their structural and optical properties can be used to stimulate brain activities by guiding the neurons through the RUTs to mimic their connections and paths.

REFERENCES

- [1] R. P. Feynman. Plenty of Room at the Bottom. *APS annual meeting*. 1959.
- [2] D. J. Barber and I. C. Freestone. An investigation of the origin of the colour of the Lycurgus Cup by analytical transmission electron microscopy. *Archaeometry* **32**, 1 (1990), 33–45.
- [3] W. Cai and V. M. Shalaev. *Optical metamaterials*. Vol. 10. 6011. Springer, 2010.
- [4] V. G. Veselago. Electrodynamics of substances with simultaneously negative and. *Usp. fiz. nauk* **92** (1967), 517.
- [5] J. B. Pendry, A. J. Holden, D. J. Robbins and W. Stewart. Magnetism from conductors and enhanced nonlinear phenomena. *IEEE transactions on microwave theory and techniques* **47**, 11 (1999), 2075–2084.
- [6] J. B. Pendry. Negative refraction makes a perfect lens. *Physical Review Letters* **85**, 18 (2000), 3966.
- [7] D. R. Smith, W. J. Padilla, D. Vier, S. C. Nemat-Nasser and S. Schultz. Composite medium with simultaneously negative permeability and permittivity. *Physical Review Letters* **84**, 18 (2000), 4184.
- [8] K. V. Sreekanth, Y. Alapan, M. ElKabbash, E. Ilker, M. Hinczewski, U. A. Gurkan, A. De Luca and G. Strangi. Extreme sensitivity biosensing platform based on hyperbolic metamaterials. *Nature Materials* **15**, 6 (2016), 621–627.
- [9] K. V. Sreekanth, Y. Alapan, M. ElKabbash, A. M. Wen, E. Ilker, M. Hinczewski, U. A. Gurkan, N. F. Steinmetz and G. Strangi. Enhancing the angular sensitivity of plasmonic sensors using hyperbolic metamaterials. *Advanced Optical Materials* **4**, 11 (2016), 1767–1772.
- [10] B. F. Díaz-Valencia, N. Porras-Montenegro, O. N. Oliveira Jr and J. R. Mejía-Salazar. Nanostructured Hyperbolic Metamaterials for Magnetoplasmonic Sensors. *ACS Applied Nano Materials* (2022).

- [11] D. Lu, H. Qian, K. Wang, H. Shen, F. Wei, Y. Jiang, E. E. Fullerton, P. K. Yu and Z. Liu. Nanostructuring multilayer hyperbolic metamaterials for ultrafast and bright green InGaN quantum wells. *Advanced Materials* **30**, 15 (2018), 1706411.
- [12] A. N. Poddubny, I. V. Iorsh and A. A. Sukhorukov. Generation of photon-plasmon quantum states in nonlinear hyperbolic metamaterials. *Physical Review Letters* **117**, 12 (2016), 123901.
- [13] R. Maas, J. Parsons, N. Engheta and A. Polman. Experimental realization of an epsilon-near-zero metamaterial at visible wavelengths. *Nature Photonics* **7**, 11 (2013), 907–912.
- [14] P. Shekhar, J. Atkinson and Z. Jacob. Hyperbolic metamaterials: fundamentals and applications. *Nano Convergence* **1**, 1 (2014), 14.
- [15] Z. Guo, H. Jiang and H. Chen. Hyperbolic metamaterials: From dispersion manipulation to applications. *Journal of Applied Physics* **127**, 7 (2020), 071101.
- [16] A. Poddubny, I. Iorsh, P. Belov and Y. Kivshar. Hyperbolic metamaterials. *Nature Photonics* **7**, 12 (2013), 948–957.
- [17] L. Ferrari, C. Wu, D. Lepage, X. Zhang and Z. Liu. Hyperbolic metamaterials and their applications. *Progress in Quantum Electronics* **40** (2015), 1–40.
- [18] C. Cortes, W. Newman, S. Molesky and Z. Jacob. Quantum nanophotonics using hyperbolic metamaterials. *Journal of Optics* **14**, 6 (2012), 063001.
- [19] S. C. Indukuri, J. Bar-David, N. Mazurski and U. Levy. Ultrasmall Mode Volume Hyperbolic Nanocavities for Enhanced Light–Matter Interaction at the Nanoscale. *ACS Nano* **13**, 10 (2019), 11770–11780.
- [20] P. Huo, S. Zhang, Y. Liang, Y. Lu and T. Xu. Hyperbolic Metamaterials and Metasurfaces: Fundamentals and Applications. *Advanced Optical Materials* **7**, 14 (2019), 1801616.
- [21] N. Maccaferri, Y. Zhao, T. Isoniemi, M. Iarossi, A. Parracino, G. Strangi and F. De Angelis. Hyperbolic meta-antennas enable full control of scattering and absorption of light. *Nano Letters* **19**, 3 (2019), 1851–1859.
- [22] C. Qian, X. Lin, Y. Yang, F. Gao, Y. Shen, J. Lopez, I. Kaminer, B. Zhang, E. Li, M. Soljacic et al. Multifrequency superscattering from subwavelength hyperbolic structures. *ACS Photonics* **5**, 4 (2018), 1506–1511.

- [23] K. V. Sreekanth, P. Mahalakshmi, S. Han, M. S. Mani Rajan, P. K. Choudhury and R. Singh. Brewster Mode-Enhanced Sensing with Hyperbolic Metamaterial. *Advanced Optical Materials* **7**, 21 (2019), 1900680.
- [24] C. L. Cortes and Z. Jacob. Super-Coulombic atom–atom interactions in hyperbolic media. *Nature Communications* **8**, 1 (2017), 1–8.
- [25] R. W. Wood. XLIV. A suspected case of the electrical resonance of minute metal particles for light-waves. A new type of absorption. *The London, Edinburgh, and Dublin Philosophical Magazine and Journal of Science* **3**, 16 (1902), 396–410.
- [26] W. L. Barnes, A. Dereux and T. W. Ebbesen. Surface plasmon subwavelength optics. *Nature* **424**, 6950 (2003), 824.
- [27] E. Ozbay. Plasmonics: merging photonics and electronics at nanoscale dimensions. *Science* **311**, 5758 (2006), 189–193.
- [28] H. Raether. Surface plasmons on smooth surfaces. *Surface plasmons on smooth and rough surfaces and on gratings*. Springer, 1988, 4–39.
- [29] P. Berini, R. Charbonneau, N. Lahoud and G. Mattiussi. Characterization of long-range surface-plasmon-polariton waveguides. *Journal of Applied Physics* **98**, 4 (2005), 043109.
- [30] E. Kretschmann. The determination of the optical constants of metals by excitation of surface plasmons. *Z. Phys* **241** (1971), 313–324.
- [31] J. Homola. Surface plasmon resonance sensors for detection of chemical and biological species. *Chemical Reviews* **108**, 2 (2008), 462–493.
- [32] S. A. Maier and H. A. Atwater. Plasmonics: Localization and guiding of electromagnetic energy in metal/dielectric structures. *Journal of Applied Physics* **98**, 1 (2005), 10.
- [33] K. M. Mayer and J. H. Hafner. Localized surface plasmon resonance sensors. *Chemical Reviews* **111**, 6 (2011), 3828–3857.
- [34] B. Gerislioglu, L. Dong, A. Ahmadvand, H. Hu, P. Nordlander and N. J. Halas. Monolithic metal dimer-on-film structure: New plasmonic properties introduced by the underlying metal. *Nano Letters* **20**, 3 (2020), 2087–2093.

- [35] S. Lee, Y. Sun, Y. Cao and S. H. Kang. Plasmonic nanostructure-based bioimaging and detection techniques at the single-cell level. *TrAC Trends in Analytical Chemistry* **117** (2019), 58–68.
- [36] J. E. Park, N. Yonet-Tanyeri, E. Vander Ende, A.-I. Henry, B. E. Perez White, M. Mrksich and R. P. Van Duyne. Plasmonic Microneedle Arrays for in Situ Sensing with Surface-Enhanced Raman Spectroscopy (SERS). *Nano Letters* **19**, 10 (2019), 6862–6868.
- [37] B. M. Reinhard, M. Siu, H. Agarwal, A. P. Alivisatos and J. Liphardt. Calibration of dynamic molecular rulers based on plasmon coupling between gold nanoparticles. *Nano Letters* **5**, 11 (2005), 2246–2252.
- [38] S. Lal, N. K. Grady, G. P. Goodrich and N. J. Halas. Profiling the near field of a plasmonic nanoparticle with Raman-based molecular rulers. *Nano Letters* **6**, 10 (2006), 2338–2343.
- [39] C.-Y. Chang, H.-T. Lin, M.-S. Lai, T.-Y. Shieh, C.-C. Peng, M.-H. Shih and Y.-C. Tung. Flexible localized surface plasmon resonance sensor with metal-insulator-metal nanodisks on PDMS substrate. *Scientific Reports* **8**, 1 (2018), 1–8.
- [40] B. Rothenhäusler and W. Knoll. Surface-plasmon microscopy. *Nature* **332**, 6165 (1988), 615–617.
- [41] B. Yildiz, M. Habib, A. Rashed and H. Caglayan. Hybridized plasmon modes in a system of metal thin film–nanodisk array. *Journal of Applied Physics* **126**, 11 (2019), 113104.
- [42] A. R. Rashed, M. Habib, N. Das, E. Ozbay and H. Caglayan. Plasmon-modulated photoluminescence enhancement in hybrid plasmonic nano-antennas. *New Journal of Physics* **22**, 9 (2020), 093033.
- [43] D. Ghindani, A. R. Rashed, M. Habib and H. Caglayan. Gate Tunable Coupling of Epsilon-Near-Zero and Plasmonic Modes. *Advanced Optical Materials* **9**, 22 (2021), 2100800.
- [44] M. Gittinger, K. Höflich, V. Smirnov, H. Kollmann, C. Lienau and M. Silies. Strongly coupled, high-quality plasmonic dimer antennas fabricated using a sketch-and-peel technique. *Nanophotonics* **9**, 2 (2020), 401–412.

- [45] M. Kaniber, K. Schraml, A. Regler, J. Bartl, G. Glashagen, F. Flassig, J. Wierzbowski and J. Finley. Surface plasmon resonance spectroscopy of single bowtie nano-antennas using a differential reflectivity method. *Scientific Reports* **6**, 1 (2016), 1–10.
- [46] Q. Wang, L. Liu, Y. Wang, P. Liu, H. Jiang, Z. Xu, Z. Ma, S. Oren, E. K. Chow, M. Lu et al. Tunable optical nanoantennas incorporating bowtie nanoantenna arrays with stimuli-responsive polymer. *Scientific Reports* **5**, 1 (2015), 1–8.
- [47] O. Ozdemir, A. M. Aygar, O. Balci, C. Kocabas, H. Caglayan and E. Ozbay. Enhanced tunability of V-shaped plasmonic structures using ionic liquid gating and graphene. *Carbon* **108** (2016), 515–520.
- [48] A. Leitis, A. Tittl, M. Liu, B. H. Lee, M. B. Gu, Y. S. Kivshar and H. Altug. Angle-multiplexed all-dielectric metasurfaces for broadband molecular fingerprint retrieval. *Science advances* **5**, 5 (2019), eaaw2871.
- [49] M. Duval Malinsky, K. L. Kelly, G. C. Schatz and R. P. Van Duyne. Nanosphere lithography: effect of substrate on the localized surface plasmon resonance spectrum of silver nanoparticles. *The Journal of Physical Chemistry B* **105**, 12 (2001), 2343–2350.
- [50] G. V. Naik, V. M. Shalaev and A. Boltasseva. Alternative plasmonic materials: beyond gold and silver. *Advanced Materials* **25**, 24 (2013), 3264–3294.
- [51] G. Subramania, A. J. Fischer and T. S. Luk. Optical properties of metal-dielectric based epsilon near zero metamaterials. *Applied Physics Letters* **101**, 24 (2012), 241107.
- [52] X. Niu, X. Hu, S. Chu and Q. Gong. Epsilon-near-zero photonics: a new platform for integrated devices. *Advanced Optical Materials* **6**, 10 (2018), 1701292.
- [53] A. Alù and N. Engheta. Light squeezing through arbitrarily shaped plasmonic channels and sharp bends. *Physical Review B* **78**, 3 (2008), 035440.
- [54] M. G. Silveirinha and N. Engheta. Theory of supercoupling, squeezing wave energy and field confinement in narrow channels and tight bends using ϵ near-zero metamaterials. *Physical Review B* **76**, 24 (2007), 245109.
- [55] A. Ciattoni, A. Marini, C. Rizza, M. Scalora and F. Biancalana. Polariton excitation in epsilon-near-zero slabs: Transient trapping of slow light. *Physical Review A* **87**, 5 (2013), 053853.

- [56] A. Baev, P. N. Prasad, M. Z. Alam and R. W. Boyd. Dynamically controlling local field enhancement at an epsilon-near-zero/dielectric interface via nonlinearities of an epsilon-near-zero medium. *Nanophotonics* **9**, 16 (2020), 4831–4837.
- [57] O. Reshef, I. De Leon, M. Z. Alam and R. W. Boyd. Nonlinear optical effects in epsilon-near-zero media. *Nature Reviews Materials* **4**, 8 (2019), 535–551.
- [58] M. Z. Alam, I. De Leon and R. W. Boyd. Large optical nonlinearity of indium tin oxide in its epsilon-near-zero region. *Science* **352**, 6287 (2016), 795–797.
- [59] C. K. Dass, H. Kwon, S. Vangala, E. M. Smith, J. W. Cleary, J. Guo, A. Alù and J. R. Hendrickson. Gap-plasmon-enhanced second-harmonic generation in epsilon-near-zero nanolayers. *ACS Photonics* **7**, 1 (2019), 174–179.
- [60] L. Rodriguez-Sune, M. Scalora, A. Johnson, C. Cojocaru, N. Akozbek, Z. Coppens, D. Perez-Salinas, S. Wall and J. Trull. Study of second and third harmonic generation from an indium tin oxide nanolayer: Influence of nonlocal effects and hot electrons. *APL Photonics* **5**, 1 (2020), 010801.
- [61] Y. Yang, J. Lu, A. Manjavacas, T. S. Luk, H. Liu, K. Kelley, J.-P. Maria, E. L. Runnerstrom, M. B. Sinclair, S. Ghimire et al. High-harmonic generation from an epsilon-near-zero material. *Nature Physics* **15**, 10 (2019), 1022–1026.
- [62] Y. He, Y. Li, Z. Zhou, H. Li, Y. Hou, S. Liao and P.-Y. Chen. Wide-band Epsilon-Near-Zero Supercoupling Control through Substrate-Integrated Impedance Surface. *Advanced Theory and Simulations* **2**, 8 (2019), 1900059.
- [63] Z. T. Xie, J. Wu, H. Fu and Q. Li. Tunable electro-and all-optical switch based on epsilon-near-zero metasurface. *IEEE Photonics Journal* **12**, 4 (2020), 1–10.
- [64] Q. Guo, Y. Cui, Y. Yao, Y. Ye, Y. Yang, X. Liu, S. Zhang, X. Liu, J. Qiu and H. Hosono. A solution-processed ultrafast optical switch based on a nanostructured epsilon-near-zero medium. *Advanced Materials* **29**, 27 (2017), 1700754.
- [65] H. Wang, X. Dai, K. Du, K. Gao, W. Zhang, S. J. Chua and T. Mei. Tuning epsilon-near-zero wavelength of indium tin oxide film via annealing. *Journal of Physics D: Applied Physics* **53**, 22 (2020), 225108.
- [66] Z. Zhang, J. Liu, Q. Hao and J. Liu. Sensitive saturable absorber and optical switch of epsilon-near-zero medium. *Applied Physics Express* **12**, 6 (2019), 065504.

- [67] Y. Kuang, Y. Liu, L. Tian, W. Han and Z. Li. A dual-slot electro-optic modulator based on an epsilon-near-zero oxide. *IEEE Photonics Journal* **11**, 4 (2019), 1–12.
- [68] E. Nahvi, I. Liberal and N. Engheta. Nonlinear metamaterial absorbers enabled by photonic doping of epsilon-near-zero metastructures. *Physical Review B* **102**, 3 (2020), 035404.
- [69] A. R. Davoyan, A. M. Mahmoud and N. Engheta. Optical isolation with epsilon-near-zero metamaterials. *Optics Express* **21**, 3 (2013), 3279–3286.
- [70] L. Vertchenko, N. Akopian and A. V. Lavrinenko. Epsilon-near-zero grids for on-chip quantum networks. *Scientific Reports* **9**, 1 (2019), 1–7.
- [71] G. E. Lio, A. Ferraro, T. Ritacco, D. M. Aceti, A. De Luca, M. Giocondo and R. Caputo. Leveraging on ENZ Metamaterials to Achieve 2D and 3D Hyper-Resolution in Two-Photon Direct Laser Writing. *Advanced Materials* **33**, 18 (2021), 2008644.
- [72] N. Engheta. Pursuing near-zero response. *Science* **340**, 6130 (2013), 286–287.
- [73] S. Ray, R. Banerjee, N. Basu, A. Batabyal and A. K. Barua. Properties of tin doped indium oxide thin films prepared by magnetron sputtering. *Journal of Applied Physics* **54**, 6 (1983), 3497–3501.
- [74] H. Agura, A. Suzuki, T. Matsushita, T. Aoki and M. Okuda. Low resistivity transparent conducting Al-doped ZnO films prepared by pulsed laser deposition. *Thin solid films* **445**, 2 (2003), 263–267.
- [75] S.-M. Park, T. Ikegami and K. Ebihara. Effects of substrate temperature on the properties of Ga-doped ZnO by pulsed laser deposition. *Thin Solid Films* **513**, 1-2 (2006), 90–94.
- [76] A. R. Rashed, B. C. Yildiz, S. R. Ayyagari and H. Caglayan. Hot electron dynamics in ultrafast multilayer epsilon-near-zero metamaterials. *Phys. Rev. B* **101** (16 2020), 165301.
- [77] K. V. Sreekanth, A. De Luca and G. Strangi. Experimental demonstration of surface and bulk plasmon polaritons in hypergratings. *Scientific Reports* **3**, 1 (2013), 1–7.

- [78] J. Kim, A. Dutta, G. V. Naik, A. J. Giles, F. J. Bezares, C. T. Ellis, J. G. Tischler, A. M. Mahmoud, H. Caglayan, O. J. Glembocki et al. Role of epsilon-near-zero substrates in the optical response of plasmonic antennas. *Optica* **3**, 3 (2016), 339–346.
- [79] S. A. Schulz, A. A. Tahir, M. Z. Alam, J. Upham, I. De Leon and R. W. Boyd. Optical response of dipole antennas on an epsilon-near-zero substrate. *Physical Review A* **93**, 6 (2016), 063846.
- [80] C. T. DeVault, V. A. Zenin, A. Pors, K. Chaudhuri, J. Kim, A. Boltasseva, V. M. Shalaev and S. I. Bozhevolnyi. Suppression of near-field coupling in plasmonic antennas on epsilon-near-zero substrates. *Optica* **5**, 12 (2018), 1557–1563.
- [81] P. B. Johnson and R.-W. Christy. Optical constants of the noble metals. *Physical Review B* **6**, 12 (1972), 4370.
- [82] J. R. DeVore. Refractive indices of rutile and sphalerite. *JOSA* **41**, 6 (1951), 416–419.
- [83] M. Habib, D. Briukhanova, N. Das, B. C. Yildiz and H. Caglayan. Controlling the plasmon resonance via epsilon-near-zero multilayer metamaterials. *Nanophotonics* **9**, 11 (2020), 3637–3644.
- [84] M. Habib, D. Briukhanova and H. Caglayan. Pinning the plasmon resonance via epsilon-near-zero metamaterials. *Metamaterials XIII*. **11769**. International Society for Optics and Photonics. 2021, 117691C.
- [85] E. J. R. Vesseur, T. Coenen, H. Caglayan, N. Engheta and A. Polman. Experimental verification of $n=0$ structures for visible light. *Physical Review Letters* **110**, 1 (2013), 013902.
- [86] C. N. Saggau, F. Gabler, D. D. Karnaushenko, D. Karnaushenko, L. Ma and O. G. Schmidt. Wafer-Scale High-Quality Microtubular Devices Fabricated via Dry-Etching for Optical and Microelectronic Applications. *Advanced Materials* **32**, 37 (2020), 2003252.
- [87] C. Vervacke, C. C. B. Bufon, D. J. Thurmer and O. G. Schmidt. Three-dimensional chemical sensors based on rolled-up hybrid nanomembranes. *RSC Advances* **4**, 19 (2014), 9723–9729.

- [88] W. Xi, C. K. Schmidt, S. Sanchez, D. H. Gracias, R. E. Carazo-Salas, S. P. Jackson and O. G. Schmidt. Rolled-up functionalized nanomembranes as three-dimensional cavities for single cell studies. *Nano Letters* **14**, 8 (2014), 4197–4204.
- [89] M. Yu, Y. Huang, J. Ballweg, H. Shin, M. Huang, D. E. Savage, M. G. Lagally, E. W. Dent, R. H. Blick and J. C. Williams. Semiconductor nanomembrane tubes: Three-dimensional confinement for controlled neurite outgrowth. *ACS Nano* **5**, 4 (2011), 2447–2457.
- [90] S. Schwaiger, A. Rottler and S. Mendach. Rolled-up metamaterials. *Advances in OptoElectronics* **2012** (2012).
- [91] Y. Zhang, D. Han, D. Du, G. Huang, T. Qiu and Y. Mei. Rolled-Up Ag-SiO_x Hyperbolic Metamaterials for Surface-Enhanced Raman Scattering. *Plasmonics* **10**, 4 (2015), 949–954.
- [92] V. Y. Prinz, V. Seleznev, A. Gutakovskiy, A. Chehovskiy, V. Preobrazhenskii, M. Putyato and T. Gavrilova. Free-standing and overgrown InGaAs/GaAs nanotubes, nanohelices and their arrays. *Physica E: Low-dimensional Systems and Nanostructures* **6**, 1-4 (2000), 828–831.
- [93] Y. Mei, G. Huang, A. A. Solovev, E. B. Ureña, I. Mönch, F. Ding, T. Reindl, R. K. Fu, P. K. Chu and O. G. Schmidt. Versatile approach for integrative and functionalized tubes by strain engineering of nanomembranes on polymers. *Advanced Materials* **20**, 21 (2008), 4085–4090.
- [94] C. C. Bof Bufon, J. D. Cojal González, D. J. Thurmer, D. Grimm, M. Bauer and O. G. Schmidt. Self-Assembled Ultra-Compact Energy Storage Elements Based on Hybrid Nanomembranes. *Nano Letters* **10**, 7 (2010), 2506–2510.
- [95] M. Li. Self-rolled-up membrane (S-RuM) capacitors and filters for radio frequency communication. *University of Illinois at Urbana-Champaign* (2017), 1–22.
- [96] V. K. Bandari, Y. Nan, D. Karnaushenko, Y. Hong, B. Sun, F. Striggow, D. D. Karnaushenko, C. Becker, M. Faghih, M. Medina-Sánchez et al. A flexible microsystem capable of controlled motion and actuation by wireless power transfer. *Nature Electronics* **3**, 3 (2020), 172–180.

- [97] C. Strelow, S. Kietzmann, A. Schramm, R. Seher, J.-P. Penttinen, T. Hakkarainen, A. Mews and T. Kipp. AlInP-based rolled-up microtube resonators with colloidal nanocrystals operating in the visible spectral range. *Applied Physics Letters* **101**, 11 (2012), 113114.
- [98] C. K. Schmidt, M. Medina-Sánchez, R. J. Edmondson and O. G. Schmidt. Engineering microrobots for targeted cancer therapies from a medical perspective. *Nature Communications* **11**, 1 (2020), 1–18.
- [99] O. V. Cangellaris, E. A. Corbin, P. Froeter, J. A. Michaels, X. Li and M. U. Gillette. Aligning synthetic hippocampal neural circuits via self-rolled-up silicon nitride microtube arrays. *ACS Applied materials & interfaces* **10**, 42 (2018), 35705–35714.
- [100] M. Habib, I. Issah, D. Briukhanova, A. R. Rashed and H. Caglayan. Wavefront control with nanohole array-based out-of-plane metasurfaces. *ACS applied nano materials* **4**, 9 (2021), 8699–8705.
- [101] E. Bermúdez-Ureña and U. Steiner. Self-rolled multilayer metasurfaces. *ACS Photonics* **6**, 9 (2019), 2198–2204.
- [102] S. Miao, S. He, M. Liang, G. Lin, B. Cai and O. G. Schmidt. Microtubular fuel cell with ultrahigh power output per footprint. *Advanced Materials* **29**, 34 (2017), 1607046.
- [103] B. Xu, X. Lin and Y. Mei. Versatile Rolling Origami to Fabricate Functional and Smart Materials. *Cell Reports Physical Science* (2020), 100244.
- [104] S. M. Harazim, W. Xi, C. K. Schmidt, S. Sanchez and O. G. Schmidt. Fabrication and applications of large arrays of multifunctional rolled-up SiO/SiO₂ microtubes. *Journal of Materials Chemistry* **22**, 7 (2012), 2878–2884.
- [105] L. Sang, H. Zhou, Z. Yang, M. D. Kraman, H. Zhao, J. A. Michaels, D. J. Sievers, J. E. Schutt-Aine, X. Li and W. Huang. Monolithic radio frequency SiN_x self-rolled-up nanomembrane interdigital capacitor modeling and fabrication. *Nanotechnology* **30**, 36 (2019), 364001.
- [106] A. A. Solovev, Y. Mei, E. Bermúdez Ureña, G. Huang and O. G. Schmidt. Catalytic microtubular jet engines self-propelled by accumulated gas bubbles. *Small* **5**, 14 (2009), 1688–1692.

- [107] Y. Mei, A. A. Solovev, S. Sanchez and O. G. Schmidt. Rolled-up nanotech on polymers: from basic perception to self-propelled catalytic microengines. *Chemical Society Reviews* **40**, 5 (2011), 2109–2119.
- [108] J. Wang, D. Karnaushenko, M. Medina-Sánchez, Y. Yin, L. Ma and O. G. Schmidt. Three-dimensional microtubular devices for lab-on-a-chip sensing applications. *ACS Sensors* **4**, 6 (2019), 1476–1496.
- [109] E. S. G. Naz, Y. Yin, J. Wang, A. Madani, L. Ma and O. G. Schmidt. Dynamic tuning of photon-plasmon interaction based on three-dimensionally confined microtube cavities. *Optics Letters* **45**, 20 (2020), 5720–5723.
- [110] P. Song, C. Chen, J. Qu, P. Ou, M. Dastjerdi, Z. Mi, J. Song and X. Liu. Rolled-up SiO_x/SiN_x microtubes with an enhanced quality factor for sensitive solvent sensing. *Nanotechnology* **29**, 41 (2018), 415501.
- [111] W. Xi, C. K. Schmidt, S. Sanchez, D. H. Gracias, R. E. Carazo-Salas, R. Butler, N. Lawrence, S. P. Jackson and O. G. Schmidt. Molecular insights into division of single human cancer cells in on-chip transparent microtubes. *ACS Nano* **10**, 6 (2016), 5835–5846.
- [112] V. A. Bolaños Quiñones, L. Ma, S. Li, M. Jorgensen, S. Kiravittaya and O. G. Schmidt. Localized optical resonances in low refractive index rolled-up microtube cavity for liquid-core optofluidic detection. *Applied Physics Letters* **101**, 15 (2012), 151107.
- [113] P. Froeter, Y. Huang, O. V. Cangellaris, W. Huang, E. W. Dent, M. U. Gillette, J. C. Williams and X. Li. Toward intelligent synthetic neural circuits: directing and accelerating neuron cell growth by self-rolled-up silicon nitride microtube array. *ACS Nano* **8**, 11 (2014), 11108–11117.
- [114] C. C. Bof Bufon, J. D. Cojal González, D. J. Thurmer, D. Grimm, M. Bauer and O. G. Schmidt. Self-assembled ultra-compact energy storage elements based on hybrid nanomembranes. *Nano Letters* **10**, 7 (2010), 2506–2510.
- [115] C. S. Martinez-Cisneros, S. Sanchez, W. Xi and O. G. Schmidt. Ultra-compact three-dimensional tubular conductivity microsensors for ionic and biosensing applications. *Nano Letters* **14**, 4 (2014), 2219–2224.

- [116] W. Huang, Z. Yang, M. D. Kraman, Q. Wang, Z. Ou, M. M. Rojo, A. S. Yalamarthy, V. Chen, F. Lian, J. H. Ni et al. Monolithic mtesla-level magnetic induction by self-rolled-up membrane technology. *Science Advances* **6**, 3 (2020), eaay4508.
- [117] Y. Y. Kim. An advanced characterization method for the elastic modulus of nanoscale thin-films using a high-frequency micromechanical resonator. *Materials* **10**, 7 (2017), 806.
- [118] C. Ho, A. Dehoux, L. Lacroix, J. Alexis, O. Dalverny, S. Châtel and B. Faure. Adhesion characterization of SiO₂ thin films evaporated onto a polymeric substrate. *International Journal of Engineering Research & Science (IJOER)* **4**, 2 (2018), 38–46.
- [119] K. M. Schulz, H. Vu, S. Schwaiger, A. Rottler, T. Korn, D. Sonnenberg, T. Kipp and S. Mendach. Controlling the spontaneous emission rate of quantum wells in rolled-up hyperbolic metamaterials. *Physical Review Letters* **117**, 8 (2016), 085503.
- [120] S. Kietzmann, C. Strelow, L. Tavares, J.-P. Penttinen, T. V. Hakkarainen, A. Schramm, A. Osadnik, A. Lutzen, J. Kjelstrup-Hansen, A. Mews et al. Organic molecular films as light-emitting and light-confining material in rolled-up Al-InP semiconductor microtube resonators. *ACS Photonics* **2**, 11 (2015), 1532–1538.
- [121] H. Vu, J. Siebels, D. Sonnenberg, S. Mendach and T. Kipp. Tunable plasmonic nanoantennas in rolled-up microtubes coupled to integrated quantum wells. *ACS Photonics* **4**, 11 (2017), 2659–2663.
- [122] E. J. Smith, Z. Liu, Y. Mei and O. G. Schmidt. Combined surface plasmon and classical waveguiding through metamaterial fiber design. *Nano Letters* **10**, 1 (2010), 1–5.
- [123] E. Smith, Z. Liu, Y. Mei and O. Schmidt. System investigation of a rolled-up metamaterial optical hyperlens structure. *Applied Physics Letters* **95**, 8 (2009), 083104.
- [124] S. Schwaiger, M. Bröll, A. Krohn, A. Stemmann, C. Heyn, Y. Stark, D. Stickler, D. Heitmann and S. Mendach. Rolled-up three-dimensional metamaterials with a tunable plasma frequency in the visible regime. *Physical Review Letters* **102**, 16 (2009), 163903.

- [125] D. Briukhanova, M. Habib, I. Issah and H. Caglayan. Low loss fishnet metamaterial via self-rolled nanotechnology. *Applied Physics Letters* **119**, 14 (2021), 141101.
- [126] S. Schwaiger, M. Klingbeil, J. Kerbst, A. Rottler, R. Costa, A. Koitmäe, M. Bröll, C. Heyn, Y. Stark, D. Heitmann et al. Gain in three-dimensional metamaterials utilizing semiconductor quantum structures. *Physical Review B* **84**, 15 (2011), 155325.
- [127] R. Kumar and K. Kajikawa. Comparison of cylinder-and planar-effective medium approximations on calculation of scattering properties of cylindrical hyperbolic metamaterials. *JOSA B* **36**, 3 (2019), 559–564.
- [128] B. C. Yildiz and H. Caglayan. Epsilon-near-zero media coupled with localized surface plasmon modes. *Physical Review B* **102**, 16 (2020), 165303.
- [129] D. C. Zografopoulos and R. Beccherelli. Tunable terahertz fishnet metamaterials based on thin nematic liquid crystal layers for fast switching. *Scientific Reports* **5**, 1 (2015), 1–11.
- [130] L. Yang, S. Yu, H. Li and T. Zhao. Multiple Fano resonances excitation on all-dielectric nanohole arrays metasurfaces. *Optics Express* **29**, 10 (2021), 14905–14916.
- [131] X. Li, M. Soler, C. I. Özdemir, A. Belushkin, F. Yesilköy and H. Altug. Plasmonic nanohole array biosensor for label-free and real-time analysis of live cell secretion. *Lab on a Chip* **17**, 13 (2017), 2208–2217.
- [132] V. M. Shalaev, W. Cai, U. K. Chettiar, H.-K. Yuan, A. K. Sarychev, V. P. Drachev and A. V. Kildishev. Negative index of refraction in optical metamaterials. *Optics Letters* **30**, 24 (2005), 3356–3358.
- [133] G. Dolling, C. Enkrich, M. Wegener, J. Zhou, C. M. Soukoulis and S. Linden. Cut-wire pairs and plate pairs as magnetic atoms for optical metamaterials. *Optics Letters* **30**, 23 (2005), 3198–3200.
- [134] S. Zhang, W. Fan, N. Panoiu, K. Malloy, R. Osgood and S. Brueck. Experimental demonstration of near-infrared negative-index metamaterials. *Physical Review Letters* **95**, 13 (2005), 137404.

- [135] S. Zhang, W. Fan, N. Panoiu, K. Malloy, R. Osgood and S. Brueck. Optical negative-index bulk metamaterials consisting of 2D perforated metal-dielectric stacks. *Optics Express* **14**, 15 (2006), 6778–6787.
- [136] J. Valentine, S. Zhang, T. Zentgraf and X. Zhang. Development of bulk optical negative index fishnet metamaterials: achieving a low-loss and broadband response through coupling. *Proceedings of the IEEE* **99**, 10 (2011), 1682–1690.
- [137] J. Valentine, S. Zhang, T. Zentgraf, E. Ulin-Avila, D. A. Genov, G. Bartal and X. Zhang. Three-dimensional optical metamaterial with a negative refractive index. *Nature* **455**, 7211 (2008), 376–379.
- [138] G. Dolling, M. Wegener, C. M. Soukoulis and S. Linden. Negative-index metamaterial at 780 nm wavelength. *Optics Letters* **32**, 1 (2007), 53–55.
- [139] C. García-Meca, J. Hurtado, J. Martí, A. Martínez, W. Dickson and A. V. Zayats. Low-loss multilayered metamaterial exhibiting a negative index of refraction at visible wavelengths. *Physical Review Letters* **106**, 6 (2011), 067402.
- [140] A. Rottler, M. Harland, M. Bröll, S. Schwaiger, D. Stickler, A. Stemmann, C. Heyn, D. Heitmann and S. Mendach. Rolled-up nanotechnology for the fabrication of three-dimensional fishnet-type GaAs-metal metamaterials with negative refractive index at near-infrared frequencies. *Applied Physics Letters* **100**, 15 (2012), 151104.
- [141] R. Ortuño, C. García-Meca, F. Rodríguez-Fortuño, J. Martí and A. Martínez. Role of surface plasmon polaritons on optical transmission through double layer metallic hole arrays. *Physical Review B* **79**, 7 (2009), 075425.
- [142] A. Minovich, D. N. Neshev, D. A. Powell and Y. S. Kivshar. Influence of the substrate on negative index fishnet metamaterials. *Optics Communications* **283**, 23 (2010), 4770–4774.
- [143] Z. Szabo, G.-H. Park, R. Hedge and E.-P. Li. A unique extraction of metamaterial parameters based on Kramers–Kronig relationship. *IEEE Transactions on Microwave Theory and Techniques* **58**, 10 (2010), 2646–2653.
- [144] J. Burch and A. Di Falco. Holography using curved metasurfaces. *Photonics*. 6. 1. Multidisciplinary Digital Publishing Institute. 2019, 8.
- [145] K. Wu, P. Coquet, Q. J. Wang and P. Genevet. Modelling of free-form conformal metasurfaces. *Nature Communications* **9**, 1 (2018), 1–8.

- [146] M. Khorasaninejad, W. T. Chen, A. Y. Zhu, J. Oh, R. C. Devlin, C. Roques-Carmes, I. Mishra and F. Capasso. Visible wavelength planar metalenses based on titanium dioxide. *IEEE Journal of Selected Topics in Quantum Electronics* **23**, 3 (2016), 43–58.
- [147] G. Yoon, K. Kim, S.-U. Kim, S. Han, H. Lee and J. Rho. Printable nanocomposite metalens for high-contrast near-infrared imaging. *ACS Nano* **15**, 1 (2021), 698–706.
- [148] G. Yoon, K. Kim, D. Huh, H. Lee and J. Rho. Single-step manufacturing of hierarchical dielectric metalens in the visible. *Nature Communications* **11**, 1 (2020), 1–10.
- [149] A. H. Naqvi and S. Lim. A beam-steering antenna with a fluidically programmable metasurface. *IEEE Transactions on Antennas and Propagation* **67**, 6 (2019), 3704–3711.
- [150] Q. Chen, D. Das, D. Chitnis, K. Walls, T. Drysdale, S. Collins and D. Cumming. A CMOS image sensor integrated with plasmonic colour filters. *Plasmonics* **7**, 4 (2012), 695–699.
- [151] I. Kim, W.-S. Kim, K. Kim, M. A. Ansari, M. Q. Mehmood, T. Badloe, Y. Kim, J. Gwak, H. Lee, Y.-K. Kim et al. Holographic metasurface gas sensors for instantaneous visual alarms. *Science Advances* **7**, 15 (2021), eabe9943.
- [152] G.-Y. Lee, G. Yoon, S.-Y. Lee, H. Yun, J. Cho, K. Lee, H. Kim, J. Rho and B. Lee. Complete amplitude and phase control of light using broadband holographic metasurfaces. *Nanoscale* **10**, 9 (2018), 4237–4245.
- [153] M. He, Y. Guo, C. Li, X. Tong, H. Liu, G. Li and L. Zhang. Metasurface-based wide-angle beam steering for optical trapping. *IEEE Access* **8** (2020), 37275–37280.
- [154] Y. Svirko, N. Zheludev and M. Osipov. Layered chiral metallic microstructures with inductive coupling. *Applied Physics Letters* **78**, 4 (2001), 498–500.
- [155] L. Zou, W. Withayachumnankul, C. M. Shah, A. Mitchell, M. Bhaskaran, S. Sriram and C. Fumeaux. Dielectric resonator nanoantennas at visible frequencies. *Optics Express* **21**, 1 (2013), 1344–1352.

- [156] J. Lin, J. B. Mueller, Q. Wang, G. Yuan, N. Antoniou, X.-C. Yuan and F. Capasso. Polarization-controlled tunable directional coupling of surface plasmon polaritons. *Science* **340**, 6130 (2013), 331–334.
- [157] B. Walther, C. Helgert, C. Rockstuhl, F. Setzpfandt, F. Eilenberger, E.-B. Kley, F. Lederer, A. Tünnermann and T. Pertsch. Spatial and spectral light shaping with metamaterials. *Advanced Materials* **24**, 47 (2012), 6300–6304.
- [158] B. A. Munk. *Frequency selective surfaces: theory and design*. John Wiley & Sons, 2005.
- [159] T.-K. Wu. Frequency selective surfaces. *Encyclopedia of RF and Microwave Engineering* (1995).
- [160] N. Yu, P. Genevet, M. A. Kats, F. Aieta, J.-P. Tetienne, F. Capasso and Z. Gaburro. Light propagation with phase discontinuities: generalized laws of reflection and refraction. *Science* **334**, 6054 (2011), 333–337.
- [161] N. Yu, F. Aieta, P. Genevet, M. A. Kats, Z. Gaburro and F. Capasso. A broadband, background-free quarter-wave plate based on plasmonic metasurfaces. *Nano Letters* **12**, 12 (2012), 6328–6333.
- [162] T. Li, Q. Wei, B. Reineke, F. Walter, Y. Wang, T. Zentgraf and L. Huang. Reconfigurable metasurface hologram by utilizing addressable dynamic pixels. *Optics Express* **27**, 15 (2019), 21153–21162.
- [163] F. Zhang, H. Yu, J. Fang, M. Zhang, S. Chen, J. Wang, A. He and J. Chen. Efficient generation and tight focusing of radially polarized beam from linearly polarized beam with all-dielectric metasurface. *Optics Express* **24**, 6 (2016), 6656–6664.
- [164] Z. Guo, L. Tian, F. Shen, H. Zhou and K. Guo. Mid-infrared polarization devices based on the double-phase modulating dielectric metasurface. *Journal of Physics D: Applied Physics* **50**, 25 (2017), 254001.
- [165] Y. Hu, X. Luo, Y. Chen, Q. Liu, X. Li, Y. Wang, N. Liu and H. Duan. 3D-Integrated metasurfaces for full-colour holography. *Light: Science & Applications* **8**, 1 (2019), 1–9.
- [166] X. Ni, S. Ishii, A. V. Kildishev and V. M. Shalaev. Ultra-thin, planar, Babinet-inverted plasmonic metalenses. *Light: Science & Applications* **2**, 4 (2013), e72–e72.

- [167] K. Nakamoto, R. Kurita, O. Niwa, T. Fujii and M. Nishida. Development of a mass-producible on-chip plasmonic nanohole array biosensor. *Nanoscale* **3**, 12 (2011), 5067–5075.
- [168] S. A. Maier. *Plasmonics: fundamentals and applications*. Springer Science & Business Media, 2007.
- [169] Y. Kurokawa and H. T. Miyazaki. Metal-insulator-metal plasmon nanocavities: Analysis of optical properties. *Physical Review B* **75**, 3 (2007), 035411.
- [170] H. T. Miyazaki and Y. Kurokawa. Squeezing visible light waves into a 3-nm-thick and 55-nm-long plasmon cavity. *Physical Review Letters* **96**, 9 (2006), 097401.
- [171] T. W. Ebbesen, H. J. Lezec, H. Ghaemi, T. Thio and P. A. Wolff. Extraordinary optical transmission through sub-wavelength hole arrays. *Nature* **391**, 6668 (1998), 667–669.
- [172] A. E. Cetin, D. Etezadi, B. C. Galarreta, M. P. Busson, Y. Eksioğlu and H. Altug. Plasmonic nanohole arrays on a robust hybrid substrate for highly sensitive label-free biosensing. *ACS photonics* **2**, 8 (2015), 1167–1174.
- [173] G. Dolling, C. Enkrich, M. Wegener, C. M. Soukoulis and S. Linden. Simultaneous negative phase and group velocity of light in a metamaterial. *Science* **312**, 5775 (2006), 892–894.
- [174] S. Zhang, W. Fan, N. Panoiu, K. Malloy, R. Osgood and S. Brueck. Experimental demonstration of near-infrared negative-index metamaterials. *Physical Review Letters* **95**, 13 (2005), 137404.
- [175] J. Valentine, S. Zhang, T. Zentgraf, E. Ulin-Avila, D. A. Genov, G. Bartal and X. Zhang. Three-dimensional optical metamaterial with a negative refractive index. *Nature* **455**, 7211 (2008), 376–379.
- [176] T. Matsui, H. T. Miyazaki, A. Miura, T. Nomura, H. Fujikawa, K. Sato, N. Ikeda, D. Tsuya, M. Ochiai, Y. Sugimoto et al. Transmission phase control by stacked metal-dielectric hole array with two-dimensional geometric design. *Optics Express* **20**, 14 (2012), 16092–16103.

- [177] T. Matsui, T. Nomura, A. Miura, H. Fujikawa, N. Ikeda, D. Tsuya, H. T. Miyazaki, Y. Sugimoto, M. Ozaki, M. Hangyo et al. Wavefront control by stacked metal-dielectric hole array with variable hole shapes. *Optics Express* **21**, 5 (2013), 6153–6161.
- [178] M. A. Othman, C. Guclu and F. Capolino. Graphene-based tunable hyperbolic metamaterials and enhanced near-field absorption. *Optics Express* **21**, 6 (2013), 7614–7632.
- [179] S. Prayakarao, B. Mendoza, A. Devine, C. Kyaw, R. Van Dover, V. Liberman and M. Noginov. Tunable VO₂/Au hyperbolic metamaterial. *Applied Physics Letters* **109**, 6 (2016), 061105.
- [180] V. Caligiuri, M. Palei, G. Biffi, S. Artyukhin and R. Krahne. A semi-classical view on epsilon-near-zero resonant tunneling modes in metal/insulator/metal nanocavities. *Nano Letters* **19**, 5 (2019), 3151–3160.

A

A.1 List of other publications

1. Issah, I., **Habib, M.**, and Caglayan, H. (2021). Long-range qubit entanglement via rolled-up zero-index waveguide. *Nanophotonics*, 10(18), 4579-4589
2. Ghindani, D., Rashed, A. R., **Habib, M.**, and Caglayan, H. (2021). Gate Tunable Coupling of Epsilon-Near-Zero and Plasmonic Modes. *Advanced Optical Materials*, 9(22), 2100800.

PUBLICATIONS

PUBLICATION

I

Plasmon-modulated photoluminescence enhancement in hybrid plasmonic nano-antennas

A. R. Rashed, M. Habib, N. Das, E. Ozbay and H. Caglayan

New Journal of Physics **22**(9) (2020), 093033

Publication reprinted with the permission of the copyright holders

**PAPER****Plasmon-modulated photoluminescence enhancement in hybrid plasmonic nano-antennas****OPEN ACCESS**

RECEIVED
8 April 2020
REVISED
23 July 2020

ACCEPTED FOR PUBLICATION
14 August 2020

PUBLISHED
11 September 2020

Alireza R Rashed¹ , Mohsin Habib¹ , Nekhel Das¹, Ekmel Ozbay² and Humeyra Caglayan^{1,3} 

¹ Faculty of Engineering and Natural Sciences, Photonics, Tampere University, 33720 Tampere, Finland

² NANOTAM-Nanotechnology Research Center, Bilkent University, 06800, Ankara, Turkey

³ Author to whom any correspondence should be addressed.

E-mail: humeyra.caglayan@tuni.fi and alireza.rashed@tuni.fi

Keywords: plasmon, nano-antennas, photoluminescence, particle plasmons, hybrid exciton-plasmon system

Supplementary material for this article is available [online](#)

Original content from this work may be used under the terms of the [Creative Commons Attribution 4.0 licence](#).

Any further distribution of this work must maintain attribution to the author(s) and the title of the work, journal citation and DOI.

**Abstract**

In this work, we performed a systematic study on a hybrid plasmonic system to elucidate a new insight into the mechanisms governing the fluorescent enhancement process. Our lithographically defined plasmonic nanodisks with various diameters act as receiver and transmitter nano-antennas to outcouple efficiently the photoluminescence of the coupled dye molecules. We show that the enhancement of the spontaneous emission rate arises from the superposition of three principal phenomena: (i) metal enhanced fluorescence, (ii) metal enhanced excitation and (iii) plasmon-modulated photoluminescence of the photoexcited nanostructures. Overall, the observed enhanced emission is attributed to the bi-directional near-field coupling of the fluorescent dye molecules to the localized plasmonic field of nano-antennas. We identify the role of exciton-plasmon coupling in the recombination rate of the sp-band electrons with d-band holes, resulting in the generation of particle plasmons. According to our comprehensive experimental analyses, the mismatch between the enhanced emission and the emission spectrum of the uncoupled dye molecules is attributed to the plasmon-modulated photoluminescence of the photoexcited hybrid plasmonic system.

1. Introduction

The control over the spontaneous emission rate of a single quantum emitter (QE) has attracted particular interest, since it provides a powerful multifunctional tool for different promising applications [1–5]. During the last two decades, rapid advances in the field of nano-plasmonics have opened avenues for extremely high energy confinement below the diffraction limit [6]. The interaction of the localized surface plasmons (LSPs) with different types of quantum emitters (QEs) has stimulated the field of plasmon-enhanced spectroscopy [7–10].

In a quantum system, the electrons promoted to the excited state can relax back to the ground state via radiative or non-radiative decay channels. Depending on the design of a hybrid system, the competition between radiative and non-radiative decay rates results in either photoluminescence (PL) quenching or enhancement process [11–14]. In an engineered hybrid plasmonic system, the near-field coupling of an excitonic element to the enhanced local field of the plasmonic nano-antenna may speed up the radiative decay rate [15–18]. This can be achieved by overlapping the LSP mode of a plasmonic cavity with resonating mode of a QE, which is oscillating at the same polarization of the plasmonic cavity [19–21]. According to Fermi's golden rule, the photonic density of states (PDOS) of a plasmonic cavity can modify the spontaneous emission of a QE, known as the Purcell effect [22–24]. The Purcell factor can be significant for nano-resonators which have a high-quality factor and provide considerable local field confinement [24]. However, the stronger confinement implies stronger plasmonic losses. Therefore, in the design of an

efficient hybrid system, an optimized trade-off between these two effects should be considered. Such optimization can be done by changing the shape, size, composition and arrangement of the nano-resonators.

Besides exploiting radiative decay rate enhancement, one can manipulate the excitation rate of the QEs to achieve more significant spontaneous emission enhancement in hybrid systems [25–27]. Similar to radiative decay rate enhancement, excitation rate enhancement is strongly dependent on the orientation of QEs' dipoles relative to the resonance mode of the nano-resonator. Urena *et al* show that the PL signal of a coupled quantum dot to the monomers and dimers of gold nano-antennas is influenced by the separate modifications of the excitation rate and the quantum yield of the hybrid systems [28]. Similarly, in another work, the authors have optimized a hybrid system, consisting of gold nano-prism antennas and CdSe/ZnS nanocrystals to increase the excitation and/or emission rates of quantum dots, resulting in a significant enhancement of their fluorescence [29].

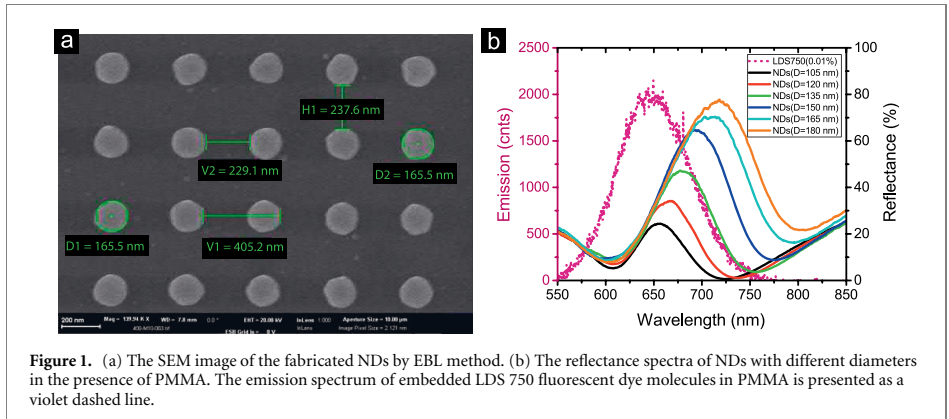
Even though the interaction between excitonic and plasmonic elements has been extensively studied in the last years, all underlying mechanisms related to the fluorescence enhancement process are not yet completely revealed. A hybrid system can be designed in such a way that in addition to the radiative decay rate enhancement and/or excitation rate enhancement, another process related to the radiative decay of particle plasmons (PPs) can contribute in the emission enhancement process.

The photoluminescence from noble metals has been reported in several earlier studies [30–33]. Through interband transitions, excitation photons of a light source with proper energy can establish non-equilibrium populations of electrons and holes in metal. The recombination of non-equilibrium populations of electrons and holes, located below and above Fermi level, can form highly localized electron–hole dipoles, leading to the polarization of the nanostructure and subsequently, the establishment of a coherent oscillation of the free electrons (PPs generation). In some studies, due to the enhanced local field around nano-antennas, some of the d-band holes undergo direct radiative recombination with electrons in the sp-band, leading to photoluminescence from the excited metals [32–35]. However, some other theoretical studies and experimental findings show that the observed PL from the photoexcited metallic structures originates from the radiative decay of the generated PPs which is associated with emitted photons [36–39]. In the experimental study of Hu *et al*, the observed PL of the photoexcited Au nanodisks (NDs) is attributed to the radiative decay of bright plasmon resonance modes [39]. They have shown the correlation between the LSP band and the acquired PL spectrum of the excited nanostructures. According to their observations, the PL intensity is depended on energy matching between excitation laser wavelength (532 nm, 2.33 eV) and plasmon resonance. Similar to this reported observation, in some studies on plasmonic hybrid systems, it is shown that the enhanced PL spectra of QEs closely tracks the LSP band of the nano-resonators [40–43]. However, to the best of our knowledge, the contribution of the plasmon-modulated PL in the enhanced emission of hybrid exciton–plasmon systems is overlooked.

The goal of this study is to realize a plasmonic hybrid system, consisting of the plasmonic nano-antennas and fluorescent dye molecules to reveal the underlying mechanisms behind the photoluminescence enhancement process. Our approach for modulating the spectral overlap between emission spectrum of the QEs and resonance band of the nano-antennas relies on modifying the diameter of NDs. We use steady-state fluorescence spectroscopy, as well as fluorescence lifetime imaging and spectroscopy methods to manifest increase of the spontaneous emission rate, as signatures of a bidirectional near-field coupling. The precisely engineered hybrid exciton–plasmon systems provide us the opportunity to exploit the enhanced local field of the nano-antennas by intensifying both excitation and spontaneous radiative decay rates. This is achieved by creating a simultaneous spectral overlap between the plasmon band of Au NDs and the emission and absorption spectra of LDS 750 fluorescent dye molecules. The photoexcited dye molecules, operating as radiating antennas, and the recombination of the photoexcited electrons in sp-band with d-band holes function as two pathways to induce plasmonic oscillation on NDs. We show that the radiative de-excitation of the generated PPs functions as an extra channel to enhance the radiative decay rate of the hybrid system. The contribution of the amplified plasmon-modulated photoluminescence in the enhanced emission of the hybrid system is manifested by the spectral shift of the enhanced emission with respect to the emission of the uncoupled dye molecules. Our results reveal the role of the bright-mode PPs in the PL enhancement process, leading to a new perspective in the engineering procedure of plasmonic hybrid systems for both fundamental science and technological applications.

2. Simulation and experimental results

We designed periodic arrays of plasmonic NDs with height of 70 nm and varied diameters from 105 to 180 nm, while keeping the period fixed as 400 nm. Figure 1(a) shows a scanning electron microscopy (SEM) image of the NDs, fabricated by standard electron-beam lithography (EBL) method on Si/SiO₂



substrate (for details see methods section). Figures S1(a) and (c) depict the simulated reflectance spectra of NDs with different diameters. The experimentally acquired reflectance spectra of the corresponding NDs are presented in figure S1(b). The comparison of the simulation and experimental results shows an excellent agreement between the design and fabrication. As the diameter increases, the strengthening and red-shift of the reflectance bands are evident in these results. The spectral shift in the resonance band of NDs with different diameters provides the opportunity to investigate the modification of the coupling efficiency between QEs and the local field of the designed nano-antennas.

In this work, we considered LDS 750 dye molecules as an appropriate QE. The fluorescent molecules with mass percent concentration of 0.01% are dissolved mono-dispersively and homogeneously in PMMA A2. For such concentration, the number of LDS 750 dye molecules located on the considered unit square area of PMMA host medium is calculated (see supplementary material (<https://stacks.iop.org/NJP/22/093033/mmedia>), section 3 and 4, for further details). The emission spectrum of the embedded LDS 750 dye molecules in PMMA is presented in figure 1(b), which is about 50 nm blue-shifted with respect to the case when they are dissolved in a polar solution [44]. One can explain the observed blue-shift according to photochemical properties of LDS 750 molecule. In the chemical structure of this hemicyanine dye, a dimethylamine group is linked to an aromatic ring (naphtha-thiazole) through an ethylene group. Due to the internal concomitant twisting motion of dimethylamine group, the formation of the twisted intramolecular charge transfer (TICT) state is the major deactivation pathway for the populated excited state. However, transition to the TICT state is strongly dependent on the viscosity and polarity of the surrounding medium [45]. In polar solvents such as ethanol and methanol, the emission originates from the TICT state rather than the locally excited state, resulting in a red-shifted emission spectrum. However, for LDS 750 molecules embedded in a rigid PMMA matrix, the emission is generated only from high-energy locally excited states. This occurs due to the hindering of large-amplitude motion, preventing the formation of TICT state, which is the relaxed state. Subsequently, transition of the excited electrons to the ground state through locally excited states results in a large blue-shift in the emission spectrum.

The measured reflectance spectra of the NDs with spin-coated PMMA is presented in figure 1(b). The presence of PMMA on NDs modifies the intensity, quality factor and spectral position of the plasmonic resonance, as compared to the case that the NDs are exposed to air (figure S1(b)). This occurs due to the change in the surrounding refractive index of NDs from air to PMMA ($n = 1.48$) [46]. The simulated reflectance spectra of NDs with PMMA layer is presented in figure S1(d). The obtained results are consistent with the acquired experimental results, confirming the role of PMMA layer in modifying the optical properties of the plasmonic nano-antennas. Furthermore, the local electric field intensity of NDs are calculated in the absence and the presence of PMMA layer (figure S2). Intensification of NDs local field in the presence of PMMA is evident in these results, leading to improve the strength of exciton-plasmon coupling in the designed hybrid system.

Figure 2(a) reports the enhanced PL of LDS 750 dye molecules in the presence of plasmonic NDs with different diameters. The observed increase in the emission intensity of the fluorescent dye molecules can be interpreted as the Purcell factor enhancement, as a result of the near-field coupling between the photoexcited QEs and plasmonic nano-resonators. However, as is discussed below, the other mechanisms contribute to the emission enhancement process. The spontaneous emission rate enhancement is correlated with the spatial overlap between fluorescent material and the plasmonic nano-antenna. In other words, the presence of the thin approximately 40 nm gain layer on top of NDs satisfies the desired condition for an

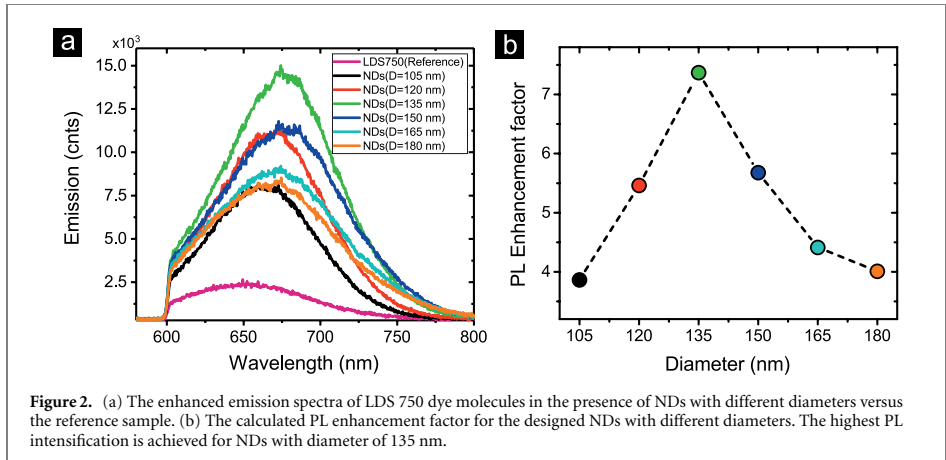


Figure 2. (a) The enhanced emission spectra of LDS 750 dye molecules in the presence of NDs with different diameters versus the reference sample. (b) The calculated PL enhancement factor for the designed NDs with different diameters. The highest PL intensification is achieved for NDs with diameter of 135 nm.

efficient interaction between dye molecules and the local fields of NDs. However, to avoid the possible self-quenching effect resulting from the direct charge transfer, a smooth 5 nm thick layer of Al_2O_3 is placed as a spacer between the active PMMA layer and NDs.

Additionally, the spectral overlap between the emission spectrum of fluorescent material and the extinction of plasmonic nanostructure is critical to accomplish an efficient emission enhancement. In the fluorescence enhancement process, both absorption and reflection properties of a nano-antenna play a role. The absorbance of a nano-antenna corresponds to the absorptive losses (dark modes) and shows the interaction ability of the resonator with the incident light. On the other hand, the reflectance of a nano-antenna shows the capability of the resonator to out-couple the confined local field (bright modes) to the far-field. The reflectance band of the fabricated NDs on the non-transparent substrate of Si/SiO_2 is a signature for the spectral position of the localized surface plasmon resonance (LSPR) band of the nano-resonators (supplementary material, figure S3). By tuning the diameter of NDs, one can achieve a desired spectral matching between the LSP resonance band of the nano-resonators and the emission spectrum of LDS 750 dye molecules. We studied this for the PL enhancement in hybrid systems that consist of LDS 750 dye molecules and NDs with different diameters, changing from 105 nm to 180 nm with 15 nm step. The samples are excited far from the NDs resonance band by a continuous wave laser, operating at 532 nm. For each sample the PL enhancement factor is calculated as the ratio between LDS 750 photoluminescence in the presence and absence of nano-antennas. As is seen in figure 2(b), the maximum PL enhancement (7 folds) is achieved for NDs with diameter 135 nm, which has the best spectral overlap of the reflectance with the emission spectrum of the fluorescent molecules.

Figure 3(a) presents the power-dependent emission peak intensity of LDS 750 dye molecules in the presence and absence of NDs with diameter of 135 nm. It reveals the significant difference in the slope of the fluorescence count-rates, while the excitation power intensity is altered. The observed slope change clarifies that the coupling efficiency between the excited gain material and nano-antennas enhances, as the intensity of the excitation power increases. Indeed, a greater number of the excited gain dipoles can induce stronger dipolar LSPs and higher-order oscillations in NDs. Furthermore, as it will be discussed later, the utilized excitation source with the energy of 2.33 eV can induce plasmon oscillation in the nano-resonators. The higher intensities of the excitation source may lead to induce stronger plasmonic resonances in NDs. Therefore, the circumstance for the occurrence of stronger gain-plasmon interactions at higher excitation power intensities can be satisfied, leading to higher PL enhancement rates.

Subsequently, the fluorescent lifetime of LDS 750 dye molecules is measured for the designed hybrid exciton-plasmon systems. The shortening of the decay rates provides a signature for the near-field interactions between LDS 750 dye molecules and the plasmonic field of NDs (figure 3(b)). The acquired time-resolved fluorescence decay curves of the designed hybrid samples, including dye molecules embedded in PMMA, which all are fitted with a bi-exponential decay function, are presented in table 1. It is worth noting that according to our experimental observations, the kinetics of LDS 750 molecules dissolved in ethanol can be fitted with single exponential decay, resulting in the measured lifetime of 365 ps. However, in a rigid environment like PMMA, the large-amplitude motion of the excited molecules can be completely blocked. Moreover, intermolecular beatings as an extra non-radiative relaxation pathway are hindered in such rigid matrix. Therefore, in addition to the spectral shift of the emitted photons, the excited state

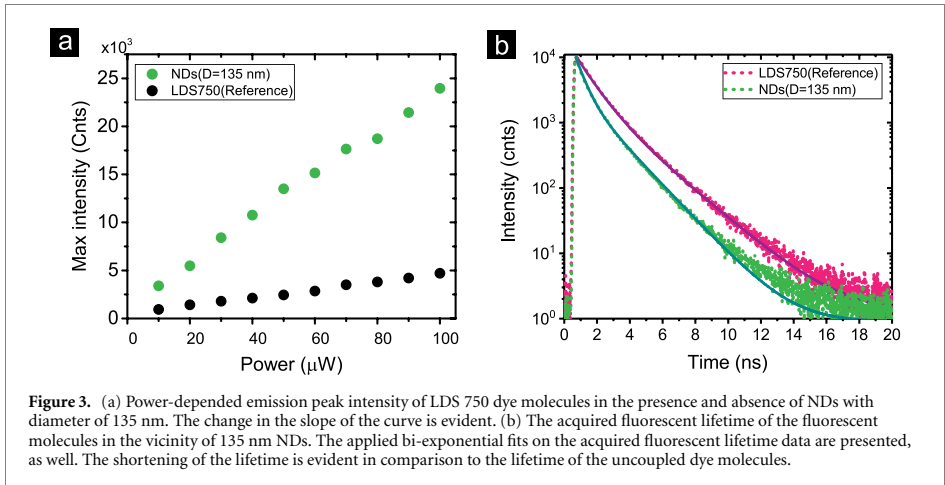


Figure 3. (a) Power-dependent emission peak intensity of LDS 750 dye molecules in the presence and absence of NDs with diameter of 135 nm. The change in the slope of the curve is evident. (b) The acquired fluorescent lifetime of the fluorescent molecules in the vicinity of 135 nm NDs. The applied bi-exponential fits on the acquired fluorescent lifetime data are presented, as well. The shortening of the lifetime is evident in comparison to the lifetime of the uncoupled dye molecules.

Table 1. Time-resolved fluorescence spectroscopy results for hybrid plasmonic systems with different diameters. τ_{Short} and τ_{Long} are the components of the bi-exponential function used to fit kinetics of embedded LDS 750 molecules in PMMA as well as hybrid systems.

	LDS 750	105 nm	120 nm	135 nm	150 nm	165 nm	180 nm
τ_{Short} (ns)	1	0.49	0.46	0.45	0.52	0.56	0.59
τ_{Long} (ns)	2.09	1.69	1.67	1.66	1.67	1.68	1.71

lifetimes of LDS 750 dye are influenced by the viscosity and rigidity of the environment. This leads a longer average fluorescent lifetime in PMMA than that in ethanol [47]. Moreover, in such a dense matrix, the monomers of dye molecules may aggregate, providing two fluorescent lifetime components rather than the one component which is observed for dissolved LDS dye molecules in ethanol. The shortening of both short and long components in the measured decay times is obvious for all samples, in comparison to the reference sample (embedded LDS 750 molecules in PMMA far from NDs). Evidently, the change in the decay rates of the coupled LDS 750 to NDs with diameter of 135 nm is much more pronounced as compared to other NDs. Indeed, as a crucial factor to achieve much more efficient exciton–plasmon interaction, the highest spectral overlap is realized for this sample.

To provide a much clearer picture of the decay rates modification related to LDS 750 dye molecules, we have performed fluorescence lifetime imaging microscopy (FLIM). In figure 4 insets, we report the processed FLIM images related to the decay time fit components of the dye molecules, placed far from ((a) and (b)) and in the close vicinity ((c) and (d)) of the NDs with diameter of 135 nm. In these images, the spots with bright colors represent short lifetime components, while dark spots stand for the long lifetime components. The presence of the brighter colors, as a footprint for the shortened lifetimes, in both fast and slow decay fit components of the hybrid systems are evident. Moreover, to provide a quantitative presentation for the acquired lifetime fit components, the corresponding histograms of the acquired FLIM images are reported in figure 4. The shorter lifetimes (faster decay rates) can be noticed in the histograms of the coupled dye molecules.

3. Theory and discussion

Modifying the diameter allowed us to tune the spectral overlap between the LSPR band of NDs and the emission spectra of LDS 750 fluorescent dye molecules. We show that there is a correlation between the efficiency of the spectral overlap and PL enhancement rate. In addition, we engineered our plasmonic hybrid system in such a way that both emission and absorption bands of the used QEs overlap simultaneously with the nano-antennas LSP resonance band. This fact is depicted in figure 5(a), for NDs with diameter of 135 nm. Such spectral overlap influences the underlying mechanisms behind the enhanced PL of the coupled dye molecules to nano-antennas. In principle, three mechanisms are involved in the spontaneous emission enhancement process of our plasmonic hybrid systems: (i) Purcell effect

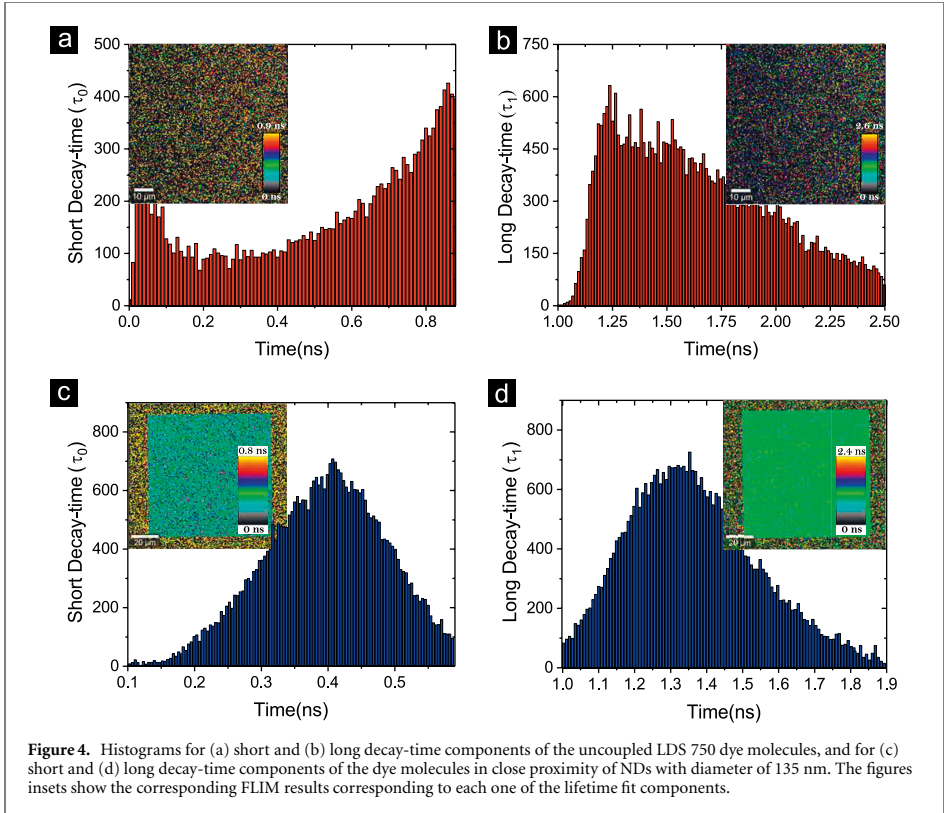


Figure 4. Histograms for (a) short and (b) long decay-time components of the uncoupled LDS 750 dye molecules, and for (c) short and (d) long decay-time components of the dye molecules in close proximity of NDs with diameter of 135 nm. The figures insets show the corresponding FLIM results corresponding to each one of the lifetime fit components.

enhancement, (ii) excitation rate enhancement, and (iii) radiative decay of the photoexcited PPs. Depending on the physical circumstances, the contribution of each one of these three mechanisms in the overall enhanced emission can be differed. These mechanisms are illustrated as a scheme in figure 5(b). In general, the spontaneous emission rate (K_{em}) of a QE depends on the quantum yield (Φ_{QE}) and the excitation rate (K_{exc}) of that emitter.

$$K_{em} = \Phi_{QE} K_{exc}. \quad (1)$$

Thus, the mechanisms behind the emission enhancement of an emitter which is located nearby a plasmonic nano-resonator can be explained based on the modification of one or both of these two parameters. For a QE located far from an optical cavity, the Φ_{QE} is defined as follow,

$$\Phi_{QE} = \frac{k_{r,0}}{k_{r,0} + k_{nr,0}} \quad (2)$$

in which the $k_{r,0}$ and $k_{nr,0}$ are intrinsic radiative and non-radiative decay rates, respectively.

The reported several times of magnitude emission rate enhancement in our hybrid exciton–plasmon systems can be explained based on the nano-antenna effect, which leads to the enhancement of the Purcell factor through modifying the Φ_{QE} . This effect, which is so-called metal enhanced fluorescence (MEF), requires spectral overlap between the emission spectrum of the excited QE and the plasmon band of the nano-antenna, as well as, the spatial proximity between the two resonating elements.

The excitation of the dye molecules out of the LSP resonance band of NDs with a 532 nm laser creates oscillating dipoles, which act as small antennas. These oscillating dipoles, at a specific dipole moment orientation [48], may induce collective oscillation of the free electrons in the plasmonic system through non-radiative energy transfer process (K_{ET} in figure 5(b)). This results in a strong oscillating dipole around plasmonic NDs and subsequently local field confinement in the nano-scale range. Embedding LDS 750 molecules in the close vicinity of the nano-antennas can intensify the PDOS. According to the Purcell effect, the plasmonic NDs acting as transmitter nano-antennas outcouple the emission of small oscillating dipoles to the far-field more efficiently [49]. One can consider the interactions between dye molecule dipoles and NDs dipoles almost bidirectional, in which the enhanced local fields around plasmonic nano-resonators

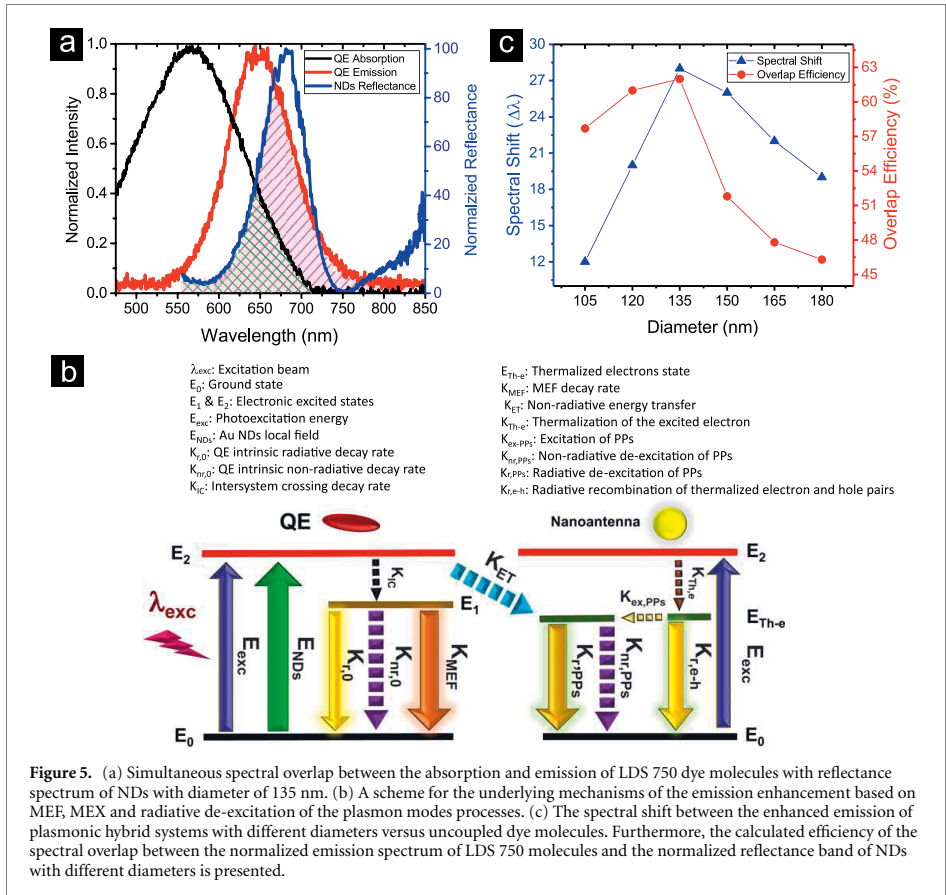


Figure 5. (a) Simultaneous spectral overlap between the absorption and emission of LDS 750 dye molecules with reflectance spectrum of NDs with diameter of 135 nm. (b) A scheme for the underlying mechanisms of the emission enhancement based on MEF, MEX and radiative de-excitation of the plasmon modes processes. (c) The spectral shift between the enhanced emission of plasmonic hybrid systems with different diameters versus uncoupled dye molecules. Furthermore, the calculated efficiency of the spectral overlap between the normalized emission spectrum of LDS 750 molecules and the normalized reflectance band of NDs with different diameters is presented.

affect the radiative decay rate of the coupled QE. The probability of such bidirectional interaction depends on the efficiency of the spectral and spatial overlaps between two oscillating dipoles of the QE and plasmonic NDs [11, 50]. Considering such bidirectional interaction, the quantum yield of LDS 750 emitter nearby a ND is given by

$$\Phi_{QE-ND} = \frac{k_{r,0} + k_{MEF}}{k_{r,0} + k_{MEF} + k_{nr,0} + k_{ET}}. \quad (3)$$

Such modification in overall radiative decay rate ($k_{r,0} + k_{MEF}$) leads to increase in the quantum yield and consequently a net increase in emission intensity, while the lifetime of the hybrid system decreases [51]. This occurs because most of the excited molecules are knocked down to the ground state through the radiative channels, rather than the non-radiative ones. The relaxed molecules are ready to reabsorb the excitation photons and participate in the photoluminescence process. According to equation (1), this results in the enhancement of the total spontaneous emission rate. This effect can be much more pronounced for a QE with lower quantum yield, since any increase in the radiative decay rate cannot influence the quantum yield if it is already close to unity [52]. The reported low quantum yield values for LDS 750 dye molecules makes it a promising candidate for emission enhancement purposes [53].

The excitation rate (K_{exc}) of a QE with an absorbance in the linear regime (i.e. far from saturation), is directly proportional to the square of the excitation field intensity and molar absorptivity of the QE. In the case of the spectral overlap between the absorption band of QEs and the plasmon band of nano-antennas, the confined electromagnetic fields around nano-antennas act as an extra channel to excite the QE. This effect is the so-called lightning rod effect [54] or metal enhanced excitation (MEX) [19, 51], in which plasmonic structure acts as a receiver nano-antenna, leading to increase the total spontaneous emission rate (K_{em}) by promoting more molecules from the ground state to the excited states. In our designed system, due to the spectral overlap between the absorption band of LDS 750 dye molecules with the plasmon band of the NDs with different diameters, the condition to enhance the excitation rate of the dye molecules is

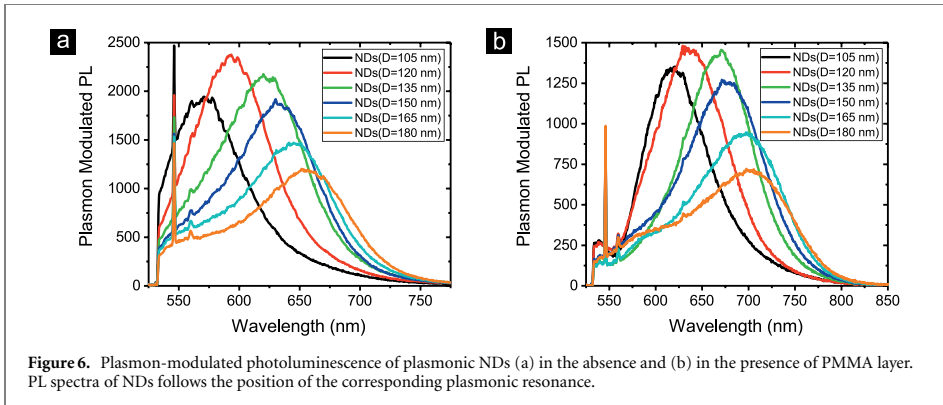


Figure 6. Plasmon-modulated photoluminescence of plasmonic NDs (a) in the absence and (b) in the presence of PMMA layer. PL spectra of NDs follows the position of the corresponding plasmonic resonance.

satisfied. Consequently, in combination with the external excitation field (E_{exc}), the localized electromagnetic fields of NDs (E_{NDs}) act as an extra excitation pathway to enhance the excitation rate of dye molecules. It is easy to distinguish the MEX from MEF, since MEF requires the spectral overlap between the emission band of the QE and the LSPR band of the nano-resonators. Furthermore, in contrast to MEF, this effect will not change the decay rate of the photoexcited molecules, but the peak position of the enhanced PL appears at the same spectral position of the PL signal related to an uncoupled QE.

Figure 5(c) shows the modification of the spectral overlap efficiency between the emission spectrum of LDS 750 dye molecules with the reflectance band of NDs with different diameters. The spectral overlap efficiency is determined as the area of the overlapping region between the NDs reflectance band and the PL spectrum of LDS 750 molecules. It can be also seen that the maximum PL enhancement factor is obtained for NDs with a diameter of 135 nm when the maximum matching occurs between the reflectance band and the emission spectrum of LDS 750 molecules (figure 2(b)). Our reported results prove the correlation between spectral overlap efficiency and the PL spectrum intensification, in which a stronger spectral overlaps result in a higher intensification of the Purcell factor. However, the PL enhancement factor for NDs with larger diameters remains almost the same as that of the smaller NDs, even if the spectral overlap efficiency reduces for NDs with larger diameters. One needs to consider that still larger NDs work as better transmitter antennas and can reradiate or scatter the photons to the far-field in a more efficient way [11]. Additionally, the larger NDs exhibit strong dipole moment and therefore, they can intensify the bi-directional near-field couplings towards radiative decay rate enhancement. On the other hand, according to the MEX effect, the broad reflectance band of NDs with larger diameters provides the required spectral overlap with the absorption spectrum of LDS 750 dye molecules to boost the excitation rate (K_{exc}). Therefore, in our designed system, the larger NDs can operate as an efficient receiver antenna, even though the efficiency of the spectral overlap with the emission spectrum of LDS 750 dye molecules diminishes.

The third mechanism in the spontaneous emission rate enhancement that should be taken into account is the radiative decay of the generated particle plasmons. The PPs can be formed either by the non-radiative energy transfer from the photoexcited gain molecules to the nano-antennas or by the non-radiative recombination of the photoexcited holes in d-band with electrons in SP-band. The specific design of our NDs and photoexcitation of these nano-resonators by using a 2.33 eV excitation source provide the required condition for the radiative decay of the generated PPs [39]. The excitation photons of the laser source promote d-band interband electrons into sp-band, well above the Fermi energy level of the gold. The thermalization of the photoexcited electrons creates inhomogeneous energy distribution of non-equilibrium electrons in the conduction band. The recombination of non-equilibrium electrons with d-band holes leads to PPs generation. These processes are illustrated in the scheme of figure 5(b).

Figure 6 shows the acquired plasmon-modulated photoluminescence of bare plasmonic NDs with various diameters in the absence and the presence of the PMMA layer. The shift of the PL signal to the higher wavelengths is observed, as the diameter of plasmonic nano-antenna increases. Moreover, in general the PL spectrum follows the reflectance band, even if it appears slightly at lower wavelengths with respect to the plasmonic resonance peak. One can expect a stronger PL signal from the NDs with larger diameters or covered with PMMA layer, as they are much more efficient scatterers, but the opposite behavior is observed instead. The observed contrast can be explained by the fact that the quantity of the generated PPs can be influenced by the population of the formed non-equilibrium electrons in the photoexcited metal and the number of available PDOS. The localization of the thermalized electrons intensifies where the number of

available PDOS is higher. In other words, as the energy mismatch between the excitation source and reflectance band of NDs ($\Delta E = E_{\text{Excitation}} - E_{\text{plasmon}}$) decreases, the probability for boosting the population of PPs increases. This explains the lower PL intensity of NDs covered by PMMA film than that of NDs exposed to air, even if they function as better scatterers in the presence of PMMA layer. In the PL results of larger NDs, one can see that the tail of the spectrum stretches towards the excitation wavelength. This is similar to the PL signal of an unpatterned gold film, resulting from the direct radiative recombination of d-band holes with sp-band electrons [39].

In our hybrid plasmonic system, the number of available PDOS can be intensified by the collective oscillation of the excited free electrons as well as by the resonant interaction between the dipoles of LDS 750 molecules with the confined local field of nano-antennas. In other words, the bi-directional interaction between gain material and plasmonic NDs operates as an extra pathway to amplify the generation of PPs. The generated PPs subsequently decay either radiatively (bright mode PPs) or non-radiatively (dark mode PPs). The radiative damping of the bright mode PPs provides an additional channel for the outcoupling of photons to the far-field in competition to the probable direct radiative recombination of the photoexcited holes with promoted electron above Fermi energy level. Therefore, by considering the plasmon-modulated PL of gold nanostructures (k_{PPs}) as an additional gateway to modify the spontaneous decay rate, the $\Phi_{\text{QE-ND}}$ of an emitter nearby a ND antenna can be rewritten as follows

$$\Phi_{\text{QE-ND}} = \frac{k_{r,0} + k_{\text{MEF}} + k_{\text{PPs}}}{k_{r,0} + k_{\text{MEF}} + k_{\text{PPs}} + k_{\text{nr},0} + k_{\text{ET}}}. \quad (4)$$

As is evident in figure 2(a), the emission peak of the enhanced PL in plasmonic hybrid systems is mismatched compared to the emission peak of the reference dye molecules. Figure 5(c) shows the red-shift of the enhanced PL peak for different diameters of plasmonic nano-antennas. Notably, the red-shift of the intensified emission spectrum goes up, as the diameter of nano-antennas increases, and it reaches the maximum for NDs with 135 nm diameter. After that it goes down for NDs with larger diameters. The observed red-shift in the PL spectra is considered as the overall evidence for the manifestation of the plasmon-modulated PL of the plasmonic nano-antennas in the enhanced PL spectra of the hybrid system. The bright mode PPs which decay radiatively track the reflectance band of NDs. Overall, the observed enhanced emission is the superposition of this process with MEF and MEX processes.

The designed hybrid exciton–plasmon system operates as a radiating antenna to outcouple efficiently the bright mode PPs to the far-field. An efficient coupling between oscillating dipoles of the photoexcited dye molecules and plasmonic antenna can induce stronger collective oscillation of the plasmonic dipoles, providing larger local density of optical states [55–57]. According Fermi’s golden rule, due to the larger number of available PDOS, the non-equilibrium electrons have a higher probability to excite PPs and subsequently the probability for the radiative decay of the PPs increases. This leads to the achieved maximum PL enhancement and the maximum PL red-shift for 135 nm NDs, in which the most efficient spectral overlap occurs. On the other hand, the reported PL red-shift for NDs with diameters larger than 135 nm is pronounced compared to smaller ones. In fact, larger NDs with stronger confined local field can act as better radiating antennas to outcouple PPs. However, by increasing diameter the performance of nano-antennas for radiating out the PPs is hindered due to the diminishing of the spectral overlap efficiency and increasing energy mismatch of ΔE . Hence, the observed intensified PL of larger NDs is attributed partially to MEF effect and MEX effect.

4. Conclusion

To summarize, we explored different underlying mechanisms related to the observed emission enhancement in our designed plasmonic hybrid systems. The systems are engineered to exploit the enhanced local field of the lithographically fabricated plasmonic NDs in the direction of both radiative decay rate and excitation rate enhancement of the QEs. We show that the simultaneous spectral overlap of a nano-antenna’s resonance band with the absorption and emission spectra of an emitter leads to enhanced emission from QEs with low quantum efficiency. The overall evidence for the manifestation of the PL enhancement via bidirectional near-field coupling is the reduction in the decay time of the excited molecule, due to the modification of the radiative and non-radiative decay rates. The measured plasmon-modulated PL signals of NDs in the presence and the absence of PMMA layer are established from polarizing nanostructures by highly localized d-hole photoexcitation. However, owing to the elaborated design of the hybrid systems, beside the non-radiative recombination of the photoexcited d-band holes with non-equilibrium electrons, the near-field coupling between the photoexcited dye molecules and NDs functions as the second pathway to imply PPs in NDs. This additional pathway leads to the amplification and more efficient outcoupling of the plasmon-modulated PL in hybrid plasmonic systems with respect to the bare plasmonic systems. We

show that in plasmonic hybrid systems with an efficient spectral overlap and therefore larger availability of PDOS this amplification process is boosted. Our theoretical and experimental analyses show that the contribution of the outcoupled PPs in the enhancement of the radiative decay rate process manifests itself as a red-shift in the enhanced emission spectrum peak of the hybrid systems as compared to that of the uncoupled dye molecules. These results provide crucial knowledge to engineer hybrid exciton–plasmon systems to unlock promising applications of nanophotonic devices.

5. Methods

5.1. Simulation

Simulations were conducted utilizing the FDTD method, implemented with the aid of a commercial software package (Lumerical FDTD Solutions). Gold nanostructures with various diameters are modeled with a frequency dependent dielectric function taken from Johnson and Christy [58], while 5 nm Al_2O_3 spacer is simulated using the reported data in reference [59]. For the case in which the surrounding environment of NDs was considered as PMMA, the dielectric constant data is adopted from reference [60]. In local field simulation, the incident field is a transverse electromagnetic plane wave with electric and magnetic fields in X and Y directions, respectively, while wave propagates in Z direction. Along with this excitation, electric dipole resonators are formed in X direction. The normalized field profiles were calculated at the maximum reflectance wavelength of the NDs and plotted in XY cross-section plane. In reflectance simulations, the reflected signal is collected from the structure surface, as the injected beam of the source is considered to propagate in the Z direction with a normal incident.

5.2. Fabrication

The Si/SiO₂ are used as substrates for fabricating plasmonic NDs as a right candidate to avoid charging effects during the EBL process. The thickness of SiO₂ on silicon substrates was 280 nm, which is deposited by plasma-enhanced chemical vapor deposition (PECVD) method to eliminate any possible polar and nonpolar impurities, the SiO₂/Si substrate are sonicated for 20 min in acetone and then soaked and rinsed with fresh acetone and IPA solvent, respectively. The positive PMMA A4 photoresist (950 K molecular weight) from microchem corp. is spin-coated at 3000 rpm for 40 s on cleaned substrate to create a layer with the thickness of approximately 200 nm. After that the spin-coated resist is baked for 90 s at 180 °C. The NDs with varied diameters from 105 to 180 nm and the constant period of 400 nm are fabricated using standard EBL method. The coated sample with PMMA is exposed to a dose of 2000 pC cm⁻² under E-beam with an accelerating voltage of 20 kV to form NDs. The exposed samples were developed with 1:1 MIBK/IPA developer for 1 min and then they are kept in IPA as the stopper solvent for 30 s. Then, the developed samples are directly blown to be dried using N₂. The metallization process is completed by depositing 70 nm thick gold layer using an E-beam evaporator machine at the constant rate of 0.5 Å s⁻¹ and a vacuum pressure of 1×10^{-6} mbar. During the entire deposition process, the sample chamber is cooled down below room temperature with the continuous flow of cold water. The nanostructures appeared after the lift-off process, by soaking the samples for 24 h in acetone. The 5 nm spacer is deposited on top of NDs using atomic layer deposition method to create a precise and smooth layer of Al₂O₃. LDS 750 dye molecules are dissolved in PMMA A2 (950 K molecular weight), provided by EM Resist LTD, with a mass percent concentration of 0.01% (see supplementary material, section 3 for further details). To avoid the aggregation of the incorporated dye molecules in PMMA, the prepared samples are sonicated at low temperature for 30 min. Moreover, to homogenize the prepared samples, the dye-PMMA samples are stirred for at least 90 s with a vortex mixer operating at 3000 rpm. Then the active PMMA layer is spin-coated on top of NDs coated with Al₂O₃ at 4000 rpm for 40 s. To avoid any change in the chemical and optical properties of the incorporated LDS 750 dye molecules in PMMA, instead of baking, the samples are left overnight to evaporate the anisole solvent at room temperature. This process leads to LDS 750 molecules embedded homogeneously in the PMMA polymer.

5.3. Characterization

Reflectance, PL, fluorescent lifetime and FLIM measurements of Au nanostructure are performed on a multi-functional WITec alpha300C confocal Raman microscopy system. The reflectance bands are acquired using an ultrahigh throughput spectrometer equipped to 150 lines/mm grating and detected using a thermoelectrically cooled, back-illuminated CCD camera. For reflectance measurements the samples are illuminated by highly bright and stable broadband light (LDLS EQ-99X) through a Zeiss EC 'Epiplan' DIC, 20× air objective (NA = 0.4, WD = 3.0 mm) and the reflected signal through the samples surfaces are detected by ultra-high throughput spectrometer, equipped with 150 lines/mm grating and a TE-cooled CCD (Andor DV 401-BV-351) camera. The reflectance spectra (Rfl) are calculated according to the

following formula

$$\text{Rfl} = \frac{I_{\text{Rfl-NDs}} - I_{\text{sub}}}{I_{\text{source}} - I_{\text{BG}}} \quad (5)$$

where $I_{\text{Rfl-NDs}}$ is the collected reflection spectrum of the nanostructures and I_{source} is the acquired spectrum of the broadband light source, which is measured using a perfect reflector. I_{sub} is the substrate reflection, acquired from the un-patterned area of the Si/SiO₂ substrate and I_{BG} stands for the background counts, acquired by the used system.

The transmittance spectra (Tra) for NDs on sapphire substrate are calculated as follows

$$\text{Tra} = \frac{I_{\text{Tra-NDs}} - I_{\text{BG}}}{I_{\text{sub}} - I_{\text{BG}}} \quad (6)$$

where $I_{\text{Tra-NDs}}$ is the collected transmission spectrum of the NDs on sapphire and here I_{sub} stands for the substrate transmission, acquired from the un-patterned area of the sapphire substrate.

The photoluminescence spectra of the control and main samples are acquired utilizing VIS-NIR Flame detector (350–1000 nm) provided by Ocean Optics with an integration time of 300 ms. The samples are excited with 532 nm CW laser and the PL signals are guided to the detector through a 50× Zeiss EC ‘Epiplan’ DIC objective, (NA = 0.75, WD = 1.0 mm). The background counts are subtracted from the measured PL spectra. To calculate the PL enhanced factor, the acquired results are normalized to the PL signal which is acquired from an un-patterned area of the spin-coated substrate with gain-doped PMMA. For power-dependend PL experiments the laser power is varied in the range of 10 to 100 mW, which is measured inside the microscope, right before impinging to the objective.

For lifetime measurements the samples are excited using a 532 nm pulsed laser beam. To generate the excitation pulses in the visible range (420–700 nm), the output of the ps super-continuum Fianium laser is connected to an acoustic optical tunable filter. The photons of the excited sample are collected using the 50× objective and detected by the single-photon avalanche diode (SPAD) detectors, provided by Picoquant, feature an extremely high photon detection efficiency up to 70%, operating in the range of 400 nm to 1100 nm. The acquired time-correlated single-photon counting data (TCSPC) is processed by a time to digital converter (TDC) module, provided by Picoquant and the results are analyzed by SymPhoTime 64 software.

To perform FLIM measurement, a motorized stage with a step size of 100 nm and reproducibility better than 0.01% is used to scan the selected area of the samples. The acquired signal is collected using 50× objective and detected by avalanche photodiode detector, provided by MPD company, operating in the spectral range 400–1050 nm and with optimized timing resolution down to 50 ps. Collected photons are processed by a TCSPC module, provided by WITec, and the results are analyzed by microscope software.

Acknowledgments

We acknowledge the financial support of Academy of Finland Flagship Programme (PREIN) (320165) and Academy of Finland Competitive funding to strengthen university research profiles (301820).

ORCID iDs

Alireza R Rashed  <https://orcid.org/0000-0002-3838-8966>

Mohsin Habib  <https://orcid.org/0000-0002-6109-9468>

Humeyra Caglayan  <https://orcid.org/0000-0002-0656-614X>

References

- [1] Senellart P, Solomon G and White A 2017 *Nat. Nanotechnol.* **12** 1026
- [2] Hertel F, Li S, Chen M, Pott L, Mehta S and Zhang J 2020 *ACS Chem. Biol.* **15** 33–8
- [3] Tame M S, McEnery K R, Özdemir Ş K, Lee J, Maier S A and Kim M S 2013 *Nat. Phys.* **9** 329–40
- [4] Aharonovich I, Englund D and Toth M 2016 *Nat. Photon.* **10** 631
- [5] Hakala T, Rekola H, Vakevainen A, Martikainen J P, Necada M, Moilanen A and Torma P 2017 *Nat. Commun.* **8** 13687
- [6] Dhawan A R *et al* 2020 *Light: Sci. Appl.* **9** 33
- [7] Emam A N, Mansour A S, Mohamed M B and Mohamed G G 2020 *Plasmonic Hybrid Nanocomposites for Plasmon-Enhanced Fluorescence and Their Biomedical Applications* (Berlin: Springer)
- [8] Ghopry S A, Alamri M, Goul R, Cook B, Sadeghi S, Gutha R, Sakidja R and Wu J Z 2020 *ACS Appl. Nano Mater.* **3** 2354–63
- [9] Norville C A, Smith K Z and Dawson J M 2020 *Appl. Opt.* **59** 2308–18
- [10] Yaraki M T, Rezaei S D and Tan Y N 2020 *Phys. Chem. Chem. Phys.* **22** 5673–87
- [11] Viste P, Plain J, Jaffiol R, Vial A, Adam P M and Royer P 2010 *ACS Nano* **4** 759–64

- [12] Rashed A R, De Luca A, Dhama R, Hosseinzadeh A, Infusino M, El Kabbash M, Ravaine S, Bartolino R and Strangi G 2015 *RSC Adv.* **5** 53245–54
- [13] Matsuda K, Ito Y and Kanemitsu Y 2008 *Appl. Phys. Lett.* **92** 211911
- [14] Anger P, Bharadwaj P and Novotny L 2006 *Phys. Rev. Lett.* **96** 113002
- [15] Shahbazyan T V 2013 *Nano Lett.* **13** 194–8
- [16] Hoang T B, Akselrod G M, Argyropoulos C, Huang J, Smith D R and Mikkelsen M H 2015 *Nat. Commun.* **6** 7788
- [17] Russell K J, Liu T-L, Cui S and Hu E L 2012 *Nat. Photon.* **6** 459–62
- [18] Berini P and De Leon I 2012 *Nat. Photon.* **6** 16
- [19] Lakowicz J R 2005 *Anal. Biochem.* **337** 171–94
- [20] Nguyen M, Kim S, Tran T T, Xu Z-Q, Kianinia M, Toth M and Aharonovich I 2018 *Nanoscale* **10** 2267–74
- [21] Zalogina A S, Savelev R S, Ushakova E V, Zograf G P, Komissarenko F E, Milichko V A, Makarov S V, Zuev D A and Shadrivov I V 2018 *Nanoscale* **10** 8721–7
- [22] Schniepp H and Sandoghdar V 2002 *Phys. Rev. Lett.* **89** 257403
- [23] Russell K J, Liu T-L, Cui S and Hu E L 2012 *Nat. Photon.* **6** 459–62
- [24] Pelton M 2015 *Nat. Photon.* **9** 427
- [25] Wenger J, Gerard D, Dintinger J, Mahboub O, Bonod N, Popov E, Ebbesen T W and Rigneault H 2008 *Opt. Express* **16** 3008–20
- [26] Anger P, Bharadwaj P and Novotny L 2006 *Phys. Rev. Lett.* **96** 113002
- [27] Lakowicz J R and Fu Y 2009 *Laser Photon. Rev.* **3** 221–32
- [28] Ureña E B, Kreuzer M P, Itzhakov S, Rigneault H, Quidant R, Oron D and Wenger J 2012 *Adv. Mater.* **24** OP314–20
- [29] Pompa P P, Martiradonna L, Torre A D, Sala F D, Manna L, De Vittorio M, Calabi F, Cingolani R and Rinaldi R 2006 *Nat. Nanotechnol.* **1** 126–30
- [30] Shahbazyan T V, Perakis I E and Bigot J-Y 1998 *Phys. Rev. Lett.* **81** 3120
- [31] Ngoc L L T, Wiedemair J, van den Berg A and Carlen E T 2015 *Opt. Express* **23** 5547–64
- [32] Boyd G T, Yu Z H and Shen Y R 1986 *Phys. Rev. B* **33** 7923
- [33] Apell P, Monreal R and Lundqvist S 1988 *Phys. Scr.* **38** 174
- [34] Varnavski O P, Mohamed M B, El-Sayed M A and Goodson T 2003 *J. Phys. Chem. B* **107** 3101–4
- [35] Mohamed M B, Volkov V, Link S and El-Sayed M A 2000 *Chem. Phys. Lett.* **317** 517–23
- [36] Shahbazyan T V 2013 *Nano Lett.* **13** 194–8
- [37] Dulkeith E, Niedereichholz T, Klar T, Feldmann J, Von Plessen G, Gittins D, Mayya K and Caruso F 2004 *Phys. Rev. B* **70** 205424
- [38] Tcherniak A, Dominguez-Medina S, Chang W-S, Swanglap P, Slaughter L S, Landes C F and Link S 2011 *J. Phys. Chem. C* **115** 15938–49
- [39] Hu H, Duan H, Yang J K W and Shen Z X 2012 *ACS Nano* **6** 10147–55
- [40] Ringler M, Schwemer A, Wunderlich M, Nichtl A, Kurzinger K, Klar T and Feldmann J 2008 *Phys. Rev. Lett.* **100** 203002
- [41] Goffard J, Gerard D, Miska P, Baudrion A L, Deturche R and Plain J 2013 *Sci. Rep.* **3** 2672
- [42] Zhao J, Cheng Y, Shen H, Hui Y Y, Wen T, Chang H C, Gong Q and Lu G 2018 *Sci. Rep.* **8** 3605
- [43] ElKabbash M et al 2019 *Phys. Rev. Lett.* **122** 203901
- [44] Udayan S, Sebastian M, Vijesh K, Nampoori V and Thomas S 2018 *J. Lumin.* **194** 428–32
- [45] Fan R, Xia Y and Chen D 2008 *Opt. Express* **16** 9804–10
- [46] Rodríguez-Fernández J, Pastoriza-Santos I, Pérez-Juste J, García de Abajo F J and Liz-Marzán L M 2007 *J. Phys. Chem. C* **111** 13361–6
- [47] Kim J, Lee M, Yang J-H and Choy J-H 2000 *J. Phys. Chem. A* **104** 1388–92
- [48] Dulkeith E, Ringler M, Klar T A, Feldmann J, Muñoz Javier A and Parak W J 2005 *Nano Lett.* **5** 585–9
- [49] Hoang T B, Akselrod G M, Argyropoulos C, Huang J, Smith D R and Mikkelsen M H 2015 *Nat. Commun.* **6** 7788
- [50] Singh M P and Strouse G F 2010 *J. Am. Chem. Soc.* **132** 9383–91
- [51] Lakowicz J R 2001 *Anal. Biochem.* **298** 1
- [52] Punj D, Mivelle M, Moparthy S B, Van Zanten T S, Rigneault H, Van Hulst N F, García-Parajó M F and Wenger J 2013 *Nat. Nanotechnol.* **8** 512
- [53] Liu C, Eliseeva S V, Luo T-Y, Muldoon P F, Petoud S and Rosi N L 2018 *Chem. Sci.* **9** 8099–102
- [54] Aktsipetrov O, Baranova I, Mishina E and Petukhov A 1984 *JETP Lett.* **40** 1012–5
- [55] Pelton M 2015 *Nat. Photon.* **9** 427–35
- [56] Nguyen M, Kim S, Tran T T, Xu Z-Q, Kianinia M, Toth M and Aharonovich I 2018 *Nanoscale* **10** 2267–74
- [57] Shahbazyan T V 2016 *Phys. Rev. Lett.* **117** 207401
- [58] Johnson P B and Christy R W 1972 *Phys. Rev. B* **6** 4370
- [59] Boidin R, Halenković T, Nazabal V, Beneš L and Němec P 2016 *Ceram. Int.* **42** 1177–82
- [60] Beadie G, Brindza M, Flynn R A, Rosenberg A and Shirk J S 2015 *Appl. Opt.* **54** F139–43

PUBLICATION

II

Hybridized plasmon modes in a system of metal thin film-nanodisk array

B. Yildiz, M. Habib, A. Rashed and H. Caglayan

Journal of Applied Physics **126**(11) (2019), 113104

Publication reprinted with the permission of the copyright holders





Hybridized plasmon modes in a system of metal thin film-nanodisk array

Cite as: J. Appl. Phys. **126**, 113104 (2019); doi: [10.1063/1.5115818](https://doi.org/10.1063/1.5115818)

Submitted: 21 June 2019 · Accepted: 4 September 2019 ·

Published Online: 20 September 2019



B. C. Yildiz,  M. Habib,  A. R. Rashed,  and H. Caglayan ^{a)} 

AFFILIATIONS

Faculty of Engineering and Natural Sciences, Photonics Laboratory, Tampere University, 33720 Tampere, Finland

^{a)}Electronic mail: humeyra.caglayan@tuni.fi

ABSTRACT

Controlling the hybridization is a very powerful tool to manipulate the modes in a single nanostructure. We investigate the hybridization between localized and propagating surface plasmons in a nanostructure system where a thin metal layer strongly interacts with a nanodisk array. Hybrid plasmon resonances are observed in the reflection spectra obtained from finite-difference time domain simulations and experimental measurements in the visible-near-infrared region. We demonstrate how the geometrical parameters of the nanostructure can be utilized to bring these plasmon modes in the strong coupling regime. The hybrid plasmon modes exhibit anticrossing with a Rabi splitting of ~ 0.1 eV, which is the signature of strong coupling. Near-field profiles of the hybrid modes exhibit a mixture of localized and propagating plasmon characteristics, with propagating modes excited on both sides of the metal film. Our design promises richer implementations in light manipulation towards novel photonic applications compared to the systems with thick metal films.

Published under license by AIP Publishing. <https://doi.org/10.1063/1.5115818>

I. INTRODUCTION

Plasmon hybridization theory¹ was developed to understand the response of complex plasmonic systems of arbitrary shapes, where multiple plasmon modes are supported. It describes the complex system as the interaction or “hybridization” of elementary plasmons supported by nanostructures. Hybridization of the elementary plasmon modes leads to a split in the plasmon resonance of the complex system into two energy levels: a bonding mode with a low-energy level and an antibonding mode with a higher energy level. The terms bonding and antibonding are similar to the molecular orbital theory, as the plasmon hybridization model is developed as the nanoscale electromagnetic analog of how atomic orbitals interact to form molecular orbitals in the electronic structure theory. This model has been successfully applied to a variety of plasmonic structures, such as metallic nanodimers,² metallic nanoshells,^{3–5} metallic nanotubes,^{6–8} and metallic nanoparticles near metal films.^{9,10} In these studies, hybridization between different localized surface plasmons (LSPs) has been investigated. It has also been of interest how LSPs and propagating counterpart of LSPs, surface plasmon polaritons (SPPs), interact with each other.^{11–16} Cesario *et al.*¹⁷ observed the extinction of a hybrid nanostructure where a 2D nanoparticle array interacts with a thin metal film, displaying multiple resonances. This observation has been attributed to

the plasmon hybridization between localized and propagating modes, with the assumption that the propagating plasmons are present only on one of the interfaces. In another work, it has been observed that triangular-shaped silver nanoparticles and a thin silver film display strong coupling, where the propagating plasmons are excited in one of the surfaces by Kretschmann configuration.¹⁸ The hybridization between LSP and guided modes on a thick metal film based on band diagrams¹⁹ and the near-field spectra has also been reported.²⁰ Alrasheed and Di²¹ theoretically presented a strong field enhancement as a result of hybridization between the magnetic plasmon resonance and propagating surface plasmons. Strong coupling between propagating plasmons and localized plasmons supported by L-shaped metal nanostructures has been demonstrated numerically.²² In these studies, the metal film supporting the SPPs is much thicker than the skin depth, and, therefore, the propagating plasmons are excited only on one of the metal-dielectric interfaces. However, the systems with thin metal layers allow the excitation of SPPs on both top and bottom interfaces, which provides more flexible control on the hybridization, as these modes can be easily tuned by the environment. Besides, allowing near-field enhancement on both interfaces, hybrid systems of thin metal films would provide potentially richer implementations in light manipulation, compared to the systems with thick metal films, particularly in surface

plasmon-enhanced fluorescence spectroscopy,²³ and plasmon-mediated energy transfer systems.²⁴

In this paper, we experimentally and theoretically demonstrate the hybridization between a continuous thin gold film deposited on a glass substrate and a periodic gold nanodisk (ND) array that is separated from the gold film by an oxide spacer layer, in the visible-near-infrared (NIR) region. Furthermore, we analyze the nature of the hybrid modes, calculate the coupling energy, and present how the coupling between the NDs and the thin metal layer is modified by the ND size and array periodicity.

II. ELEMENTARY PLASMON RESONANCES

The studied system (shown in Fig. 1) supports the elementary plasmon modes of its components: an ND array and a thin metal film. The ND array supports a single localized resonance (LSP mode). The continuous metal film supports SPP modes that can be excited by the periodicity of the ND array as long as the ND array and the thin metal film interact with each other.

To determine the elementary LSP modes, we perform finite-difference time domain (FDTD)²⁵ simulations using Lumerical FDTD Solutions. We calculate the scattering cross section of a periodic ND array on 50 nm of the Al₂O₃ (oxide) layer, on a glass substrate, without the thin metal layer. The thickness of the gold NDs is 70 nm. The refractive indices of the glass and oxide materials are set constant to $n = 1.45$ and $n = 1.65$, respectively. We use the tabulated experimental data provided by Johnson and Christy²⁶ to simulate the electric permittivity of gold. The boundary conditions are periodic along the directions parallel to the plane wave source injection (z axis) and perfectly matched layers (PML) in the propagation direction. We note that by considering the scattering cross section of an ND array, but not an isolated ND, we encounter any possible interaction among the NDs in determining the elementary LSP mode. In fact, a full treatment of the plasmon response of the ND array would encounter the lattice effect, known as surface lattice resonance (SLR),^{27,28} arising out of the coupling between the plasmon resonance of the individual NDs and diffracted waves due to the lattice geometry. Since we focus on the hybridization phenomenon, in order to keep the model simple, we consider the plasmon response of the ND array as an LSP resonance, rather than an SLR, relying on the fact that the plasmon resonance is dominantly determined by the ND size, but not by the periodicity. The resonances of the ND arrays of fixed periodicity, $p = 460$ nm, for ranging values of the ND diameter, d , from 100 nm to 180 nm,

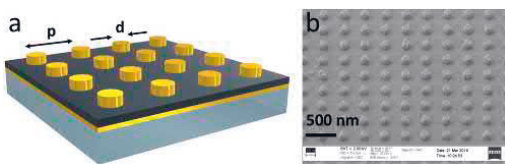


FIG. 1. (a) Schematic of the hybrid nanostructure, showing the periodicity p and nanodisk diameter d . (b) SEM image taken from the sample with $p = 460$ nm and $d = 180$ nm.

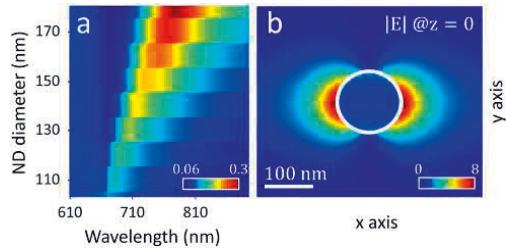


FIG. 2. (a) Localized plasmon modes of the ND arrays for fixed periodicity, $p = 460$ nm, and varying ND diameters, $d = 100$ – 180 nm. The color bar shows the scattering cross section in units of μm^2 . (b) On-resonance (700 nm) field profile at $z = 0$ plane for $p = 460$ nm and $d = 130$ nm. The color bar shows the electric field enhancement.

with steps of 10 nm are shown in Fig. 2(a). This is a typical localized plasmon resonance resulted from the dipolar charge alignments on the NDs [Fig. 2(b)] in response to the incident field and determined fundamentally by the size and material of the ND as well as the environment.²⁹ We observe that the elementary LSP resonances of the system vary between 670 and 780 nm, almost linearly with the ND size.

Next, we obtain the elementary SPP modes of the system. These SPP modes are supported by the continuous thin gold layer and depend certainly on the surrounding media. The SPP modes are calculated for the multilayer structure with semi-infinite layers of air (region I) on the top and glass (region IV) at the bottom and two finite-thickness layers in between; an oxide layer with thickness $a = 50$ nm (region II); and a gold layer with thickness $b = 30$ nm (region III). In such a system, each single metal-dielectric interface can sustain bound SPPs. If the separation between adjacent interfaces is small, i.e., the metal thickness is comparable to the skin depth (~ 25 nm), the interactions between SPPs along each of the interfaces provide coupled SPP modes. To obtain these modes, we first write the E_x and H_y fields in each of the four regions. The solution of the wave equation, together with the continuity of E_x and H_y fields at the three boundaries, gives the analytical implicit dispersion relation. Hence, the propagation constant of the SPP, β , is expressed as follows:

$$\frac{k_3 \frac{k_3/\epsilon_3 + k_1/\epsilon_1}{k_3/\epsilon_3 - k_1/\epsilon_1} e^{2k_3 b} - 1}{\epsilon_3 \frac{k_3/\epsilon_3 + k_4/\epsilon_4}{k_3/\epsilon_3 - k_4/\epsilon_4} e^{2k_3 b} + 1} = \frac{k_2 \frac{k_1/\epsilon_1 - k_2/\epsilon_2}{k_1/\epsilon_1 + k_2/\epsilon_2} e^{-2k_2 a} - 1}{\epsilon_2 \frac{k_1/\epsilon_1 - k_2/\epsilon_2}{k_1/\epsilon_1 + k_2/\epsilon_2} e^{-2k_2 a} + 1}, \quad (1)$$

where $a(b)$ is the thickness of the region II (III) and $k_i^2 = \beta^2 - \epsilon_i k_0^2$ is the component of the wave vector perpendicular to the interface associated with each of the regions ($i = 1, 2, 3, 4$), with k_0 being the magnitude of the vacuum wavevector and ϵ_i the electric permittivity. We numerically solve this equation for varying values of the oxide thickness, a (not shown), and the metal thickness, b (Fig. 3).

Although it is not presented here, based on these calculations, we observe that for small values of the oxide thickness (10–30 nm),

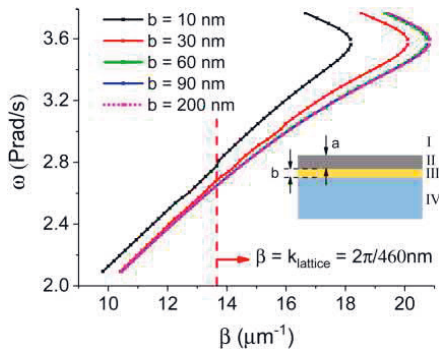


FIG. 3. SPP dispersion relation for fixed thickness of the oxide layer (region II), $a = 50$ nm, and different thicknesses of the metal layer (region III), b . In this work, b is 30 nm, which is shown by the red curve. The red perpendicular dashed line shows the $\beta = k_{\text{lattice}}$ line, where the SPP mode can be excited for a periodic structure of periodicity, $p = 460$ nm.

the dispersion curves are very similar to the dispersion of the air-gold-glass model and not affected from the existence of the oxide layer. On the other hand, for moderate values (40–80 nm), the dispersion curves lie between the ones calculated from the air-gold-glass model and oxide-gold-glass model. Finally, when a is equal or larger than ~ 100 nm, the system behaves as an oxide-gold-glass structure, completely ignoring the presence of air on the top. In this work, the oxide layer is 50 nm; hence, the complete model (air-oxide-gold-glass) is required. The oxide layer thickness is set by considering the maximum interaction regime between the LSP and SPP modes.

Figure 3 shows the dispersion curves of five different metal thicknesses, b , where the oxide layer thickness is fixed to $a = 50$ nm. We observe that the dispersion curves for metal thicknesses comparable (30 nm) with, and less (10 nm) than the skin depth, are distinct from the ones for larger thicknesses, where SPPs propagate along the single interface. In this work, the metal thickness, b , is 30 nm. Therefore, SPP propagation is expected to emerge at each of the interfaces. To excite an SPP mode, the momentum of the SPP wave is required to be matched either with one of the x component of the incident light or any additional momentum contribution. In the studied case, the light is normally incident, and hence, the only way to excite the SPP modes would be using the periodicity of the ND array as gratings. Therefore, the elementary SPP resonances of the system are found at the intersections of the red dispersion curve with $\beta = k_{\text{lattice}} (= 2\pi/p)$ lines, for any periodicity, p , in Fig. 3. We find that the elementary SPP resonances of the system vary between 620 and 820 nm, almost linearly with p , varying in the range of 400–540 nm.

III. HYBRIDIZED PLASMON RESONANCES

The hybridized plasmon modes of the overall system are demonstrated experimentally by the reflection spectra, where two

pronounced resonances are observed. We fabricate the nanostructure shown in Fig. 1, for varying values of d and p . The 30 nm metal layer is deposited on a glass substrate, using an electron beam evaporator, and the 50 nm oxide layer is deposited using the atomic layer deposition technique. The electron beam lithography technique is used to fabricate the array of NDs on top of the oxide layer. The thickness of the NDs is 70 nm. The SEM image of the fabricated sample with $p = 460$ nm and $d = 180$ nm is presented in Fig. 1(b). Reflection measurements are performed by a confocal microscope, where the incident light is focused on the nanostructure by a $50\times$ objective. The reflected light is collected by a CCD spectrometer. The acquired signal is normalized to the reflected beam from a perfect mirror.

Experimental reflection spectra are shown by solid lines in Fig. 4. In Fig. 4(a), we present two modes for a fixed periodicity of $p = 460$ nm and increasing ND diameter, d , from 160 nm to 180 nm. In Fig. 4(b), we observe the reflection spectra for a fixed ND diameter of $d = 140$ nm and increasing periodicity from 400 nm to 440 nm. We refer the two resonances as the first hybrid resonance, $\lambda_{\text{HYB}}^{(+)}$ (short wavelength or high energy), and the second hybrid resonance, $\lambda_{\text{HYB}}^{(-)}$ (long wavelength or low energy), for the rest of the paper. The dashed lines are obtained from FDTD simulations, which agree with the experimental data. It is notable that for the case of fixed p , changing d does not alter the first hybrid resonance but shifts the second one to the right [Fig. 4(a)]. On the other hand, the case of fixed d and changing p exhibits a larger shift in the first hybrid resonance than the one in the second hybrid resonance [Fig. 4(b)].

To understand the hybridization between plasmon modes comprehensively, we study the system more thoroughly by observing the resonances for a wide range of periodicity and ND size and

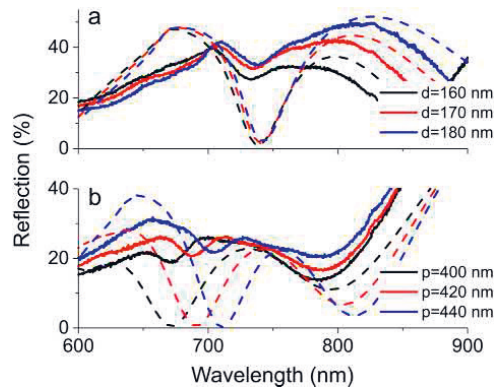


FIG. 4. Reflection spectra of the overall system for (a) fixed periodicity, $p = 460$ nm, and changing ND diameter, $d = 160, 170,$ and 180 nm and for (b) fixed $d = 140$ nm and changing $p = 400, 420,$ and 440 nm. Solid lines are obtained from reflection measurements, and dashed lines are obtained from FDTD simulations.

compare these with the elementary plasmon resonances. Figure 5 shows both the hybrid and the elementary plasmon resonances of the system for the fixed periodicity, $p = 460$ nm, and varying ND diameters in panel a and for the fixed ND diameter, $d = 130$ nm, and varying periodicities in panel b. The reflection spectra display two distinct resonances as stated earlier. The first hybrid resonance (pink lines) and the second hybrid resonance (blue lines) for changing periodicities and diameters are obtained from FDTD simulations. Black lines are the elementary LSP resonance that is obtained from the scattering cross-section simulations [as shown in Fig. 2(a)]. Red lines are the elementary SPP resonance that is calculated from the dispersion relation of the three-interface model, shown in Fig. 3. We observe both for periodicity and ND diameter sweeps that the first and the second resonances of the overall system are very close to the elementary resonance lines, except at and around the intersections of these lines. For the cases away from the anticrossing point, the two resonances are associated with the elementary LSP and SPP modes. They are weakly hybridized modes, dominantly carrying characteristics of one of the elementary modes. At the intersection, which corresponds to $p = 460$ nm and $d = 130$ nm, the first and second resonances, 675 nm and 760 nm, respectively, are split from the elementary LSP and SPP resonances, both of which are originally at ~ 700 nm. The anticrossing behavior shows that the ND array and the continuous thin gold film are in the strong coupling regime.³⁰ In this regime, Rabi splitting of the elementary plasmon mode energies of the same amount arises because of two hybridized modes with different local field distributions. At the anticrossing point, the resonances are no longer associated with the elementary LSP or SPP modes; instead, they are strongly hybridized plasmon modes, carrying characteristics of both the plasmon modes. To demonstrate this, we obtain the

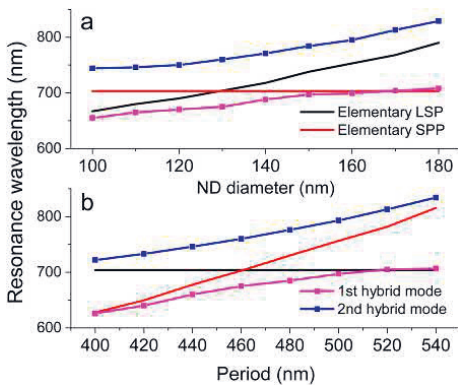


FIG. 5. Elementary and hybrid plasmon modes for (a) varying ND diameter, d , with the fixed periodicity $p = 460$ nm and for (b) varying p , with the fixed $d = 130$ nm. Red solid lines: SPP resonance calculated from the dispersion relation given by Eq. (1). Black solid lines: Scattering cross-sectional peak of the ND array. Pink and blue lines: the first and the second resonances of the reflection spectrum.

on-resonance field and phase profiles of the hybrid modes at the anticrossing point. Figures 6(a)–6(d) show the magnitude of the electric and magnetic fields, and Figs. 6(e)–6(h) show the phase profiles of the field components at the resonance wavelengths ($\lambda_{HYB}^{(\pm)}$) of the system of periodicity 460 nm and ND diameter 130 nm. We present the reflection, transmission, and absorption spectra of the hybrid nanostructure with the same geometrical properties in Fig. 6(i). We observe characteristics of both LSP and SPP modes in both field profiles. At $\lambda_{HYB}^{(+)} = 675$ nm, we observe a

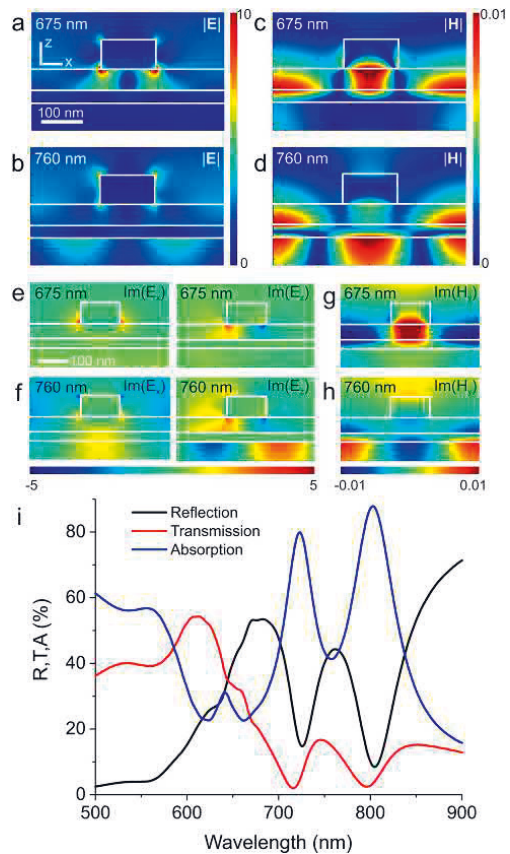


FIG. 6. Normalized field (a)–(d) and phase profiles (e)–(h) at the $y = 0$ plane, at the first (675 nm) and second (760 nm) resonances of the reflection spectrum (indicated at the upper left corner of each profile), simulated for the anticrossing point where $p = 460$ nm and $d = 130$ nm. White borders indicate the borders of the nanostructure system. (i) Reflection, transmission, and absorption spectrum, calculated at the anticrossing point.

mixture of a dipolar localized mode and a propagating mode along the gold-oxide interface. On the other hand, at $\lambda_{HYB}^{(-)}$, which is 760 nm, we observe a mixture of a quadrupole localized mode and a propagating mode along the glass-gold interface, which would not be possible with a thick metal layer. This is the key outcome of this work. Contrarily to the case of a hybrid system where a thick metal layer is employed, rather than a thin one, the proposed system provides field confinement on both of the metal surfaces. Since the resonances of this system are hybridized modes of plasmon fields, they could be flexibly tuned by the geometrical parameters: periodicity, ND diameter, and layer thicknesses, as well as the material types. As a comparison with other platforms where the propagating modes are generated without hybridization, tunability is limited with the material type in prism-coupled configurations and with environment and periodicity in grating-coupled configurations.

IV. RABI SPLITTING OF THE COUPLED MODES

Finally, we complete the hybridization picture by calculating, theoretically, the energies of the hybrid modes. We examine the coupling between two plasmonic modes, which can be considered as two coupled harmonic oscillators. We use a simple model of two coupled undamped harmonic oscillators to calculate the individual LSP and SPP resonances by using the Rabi split energy found in Sec. III. When the coupling strength exceeds the decoherence rate of the uncoupled oscillators, strong coupling occurs, and the energy exchange between the oscillators becomes the dominant

relaxation channel. In this regime, the energy levels of hybrid modes can be significantly altered, in which Rabi splitting is observed as a distinguishable characteristic of the optical response.^{11,31–34} The hybrid modes resulting from the strong interaction of such two coupled oscillators are given by the expression

$$\epsilon_{HYB}^{(\pm)} = \frac{1}{2}(\epsilon_{LSP} + \epsilon_{SPP}) \pm \frac{1}{2}\sqrt{(\epsilon_{LSP} - \epsilon_{SPP})^2 + 4|\Delta|^2}, \quad (2)$$

where $\epsilon_{LSP(SPP)}$ is the energy of the uncoupled LSP (SPP) mode, in units of electron volt, that is calculated using $\epsilon_{LSP(SPP)} = hc/\lambda_{LSP(SPP)}$, with c being the speed of light in vacuum and h the Planck constant. Δ is the energy shift term (Rabi splitting energy = 2Δ). The half of the split between the first and the second resonances of the reflection spectrum at the anticrossing point can be considered as the shift term in this formula, which is found as $\Delta = 105$ meV. Using this, in Eq. (2), we calculate the theoretical low- and high-energy modes at the anticrossing point, where both of the uncoupled mode energies are the same ($\lambda_{LSP} = \lambda_{SPP} = 700$ nm). The theoretical hybrid resonance wavelengths are given in Fig. 7, together with the completed hybridization scheme of the proposed structure in the strong coupling regime. The calculated high- and low-energy modes (661 and 745 nm) are slightly different than what we obtain from the reflection spectrum (675 and 760 nm). The theoretical coupled oscillator model in the strong coupling regime reproduces the results of Sec. III.

V. CONCLUSIONS

In summary, we observe hybridization between localized and propagating plasmon modes in a coupled system of a gold nanodisk array and a continuous thin gold film. The strong coupling regime is obtained by the anticrossing behavior of hybrid plasmon resonances for varying ND diameters and structure periodicities. We observe that the energy shift is the highest at the anticrossing point, which corresponds to the same resonance wavelengths of the elementary LSP and SPP modes. The on-resonance field profiles display a mixture of LSP and SPP characteristics. The localized nature is dipolar in the first hybrid resonance, whereas it is quadrupolar in the second hybrid resonance. The propagating part of the hybrid mode is dominant along the gold-oxide interface in the first hybrid resonance and along the gold-glass interface in the second one. Such a rich-feature nanostructure follows from the control over the geometrical parameters, as we report here, and it is possible to further optimize this system by different dielectric materials. This hybrid system with two distinct resonances would be beneficial in energy transfer systems and sensing. Most importantly, allowing the excitation of SPPs at each surface, the proposed model provides flexibility in plasmon-mediated applications, where the propagating plasmons are utilized. One can benefit from the field confinement at the back side of the metal layer, in addition to the front side, in quantum emitter-metal hybrid nanostructure systems.³⁵ It is also possible to manipulate the energy transfer between quantum emitters and plasmon fields so that the emitters are excited at one plasmon resonance wavelength, whereas they emit at the other, in a configuration where the emitters are located on each side of the metal layer.

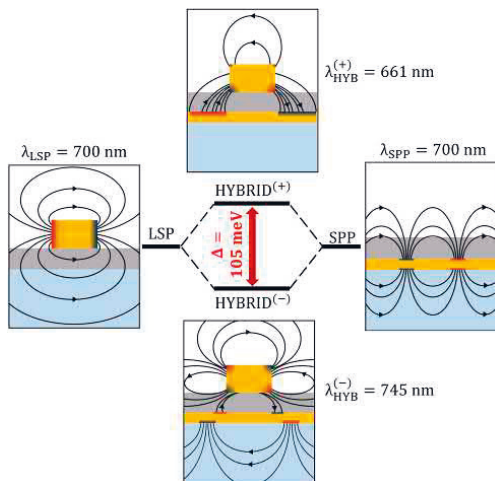


FIG. 7. Hybridization scheme. Hybrid mode resonance wavelengths are calculated using the strong interaction of two coupled oscillators, with $\Delta = 105$ meV, which is obtained from the reflection spectra.

ACKNOWLEDGMENTS

This work is a part of the Academy of Finland Flagship Programme, Photonics Research and Innovation (PREIN), Decision No. 320165, and competitive funding to strengthen university research profiles funded by the Academy of Finland (Decision No. 301820). B.C.Y. would like to acknowledge the support from the Finnish Foundation for Technology Promotion.

REFERENCES

- ¹E. Prodan, C. Radloff, N. J. Halas, and P. Nordlander, "A hybridization model for the plasmon response of complex nanostructures," *Science* **302**, 419–422 (2003).
- ²P. Nordlander, C. Oubre, E. Prodan, K. Li, and M. I. Stockman, "Plasmon hybridization in nanoparticle dimers," *Nano Lett.* **4**, 899–903 (2004).
- ³E. Prodan and P. Nordlander, "Plasmon hybridization in spherical nanoparticles," *J. Chem. Phys.* **120**, 5444–5454 (2004).
- ⁴C. Radloff and N. J. Halas, "Plasmonic properties of concentric nanoshells," *Nano Lett.* **4**, 1323–1327 (2004).
- ⁵D. W. Brandl, C. Oubre, and P. Nordlander, "Plasmon hybridization in nanoshell dimers," *J. Chem. Phys.* **123**, 024701 (2005).
- ⁶A. Moradi, "Plasmon hybridization in metallic nanotubes," *J. Phys. Chem. Solids* **69**, 2936–2938 (2008).
- ⁷A. Moradi, "Plasmon hybridization in metallic nanotubes with a nonconcentric core," *Opt. Commun.* **282**, 3368–3370 (2009).
- ⁸A. Moradi, "Plasmon hybridization in coated metallic nanowires," *J. Opt. Soc. Am. B* **29**, 625 (2012).
- ⁹P. Nordlander and E. Prodan, "Plasmon hybridization in nanoparticles near metallic surfaces," *Nano Lett.* **4**, 2209–2213 (2004).
- ¹⁰F. Le, N. Z. Lwin, N. J. Halas, and P. Nordlander, "Plasmonic interactions between a metallic nanoshell and a thin metallic film," *Phys. Rev. B* **76**, 165410 (2007).
- ¹¹H. Shan, Y. Yu, X. Wang, Y. Luo, S. Zu, B. Du, T. Han, B. Li, Y. Li, J. Wu, F. Lin, K. Shi, B. K. Tay, Z. Liu, X. Zhu, and Z. Fang, "Direct observation of ultrafast plasmonic hot electron transfer in the strong coupling regime," *Light Sci. Appl.* **8**, 9 (2019).
- ¹²Q. Li, J. Gao, H. Yang, H. Liu, X. Wang, Z. Li, and X. Guo, "Tunable plasmonic absorber based on propagating and localized surface plasmons using metal-dielectric-metal structure," *Plasmonics* **12**, 1037–1043 (2017).
- ¹³C. V. Hoang, K. Hayashi, Y. Ito, N. Gorai, G. Allison, X. Shi, Q. Sun, Z. Cheng, K. Ueno, K. Goda, and H. Misawa, "Interplay of hot electrons from localized and propagating plasmons," *Nat. Commun.* **8**, 771 (2017).
- ¹⁴G. Lévêque and O. J. F. Martin, "Optical interactions in a plasmonic particle coupled to a metallic film," *Opt. Express* **14**, 9971 (2006).
- ¹⁵T. Weber, T. Kiel, S. Irsen, K. Busch, and S. Linden, "Near-field study on the transition from localized to propagating plasmons on 2D nano-triangles," *Opt. Express* **25**, 16947 (2017).
- ¹⁶W. Cui, W. Peng, L. Yu, X. Luo, H. Gao, S. Chu, and J.-F. Masson, "Hybrid nanodisk film for ultra-narrowband filtering, near-perfect absorption and wide range sensing," *Nanomaterials* **9**, 334 (2019).
- ¹⁷J. Cesario, R. Quidant, G. Badenes, and S. Enoch, "Electromagnetic coupling between a metal nanoparticle grating and a metallic surface," *Opt. Lett.* **30**, 3404 (2005).
- ¹⁸S. Balci, E. Karademir, and C. Kocabas, "Strong coupling between localized and propagating plasmon polaritons," *Opt. Lett.* **40**, 3177–3180 (2015).
- ¹⁹W. Zhou, J. Y. Suh, Y. Hua, and T. W. Odom, "Hybridization of localized and guided modes in 2D metal-insulator-metal nanocavity arrays," *J. Phys. Chem. C* **117**, 2541–2546 (2013).
- ²⁰Y. Chu and K. B. Crozier, "Experimental study of the interaction between localized and propagating surface plasmons," *Opt. Lett.* **34**, 244 (2009).
- ²¹S. Alrasheed and E. Di, "Giant magnetic field enhancement in hybridized MIM structures," *IEEE Photonics Technol. Lett.* **29**, 2151–2154 (2017).
- ²²J. Chen and J. Hu, "Strong coupling between localized and propagating surface plasmon modes in a noncentrosymmetric metallic photonic slab," *J. Opt. Soc. Am. B* **31**, 1600–1606 (2014).
- ²³L. Touahir, A. T. A. Jenkins, R. Boukherroub, A. C. Gouget-Laemmel, J.-N. Chazalviel, J. Peretti, F. Ozanam, and S. Szunerits, "Surface plasmon-enhanced fluorescence spectroscopy on silver based SPR substrates," *J. Phys. Chem. C* **114**, 22582–22589 (2010).
- ²⁴P. Andrew and W. L. Barnes, "Energy transfer across a metal film mediated by surface plasmon polaritons," *Science* **306**, 1002–1005 (2004).
- ²⁵A. Taflov and S. C. Hagness, *Computational Electrodynamics: The Finite-Difference Time-Domain Method* (Artech House, 2005), p. 1006.
- ²⁶P. B. Johnson and R. W. Christy, "Optical constants of the noble metals," *Phys. Rev. B* **6**, 4370–4379 (1972).
- ²⁷V. G. Kravets, A. V. Kabashin, W. L. Barnes, and A. N. Grigorenko, "Plasmonic surface lattice resonances: A review of properties and applications," *Chem. Rev.* **118**, 5912–5951 (2018).
- ²⁸D. Khlopin, F. Laux, W. P. Wardley, J. Martin, G. A. Wurtz, J. Plain, N. Bonod, A. V. Zayats, W. Dickson, and D. Gérard, "Lattice modes and plasmonic linewidth engineering in gold and aluminum nanoparticle arrays," *J. Opt. Soc. Am. B* **34**, 691 (2017).
- ²⁹K. L. Kelly, E. Coronado, L. L. Zhao, and G. C. Schatz, "The optical properties of metal nanoparticles: The influence of size, shape, and dielectric environment," *J. Phys. Chem. B* **107**, 668–677 (2003).
- ³⁰A. Ghoshal and P. G. Kik, "Theory and simulation of surface plasmon excitation using resonant metal nanoparticle arrays," *J. Appl. Phys.* **103**, 113111 (2008).
- ³¹M.-E. Kleemann, R. Chikkaraddy, E. M. Alexeev, D. Kos, C. Carnegie, W. Deacon, A. C. de Pury, C. Große, B. de Nijs, J. Mertens, A. I. Tartakovskii, and J. J. Baumberg, "Strong-coupling of WSe₂ in ultra-compact plasmonic nanocavities at room temperature," *Nat. Commun.* **8**, 1296 (2017).
- ³²R. Thomas, A. Thomas, S. Pullanchery, L. Joseph, S. M. Somasundaran, R. S. Swathi, S. K. Gray, and K. G. Thomas, "Plexitons: The role of oscillator strengths and spectral widths in determining strong coupling," *ACS Nano* **12**, 402–415 (2018).
- ³³A. Konrad, A. M. Kern, M. Brecht, and A. J. Meixner, "Strong and coherent coupling of a plasmonic nanoparticle to a subwavelength Fabry-Pérot resonator," *Nano Lett.* **15**, 4423–4428 (2015).
- ³⁴L. Shi, T. Hakala, H. Rekola, J.-P. Martikainen, R. Moerland, and P. Törmä, "Spatial coherence properties of organic molecules coupled to plasmonic surface lattice resonances in the weak and strong coupling regimes," *Phys. Rev. Lett.* **112**, 153002 (2014).
- ³⁵P. Vasa and C. Lienau, "Strong light-matter interaction in quantum emitter/metal hybrid nanostructures," *ACS Photonics* **5**, 2–23 (2018).

PUBLICATION

III

Controlling the plasmon resonance via epsilon-near-zero multilayer metamaterials

M. Habib, D. Briukhanova, N. Das, B. C. Yildiz and H. Caglayan

Nanophotonics 9(11) (2020), 3637–3644

Publication reprinted with the permission of the copyright holders



Research article

Mohsin Habib, Daria Briukhanova, Nekhel Das, Bilge Can Yildiz and Humeyra Caglayan*

Controlling the plasmon resonance via epsilon-near-zero multilayer metamaterials

<https://doi.org/10.1515/nanoph-2020-0245>

Received April 21, 2020; accepted July 11, 2020; published online July 26, 2020

Abstract: Localized plasmon resonance of a metal nano-antenna is determined by its size, shape and environment. Here, we diminish the size dependence by using multilayer metamaterials as epsilon-near-zero (ENZ) substrates. By means of the vanishing index of the substrate, we show that the spectral position of the plasmonic resonance becomes less sensitive to the characteristics of the plasmonic nano-structure and is controlled mostly by the substrate, and hence, it is pinned at a fixed narrow spectral range near the ENZ wavelength. Moreover, this plasmon wavelength can be adjusted by tuning the ENZ region of the substrate, for the same size nanodisk (ND) array. We also show that the difference in the phase of the scattered field by different size NDs at a certain distance is reduced when the substrate is changed to ENZ metamaterial. This provides effective control of the phase contribution of each nanostructure. Our results could be utilized to manipulate the resonance for advanced metasurfaces and plasmonic applications, especially when precise control of the plasmon resonance is required in flat optics designs. In addition, the pinning wavelength can be tuned optically, electrically and thermally by introducing active layers inside the hyperbolic metamaterial.

Keywords: epsilon near zero; hyperbolic metamaterial; localized surface plasmon; pinning effect.

1 Introduction

In the last two decades, a new frontier has been opened up with plasmonics. An enormous range of technological

development has become possible by perfect light absorption, controlled propagation to certain directions or light confinement within a subwavelength volume [1–4]. Plasmonic light confinement has been utilized in bio-sensors [5–8], cellular imaging devices [9], surface-enhanced Raman spectroscopy [10] and nanoplasmonic rulers [11, 12]. To enable these applications, light is trapped around subwavelength metal nanoantennas at the localized surface plasmon resonance (LSPR) wavelength [13, 14], with enhanced electric fields. Size, shape, composition and arrangement of nanoantennas, as well as the dielectric environment surrounding them, have been extensively studied to obtain precise control over the LSPR [15, 16]. However, substrates were overlooked in these studies since mostly dielectric substrates, e.g. glass or silicon, were used. Metallic substrates were employed only in limited applications, such as hybridization between localized and propagating surface plasmons [17] or refractive index sensing [18].

One of the unusual materials of a growing interest is an epsilon-near-zero (ENZ) material, characterized by its permittivity (ϵ) being close to zero at certain wavelengths. These materials have been utilized in beam shaping and steering [19, 20], subwavelength tunnelling [21, 22] and enhanced nonlinear interactions [23]. Only recently, ENZ materials were used as substrates to control the LSPR of plasmonic antennas [24–27], revealing their great potential for plasmon-ENZ systems. However, only transparent conductive oxides, such as indium tin oxide and aluminium-doped zinc oxide, are used in these studies. These are naturally occurring ENZ materials with ENZ wavelengths in near-infrared and mid-infrared (MIR) regions [28]; hence, applications involving these materials are limited to those wavelength ranges. On the other hand, noble metals, such as gold (Au) and silver (Ag), have real permittivities $\text{Re}(\epsilon)$ close to zero in the ultraviolet region with very high imaginary permittivities ($\text{Im}(\epsilon)$), preventing them from being effective ENZ materials. However, it is possible to engineer an effective material capable of supporting a vanishingly small permittivity in the desired wavelength range. A metamaterial composed of alternating layers of metal and dielectric was previously

*Corresponding author: Humeyra Caglayan, Faculty of Engineering and Natural Sciences, Photonics, Tampere University, 33720 Tampere, Finland, E-mail: humeyra.caglayan@tuni.fi. <https://orcid.org/0000-0002-0656-614X>

Mohsin Habib, Daria Briukhanova, Nekhel Das and Bilge Can Yildiz: Faculty of Engineering and Natural Sciences, Photonics, Tampere University, 33720 Tampere, Finland. <https://orcid.org/0000-0002-6109-9468> (M. Habib)

demonstrated to exhibit ENZ in the visible region [29–31] with a potential of ultrafast tuning [32]. Metamaterials with this geometry are known as hyperbolic metamaterials (HMMs) due to their hyperbolic wave-vector diagram [30].

In this work, by employing HMMs as ENZ substrates, we experimentally demonstrate how to control LSPR of a plasmonic nanoantenna array without changing its dimensions in the visible region. We present that not only the plasmon resonance wavelength can be pinned, although the nanodisk (ND) diameter is changed, but also it can easily be adjusted to another operating wavelength by changing the material composition of the substrate without any changes in the ND array. Furthermore, we show the effect of an ENZ substrate on the phase of the scattered field from different size NDs. This modification over the plasmon resonance relaxes the requirements on precise control of subwavelength features and provides flexibility in the design of the plasmonic nanostructures in flat optics

applications by giving another option for tuning or compensating the fabrication errors.

The HMM substrates used in this study are composed of three bilayers of Au and titanium dioxide (TiO_2). The optical properties of these metamaterials are modelled by the effective medium theory (EMT) [30, 33–38]. The HMM serves as a uniaxial medium with permittivity given by a tensor $\epsilon = [\epsilon_{xx}, \epsilon_{yy}, \epsilon_{zz}]$, where in-plane isotropic/parallel components are defined as $\epsilon_{xx} = \epsilon_{yy} = \epsilon_{\parallel}$. The third component which is out of the plane (perpendicular component) is defined as $\epsilon_{zz} = \epsilon_{\perp}$. The parallel and perpendicular components of permittivity of a medium composed of alternating thin layers of metal and dielectric are defined as follows:

$$\epsilon_{\parallel} = \rho\epsilon_m + (1 - \rho)\epsilon_d \quad (1)$$

$$\epsilon_{\perp} = \frac{\epsilon_m\epsilon_d}{\rho\epsilon_d + (1 - \rho)\epsilon_m} \quad (2)$$

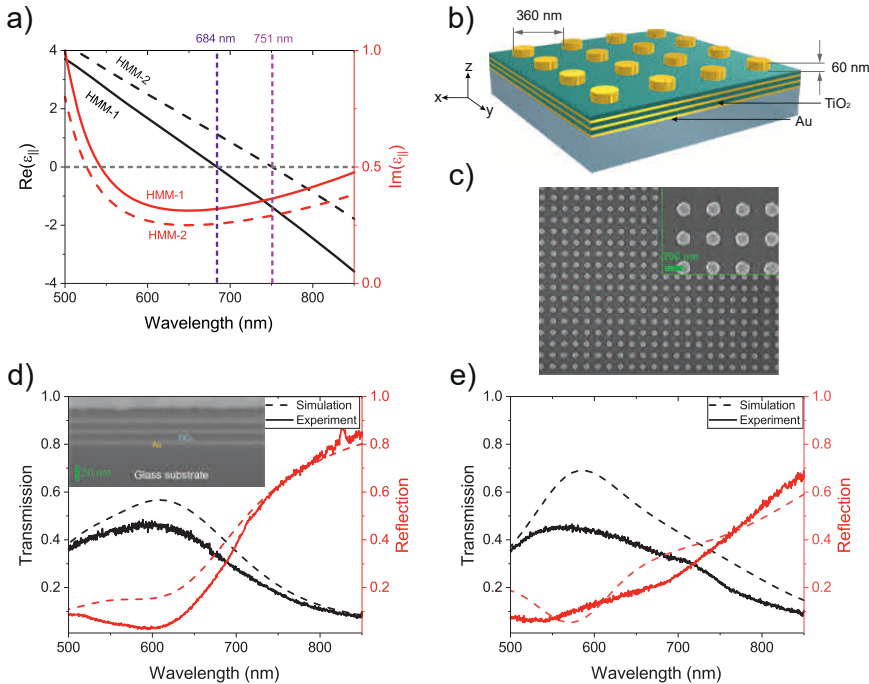


Figure 1: (a) The $\text{Re}(\epsilon_{\parallel})$ (black lines) and $\text{Im}(\epsilon_{\parallel})$ (red lines) of HMM-1 (solid lines) and HMM-2 (dashed lines). The crossover of $\text{Re}(\epsilon_{\parallel})$ for HMM-1 (violet dotted line) and HMM-2 (magenta dotted line) are highlighted. (b) The schematic of NDs on HMM and (c) the scanning electron microscopy (SEM) image of NDs on HMM-1. The simulated (dashed lines) and measured (solid lines) spectra of transmission (black lines) and reflection (red lines) results for (d) HMM-1 and (e) HMM-2. The inset of (d) shows the SEM image of HMM-1. HMM, hyperbolic metamaterial; ND, nanodisk.

where $\rho = t_m/(t_m + t_d)$ is the metal filling fraction, with $t_{m(d)}$ being the thickness of the metal (dielectric) layer, and ϵ_m and ϵ_d are permittivity values of metal and dielectric, respectively [30]. At specific wavelengths, a component of the permittivity tensor of the metamaterial either passes through zero (ENZ) or a resonant pole (epsilon-near-pole). The multilayer HMM shows the ENZ properties when the real part of ϵ_{\parallel} ($\text{Re}(\epsilon_{\parallel})$) component crosses zero and imaginary component ($\text{Im}(\epsilon_{\parallel})$) is very small [30]. It is important to note that both dielectric and metallic nature of the substrate can affect the plasmon resonance significantly [18]. However, the substrate with ENZ properties results in slowing down of the resonance shift which is defined as pinning effect [26, 27].

In order to explore this, we designed two substrates which are referred as HMM-1 and HMM-2 and studied their effect on the plasmon resonance at their corresponding ENZ regions. Au thickness is 10 nm for both of them, but TiO_2 thickness is 25 nm for HMM-1, whereas 45 nm for HMM-2, providing the ENZ conditions at 684 and 751 nm,

respectively. Figure 1(a) shows numerically calculated $\text{Re}(\epsilon_{\parallel})$ and $\text{Im}(\epsilon_{\parallel})$ using Equation 1. The $\text{Re}(\epsilon_{\perp})$ and $\text{Im}(\epsilon_{\perp})$ are calculated using Eq (2) and presented in SI-Figure 5. The simulated and measured transmission and reflection spectra of HMM-1 and HMM-2 (Figure 1(d) and 1(e)) are in good agreement with the projection of the calculated permittivity values. Finite-difference time-domain (FDTD) simulations were performed in Lumerical FDTD Solutions (see Methods for details).

2 Results and discussion

In this study, a set of ND arrays of increasing diameters on different substrates is investigated. Schematic of one of the ND arrays is presented in Figure 1(b). The diameter of the NDs is changed from 120 to 180 nm, while the thickness is kept 60 nm. Figure 2 shows the evolution of the calculated nanoantenna resonances (transmission dip) with increasing diameter on different substrates (glass, HMM-1 and HMM-2).

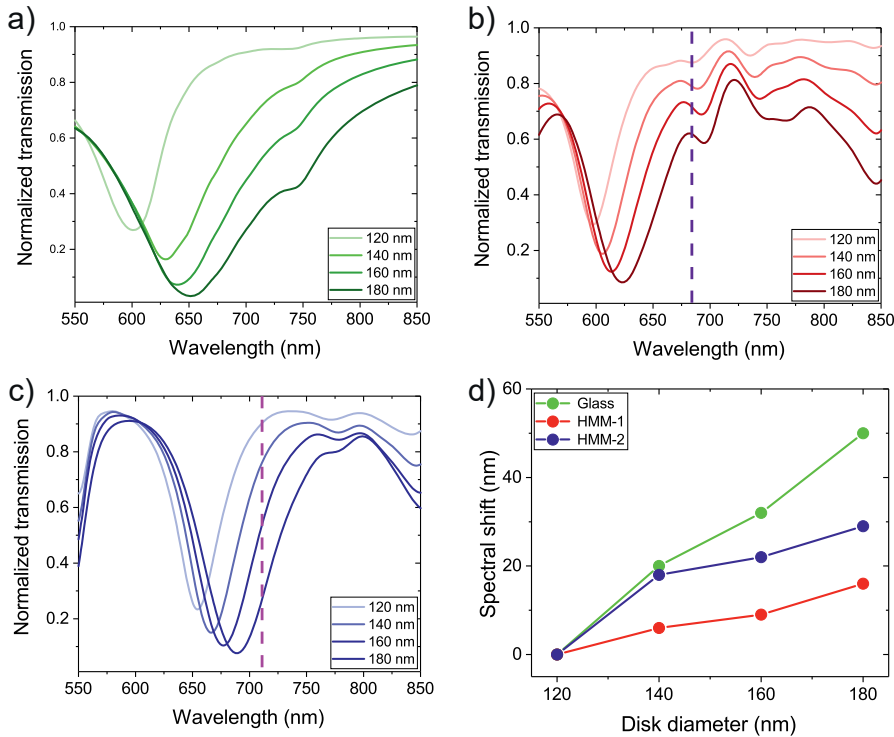


Figure 2: Evolution of the plasmon resonance with varying diameters of NDs on (a) glass (b) HMM-1, (c) HMM-2 and (d) spectral shift of the resonance, calculated by FDTD simulations. FDTD, finite-difference time-domain; HMM, hyperbolic metamaterial; ND, nanodisk.

The comparison of the spectral shifts of the plasmon resonances reveals that the change is much smaller when the NDs are on the ENZ substrates, compared to the case of the glass substrate. That is to say, the resonance of the NDs on the ENZ substrates is pinned near the ENZ wavelengths. Moreover, the ENZ substrates having different ENZ wavelengths control the pinning effect at those wavelengths.

To observe the pinning effect experimentally, we fabricated ND arrays on glass, HMM-1 and HMM-2 substrates using standard electron-beam lithography (EBL) and lift-off process (see Methods for details). Figure 1(c) shows the scanning electron microscope (SEM) image of a fabricated sample on HMM-1. Transmission spectra of NDs on glass with different diameters are presented in Figure 3(a). A resonance shift from 628 to 678 nm is observed, by changing the disk diameter from 120 to 180 nm. The same amount of modification in the diameter for the NDs on HMM-1 changes the plasmon resonance only within a smaller wavelength region of $659 \text{ nm} \leq \lambda \leq 675 \text{ nm}$,

as shown in Figure 3(b). We note that the transmission spectra are normalized to the transmission of the HMM-1 without the NDs. The LSPR of the antenna is not only determined by its size anymore when it is located on the ENZ substrate. This phenomenon is a consequence of the interaction between the resonating antennas, as well as the ENZ substrate. It is also possible to obtain this effect for an antenna array of the same size, at a different wavelength region, by adjusting the composition of the substrate. When the ND array is on HMM-2 having an ENZ wavelength at 751 nm, the pinning effect is observed in the region $703 \text{ nm} \leq \lambda \leq 732 \text{ nm}$, as shown in Figure 3(c). The pinning effect is observed around the ENZ region of the corresponding HMM substrate.

Plasmonic nanoantennas scatter the incident field to all directions towards two different media: substrate and air. The relative efficiency of the scattering is determined by the dielectric constants of the two media. Therefore, effective permittivity of the local environment

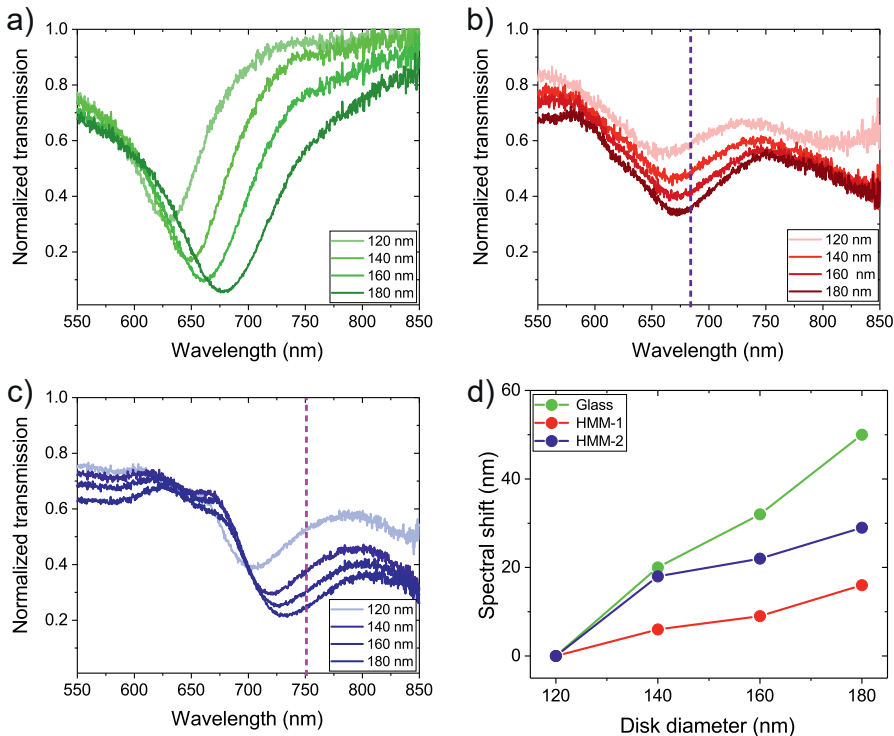


Figure 3: Normalized transmission spectra of the fabricated ND arrays, with disk diameters of 120, 140, 160 and 180 nm on three different substrates: (a) glass (green), (b) HMM-1 (red) and (c) HMM-2 (blue). The ENZ points of HMM-1 and HMM-2 are highlighted by violet and magenta vertical dashed lines in the associated graphs, respectively. (d) The spectral shifts in the resonance wavelengths of the NDs on glass, HMM-1 and HMM-2. HMM, hyperbolic metamaterial; ND, nanodisk; ENZ, epsilon-near-zero.

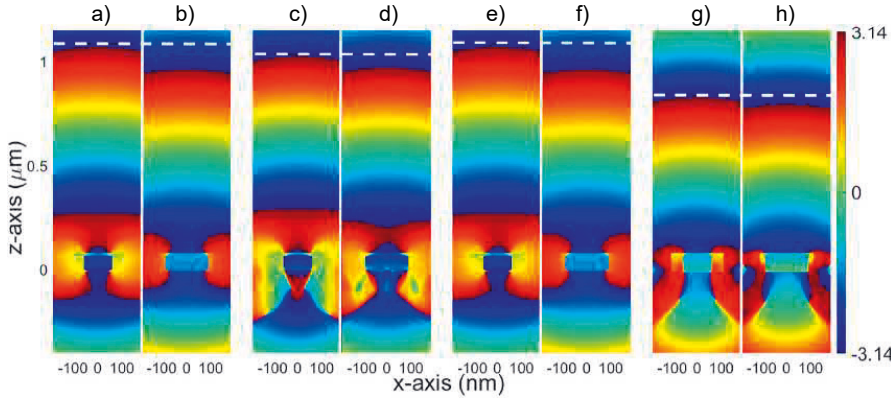


Figure 4: Phase profiles (in the unit of radian) of x component of the scattered E-field up to 2λ from the NDs of diameters (a) 120 nm and (b) 180 nm on glass at $\lambda = 684$ nm and (c) 120 nm and (d) 180 nm on HMM-1 at 684 nm. Similarly, (e) 120 nm and (f) 180 nm on glass at $\lambda = 751$ nm and (g) 120 nm and (h) 180 nm on HMM-2 at $\lambda = 751$ nm. White dotted lines are added for better visual comparison. HMM, hyperbolic metamaterial; ND, nanodisk.

can be defined as $\epsilon_{\text{eff}} = (\epsilon_{\text{sub}} + \epsilon_{\text{air}})/2$. When the substrate is a low-loss ENZ medium, the value of the effective index $\left(n_{\text{eff}} = \sqrt{[\sqrt{\text{Re}(\epsilon_{\text{eff}})^2 + \text{Im}(\epsilon_{\text{eff}})^2} + \text{Re}(\epsilon_{\text{eff}})]/2} \right)$ becomes almost zero at the ENZ region. The resonance frequency of an antenna can be approximated as $\lambda_{\text{res}} \approx 2n_{\text{eff}}(D + 2\delta)$, where $D + 2\delta$ is the effective length of the antenna with a diameter (D) and evanescent extension of the resonant mode (δ) [26].

The vanishing index of refraction (reduced real permittivity) of the substrate limits the spectral shifting of the antenna resonance beyond the ENZ condition [26, 27]. Hence, when an antenna is on an ENZ substrate, an increase in the diameter of the ND antenna is compensated by small n_{eff} , reducing the amount of the shift in the LSPR near the ENZ wavelength, as observed in our experiments. The spectral shift in the plasmon resonance, with respect to the resonance wavelength of the ND arrays with 120 nm diameter, for each sample, is shown in Figure 3(d). The experimental results display a good agreement with the simulation results. The ND arrays on glass exhibit a total shift of 50 nm, whereas the shifts observed in the ND arrays on HMM-1 and HMM-2 are 16 and 29 nm, respectively. The shift in the resonance for HMM-1 is three times less than the one for glass. However, for HMM-2, it is half of the resonance shift obtained for the glass case. The shift in the resonance for HMM-1 is more suppressed compared to HMM-2 because the ENZ region of HMM-1 ($660 \text{ nm} \leq \lambda \leq 690 \text{ nm}$) is intentionally designed at the resonance wavelength of the antenna (on glass). On the other hand, the ENZ region ($730 \text{ nm} \leq \lambda \leq 780 \text{ nm}$) of HMM-2 is far away from the resonance of the antenna (on glass).

The possibility to tune the ENZ region by simply changing the thickness of TiO_2 allows us to probe the pinning effect for HMM-1 and HMM-2 at two different wavelengths. Similar to the transmission minimum, the shift in the scattering peak of the ND antenna is suppressed three times for the ENZ substrates, compared to glass (see SI-Figure 8).

To further examine the scattering of NDs on different substrates, we calculate the phase of the x component of the scattered electric field (E-field) for the NDs of 120 and 180 nm diameter on glass and HMM-1 at 684 nm (Figure 4(a–d)) and on glass and HMM-2 at 751 nm (Figure 4(e–h)). The difference in the phase of the E-fields at a distance of $\sim 2\lambda$ from the surface of the NDs (120 and 180 nm diameters) is 56 degrees when the substrate is glass. However, this difference reduces to 21 degrees when the substrate is changed to ENZ metamaterial. This provides possibilities for the effective control of the phase contribution of each nanostructure.

3 Conclusion and outlook

In conclusion, with this study, we reveal the effect of the ENZ metamaterials as a substrate. Due to the unique feature of ENZ media, we showed that one can diminish the effects of the size of the nanostructure on the spectral position of plasmon resonance. We present the pinning effect of HMM-based ENZ substrates on the LSPR of Au NDs. The plasmon resonance of the same ND is pinned at two different regions as a result of the substrates with different

ENZ wavelengths. Transmission spectra of the NDs, fabricated on glass, HMM-1 (ENZ at 684 nm) and HMM-2 (ENZ at 751 nm), display 50, 16 and 29 nm of spectral shifts in the resonance, respectively, as the disk diameter increases. The spectral shift of the NDs on HMMs is suppressed at least three times due to almost zero index of the substrate. Moreover, the phase of the scattered field from a ND is affected by the ENZ properties of the substrate providing flexibility on the phase modification.

Controlling the plasmonic resonance via substrate properties will open an entirely new avenue. For example, this will provide an efficient method to control the emission properties of quantum emitters and scattering properties of nanoparticles. We foresee that the improved low-loss ENZ substrates and dynamic tunability of the ENZ wavelength will bring more implementations to this platform. Recently, it has been shown that the large nonlinear optical response of ENZ materials [32, 39] provides optical tuning of ENZ wavelength. Similarly, the graphene-based tunable HMM [40] can be used in the MIR range to electrically tune the pinning wavelength. Another perspective would be using the function of vanadium dioxide as a phase-changing material in the HMM layers [41] to thermally turn on and off the pinning effect. The control over the plasmon resonance by designing an ENZ substrate and tuning its properties dynamically enables compensation of the fabrication error from visible to infrared region. Metal-insulator-metal-based tunable ENZ cavities [22] can be used to obtain a pinning effect in waveguides. Overall, these results may facilitate efficient sensing, better beam-steering applications and less cross-talk for on-chip nanophotonic devices in flat optics designs.

4 Methods

4.1 Numerical simulations

We use the commercially available software, Lumerical FDTD Solutions, for 3D electromagnetic simulations of transmission, reflection and field profiles of the samples. We use the experimental dielectric functions provided in the literature to model Au [42], SiO₂ [43] and TiO₂ [44]. HMM-1 and HMM-2 media are modelled with the help of dielectric functions obtained by effective medium approach, as shown in Figure 1(a). The overall thicknesses of the HMM-1 and HMM-2 media are 105 and 165 nm, respectively. The thickness of the NDs is 60 nm and the diameter is ranged from 120 to 180 nm. Conformal meshing is used in the simulations, while a finer mesh constraint to 4 nm is employed in the region enclosing the ND, to get a better resolution.

For the transmission and reflection simulations, the unit cell of size 360 nm is illuminated by a linearly (x) polarized plane wave source of wavelengths 500–900 nm. The boundary conditions (BCs) are set to periodic in the directions parallel to the source propagation

(x , y) and perfectly matched layers (PMLs) in the direction perpendicular to the source propagation (z).

To simulate the scattered electric field profiles, the BCs are set to PMLs in all directions. We use a linearly (x) polarized plane wave source of wavelengths 500–900 nm. The source profile is obtained using the total-field scattered-field option (enclosing the ND). It separates the computation region into two distinct regions; one contains the total field (i.e. the sum of the incident and scattered fields), while the second region contains only the scattered field. A power monitor covering the whole simulation region is used to collect the scattered field at the ENZ wavelengths of each HMM.

4.2 Fabrication

For the fabrication of HMM substrates, the 500- μm -thick fused silica substrate is cleaned in acetone, isopropanol (IPA) with 10 min sonication and blow drying under nitrogen (N₂) flow. The plasma cleaning is used for thorough cleaning of organic contaminants from the surface. Once the samples are cleaned, 10 nm of Au and 25/45 nm of TiO₂ are deposited using electron beam deposition. About 1 nm of Ti is deposited before each gold layer to improve the adhesion at the rate of 0.5 Å/s. The SEM image of HMM-1 is obtained after focused ion beam milling, shown in the inset of Figure 1(d).

The periodic arrays of NDs are fabricated by standard EBL using 20 KeV and 10 μm aperture. The cleaned glass and fabricated HMM samples are spin coated with poly(methyl methacrylate) (PMMA)-A4 at 3000 rotation per minutes (rpm) for 40 s. The spin coated samples are baked at 180 C for 90 s in order to evaporate the anisole solution in PMMA-A4. The 100 \times 100 μm^2 write field is used to create the NDs with the area dose of 300 $\mu\text{C}/\text{cm}^2$. The exposed samples are developed for 60 s in methylisobutylketone:IPA solution at the ratio of 1:3 and 30 s in IPA to stop the development process. The developed samples are loaded in the electron beam evaporation deposition chamber. Similar to HMM fabrication, 1 nm of Ti is used as an adhesion layer, followed by 60 nm of Au deposition at the rate of 0.5 Å/s. The S-1165 remover is used to lift off the metals, and the samples are left in the solution to heat up to 80 C. When the desired temperature is reached, the hot plate is turned off and the samples are kept in the solution for 5 min. Once the cracks start to appear in the metal thin films, the gentle stirring removes all the unwanted metal from the sample. The sample is rinsed in water, acetone and IPA and blow dried under N₂ flow to get rid of residual metal films. Four different matrices are fabricated for 120, 140, 160 and 180 nm disk size by changing the dose factor.

4.3 Optical characterization

Transmission spectra are measured using a Confocal Raman microscope from WiTec (alpha300R). The samples are excited with a broadband light source (Energetiq EQ-99XFC LDLS, spectrum 190–2100 nm). The optical beam is focused on the sample surface by using a 20 \times objective lens (ZEISS EC EPIPLAN 20X/0.4) at normal incidence. To detect the transmission spectra, a 50 \times objective lens (ZEISS EC EPIPLAN 50X/0.75) is placed at the back focal plane to collect transmitted light in the normal direction. The collected light is coupled to an optical fibre connected to a spectrometer (Ocean Optics Flame UV-VIS Spectrometer, detection range 40–900 nm). We first measure the transmission spectrum from the glass substrate. Then, we measure the transmission spectrum of the ND arrays, which is normalized to the

spectrum of glass. Similarly, the transmission spectra of the NDs on HMMs are normalized to transmission from HMM substrates.

Acknowledgement: The authors acknowledge the financial support of the European Research Council (Starting Grant project aQUARIUM; Agreement No. 802986) and Academy of Finland Flagship Programme (PREIN) (320165).

Author contribution: All the authors have accepted responsibility for the entire content of this submitted manuscript and approved submission.

Research funding: The authors acknowledge the financial support of the European Research Council (Starting Grant project aQUARIUM; Agreement No. 802986) and Academy of Finland Flagship Programme (PREIN) (320165).

Conflict of interest statement: The authors declare no conflicts of interest regarding this article.

References

- [1] W. L. Barnes, A. Dereux, and T. W. Ebbesen, "Surface plasmon subwavelength optics," *Nature*, vol. 424, no. 6950, p. 824, 2003.
- [2] E. Ozbay, "Plasmonics: merging photonics and electronics at nanoscale dimensions," *Science*, vol. 311, no. 5758, pp. 189–193, 2006.
- [3] H. Raether, "Surface plasmons on smooth surfaces," in *Surface Plasmons on Smooth and Rough Surfaces and on Gratings*, Berlin, Heidelberg, Springer, 1988, pp. 4–39.
- [4] P. Berini, R. Charbonneau, N. Lahoud, and G. Mattiussi, "Characterization of long-range surface-plasmon-polariton waveguides," *J. Appl. Phys.*, vol. 98, no. 4, p. 043109, 2005.
- [5] A. G. Brolo, "Plasmonics for future biosensors," *Nat. Photonics*, vol. 6, no. 11, p. 709, 2012.
- [6] H. Im, H. Shao, Y. I. Park, et al., "Label-free detection and molecular profiling of exosomes with a nano-plasmonic sensor," *Nat. Biotechnol.*, vol. 32, no. 5, p. 490, 2014.
- [7] Y. Shen, J. Zhou, T. Liu, et al., "Plasmonic gold mushroom arrays with refractive index sensing figures of merit approaching the theoretical limit," *Nat. Commun.*, vol. 4, no. 1, pp. 1–9, 2013.
- [8] J. Liu, M. Jalali, S. Mahshid, and S. Wachsmann-Hogiu, "Are plasmonic optical biosensors ready for use in point-of-need applications?," *Analyst*, vol. 145, no. 2, pp. 364–384, 2020.
- [9] S. Lee, Y. Sun, Y. Cao, and S. H. Kang, "Plasmonic nanostructure-based bioimaging and detection techniques at the single-cell level," *TrAC-Trend Anal. Chem.*, vol. 117, pp. 58–68, 2019.
- [10] J. E. Park, N. Yonet-Tanyeri, E. Vander Ende, et al., "Plasmonic microneedle arrays for in situ sensing with surface-enhanced Raman spectroscopy (SERS)," *Nano Lett.*, vol. 19, no. 10, pp. 6862–6868, 2019.
- [11] B. M. Reinhard, M. Siu, H. Agarwal, A. Paul Alivisatos, and J. Liphardt, "Calibration of dynamic molecular rulers based on plasmon coupling between gold nanoparticles," *Nano Lett.*, vol. 5, no. 11, pp. 2246–2252, 2005.
- [12] S. Lal, N. K. Grady, G. P. Goodrich, and N. J. Halas, "Profiling the near field of a plasmonic nanoparticle with Raman-based molecular rulers," *Nano Lett.*, vol. 6, no. 10, pp. 2338–2343, 2006.
- [13] S. A. Maier and H. A. Atwater, "Plasmonics: localization and guiding of electromagnetic energy in metal/dielectric structures," *J. Appl. Phys.*, vol. 98, no. 1, p. 10, 2005.
- [14] K. M. Mayer and J. H. Hafner, "Localized surface plasmon resonance sensors," *Chem. Rev.*, vol. 111, no. 6, pp. 3828–3857, 2011.
- [15] M. Paul, "Not all that's gold does glitter," *MRS Bull.*, vol. 26, no. 12, pp. 1009–1014, 2001.
- [16] E. Hao and G. C. Schatz, "Electromagnetic fields around silver nanoparticles and dimers," *J. Chem. Phys.*, vol. 120, no. 1, pp. 357–366, 2004.
- [17] B. C. Yildiz, M. Habib, A. R. Rashed, and H. Caglayan, "Hybridized plasmon modes in a system of metal thin film–nanodisk array," *J. Appl. Phys.*, vol. 126, no. 11, p. 113104, 2019.
- [18] B. Gerislioglu, L. Dong, A. Ahmadiwand, H. Hu, P. Nordlander, and N. J. Halas, "Monolithic metal dimer-on-film structure: new plasmonic properties introduced by the underlying metal," *Nano Lett.*, vol. 20, no. 3, pp. 2087–2093, 2020.
- [19] P. Moitra, Y. Yang, Z. Anderson, I. I. Kravchenko, D. P. Briggs, and J. Valentine, "Realization of an all-dielectric zero-index optical metamaterial," *Nat. Photonics*, vol. 7, no. 10, pp. 791–795, 2013.
- [20] H. Hajian, E. Ozbay, and H. Caglayan, "Beaming and enhanced transmission through a subwavelength aperture via epsilon-near-zero media," *Sci. Rep.*, vol. 7, no. 1, pp. 1–8, 2017.
- [21] M. G. Silveirinha and N. Engheta, "Theory of supercoupling, squeezing wave energy, and field confinement in narrow channels and tight bends using ϵ near-zero metamaterials," *Phys. Rev. B*, vol. 76, no. 24, p. 245109, 2007.
- [22] V. Caligiuri, M. Palei, G. Biffi, S. Artyukhin, and R. Krahn, "A semi-classical view on epsilon-near-zero resonant tunneling modes in metal/insulator/metal nanocavities," *Nano Lett.*, vol. 19, no. 5, pp. 3151–3160, 2019.
- [23] M. Z. Alam, S. A. Schulz, J. Upham, I. De Leon, and R. W. Boyd, "Large optical nonlinearity of nanoantennas coupled to an epsilon-near-zero material," *Nat. Photon.*, vol. 12, no. 2, p. 79, 2018.
- [24] X. Duan, F. Zhang, Z. Qian, et al., "Accumulation and directionality of large spontaneous emission enabled by epsilon-near-zero film," *Optic Express*, vol. 27, no. 5, pp. 7426–7434, 2019.
- [25] S. A. Schulz, A. A. Tahir, M. Z. Alam, J. Upham, I. De Leon, and R. W. Boyd, "Optical response of dipole antennas on an epsilon-near-zero substrate," *Phys. Rev.*, vol. 93, no. 6, p. 063846, 2016.
- [26] J. Kim, A. Dutta, G. V. Naik, et al., "Role of epsilon-near-zero substrates in the optical response of plasmonic antennas," *Optica*, vol. 3, no. 3, pp. 339–346, 2016.
- [27] C. T. DeVault, V. A. Zenin, A. Pors, et al., "Suppression of near-field coupling in plasmonic antennas on epsilon-near-zero substrates," *Optica*, vol. 5, no. 12, pp. 1557–1563, 2018.
- [28] U. Koch, C. Hoessbacher, J. Niegemann, C. Hafner, and J. Leuthold, "Digital plasmonic absorption modulator exploiting epsilon-near-zero in transparent conducting oxides," *IEEE Photonics J.*, vol. 8, no. 1, pp. 1–13, 2016.
- [29] J. Gao, L. Sun, H. Deng, C. J. Mathai, S. Gangopadhyay, and X. Yang, "Experimental realization of epsilon-near-zero metamaterial slabs with metal-dielectric multilayers," *Appl. Phys. Lett.*, vol. 103, no. 5, p. 051111, 2013.

- [30] P. Shekhar, J. Atkinson, and Z. Jacob, "Hyperbolic metamaterials: fundamentals and applications," *Nano convergence*, vol. 1, no. 1, p. 14, 2014.
- [31] R. Maas, J. Parsons, N. Engheta, and A. Polman, "Experimental realization of an epsilon-near-zero metamaterial at visible wavelengths," *Nat. Photon.*, vol. 7, no. 11, pp. 907–912, 2013.
- [32] A. R. Rashed, B. C. Yildiz, S. R. Ayyagari, and H. Caglayan, "Hot electron dynamics in ultrafast multilayer epsilon-near-zero metamaterials," *Phys. Rev. B*, vol. 101, p. 165301, 2020.
- [33] P. Alexander, I. Iorsh, P. A. Belov, and Y. Kivshar, "Hyperbolic metamaterials," *Nat. Photonics*, vol. 7, no. 12, p. 948, 2013.
- [34] L. Ferrari, C. Wu, D. Lepage, X. Zhang, and Z. Liu, "Hyperbolic metamaterials and their applications," *Prog. Quant. Electron.*, vol. 40, pp. 1–40, 2015.
- [35] C. L. Cortes, W. Newman, S. Molesky, and Z. Jacob, "Quantum nanophotonics using hyperbolic metamaterials," *J. Optic.*, vol. 14, no. 6, p. 063001, 2012.
- [36] S. R. K. C. Indukuri, J. Bar-David, N. Mazurski, and U. Levy, "Ultrasmall mode volume hyperbolic nanocavities for enhanced light–matter interaction at the nanoscale," *ACS Nano*, vol. 13, no. 10, pp. 11770–11780, 2019.
- [37] Z. Guo, H. Jiang, and H. Chen, "Hyperbolic metamaterials: from dispersion manipulation to applications," *J. Appl. Phys.*, vol. 127, no. 7, p. 071101, 2020.
- [38] P. Huo, S. Zhang, Y. Liang, Y. Lu, and T. Xu, "Hyperbolic metamaterials and metasurfaces: fundamentals and applications," *Adv. Opt. Mater.*, vol. 7, no. 14, p. 1801616, 2019.
- [39] M. Z. Alam, I. De Leon, and R. W. Boyd, "Large optical nonlinearity of indium tin oxide in its epsilon-near-zero region," *Science*, vol. 352, no. 6287, pp. 795–797, 2016.
- [40] A. K. O. Mohamed, C. Guclu, and F. Capolino, "Graphene-based tunable hyperbolic metamaterials and enhanced near-field absorption," *Optic Express*, vol. 21, no. 6, pp. 7614–7632, 2013.
- [41] S. Prayakarao, B. Mendoza, A. Devine, et al., "Tunable VO₂/Au hyperbolic metamaterial," *Appl. Phys. Lett.*, vol. 109, no. 6, p. 061105, 2016.
- [42] P. B. Johnson, and R.-W. Christy, "Optical constants of the noble metals," *Phys. Rev. B*, vol. 6, no. 12, p. 4370, 1972.
- [43] I. H. Malitson, "Interspecimen comparison of the refractive index of fused silica," *Josa*, vol. 55, no. 10, pp. 1205–1209, 1965.
- [44] J. R. DeVore, "Refractive indices of rutile and sphalerite," *JOSA*, vol. 41, no. 6, pp. 416–419, 1951.

Supplementary material: The online version of this article offers supplementary material (<https://doi.org/10.1515/nanoph-2020-0245>).

PUBLICATION

IV

Self-rolling epsilon-near-zero metamaterials

M. Habib, I. Issah, D. Briukhanova, E. Bermúdez-Ureña and H. Caglayan

*Accepted for publication in *Advanced Optical Materials* X(X) (2022), X*

Publication reprinted with the permission of the copyright holders

PUBLICATION

V

Low loss fishnet metamaterial via self-rolled nanotechnology

D. Briukhanova, M. Habib, I. Issah and H. Caglayan

Applied Physics Letters 119(14) (2021), 141101

Publication reprinted with the permission of the copyright holders

Low loss fishnet metamaterial via self-rolled nanotechnology

Cite as: Appl. Phys. Lett. **119**, 141101 (2021); doi: 10.1063/5.0063120

Submitted: 12 July 2021 · Accepted: 21 September 2021 ·

Published Online: 4 October 2021



Daria Briukhanova,¹ Mohsin Habib,¹ Ibrahim Issah,¹ and Humeyra Caglayan^{a)}

AFFILIATIONS

Faculty of Engineering and Natural Science, Photonics, Tampere University, 33720 Tampere, Finland

^{a)}Author to whom correspondence should be addressed: humeyra.caglayan@tuni.fi

ABSTRACT

We propose and demonstrate the fabrication of a curved fishnet metamaterial integrated into a rolled-up tube (RUT) that consists of eight alternating layers of gold and silicon dioxide. We adopt a self-rolled technique for the fabrication of metal/dielectric microtubes with large enough diameters for optical characterization. We experimentally characterize the fabricated fishnet structure, and by means of numerical calculations, we show that the fabricated structure possesses a negative refractive index with a high figure of merit. We demonstrate that the negative refractive index region can be tuned by precisely controlling the dimensions of the holes forming the metamaterial. The results of this study open up the possibility to obtain a simple, fast, and flexible platform for the fabrication of RUT-based metamaterials for bioimaging and sensing applications.

Published under an exclusive license by AIP Publishing. <https://doi.org/10.1063/5.0063120>

The possibility to build superlens,^{1,2} subwavelength imaging,³ invisibility cloak,⁴ and engineer complex metallo-dielectric⁵ motivated scientists to work extensively on the topic of optical negative index metamaterials (NIMs). Theoretically, the existence of NIMs, where both permittivity (ϵ) and permeability (μ) are negative, was proved half a century ago.⁶ However, due to the constraints present in obtaining a naturally existing material with negative permeability, new and exotic artificially engineered materials proposed by different authors have gained much attention in modern physics. Typically, a pair of short wires aligned with an electric field supports resonance with $\epsilon < 0$, and the wires along the magnetic field \mathbf{H} , direction act as magnetic resonators, providing negative μ .^{7,8} Even though such arrangement supports NIM, overlapping electric and magnetic resonances is a very difficult task. As a solution to this, a fishnet structure was introduced to realize both $\mu < 0$ and $\epsilon < 0$ at near-infrared (NIR) frequencies.^{9,10}

Most of the experimentally implemented optical fishnet metamaterials consist of a multilayer structure and require multiple evaporation steps to obtain a bulk fishnet metamaterial.^{11–15} The fabrication process can be laborious, especially when many functional layers are needed with precise thicknesses. Over the past years, self-rolled nanotechnology is proved to be an efficient technique for the fabrication of curved multilayer structures,^{14–18} as they overcome the problem of multiple depositions steps. Rottler *et al.* have shown curved fishnet metamaterial consisting of six alternating layers, using semiconductor strained gallium arsenide (GaAs)/indium GaAs (InGaAs) layers on

top of the aluminum arsenide (AlAs) sacrificial layer that was grown by molecular beam epitaxy (MBE).¹⁹ Upon etching the sacrificial layer, the strained layers start to roll, and in this way, it simplifies the process of multiple depositions and obtaining fishnet metamaterials. However, the circular nature of the rolled-up structure brings the challenge to the spectral characterization of the fishnet metamaterials especially when the diameter is small. Therefore, although a prototype of a fishnet metamaterial was fabricated, the NIM behavior of such curved fishnet structures has not been realized. One of the possible solutions to the problem is to achieve bigger rolled-up tubes (RUTs) using other materials such as silicon nitride (Si_3N_4), silica ($\text{SiO}_2/\text{SiO}_2$), and noble metals. Recently, such RUTs with bigger diameters have been demonstrated for biological applications.^{16,20–23}

In this work, we experimentally demonstrate a curved fishnet metamaterial that consists of eight alternating layers of gold (Au) and silicon dioxide (SiO_2). RUTs are fabricated by utilizing resist as a sacrificial layer. The nanohole structures are then milled through the upper wall of a tube. The resist-based RUTs provide the possibility to include different kinds of materials into the layers of a tube with controllable diameters. The fabricated structure exhibits a negative index of refraction at a range from 700 to 900 nm with the maximum figure of merit (FOM) of 2.76. In addition to efficient design, we experimentally demonstrate that the reflectance from the fishnet structure on rolled-up tubes exhibits low loss. Moreover, we tune the wavelength of the negative refractive index range by

adjusting the length and the width of the nanoholes forming the fishnet metamaterials.

The fishnet structure consists of rectangular nanoholes on eight alternating layers of Au and SiO₂ with the periodicity of 400 nm along both x - and y -axes. The schematic of the structure is shown in Fig. 1(a). To investigate the effect of the size of rectangular holes on the resonance, we simulated the fishnet structure using a commercially available Ansys Lumerical finite-difference time-domain (FDTD) solver. The size of the hole is fixed along the x -axis to $w = 230$ nm and is changed from $l = 190$ to 270 nm with the step size of 20 nm along the y -axis. The reflectance spectra of the fishnet structure with different hole sizes excited with y -polarized plane wave source are presented in Fig. 2. By increasing the size of the hole along the y -axis, we observe a blueshift in the resonance from 828 to 727 nm. The holes embedded in the RUT generate two resonances relative to the direction of the incident electric and magnetic field components. The cross section along the magnetic field exhibits magnetic resonance, while the opposite cross section along the electric field exhibits electric resonance. These two resonance effects result in the negativity of μ and ϵ of the proposed fishnet structure.

To experimentally realize the fishnet structure, we adopted a resist-based rolled-up technique to reduce the deposition steps for metal and dielectric layers. Instead of costly and tedious MBE deposition, we used a spin-coated photoresist as a sacrificial layer. Such a sacrificial layer can be easily etched without compromising the quality of obtained tubes. In addition, the fishnet structure integrated into the wall of RUT eliminates an undesirable effect caused by the substrate of decreasing the negative refractive response, especially prominent in the structures with a small number of functional layers.²⁴ We deposited 60 nm of SiO₂ and 20 nm of Au on top of a photoresist. By quickly removing the photoresist with acetone, we were able to form tubes with large diameters (~ 10 μm). The schematic image of RUT is given in Fig. 1(b). The fishnet structures were created using the FIB milling method. The large diameter of RUT supported an array with 20 unit cells along the x -axis and 30 unit cells along the y -axis on the upper curvature of the tube. The number of unit cells was limited by the size of the curvature of the tube. As the length of the tube is sufficient, we fabricated all of the five designs on the same tube to maintain the same material environment and focusing surface for the measurements. The array size of 8×12 μm^2 is sufficiently large to be characterized using a $100\times$ microscope objective. Overall, we fabricated five different fishnet structures on a 75 μm long RUT (see the supplementary material). Figure 3 shows microscope and scanning electron microscope (SEM) images of the fabricated structure on top of the

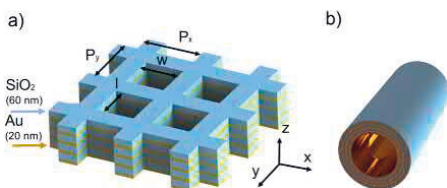


FIG. 1. (a) Schematic representation of a fishnet structure unit cell, where P_x and P_y are set to be 400 nm, $w = 230$ nm and l is changed from 190 to 270 nm. (b) Schematic representation of the RUT.

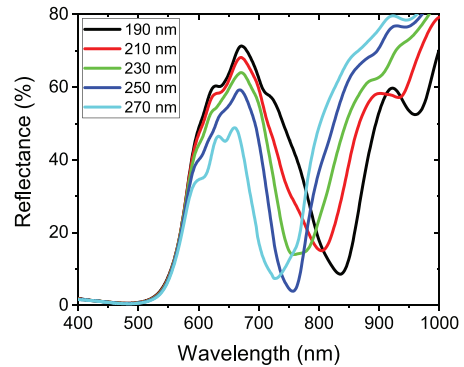


FIG. 2. Numerically calculated reflectance from the fishnet with five different hole sizes.

RUT. The RUT formation was confirmed by taking microscopy images. We took the SEM images from the top of the tube to verify the quality of the structure, see Figs. 3(c)–3(g). For structural analysis such as the RUT quality and the number of layers, a cross-sectional SEM image was taken, as shown in Fig. 3(h).

The fabricated fishnet structures were characterized using the $100\times$ objective and y -polarized broadband white light source (Energetiq EQ-99XFC LDLC, spectrum 190–2100 nm). The reflection spectrum of the fishnet from the upper curvature of the RUT was obtained with respect to the acquired reflection from the unpatterned area of the Si/SiO₂ substrate. Figure 4 presents the reflectance measurements for different hole lengths. The resonance for the smallest hole size appears at 870 nm and blueshifts toward the lower wavelength as the size of the hole is increased. These results are in a good agreement with the simulated results presented in Fig. 2. In this work,

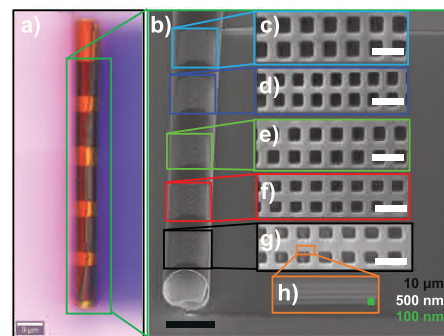


FIG. 3. (a) A microscope image of the RUT with eight alternating metal and dielectric layers with a fishnet pattern on the upper curvature (top view). (b) SEM image of the same RUT. A zoom-in of a fishnet with hole size (c) 270, (d) 250, (e) 230, (f) 210, and (g) 190 nm. (h) An SEM cross section image of the RUT wall.

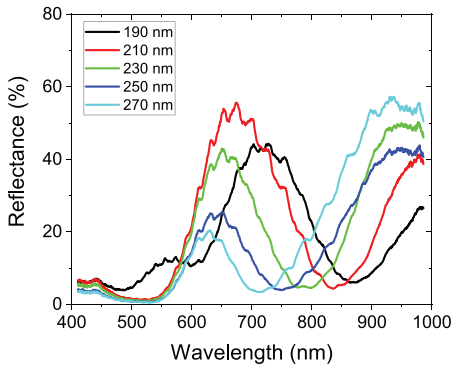


FIG. 4. Experimentally measured reflectance from the fishnet with five different hole sizes.

we overcome the characterization limit of nanostructures on the RUT walls.

Finally, we analytically calculated the refractive index of the simulated and fabricated fishnet structures using the parameter retrieval method (S-parameter)²⁵ (see the [supplementary material](#) for details). The negative index is observed around the resonance region of the reflectance spectrum of the structures. Therefore, we limited the calculation range of the S-parameters from 700 to 950 nm. In addition to resonance wavelength, the quality factor (Q-factor) of the resonance is important. The Q-factor of two longest structures [Figs. 3(c) and 3(d)] are low. Therefore, we only focused on the index of the first three structures (190, 210, and 230 nm). Figures 5(a)–5(c) shows real and imaginary parts of refractive index for 190, 210, and 230 nm case, respectively. The fishnet design with a high Q-factor (190 nm case) has the largest negative index value compared to two other cases. The negative index region is highlighted by gray color in each graph. However, the large value of the real index [Re(n)] is not the only criteria to design NIMs. In order to define a high-quality NIM, one needs to define the imaginary part [Im(n)] as well as the Re(n). A figure of

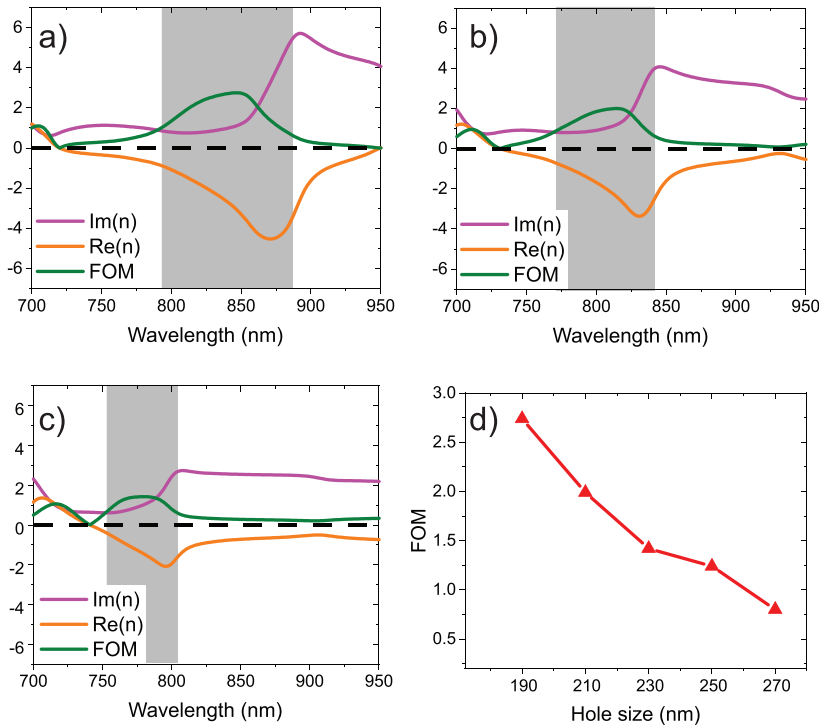


FIG. 5. The refractive index calculated with the S-parameter retrieval method for fishnet structure with hole size (a) 190, (b) 210, and (c) 230 nm. (d) FOM of all fishnet structures vs the holes' size.

merit (FOM) was used to calculate the ratio between $\text{Re}(n)$ and $\text{Im}(n)$ [$\text{FOM} = \text{Re}(n)/\text{Im}(n)$]. The maximum value of the calculated FOM for the fabricated structures is 2.76. This FOM is three times higher than in the work based on the rolled-up structures reported earlier,¹⁹ which indicates the low-loss feature of the fishnet metamaterial in this work.

In conclusion, we demonstrated the fabrication of low-loss fishnet metamaterials integrated in the RUT consisting of eight alternating layers of metals and dielectrics. In our fabrication, we used resist-based rolled-up nanotechnology to simplify the fabrication procedure of RUTs and achieved microtubes with a diameter as large as $10\ \mu\text{m}$. The FIB technique was used to obtain the nanoholes with different dimensions on the fabricated RUT. We experimentally characterized the obtained curved fishnet metamaterials, which are in good agreement with the theoretical calculations. By the numerical calculations, we also demonstrated that our structures exhibit a negative index. We showed that the negative index region can be tuned by precise control of the holes size, from $\lambda = 887$ to $\lambda = 717$ nm. We obtained the FOM as high as 2.76 in the NIR range.

The curved metamaterial, in general, opens up the possibility to prepare three-dimensional devices. It is favorable to control the region of the negative refractive index. We found out that by controlling the size of the fishnet, we can tune the NIM response. The results that we obtained are especially beneficial from the point of view of the easily available fabrication materials. Indeed, our results show a simple and flexible platform that can be used for fabrication of RUT-based metamaterials. It is possible to shift the NIM response toward the visible spectrum by using silver Ag based RUTs. Moreover, the RUT with the embedded fishnet structure can possibly serve as the microfluidic channel where biological imaging and sensing can be done.

See the [supplementary material](#) for the S-parameters calculations and sample fabrication details.

We acknowledge the financial support of the European Research Council (Starting Grant project aQUARUM; Agreement No. 802986) and Academy of Finland Flagship Programme (PREIN) (No. 320165). For this work, Tampere Microscopy Center facilities were used at Tampere University.

AUTHOR DECLARATIONS

Author Contributions

D.B. and M.H. contributed equally to this work.

DATA AVAILABILITY

The data that support the findings of this study are available from the corresponding author upon reasonable request.

REFERENCES

- J. B. Pendry, "Negative refraction makes a perfect lens," *Phys. Rev. Lett.* **85**, 3966 (2000).
- X. Zhang and Z. Liu, "Superlenses to overcome the diffraction limit," *Nat. Mater.* **7**, 435 (2008).
- V. M. Shalaev, "Optical negative-index metamaterials," *Nat. Photonics* **1**, 41 (2007).
- D. Schurig, J. J. Mock, B. J. Justice, S. A. Cummer, J. B. Pendry, A. F. Starr, and D. R. Smith, "Metamaterial electromagnetic cloak at microwave frequencies," *Science* **314**, 977 (2006).
- J. Yang, C. Sauvan, H. T. Liu, and P. Lalanne, "Theory of fishnet negative-index optical metamaterials," *Phys. Rev. Lett.* **107**, 043903 (2011).
- V. G. Veselago, "The electrodynamics of substances with simultaneously negative values of permittivity and permeability," *Sov. Phys. Usp.* **10**, 509 (1968).
- V. M. Shalaev, W. Cai, U. K. Chettiar, H.-K. Yuan, A. K. Sarychev, V. P. Drachev, and A. V. Kildishev, "Negative index of refraction in optical metamaterials," *Opt. Lett.* **30**, 3356 (2005).
- G. Dolling, C. Enkrich, M. Wegener, J. F. Zhou, C. M. Soukoulis, and S. Linden, "Cut-wire pairs and plate pairs as magnetic atoms for optical metamaterials," *Opt. Lett.* **30**, 3198 (2005).
- S. Zhang, W. Fan, N. C. Panoiu, K. J. Malloy, R. M. Osgood, and S. R. Brueck, "Experimental demonstration of near-infrared negative-index metamaterials," *Phys. Rev. Lett.* **95**, 137404 (2005).
- S. Zhang, W. Fan, N. C. Panoiu, K. J. Malloy, R. M. Osgood, and S. R. Brueck, "Optical negative-index bulk metamaterials consisting of 2D perforated metal-dielectric stacks," *Opt. Express* **14**, 6778 (2006).
- J. Valentine, S. Zhang, T. Zentgraf, E. Ulin-Avila, D. A. Genov, G. Bartal, and X. Zhang, "Three-dimensional optical metamaterial with a negative refractive index," *Nature* **455**, 376 (2008).
- G. Dolling, M. Wegener, C. M. Soukoulis, and S. Linden, "Negative-index metamaterial at 780 nm wavelength," *Opt. Lett.* **32**, 53 (2007).
- C. García-Meca, J. Hurtado, J. Martí, A. Martínez, W. Dickson, and A. V. Zayats, "Low-loss multilayered metamaterial exhibiting a negative index of refraction at visible wavelengths," *Phys. Rev. Lett.* **106**, 067402 (2011).
- V. Y. Prinz, V. A. Seliznev, A. K. Gutakovskiy, A. V. Chehovskiy, V. V. Preobrazhenskii, M. A. Putyato, and T. A. Gavrilova, "Free-standing and overgrown InGaAs/GaAs nanotubes, nanohelices and their arrays," *Physica E* **6**, 828 (2000).
- S. Schwaiger, A. Rottler, and S. Mendach, "Rolled-up metamaterials," *Adv. Optoelectron.* **2012**, 782864.
- M. Medina-Sánchez, B. Ibarlucea, N. Pérez, D. D. Karnausenko, S. M. Weiz, L. Baraban, G. Cuniberti, and O. G. Schmidt, "High-performance three-dimensional tubular nanomembrane sensor for DNA detection," *Nano Lett.* **16**, 4288 (2016).
- D. Brick, V. Engemaier, Y. Guo, M. Grossmann, G. Li, D. Grimm, O. G. Schmidt, M. Schubert, V. E. Gusev, M. Hettich, and T. Dekorsy, "Interface adhesion and structural characterization of rolled-up GaAs/In_{0.2}Ga_{0.8}As multilayer tubes by coherent phonon spectroscopy," *Sci. Rep.* **7**, 5385 (2017).
- E. Bermúdez-Ureña and U. Steiner, "Self-rolled multilayer metasurfaces," *ACS Photonics* **6**, 2198 (2019).
- A. Rottler, M. Harland, M. Bröll, S. Schwaiger, D. Stickler, A. Stemmann, C. Heyn, D. Heitmann, and S. Mendach, "Rolled-up nanotechnology for the fabrication of three-dimensional fishnet-type GaAs-metal metamaterials with negative refractive index at near-infrared frequencies," *Appl. Phys. Lett.* **100**, 151104 (2012).
- S. M. Harazim, W. Xi, C. K. Schmidt, S. Sanchez, and O. G. Schmidt, "Fabrication and applications of large arrays of multifunctional rolled-up SiO₂/SiO₂ microtubes," *J. Mater. Chem.* **22**, 2878 (2012).
- D. Grimm, C. C. Bof Bufon, C. Deneke, P. Atkinson, D. J. Thurmer, F. Schäffel, S. Gorantla, A. Bachmatiuk, and O. G. Schmidt, "Rolled-up nanomembranes as compact 3D architectures for field effect transistors and fluidic sensing applications," *Nano Lett.* **13**, 213 (2013).
- W. Xi, C. K. Schmidt, S. Sanchez, D. H. Gracias, R. E. Carazo-Salas, S. P. Jackson, and O. G. Schmidt, "Rolled-up functionalized nanomembranes as three-dimensional cavities for single cell studies," *Nano Lett.* **14**, 4197 (2014).
- W. Xi, C. K. Schmidt, S. Sanchez, D. H. Gracias, R. E. Carazo-Salas, R. Butler, N. Lawrence, S. P. Jackson, and O. G. Schmidt, "Molecular insights into division of single human cancer cells in on-chip transparent microtubes," *ACS Nano* **10**, 5835 (2016).
- A. Minovich, D. N. Neshev, D. A. Powell, and Y. S. Kivshar, "Influence of the substrate on negative index fishnet metamaterials," *Opt. Commun.* **283**, 4770 (2010).
- D. R. Smith, D. C. Vier, T. Koschny, and C. M. Soukoulis, "Electromagnetic parameter retrieval from inhomogeneous metamaterials," *Phys. Rev. E* **71**, 036617 (2005).

PUBLICATION

VI

Wavefront control with nanohole array-based out-of-plane metasurfaces

M. Habib, I. Issah, D. Briukhanova, A. R. Rashed and H. Caglayan

ACS Applied nano materials 4(9) (2021), 8699–8705

Publication reprinted with the permission of the copyright holders

Wavefront Control with Nanohole Array-Based Out-of-Plane Metasurfaces

Mohsin Habib, Ibrahim Issah, Daria Briukhanova, Alireza R. Rashed, and Humeyra Caglayan*

Cite This: *ACS Appl. Nano Mater.* 2021, 4, 8699–8705

Read Online

ACCESS |

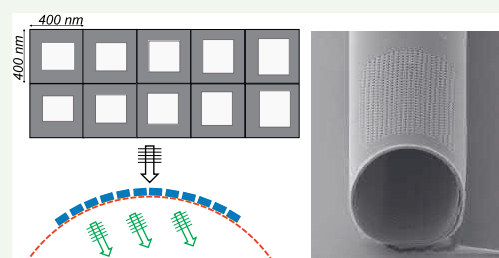
Metrics & More

Article Recommendations

Supporting Information

ABSTRACT: Planar metasurfaces provide exceptional wavefront manipulation at the subwavelength scale by controlling the phase of the light. Here, we introduce an out-of-plane nanohole-based metasurface design with the implementation of a unique self-rolling technique. The photoresist-based technique enables the fabrication of the metasurface formed by nanohole arrays on gold (Au) and silicon dioxide (SiO₂) rolled-up microtubes. The curved nature of the tube allows the fabrication of an out-of-plane metasurface that can effectively control the wavefront compared to the common planar counterparts. This effect is verified by the spectral measurements of the fabricated samples. In addition, we analytically calculated the dispersion relation to identify the resonance wavelength of the structure and numerically calculate the phase of the transmitted light through the holes with different sizes. Our work forms the basis for the unique platform to introduce a new feature to the metasurfaces, which may find many applications from stacked metasurface layers to optical trapping particles inside the tube.

KEYWORDS: metasurfaces, rolled-up tubes, wavefront control, nanoholes



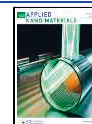
INTRODUCTION

In recent years, metamaterials with unusual electromagnetic properties have provided extensive control on the response of electromagnetic waves with the arrangement of subwavelength antennas.^{1,2} Particularly, the two-dimensional counterparts of metamaterials (metasurfaces) have been extensively studied to achieve applications such as metalenses,^{3–5} beam steering devices,⁶ color filters,⁷ visual gas sensing,⁸ holography,⁹ and optical trapping¹⁰ devices. Different levels of manipulation and efficiency were obtained in these applications, which are provided by the arrangement of different antennas such as V-shaped antennas,¹¹ elliptical,¹² square nanoposts,¹³ and perforated nanovoids or nanoholes.^{14,15} Especially, the nanohole arrays contribute to the flexible metasurface platforms with different applications due to their top-down approach for incorporating various materials.¹⁶

Notably, when these nanohole arrays are obtained on the structures comprising stacked metal-dielectric layers, the spectral response is much richer as the additionally supported surface plasmon polaritons (SPP) modes arise. Not only single-interface (external) SPP¹⁷ but also a gap (internal) SPP^{18,19} are supported in these nanohole arrangements introduced on a thin metal layer or metal/dielectric stacks. Over the last several years, these nanohole arrays delivered interesting features and applications from extraordinary transmission²⁰ to enhanced biosensing²¹ and realization of the negative refractive index.^{22–24} Lately, Matsui et al. brought metal-dielectric hole

arrays to the metasurface applications using different shapes to control the phase of the transmitted light.²⁵ Additionally, an inclined wavefront for beam steering in the near-infrared range has been achieved using a gradual change in the hole size.^{2,6} These inverted metasurfaces in contrast to the regular ones lead to a significantly higher signal-to-noise ratio and efficient focusing of the incident light.¹⁵ However, the fabrication of such structures is typically based on subsequential layer deposition of metal and dielectric, which require precise control on the deposition of each layer. For research applications, such an approach is not only time-consuming but also limited by the uniformity and reproducibility of each layer, given the involvement of multiple steps of deposition. Yet, a unique self-rolling mechanism of multilayer metal and dielectric/semiconductor materials with fewer deposition steps can provide an excellent solution to these challenges. The strain-induced self-rolling method, known as the thin-film self-rolling technique for three-dimensional (3D) rolled-up tubes (RUTs), has been used in different fields after it was introduced in semiconductor bilayers grown by molecular beam epitaxy (MBE),²⁷ including

Received: May 2, 2021
Accepted: July 15, 2021
Published: August 2, 2021



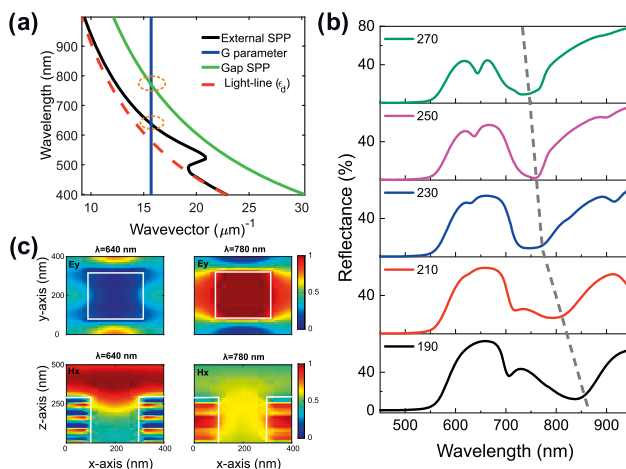


Figure 1. (a) Dispersion curves of the external and gap SPP modes excited by metamaterials milled with holes. The light-line ϵ_d shows the dispersion relation of the dielectric medium and the G parameter corresponds to the reciprocal lattice vector of the stacked holes. The two orange circular insets illustrate the relation of SPPs and the conservation of momentum as a function of the lattice periodicity. (b) Reflectance curves of five different hole sizes. The gray line shows the blue shift in the reflectance spectra as a function of different hole sizes. (c) y component of electric field (E_y) in the x - y plane from the top at 640 and 780 nm are presented in top panels. Similarly, a cross section view of the x component of magnetic field (H_x) at 640 and 780 nm are presented in bottom panels.

electronic,²⁸ magnetoelectronic devices,²⁹ single-cell culture study,³⁰ and biological sensing.^{31–33} Although applying a self-rolling method to fold more complex structures opens new ways to produce 3D photonic micro-objects with novel designs and optical properties, it has not been adopted yet into metasurfaces.

This work introduces another degree of control over the design of planar metasurfaces by providing an out-of-plane contribution to wavefront modification. We utilized the curvature of strain-driven self-rolling three-dimensional RUTs formed of gold (Au) and silicon dioxide (SiO_2) layers to obtain a unique metasurface with rectangular nanohole arrays. Nanoholes were fabricated on the multilayer metal/dielectric walls of the RUTs with different sizes to introduce a gradual shift to the phase of the transmitted light. While enriched dispersion provides the coupling to hybrid plasmon modes, the metasurfaces on the RUTs wall provide additional degrees of freedom to modify the dispersion of the planar structures. The circular curvature of RUTs provides an extra phase difference that leads to an additional wavefront control mechanism compared to the planar metasurface designs. Our approach of using RUTs does not only reduces the fabrication time and the related challenges but also grants a powerful and unique wavefront control and dispersion engineering platform. The integration of self-rolling systems with the advanced metasurfaces enables various unique optical functionalities from stacked nonlinear^{34,35} metasurface layers to optical trapping of particles inside the tube.

■ METASURFACE DESIGN

To facilitate the properties of the modes in nanohole-based metasurface design, we implemented the dispersion relation of the stacked metal-dielectric film and illustrate the different plasmon mode excitations using the Helmholtz equations (see the Supporting Information for details). Although the proposed formulation is an approximation of the metasurface design, it can

be extended to the general case of multiple layers with random permittivities. This formulation is used to elucidate the properties of SPPs, the propagating modes on the surface, and the inside of the stacked hole metal-dielectric layers. Predominately, localized surface plasmon excitation in metamaterials is relevant due to its distinguishing feature of confining an optical field in the subwavelength regime and guiding the optical field to a relatively long distance. These external and gap plasmon modes, excited by the metamaterials with holes, have been of interest and used to understand the acquired resonances in the reflectance spectra.³⁶

To account for the periodic nanoholes embedded in the multilayered structure (20 nm of an Au layer and 60 nm of SiO_2), we implemented the dispersion relation between the wavevector $|k_{\text{spp}}|$ and the reciprocal lattice vectors to illustrate that the interaction between an incident optical field and SPP obeys the conservation of energy and momentum (see Supporting Information for details). Figure 1a illustrates the reciprocal lattice vectors G_{ij} for the stacked hole arrays, the external SPP, gap SPP, and the light-line of the dielectric media. The relation between the SPPs and the conservation of momentum is linked to the reflectance resonance dip, as shown in Figure 1b.

Once the dispersion of the stacked layers is identified, the effect of the rectangular hole size on the resonance was investigated by a finite difference time domain (FDTD) solver (Ansys Lumerical FDTD Solutions). The reflection spectra of nanoholes with different sizes reveal the gradual change in the resonance wavelength from 830 to 750 nm. The design is composed of eight alternative layers of SiO_2 and Au with periodic hole arrays. The periodicity of the hole is 400 nm in both x - and y -axes. The hole size is fixed along the x -axis (230 nm) and changed from 190 to 270 nm along the y -axis with a step size of 20 nm. Figure 1b presents the blue shift in the reflection spectra for the y -polarized illumination, with the

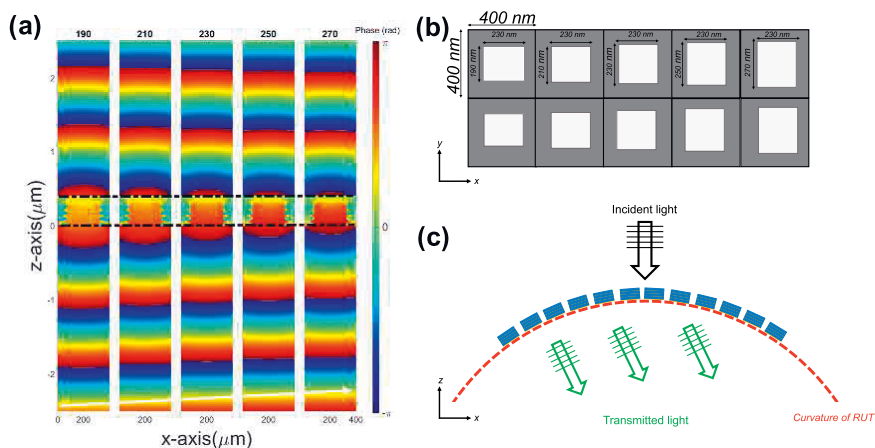


Figure 2. (a) Phase profile (units in radians) of the y component of the E -field up to 2λ from the nanoholes changing along the y -axis from 190 to 270 nm at $\lambda = 750$ nm. A white arrow is added for better visual comparison. (b) Top view of varied hole size structures is used to obtain wavefront control. A unit cell is composed of five different hole sizes. (c) Schematics of inclined wavefront transmitted inside the RUT with nanoholes on the top curvature.

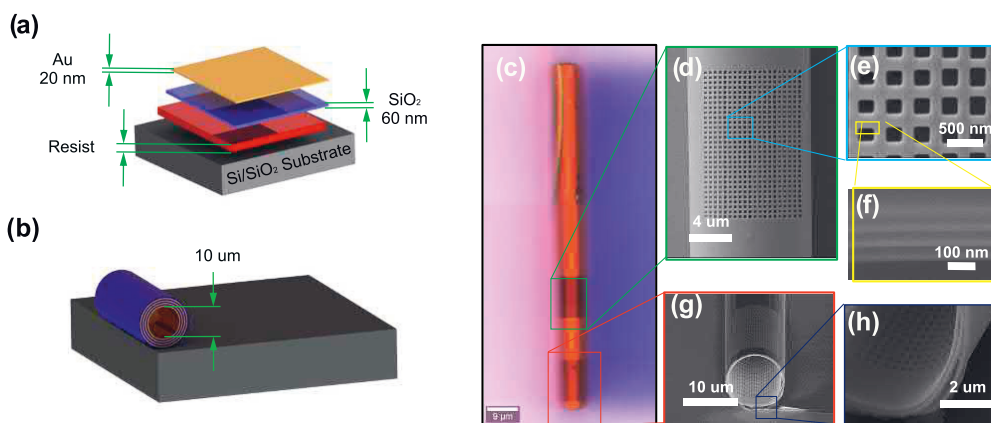


Figure 3. Sketch of the sample geometry showing the thin films deposited on top of the resist that rolls up from the substrate when resist was removed. (a) Thick resist ($2\ \mu\text{m}$) was used as a sacrificial layer on the top Si/SiO₂ substrate; 60 nm SiO₂ and 20 nm Au were used as strained layers. (b) Released thin films resulting in the formation of RUT with a diameter of $10\ \mu\text{m}$. (c) Optical microscopy image of RUT with nanoholes. The scanning electron microscopy (SEM) images from (d, e) top, (f) cross section, and (g, h) bottom corner.

gradual size increase of the periodic nanohole arrays (see the [Methods](#) section for details).

We calculated the mode profile at 640 and 780 nm for the 230 nm nanohole case, which corresponds to external SPP and gap SPP, respectively. In [Figure 1c](#), the top two panels show the y component of the electric (E) field in the x - y plane. The bottom panels show the x component of the magnetic (H) field; the cutting plane was in the middle of the unit cell with normalized color codes. The first mode at 640 nm indicates that the fields are propagating on the top layer of the metal and air interface, an indication of external SPP. On the other hand, in the other mode, the fields are localized inside the hole and dielectric between the metal layers at 780 nm. Thus, the mode profile at 780 nm is evidence of the gap SPPs, which can be controlled by

changing the hole size. [Figure S2](#) presents E_y for a multiple unit cell at $\lambda = 640$ and 780 nm.

As the modes provided by the different size nanoholes were identified, it is possible to bring them together in the design of the metasurface. To investigate this, the change in the phase of the E -field by increasing the hole size was simulated at $\lambda = 750$ nm. [Figure 2a](#), shows the numerically calculated phase profile of five different hole sizes up to 2λ along the direction of the propagation (z -axis). As the hole size changes from 190 to 270 nm, the transmitted light experiences an additional phase. Thus, increasing the hole size from 190 to 270 nm gradually with a step size of 20 nm along the polarization direction (while keeping other parameters fixed) will introduce a gradual change of 0.95 radians in the phase. Although this can be optimized further for

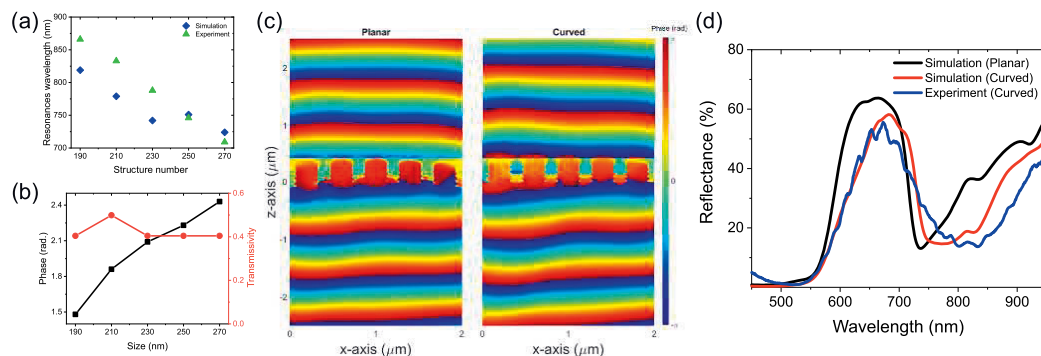


Figure 4. Comparison of different hole size (a) resonance dips in reflection, (b) transmission intensity and phase at $\lambda = 750$ nm, (c) phase response of the y component E -field at $\lambda = 750$ nm for planar and curved metasurfaces with different hole sizes, respectively, (d) simulated and measured reflectance spectra of the fabricated sample with nanoholes of different sizes from the planar (black) and curved metasurface (red (simulation) and blue (experiment)) along y polarization.

specific applications, this is sufficient to explore the proof-of-concept in this work.

The numerical results confirm that using a transition in the hole sizes leads to an inclined phase that can be used to control the wavefront for changing the propagation direction or focusing. Figure 2b presents the top view of the proposed design of the nanoholes with different side lengths changing from 190 to 270 nm along the y -axis, which is placed in a supercell of $2 \mu\text{m}$. Although this simple planar design based on the metal-dielectric stacks works efficiently to control the wavefront, it is limited by the variation of the planar nanohole dimensions. Therefore, the additional phase control requires the extension of the metasurfaces design to out-of-plane. Motivated by the recent advances in the three-dimensional self-rolling RUTs and the fabrication of inverse metasurfaces, we combined these features in the out-of-plane metasurface on these 3D photonic microstructures. Figure 2c shows the cross-sectional view of the proposed metasurface design with the additional control, which is achieved by introducing a curve to the planar nanohole array.

RESULTS AND DISCUSSION

To experimentally realize out-of-plane metasurfaces for wavefront control, RUTs were fabricated using a self-rolling mechanism. The first rolled-up tubes were fabricated by Prinz et al. using a strained indium arsenide/gallium arsenide (InAs/GaAs) bilayer with lattice mismatch.³⁷ Although the main fabrication approach is similar, we have adopted this technique to our study by changing the material layers and most importantly the sacrificial layer. The defined pattern was used to control the size and number of turns in the RUTs. This area was coated with 60 nm SiO_2 and 20 nm Au. As these thin films inherit the strain due to the different deposition rates, this strain generates the RUT formation when released by etching/removing the sacrificial layer with acetone (see the Methods section for details). The diameter of the tubes was controlled by changing the thickness of SiO_2 and Au. Additionally, the type of stress on each layer defines the direction of rolling.³⁷ To achieve the rolling in an upward direction, we first deposit SiO_2 with compressive stress at a low deposition rate and then Au with tensile stress by adding an adhesive layer of titanium (Ti) at a high deposition rate, as schematically shown in Figure 3a, b.

In addition to the thin-film stress, the type of sacrificial layer plays an important role in this process. The speed of rolling depends on the etch rate of the sacrificial layer, which also defines the diameter of the tube. The faster the sacrificial layer is removed, the more strained material is available to roll. Therefore, the size of the circumference of the tube gets bigger if the sacrificial layer is removed abruptly. For this study, a photolithography resist was chosen as a sacrificial layer. The resist was removed in 15 seconds (s), restricting the Au and SiO_2 layers to get compact rolling compared to other sacrificial layers that take hours to etch. Therefore, the use of the resist not only yielded to bigger diameter microtubes compared to other sacrificial layers such as aluminum arsenide (AlAs)²⁷ or germanium (Ge)³⁸ but also provided a quick process with tight rolled layers.

We targeted a diameter of $10 \mu\text{m}$ with this process to introduce the effect of the curvature on the spectral response of the metasurfaces and also to overcome the characterization limitations. A tube with a diameter of $10 \mu\text{m}$ supplies a surface area that is big enough to accommodate $20\times$ unit cells of 400 nm (or four supercells). In addition, the curvature of such diameter provides the out-of-plane effect with respect to the operating wavelength. Once the desired diameter of $10 \mu\text{m}$ is achieved, we specified the number of turns and the size of the tube by designing the rectangular pattern. The short side of the rectangle defines the length of the tube and the number of turns is the function of the longer side of the tube, as the rolling happens along the longer edge of the rectangle. A $75 \times 125 \mu\text{m}^2$ rectangular pattern was used to achieve the $75 \mu\text{m}$ long tube with four turns, meaning eight alternative layers of SiO_2 and Au. The nanohole arrays were obtained using focused ion beam (FIB) milling on the upper curvature of RUT. The optical microscopy image and the scanning electron microscopy (SEM) images of the milled area ($8 \times 12 \mu\text{m}^2$) (see the Methods section for details) are presented in Figure 3c–h. The quality of the tube is first confirmed using an optical microscope, as shown in Figure 3c. The FIB milling is performed on the center of the curvature to achieve better quality metasurfaces, presented in Figure 3d, as a complete device, and a supercell in Figure 3e. The cross-sectional SEM image is taken to confirm the number of bilayers, as shown in Figure 3f. The tilted images are used to

measure the diameter and rolling quality of the tubes, as shown in Figure 3g, h, respectively.

Additionally, metasurfaces formed by array of nanoholes with a constant size were fabricated for five different sizes on the same RUT. Figure 4a highlights the resonance value for five different hole sizes used in the design of the out-of-plane metasurfaces. The resonance from simulation (blue diamonds) and fabricated samples (green triangles) shows quite a good agreement. To control the wavefront of light, it is important to achieve a maximum phase difference. However, this phase difference should be achieved with low modulation in the intensity of the transmitted light. Figure 4b presents the comparison between the transmission intensity (red line with circles) and phase (black line with rectangles) of the transmitted light at $\lambda = 750$ nm, showing that the proposed metasurface has minimum intensity modulation. However, changing the hole size from 190 to 270 nm results in a ~ 1 radian phase difference, which is suitable for the proof-of-concept phase control in out-of-plane metasurfaces.

Figure S3 comparatively presents the phase profile for two different cases (planar metasurfaces and curved metasurfaces) with a single hole size (190 nm). The planar metasurfaces with equal hole size confirm no phase gradient and the electromagnetic field propagates forward without any change in the propagation direction. Contrary to that, the curved metasurfaces with the same hole size slightly bend the light toward the center of the tube. This unique nature of the curved metasurface introduces an additional control to the light propagating inside the tube compared to that of the planar case. The curvature of RUT brings a new degree of freedom to control light in a more effective manner compared to planar metasurfaces.

Finally, we investigated the role of the curvature on the wavefront propagation inside the RUT with nanohole arrays. To identify this, first, the phase response from the metasurfaces with a uniform hole size at $\lambda = 750$ nm was calculated. Then, to mimic the effect of the curvature, we calculated the phase response of the metasurfaces with five different hole sizes in a supercell ($2 \mu\text{m}$). The change in the hole size along the y -axis introduces a gradual change in the phase, leading to steady wavefront control in one direction (Figure 4c). The change in the phase for the planar case is due to the change in the hole size. However, the phase response for the out-of-plane metasurfaces has additional bending, which is the outcome of the curvature of the tube. The curvature of the RUT defines the additional phase component for the out-of-plane nanohole-based metasurfaces. For our RUT, each hole has a tilt of 6° compared to the adjacent nanohole. We calculate the phase response of the 230 nm hole case for five different angles to see the effect of the curvature of the tube in addition to the hole size. Figure S4 presents the phase response of five different angles. The results show that the curvature of the RUT brings an additional phase control compared to the planar case, which only depends on the size of the hole. For a single unit cell, we obtained a change of 0.77 radian in the phase, while changing the tilt angle from 12° to -12° (see the Supporting Information for details).

The fabricated samples were characterized using a confocal microscope with results presented in Figure 4d. The simulation results are presented in the same figure for two different metasurfaces with planar (in black) and curved (in red) metasurfaces, which are illuminated by a y -polarized light source. The measurement (in blue) has a better agreement with the numerically calculated results for the curved metasurface design (see the Methods section for details). The spectral

response of the supercell is an average of all of the individual holes. The experimental results show that the out-of-plane metasurfaces will be different from the planar metasurfaces. This new degree of freedom will allow better control of light and will open an entirely new avenue to utilize the light inside the tube. This controlled propagation of light can be used to selectively manipulate and sense the particles inside the RUT.

CONCLUSIONS AND OUTLOOK

In conclusion, we introduced a new characteristic to the metasurfaces that use the advantage of a self-rolling mechanism to reduce the fabrication steps of multilayered structures and effectively control the optical field in contrast to planar metasurfaces. The dispersion relation for the metal/dielectric multilayer structures was analytically calculated to predict the resonance values for internal and external SPPs. In addition, we numerically calculated the resonance wavelength and the phase profile of each nanohole to design the metasurface. We experimentally realized the unique metasurfaces via the self-rolling mechanism and the FIB technique and measured the reflectance spectra of the fabricated metasurfaces. The numerically studied wavefront demonstrates the effect of the curvature on the wavefront defined by the metasurface. Another key result obtained in this study is the usage of the resist as a sacrificial layer. This yields a cost-effective, fast, and easy method to obtain RUTs that can be utilized in different metasurface-based applications.

While our samples demonstrate desired properties, it is possible to further improve the properties using the optimized RUT curvature for the operating wavelength. Additionally, the out-of-plane metasurfaces can be improved further using the neural network techniques for the metasurface design, better modeling approach,³⁹ and increasing the number of meta-atoms (nanoholes) in a supercell. This will allow higher phase difference and even better wavefront control. Moreover, the signal-to-noise ratio/efficiency of meta-atoms can be improved using thin metal layers. Apart from that, our approach can be used to fabricate more complex structures on RUTs, for example, Babinet-inverted nanoantennas,¹⁵ to achieve metalenses for focusing and imaging purposes inside the tube. Overall, the results of this study open a unique platform for out-of-plane metasurface design, which provides possibilities for new kinds of metalenses, beam steering, and optical trapping of particles inside the RUTs. These applications may also lead to different platforms when integrated with already demonstrated properties of the RUTs such as wireless energy transfer, tunable shape, and neural guidance.

METHODS

Numerical Simulations. The optical response of fabricated nanoholes inside the eight alternative layers of Au/SiO₂ is numerically calculated using Ansys Lumerical FDTD Solutions. 3D electromagnetic simulations of reflection, phase, and E -field profiles were performed. We used the experimental dielectric functions provided in the literature to model Au⁴⁰ and SiO₂.^{41,41} To obtain the optical response of nanoholes with different side lengths, we set our boundary conditions to periodic along the x - and y -axes and perfectly matched layer (PML) in the direction of propagation (z). The unit cell of size 400 nm was illuminated by a linearly polarized plane wave source in the y direction with a 450–950 nm spectral range. A conformal mesh of 4 nm was used in the simulation region while a finer mesh of 2 nm was employed in the region enclosing the multilayers to get better resolution.

The reflection results for a single unit cell with five different hole sizes were calculated along y polarization. However, the electric field was

calculated by exciting the samples with the same linearly polarized total-field scattered-field (TFSF) source in the y direction with PML boundary conditions along x , y , and z axes. The complete supercell with the same and different holes was designed to see the effect of planar and curved RUTs on the wavefront control and electromagnetic field manipulations. A uniform mesh of 4 nm was used to obtain a better resolution in the distribution of the electric field.

Fabrication. For the fabrication of RUTs, a 500 μm thick silicon (Si) substrate coated with 280 nm SiO_2 was cleaned in acetone and isopropanol (IPA) with 10 minutes (min) sonication, and blow-dried under nitrogen (N_2) flow. To clean the organic contaminants, oxygen plasma cleaning was done for 10 min. Once the samples were thoroughly cleaned, they were coated with a thin layer of hexamethyldisilazane (HMDS) at 125 $^\circ\text{C}$ to improve the adhesion of the photolithography resist. The AZE13012 resist was spin-coated at 3000 rounds per minute (RPM) for 40 s. The resist was soft baked at 90 $^\circ\text{C}$ for 90 s. The spin-coated samples were exposed using the Suss MA6 mask aligner for 4 s under an ultraviolet (UV) lamp using the rectangular pattern in the mask. The postbaking process was done at 110 $^\circ\text{C}$ for 60 s. The samples were developed for 60 s using an MIF 726 developer and then rinsed three times in deionized water.

The developed samples were coated with 60 nm SiO_2 using electron beam deposition at a rate of 0.1 nm/s . The thickness of SiO_2 was confirmed using an ellipsometer. In the second step of deposition, the samples were coated with 2 nm Ti and 20 nm Au at 0.3 nm/s . The Ti layer was used for better adhesion of Au. Acetone was used to lift off the thin films on top of the resist. The samples were placed gently inside a beaker containing acetone. The samples were kept in acetone for 5 min, then moved to IPA for 30 s, and blow-dried under N_2 flow. While removing the resist, SiO_2 and Au layers started to roll due to the stress introduced during the deposition process. An optical microscope was used to ensure the quality of the tubes.

A Zeiss Crossbeam 540 FIB machine was used to mill the samples. The acceleration energy of Gallium ions was 30 KeV. The ion current used in the experiments was not determined because it was not calibrated, but a 1 pA probe was used.

Optical Characterization. Reflectance spectra were measured using a Confocal Raman microscope from WiTec (alpha300R). The samples were excited with a broad-band light source (Energetiq EQ-99XFC LDLC, spectrum 190–2100 nm). The optical beam was focused on the curvature of the tube with metasurfaces using a Zeiss “Epiplan-Neofluar” 100 \times objective (NA = 0.7 WD = 0.31 mm) with a linear polarizer operating in the visible range. To detect the reflected signal, the same objective was used to collect the light in the normal direction. The collected light was coupled to an optical fiber connected to an Ocean Optics Flame UV–vis Spectrometer, with a detection range from 400 to 980 nm. We first measured the reflection spectrum from a reference Ag mirror. Then, we measured the reflection spectrum from the nanorectangle array on the curved RUT. The reflectance spectra (reflectance) were calculated according to the following formula

$$\text{reflectance} = \frac{I_{\text{sample}} - I_{\text{sub}}}{I_{\text{source}} - I_{\text{BG}}} \quad (1)$$

where I_{sample} is the collected reflection spectrum of the nanostructures; I_{source} is the acquired spectrum of the broad-band light source, which is measured using a perfect reflector; I_{sub} is the substrate reflection, acquired from the unpatterned area of the Si/ SiO_2 substrate; and I_{BG} stands for the background counts, acquired by the used system.

■ ASSOCIATED CONTENT

Supporting Information

The Supporting Information is available free of charge at <https://pubs.acs.org/doi/10.1021/acsnanm.1c01178>.

The video file showing the formation of the tubes (MP4)

The dispersion relation of the multilayered metamaterial and the phase of E -field response of the supercell with the same hole sizes for planar and curved cases (PDF)

■ AUTHOR INFORMATION

Corresponding Author

Humeyra Caglayan – Faculty of Engineering and Natural Science, Photonics, Tampere University, 33720 Tampere, Finland; orcid.org/0000-0002-0656-614X; Email: humeyra.caglayan@tuni.fi

Authors

Mohsin Habib – Faculty of Engineering and Natural Science, Photonics, Tampere University, 33720 Tampere, Finland; orcid.org/0000-0002-6109-9468

Ibrahim Issah – Faculty of Engineering and Natural Science, Photonics, Tampere University, 33720 Tampere, Finland; orcid.org/0000-0001-7663-4972

Daria Briukhanova – Faculty of Engineering and Natural Science, Photonics, Tampere University, 33720 Tampere, Finland

Alireza R. Rashed – Faculty of Engineering and Natural Science, Photonics, Tampere University, 33720 Tampere, Finland

Complete contact information is available at: <https://pubs.acs.org/10.1021/acsnanm.1c01178>

Notes

The authors declare no competing financial interest.

■ ACKNOWLEDGMENTS

The authors acknowledge the financial support from the European Research Council (Starting Grant project aQUAR-iUM; Agreement No. 802986) and the Academy of Finland Flagship Programme (PREIN) (320165). This work made use of Tampere Microscopy Center facilities at the Tampere University.

■ REFERENCES

- (1) Yu, N.; Genevet, P.; Kats, M. A.; Aieta, F.; Tietjen, J.-P.; Capasso, F.; Gaburro, Z. Light propagation with phase discontinuities: generalized laws of reflection and refraction. *Science* **2011**, *334*, 333–337.
- (2) Yu, N.; Capasso, F. Flat optics with designer metasurfaces. *Nat. Mater.* **2014**, *13*, 139–150.
- (3) Khorasaninejad, M.; Chen, W. T.; Zhu, A. Y.; Oh, J.; Devlin, R. C.; Roques-Carmes, C.; Mishra, I.; Capasso, F. Visible wavelength planar metalenses based on titanium dioxide. *IEEE J. Sel. Top. Quantum Electron.* **2017**, *23*, 43–58.
- (4) Yoon, G.; Kim, K.; Kim, S.-U.; Han, S.; Lee, H.; Rho, J. Printable nanocomposite metalens for high-contrast near-infrared imaging. *ACS Nano* **2021**, *15*, 698–706.
- (5) Yoon, G.; Kim, K.; Huh, D.; Lee, H.; Rho, J. Single-step manufacturing of hierarchical dielectric metalens in the visible. *Nat. Commun.* **2020**, *11*, No. 2268.
- (6) Naqvi, A. H.; Lim, S. A beam-steering antenna with a fluidically programmable metasurface. *IEEE Trans. Antennas Propag.* **2019**, *67*, 3704–3711.
- (7) Chen, Q.; Das, D.; Chitnis, D.; Walls, K.; Drysdale, T.; Collins, S.; Cumming, D. A CMOS image sensor integrated with plasmonic colour filters. *Plasmonics* **2012**, *7*, 695–699.
- (8) Kim, I.; Kim, W.-S.; Kim, K.; Ansari, M. A.; Mehmood, M. Q.; Badloe, T.; Kim, Y.; Gwak, J.; Lee, H.; Kim, Y.-K.; Rho, J. Holographic metasurface gas sensors for instantaneous visual alarms. *Sci. Adv.* **2021**, *7*, No. eabe9943.
- (9) Lee, G.-Y.; Yoon, G.; Lee, S.-Y.; Yun, H.; Cho, J.; Lee, K.; Kim, H.; Rho, J.; Lee, B. Complete amplitude and phase control of light using broadband holographic metasurfaces. *Nanoscale* **2018**, *10*, 4237–4245.

- (10) He, M.; Guo, Y.; Li, C.; Tong, X.; Liu, H.; Li, G.; Zhang, L. Metasurface-based wide-angle beam steering for optical trapping. *IEEE Access* **2020**, *8*, 37275–37280.
- (11) Yu, N.; Aieta, F.; Genevet, P.; Kats, M. A.; Gaburro, Z.; Capasso, F. A broadband, background-free quarter-wave plate based on plasmonic metasurfaces. *Nano Lett.* **2012**, *12*, 6328–6333.
- (12) Zhang, F.; Yu, H.; Fang, J.; Zhang, M.; Chen, S.; Wang, J.; He, A.; Chen, J. Efficient generation and tight focusing of radially polarized beam from linearly polarized beam with all-dielectric metasurface. *Opt. Express* **2016**, *24*, 6656–6664.
- (13) Guo, Z.; Tian, L.; Shen, F.; Zhou, H.; Guo, K. Mid-infrared polarization devices based on the double-phase modulating dielectric metasurface. *J. Phys. D: Appl. Phys.* **2017**, *50*, No. 254001.
- (14) Hu, Y.; Luo, X.; Chen, Y.; Liu, Q.; Li, X.; Wang, Y.; Liu, N.; Duan, H. 3D-Integrated metasurfaces for full-colour holography. *Light: Sci. Appl.* **2019**, *8*, No. 86.
- (15) Ni, X.; Ishii, S.; Kildishev, A. V.; Shalaev, V. M. Ultra-thin, planar, Babinet-inverted plasmonic metalenses. *Light: Sci. Appl.* **2013**, *2*, e72.
- (16) Nakamoto, K.; Kurita, R.; Niwa, O.; Fujii, T.; Nishida, M. Development of a mass-producible on-chip plasmonic nanohole array biosensor. *Nanoscale* **2011**, *3*, 5067–5075.
- (17) Maier, S. A. *Plasmonics: Fundamentals and Applications*; Springer Science & Business Media, 2007.
- (18) Kurokawa, Y.; Miyazaki, H. T. Metal-insulator-metal plasmon nanocavities: Analysis of optical properties. *Phys. Rev. B: Condens. Matter Mater. Phys.* **2007**, *75*, No. 035411.
- (19) Miyazaki, H. T.; Kurokawa, Y. Squeezing visible light waves into a 3-nm-thick and 55-nm-long plasmon cavity. *Phys. Rev. Lett.* **2006**, *96*, No. 097401.
- (20) Ebbesen, T. W.; Lezec, H. J.; Ghaemi, H.; Thio, T.; Wolff, P. A. Extraordinary optical transmission through sub-wavelength hole arrays. *Nature* **1998**, *391*, 667–669.
- (21) Cetin, A. E.; Etezadi, D.; Galarreta, B. C.; Busson, M. P.; Eksioğlu, Y.; Altug, H. Plasmonic nanohole arrays on a robust hybrid substrate for highly sensitive label-free biosensing. *ACS Photonics* **2015**, *2*, 1167–1174.
- (22) Dolling, G.; Enkrich, C.; Wegener, M.; Soukoulis, C. M.; Linden, S. Simultaneous negative phase and group velocity of light in a metamaterial. *Science* **2006**, *312*, 892–894.
- (23) Zhang, S.; Fan, W.; Panoiu, N.; Malloy, K.; Osgood, R.; Brueck, S. Experimental demonstration of near-infrared negative-index metamaterials. *Phys. Rev. Lett.* **2005**, *95*, No. 137404.
- (24) Valentine, J.; Zhang, S.; Zentgraf, T.; Ulin-Avila, E.; Genov, D. A.; Bartal, G.; Zhang, X. Three-dimensional optical metamaterial with a negative refractive index. *Nature* **2008**, *455*, 376–379.
- (25) Matsui, T.; Miyazaki, H. T.; Miura, A.; Nomura, T.; Fujikawa, H.; Sato, K.; Ikeda, N.; Tsuya, D.; Ochiai, M.; Sugimoto, Y.; Ozaki, M. Transmission phase control by stacked metal-dielectric hole array with two-dimensional geometric design. *Opt. Express* **2012**, *20*, 16092–16103.
- (26) Matsui, T.; Nomura, T.; Miura, A.; Fujikawa, H.; Ikeda, N.; Tsuya, D.; Miyazaki, H. T.; Sugimoto, Y.; Ozaki, M.; Hangyo, M.; Asakawa, K. Wavefront control by stacked metal-dielectric hole array with variable hole shapes. *Opt. Express* **2013**, *21*, 6153–6161.
- (27) Prinz, V.; Seleznev, V.; Gutakovskiy, A.; Chehovskiy, A.; Preobrazhenskii, V.; Putyato, M.; Gavrilo, T. Free-standing and overgrown InGaAs/GaAs nanotubes, nanohelices and their arrays. *Phys. E* **2000**, *6*, 828–831.
- (28) Li, M. Self-rolled-up membrane (S-RuM) capacitors and filters for radio frequency communication. *University of Illinois at Urbana-Champaign* 2017, 1 22.
- (29) Huang, W.; Yu, X.; Froeter, P.; Xu, R.; Ferreira, P.; Li, X. On-chip inductors with self-rolled-up SiN x nanomembrane tubes: A novel design platform for extreme miniaturization. *Nano Lett.* **2012**, *12*, 6283–6288.
- (30) Xi, W.; Schmidt, C. K.; Sanchez, S.; Gracias, D. H.; Carazo-Salas, R. E.; Jackson, S. P.; Schmidt, O. G. Rolled-up functionalized nanomembranes as three-dimensional cavities for single cell studies. *Nano Lett.* **2014**, *14*, 4197–4204.
- (31) Huang, G.; Bolanos Quinones, V. A.; Ding, F.; Kiravittaya, S.; Mei, Y.; Schmidt, O. G. Rolled-up optical microcavities with subwavelength wall thicknesses for enhanced liquid sensing applications. *ACS Nano* **2010**, *4*, 3123–3130.
- (32) Medina-Sánchez, M.; Ibarlucea, B.; Perez, N.; Karnaushenko, D. D.; Weiz, S. M.; Baraban, L.; Cuniberti, G.; Schmidt, O. G. High-performance three-dimensional tubular nanomembrane sensor for DNA detection. *Nano Lett.* **2016**, *16*, 4288–4296.
- (33) Smith, E. J.; Xi, W.; Makarov, D.; Mönch, I.; Harazim, S.; Quiñones, V. A. B.; Schmidt, C. K.; Mei, Y.; Sanchez, S.; Schmidt, O. G. Lab-in-a-tube: ultracompact components for on-chip capture and detection of individual micro-/nanoorganisms. *Lab Chip* **2012**, *12*, 1917–1931.
- (34) Rashed, A. R.; Yildiz, B. C.; Ayyagari, S. R.; Caglayan, H. Hot electron dynamics in ultrafast multilayer epsilon-near-zero metamaterials. *Phys. Rev. B: Condens. Matter Mater. Phys.* **2020**, *101*, No. 165301.
- (35) Bin-Alam, M. S.; Reshef, O.; Mamchur, Y.; Alam, M. Z.; Carlow, G.; Upham, J.; Sullivan, B. T.; Ménard, J.-M.; Huttunen, M. J.; Boyd, R. W.; Dolgaleva, K. Ultra-high-Q resonances in plasmonic metasurfaces. *Nat. Commun.* **2021**, *12*, No. 974.
- (36) Ortuño, R.; García-Meca, C.; Rodríguez-Fortuño, F.; Martí, J.; Martínez, A. Role of surface plasmon polaritons on optical transmission through double layer metallic hole arrays. *Phys. Rev. B: Condens. Matter Mater. Phys.* **2009**, *79*, No. 075425.
- (37) Deneke, C.; Müller, C.; Jin-Phillipp, N.; Schmidt, O. Diameter scalability of rolled-up In (Ga) As/GaAs nanotubes. *Semicond. Sci. Technol.* **2002**, *17*, No. 1278.
- (38) Bermúdez-Ureña, E.; Steiner, U. Self-rolled multilayer metasurfaces. *ACS Photonics* **2019**, *6*, 2198–2204.
- (39) Wu, K.; Coquet, P.; Wang, Q. J.; Genevet, P. Modelling of free-form conformal metasurfaces. *Nat. Commun.* **2018**, *9*, No. 3494.
- (40) Johnson, P. B.; Christy, R.-W. Optical constants of the noble metals. *Phys. Rev. B: Condens. Matter Mater. Phys.* **1972**, *6*, 4370.
- (41) Malitson, I. H. Interspecimen comparison of the refractive index of fused silica. *J. Opt. Soc. Am.* **1965**, *55*, 1205–1209.

